Development of a multi-scale approach for modeling cast duplex stainless behavior

Maxime Mollens

To cite this version:

Maxime Mollens. Development of a multi-scale approach for modeling cast duplex stainless behavior. Material chemistry. Université Paris-Saclay, 2022. English. NNT : 2022UPAST168 . tel-03968930

HAL Id: tel-03968930
https://theses.hal.science/tel-03968930

Submitted on 2 Feb 2023

HAL is a multi-disciplinary open access archive for the deposit and dissemination of scientific research documents, whether they are published or not. The documents may come from teaching and research institutions in France or abroad, or from public or private research centers.

L'archive ouverte pluridisciplinaire **HAL**, est destinée au dépôt et à la diffusion de documents scientifiques de niveau recherche, publiés ou non, émanant des établissements d'enseignement et de recherche français ou étrangers, des laboratoires publics ou privés.

Development of a multi-scale approach for modeling cast duplex stainless steel behavior

Modélisation du comportement d'un acier inoxydable austéno-ferritique moulé vieilli par une approche multi-échelle

Thèse de doctorat de l'université Paris-Saclay

École doctorale n° 579, Sciences mécaniques et énergétiques, matériaux et géosciences (SMEMAG)
Spécialité de doctorat: Mécanique des matériaux
Graduate School : Sciences de l'ingénierie et des systèmes
Référent : ENS Paris-Saclay

Thèse préparée au **LMPS** - **Laboratoire de Mécanique Paris-Saclay** (**Université Paris-Saclay, CentraleSupélec, ENS Paris-Saclay, CNRS**), sous la direction de **Stéphane ROUX**, directeur de recherche CNRS, du co-encadrement de **François HILD**, directeur de recherche CNRS, de **Adrien GUERY**, ingénieur-chercheur (EDF R&D) et de la supervision de **Dominique LOISNARD**, cadre technique (EDF R&D)

Thèse soutenue à Paris-Saclay, le 21 novembre 2022, par

Maxime MOLLENS

Composition du jury

Membres du jury avec voix délibérative

Stéphane Berbenni Directeur de recherche CNRS, LEM3, Université de Lorraine	Président
Maurine Montagnat Directrice de recherche CNRS, Institut des Géo-sciences de l'Environnement, Université Grenoble Alpes	Rapporteur, Examinateur
Lionel Germain Professeur, LEM3, Université de Lorraine	Rapporteur, Examinateur
Johan Hoefnagels Professeur, Eindhoven University of Technology	Examinateur

THESE DE DOCTORAT

NNT : 2022UPAST168

Remerciements

"J'ai toujours honoré ceux qui défendent
la grammaire ou la logique.
On se rend compte cinquante ans après
qu'ils ont conjuré de grands périls."
Marcel Proust
À la recherche du temps perdu

Je ne saurais commencer cet avant-propos sans rappeler que l'aboutissement de cette thèse est un travail collectif. L'origine des contributions à la réalisation de ce manuscrit a une portée si grande qu'il m'est difficile de citer ici tout le monde sans m'exposer à un risque d'oubli plus que certain. Ainsi, que toutes les personnes avec qui j'ai pu partager des moments d'amitié et de fraternité durant ces trois années soient informées ici de leur bienfaisance, qui m'inspire la plus sincère gratitude.

Je tiens à remercier Monsieur Stéphane Berbenni de m'avoir fait l'honneur de présider le jury ainsi que Messieurs Johan Hoefnagels et Dominique Loisnard pour avoir accepté de faire partie de ce jury . Merci à Madame Maurine Montagnat et Monsieur Lionel Germain pour leur lecture attentive du manuscrit et plus globalement pour avoir accepté le rôle difficile de rapporteur.

Je ne pourrais cependant pas rester totalement impartial. Je dois une majeure partie de ma motivation durant ces trois années à l'encadrement de l'équipe Eikologie, qui a accepté de diriger cette thèse. Les deux personnes qui en sont responsables ont su créer une atmosphère propice à un investissement profond de ses membres où la science et la recherche sont bien éloignées de l'image d'Épinal du chercheur isolé travaillant seul derrière son bureau. Je témoigne donc ici toute ma gratitude envers Stéphane Roux qui affiche un dévouement sans faille à la recherche et aux doctorants qu'il encadre. Ses conseils, ses encouragements, son ouverture d'esprit et ses idées toujours plus originales en réponse aux questions (qui n'ont parfois même pas été posées !) resteront, pour moi, une référence dans toute démarche scientifique que j'entreprendrai. J'exprimerai difficilement moins de gratitude envers François Hild. Son dynamisme et son enthousiasme lors des réunions hebdomadaires ou de nos conversations sont source de motivation. François n'est pas non plus avare lorsqu'il s'agit d'apporter de l'aide, des conseils avisés ou pour me rappeler que "ce qu'il y a de génial avec la corrélation d'images [numériques] (globale bien entendu !) c'est que même quand on pense que ça ne va pas fonctionner, on est surpris de voir que ça fonctionne !".

La vie de doctorant fut aussi agréable grâce à tous les collègues du LMPS avec qui discuter autour d'un café m'a permis d'exercer régulièrement mes talents de protestataire du café de l'angle de la rue pendant ces trois années. Ceux qui ont compris que j'ai le goût pour l'éristique plutôt qu'un mauvais caractère et qui ont partagé ces moments de discussions avec moi (et qui ont parfois hérité de cette pathologie) sont ici chaleureusement remerciés.

J'ai eu la chance de bénéficier d'un cadre tout aussi engageant au sein du département MMC d'EDF R&D. La confiance et la liberté qui m'ont été accordées sont à l'origine de la bonne synergie qui a opéré entre tous les acteurs de cette thèse. Pour cela je remercie grandement Adrien Guery sans qui ce travail n'aurait pas été la même. Il a su remettre en perspective et discuter les résultats aux moments opportuns. Ses conseils et idées dans l'articulation des travaux de recherche en lien avec les objectif d'un partenaire industriel ont toujours été une aide précieuse.

J'ai aussi eu la chance d'avoir à ma disposition d'excellentes équipes *discussion* à EDF, que ce soit au sein du groupe Mécanique ou du groupe Métallurgie aux Renardières. Il fait bon travailler dans ce type d'ambiance et je suis heureux de poursuivre la micromécanique avec eux à la suite du doctorat. Merci aux habitants du MAI, et au bâtiment C24 pour l'accueil chaleureux que j'ai reçu dès mon arrivée en thèse et pour les amitiés que j'ai pu y nouer.

Enfin merci à ma famille et à Eva d'avoir dû endosser le rôle le plus difficile dans la rédaction de ce manuscrit. Je ne serais pas parvenu jusqu'ici sans vous et pour cela, je vous dédie ce manuscrit.

Contents

“Nos biens sont protégés par la loi,
est-il acceptable que la vie ne le soit pas ?”
Aurélien Barrau

Résumé français étendu

Le suivi de l'intégrité mécanique des composants des réacteurs à eau préssurisée est d'une importance majeure pour justifier de leur bon fonctionnement sur le long terme. Certains de ces composants sont soumis à un environnement qui peut altérer leurs propriétés. C'est le cas des composants moulés en acier inoxydable austéno-ferritique du circuit primaire principal dont les propriétés mécaniques sont dégradées au cours du temps par un maintien constant à une température élevée autour de 300°C. Ce maintien en température est à l'origine d'une modification de la microstructure d'une des deux phases constitutives de l'alliage (la ferrite) qui se manifeste à l'échelle du composant par une fragilisation du matériau. Les mécanismes physiques à l'origine de cette fragilisation sont bien connus et ont été abondamment étudiés [Bon90, Cho91]. Des modèles empiriques permettant d'évaluer la cinétique de vieillissement en fonction des conditions de température et de la composition chimique de l'alliage ont été proposés [Cho91]. Cependant, les mécanismes de déformation et d'endommagement pouvant mener à la rupture ainsi que leur évolution avec le vieillissement ne sont pas entièrement connus. Ils résultent de la microstructure complexe de ces alliages formée par l'agencement des deux phases et de leur différence de comportement. Plusieurs études ont été menées pour tenter de proposer un modèle incluant les répartitions locales des champs mécaniques entre les deux phases [Ver96, Bug99]. Cependant, aucune donnée locale mesurée n'a permis de confirmer la véracité de ces modèles. L'objectif de l'étude menée dans cette thèse est de proposer un modèle de comportement multi-échelle intégrant les différentes propriétés de la microstructure en s'appuyant sur de nouvelles caractérisations expérimentales aux échelles d'intérêt. Ces caractérisations visent à lier des informations microstructurales acquises par diffraction d'électrons rétrodiffusés (EBSD) à des champs mécaniques mesurés par corrélation d'images numériques (CIN) pendant un essai *in situ* dans un microscope électronique à balayage (MEB).

Les cartographies d'orientations cristallographiques mettent en évidence une imbrication complexe de l'austénite (Figure 1(a,b)) et de la ferrite (Figure 1(c,d)). Leur répartition spatiale et les paramètres liant la cristallographie des deux phases sont difficiles à décrire de prime abord. Pourtant, l'austénite semble présenter des propriétés remarquables sur ces cartes, notamment une forme très allongée. La surface totale caractérisée (plus de 100 mm^2) ainsi que des outils de traitement des orientations spécifiques développés ont permis d'en donner une lecture à la lumière des mécanismes de solidification (Chapitre 2). La structure du matériau est formée de plusieurs échelles imbriquées les unes dans les autres et couvrant plusieurs ordres de grandeur allant de la dizaine de nanomètres (échelle où les mécanismes de vieillissement sont décrits) au millimètre. Afin de s'affranchir de la complexité apparente de la structure du matériau, une description simplifiée intégrant les caractéristiques d'intérêt pour la mécanique a été proposée.

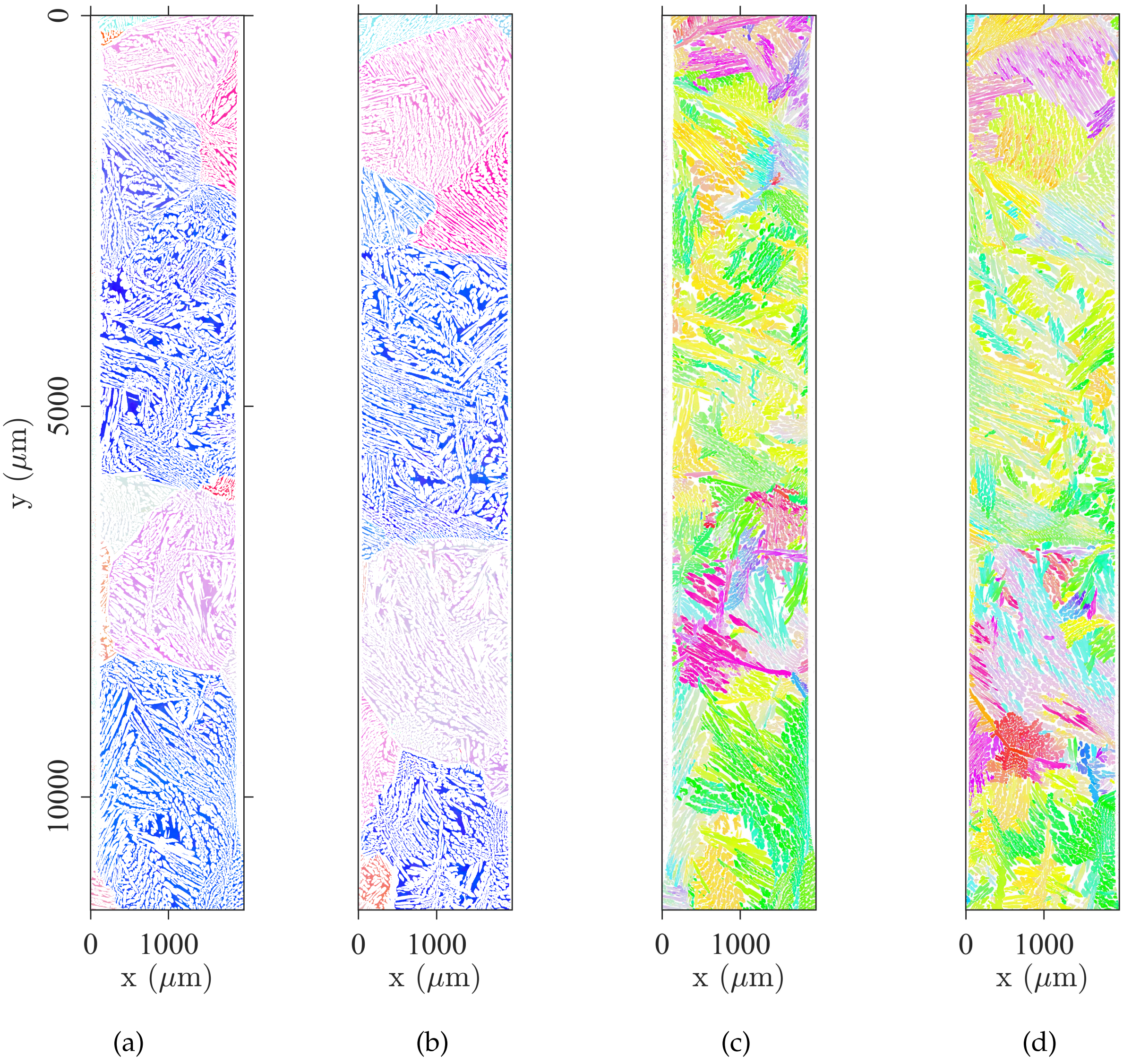

(a) (b) (c) (d)

Figure 1: Microstructure d'un acier inoxydable austéno-ferritique moulé vieilli acquise sur les deux faces d'une éprouvette d'un millimètre d'épaisseur. (a,c) Orientations ferritiques seulement, montrant la trace des grains ferritiques équiaxes et millimétriques obtenus lors de la première phase de solidification. La majorité de ces grains se retrouve sur les deux faces. (b,d) Orientations austénitiques montrant le réseau de lattes qui a crû à partir de grains ferritiques. Certains paquets de lattes se retrouvent d'une face à l'autre mais le réseau est globalement plus complexe à décrire en trois dimensions.

La plus petite échelle considérée dans la description mécanique est celle des lattes. Sa taille caractéristique s'étend de dix à cent micromètres. Elle correspond à la plus petite échelle où les deux phases peuvent localement être associées à une structure et une orientation cristallographique relativement homogène. C'est aussi l'échelle où la structure de chaque phase présente une morphologie très allongée donnant son nom à cette échelle. La seconde échelle d'intérêt pour la mécanique est le paquet de lattes. Cette échelle est formée par un ensemble de lattes adjacentes ayant une orientation morphologique et cristallographique commune. Ces aggrégats peuvent être formés d'une à plusieurs dizaines de lattes et par conséquent héritent de la plus grande longueur caractéristique de la plus petite échelle (de la dizaine à plusieurs centaines de micromètres). Comme les propriétés morphologiques et cristallographiques des phases sont homogènes à l'intérieur d'un aggrégat, celui-ci peut être homogénéisé de manière acceptable d'un point de vue mécanique connaissant ses propriétés. Un traitement spécifique des cartes d'orientation acquises par EBSD a permis de montrer que ces aggrégats sont, au premier ordre, décrit par un stratifié ferrite-austénite, dont les proportions de phase locales et la direction des plis dans le volume sont connues par la seule donnée des cartes d'orientations cristallographiques mesurées (Chapitre 2). La plus grande échelle mesurée sur ces cartes est l'échelle du grain de ferrite. Elle regroupe un ensemble de paquets de lattes adjacents ayant une orientation crystallographique de la phase ferritique commune. Les frontières des aggrégats de cette échelle correspondent à celles d'un réseau polygonal classique de grains équiaxes millimétriques issus de la première phase de solidification. Ce type de réseau a fait l'objet de nombreuses études et est classiquement reproduit par une téssélation de Voronoi, par exemple [Zeg07].

Une fois toutes ces échelles décrites, il convient d'observer comment elles intéragissent sous contrainte et comment un chargement macroscopique est localement redistribué. Pour cela, les cartographies d'orientation ont été superposées avec des champs mécaniques mesurés lors d'essais *in situ* dans un MEB sur plusieurs éprouvettes représentatives de différents états de vieillissement (Chapitre 3). Ces champs ont été obtenus par CIN et bénéficient à la fois d'une forte résolution et d'une grande dimension afin de couvrir au mieux toutes les échelles décrites précédemment. Les corrections d'imageries inhérentes à la technique d'acquisition et un appairage précis avec les cartographies EBSD (Figure 2) ont été menés afin de garantir la justesse et la richesse de l'information mesurée.

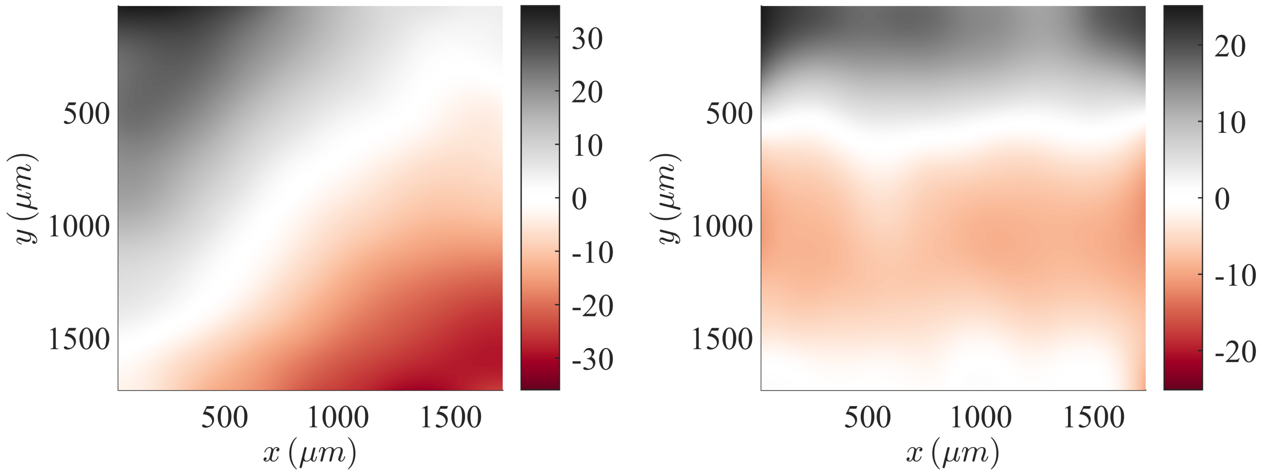

(a) $U_x - \overline{U_x}$ (μm) ($\overline{U_x} = 50.4$ µm) (b) $U_y - \overline{U_y}$ (μm) ($\overline{U_y} = -13.7$ µm)

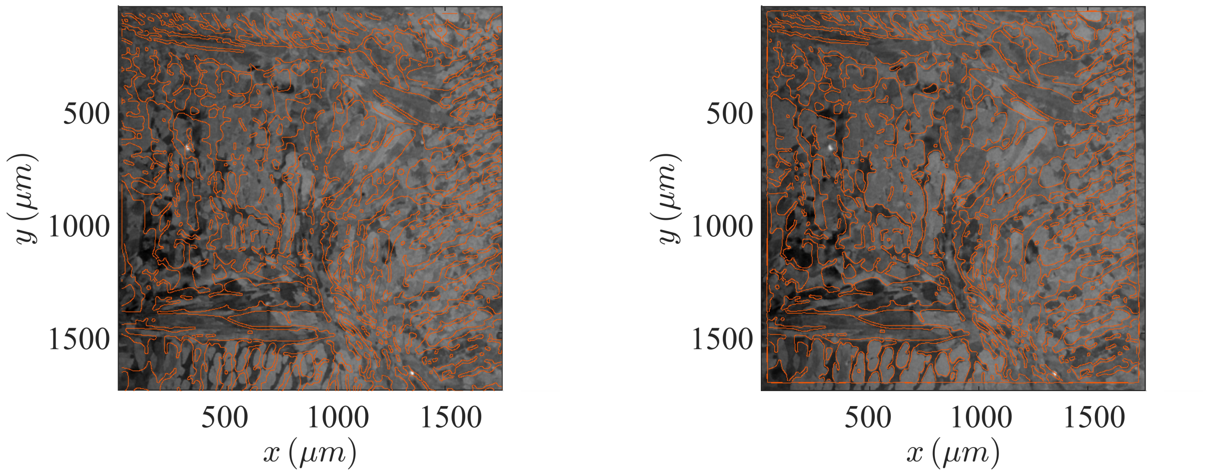

(c) (d)

Figure 2: Appairage des images MEB avec les cartographies EBSD par CIN régularisée sur les joints de grains. (a) Correction dans la direction $\boldsymbol{x}$ (µm). (b) Correction dans la direction $\boldsymbol{y}$ (µm). Joints de grains repérés par EBSD superposés sur une image MEB utilisée pour les mesures de champs avant (c) et après (d) appairage.

La mise en relation des champs de déformation et de la microstructure a permis de mettre en évidence la répartition des déformations dans les deux phases au cours d'essais de traction (Chapitre 3). Dans le cas du matériau non vieilli (Figure 3(a)), il a été montré que la déformation suit l'orientation morphologique des paquets de lattes. Les mécanismes de déformation des deux phases à la plus petite échelle étant différents, la déformation est plus forte dans l'austénite. Malgré un niveau moyen de déformation plus faible, la ferrite accomode la majorité des déformations aux joints de grains avec l'austénite et ne semble nullement empêcher certaines zones d'être déformées en raison de sa faible proportion de phase et donc de sa faible influence mécanique relative. Il en résulte que la déformation est globalement diffuse à l'échelle des grains ferritiques.

Pour les matériaux les plus vieillis (Figure 3(b)), les mécanismes de déformations sont drastiquement modifiés. L'influence relative de la phase ferritique dans la distribution des déformations est augmentée par le vieillissement qui durcit et fragilise fortement cette dernière. La déformation est fortement contrainte aux joints de grain ferrite-austénite pour cet état. En conséquence, les zones fortement déformées sont localement plus éparses et les zones fortement contraintes rendent le comportement macroscopique moyen endommageant de manière prématurée. Il a aussi été observé qu'une contrainte plus importante est exercée sur les frontières délimitant les aggrégats correspondant aux grains ferritiques primaires avec le vieillissement.

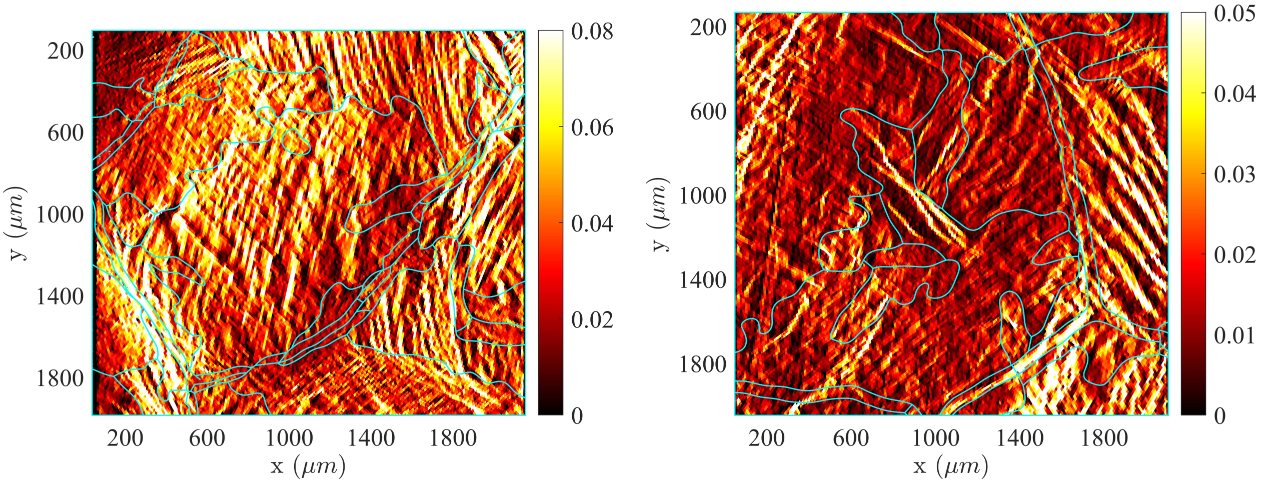

(a)

(b)

Figure 3: Exemples de champs de déformation mesurés pendant un essai *in situ* dans la direction de sollicitation. (a) Matériau à l'état de réception pour une déformation macroscopique imposée de 4%. (b) Matériau vieilli 10000 h à 350°C pour une déformation macroscopique imposée de 2%.

Afin d'inclure l'ensemble des observations dans un modèle de comportement mécanique, il a été choisi de s'appuyer sur une approche multi-échelle décrivant les différentes échelles de la microstructure ainsi que leurs paramètres influant sur les champs mécaniques. La plus petite échelle est décrite par un comportement de plasticité cristalline de type Méric-Cailletaud [Mer91a, Mer91b]. Cette loi est introduite dans une représentation géométrique schématique du paquet de lattes sous forme de stratifié (Figure 4) incluant les paramètres morphologique et cristallographique mesurés expérimentalement. Le comportement moyen du stratifié est ensuite assimilé à une loi de plasticité anisotrope de type Cazacu-Barlat [Caz01]. Il a été montré que la paramétrisation de cette loi permettait de reproduire fidèlement le comportement asymptotique moyen du paquet de lattes. Enfin, un générateur de microstructure s'appuyant sur les mécanismes de formation des deux phases a été proposé afin de créer une paramétrisation spatiale cohérente des paquets de lattes et ainsi d'effectuer une transition d'échelle jusqu'à celle des grains ferritiques.

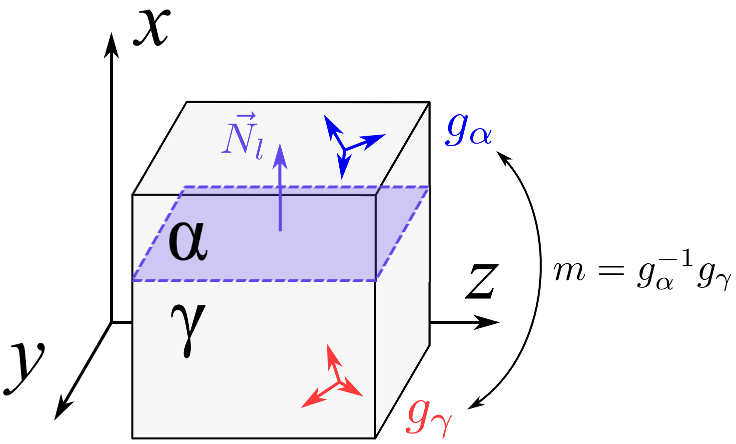

Figure 4: Modèle géométrique de l'échelle intermédiaire décrivant les paquets de lattes.

L'étude menée a permis de comprendre et décrire la microstructure des aciers austéno-ferritiques utilisés dans la fabrication des conduites du circuit de refroidissement primaire des REP en mettant à profit les avancées technologiques dans les techniques de caractérisation microstructurale. Ces cartographies d'orientations ont permis d'enrichir l'information des champs de déformation mesurés et de comprendre les mécanismes mis en jeu dans chaque phase et à chaque échelle à différents états de vieillissement. L'ensemble des données expérimentales acquises a permis d'orienter la modélisation vers une nouvelle approche incluant l'ensemble des paramètres influents. Le schéma multi-échelle proposé doit cependant encore être recalé aux différentes échelles. En particulier, l'identification des paramètres de loi de plasticité cristalline reste un défi en raison du manque d'information dans le volume des éprouvettes caractérisées. Afin de pallier cette difficulté, il serait séduisant, dans le futur, d'extrapoler l'information microstructurale de surface dans la profondeur de manière fiable. En ce sens, les techniques d'apprentissage développées récemment dans l'analyse de données peuvent fournir une première approche. D'autres techniques de caractérisations peuvent aussi venir compléter les mesures de champs dans l'identification de ces paramètres. Les essais d'indentation combinés à des mesures de topographie ont reçu une attention particulière et pourrait être une alternative intéressante mais elles introduisent leurs propres difficultés qu'il conviendra alors de maîtriser.

Chapter 1

General introduction

1.1 Industrial background

Representing approximately 77% of France total electrical power generation in 2016, the 56 nuclear reactors in the country are of great importance for ensuring safe and steady production. Existing nuclear production is also to play a significant role in executing plans to meet the energy transition goals [RTE22]. With an average age exceeding thirty years and feedback from security breaches such as the Fukushima disaster, considerable investments were made to reinforce nuclear power plant security and make an extended lifetime feasible. In this respect, EDF is committed to leading a major program toward power plants. One of the main focuses of this program is to master and anticipate the wear and tear of the structural components of plants accurately. The main primary cooling circuit (Figure 1.1) of pressurized water reactors (PWR) in nuclear power plants is one of the critical systems. The circuit handles hot and pressurized water transfer from the vessel to the steam generator. It must fulfill two main functions: carry the thermal energy accumulated by water and regulate the temperature inside the vessel by controlling water flow. However, the continuous pressure and thermal conditions induce high constraints on the circuit components. In particular, the Cast Duplex Stainless Steel (CDSS) (also called austenoferritic stainless steel from its two constituting iron allotropes) out of which pipes and elbows (Figure 1.2), between the steam generator and the vessel, are made undergo a microstructural transformation at a nanometric scale slowly modifying the macroscopic material response. This transformation combines the "475°C embrittlement" [Gro73] typically found in chromium steels and the precipitation of the Ni- and Si-enriched G-phase [Lea92, Aug90]. It leads to a hardening of the ferritic phase and a loss of toughness of the material [Bon90, Cho91]. Every ten years, nuclear power plant utilities must demonstrate that thermal aging effects are not impairing the safe operation of main primary coolant systems for ten more years. The demonstration involves non-destructive inspection to assess that no evidence of crack initiation, either by fatigue or corrosion, is found.

While the effect of aging on mechanical properties is well-known and is accurately estimated for a wide range of chemical compositions thanks to the extensive database set up by EDF [Leo13], the physical description of the deformation mechanisms leading to fracture remains unclear. At the scale describing the interface between the two phases, a modification of deformation and damage mechanisms with aging has clearly been identified [Jol92, Ver97, DG98, Bug00]. However, the striking scatter observed in crack nucleation [Jol92] and some tensile properties are still unexplained by the developed models. One of the leading causes could be that the microstructure description remained too coarse despite its very peculiar properties.

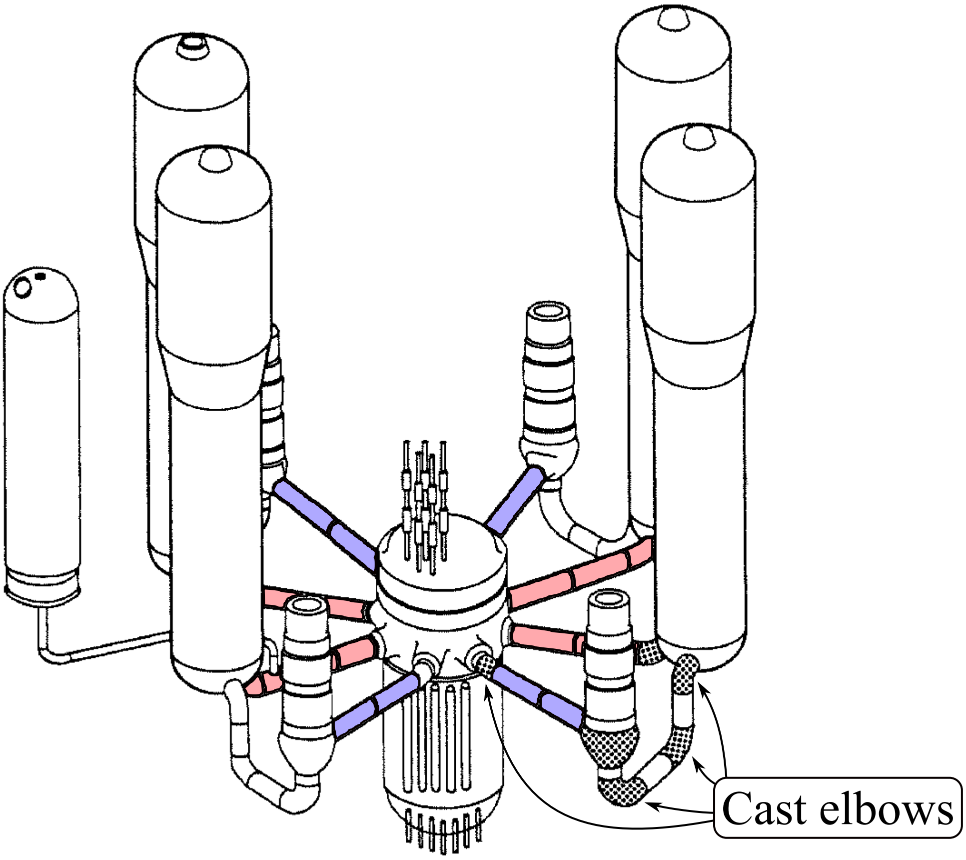

Figure 1.1: Schematic view of a pressurized water reactor. Pipings are made of duplex stainless steel and are formed by means of a casting process. Water in cold legs (blue pipes) is about 286°C while it reaches 325°C in hot legs (red pipes). Adapted from [Bug00].

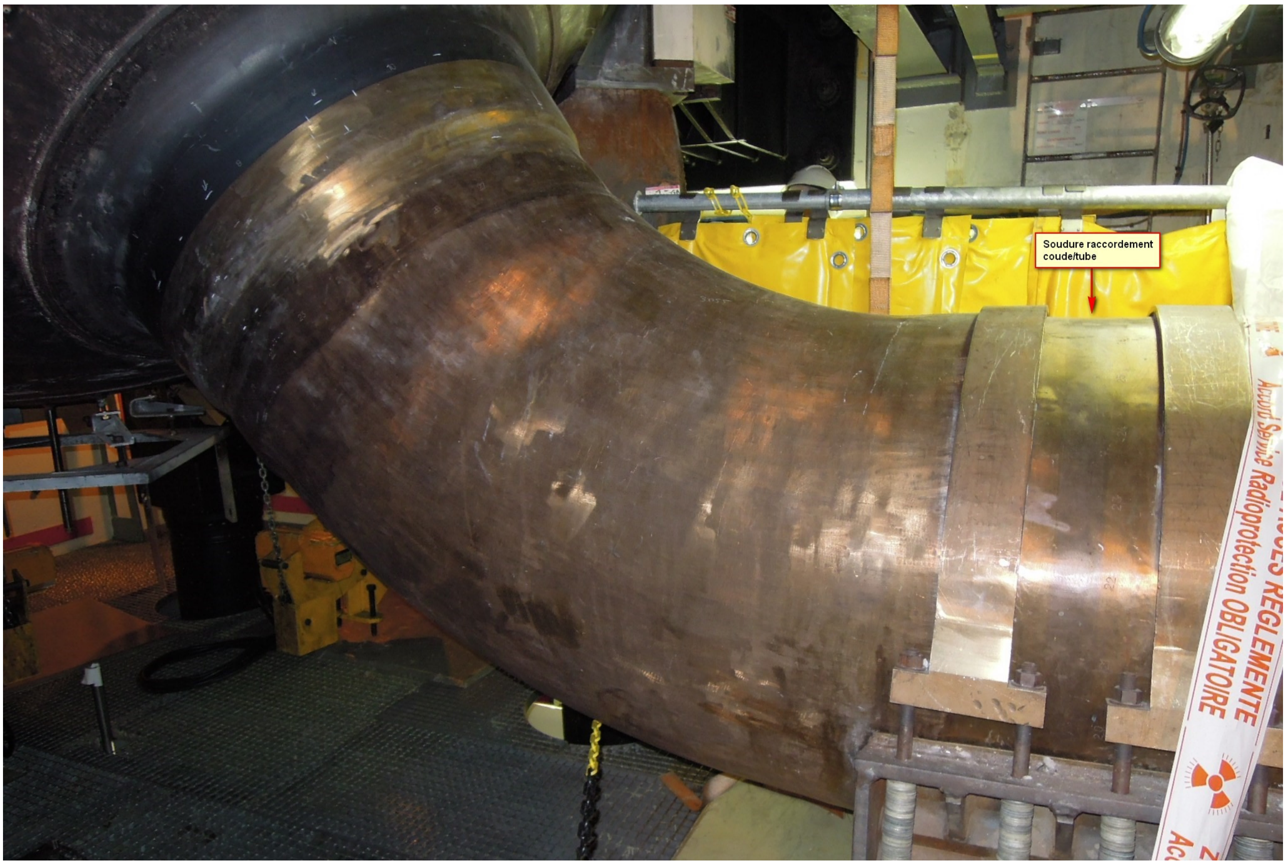

Figure 1.2: Photography of an elbow in its operating environment.

1.2 Monitoring and predicting cast component aging

Models already proposed for estimating the CDSS response under mechanical loadings [Ver97, DG98, Bug00, Mci00] are based on observations in a wide range of scales. At the beginning, different types of mechanical tests allowed to acquire data for characterizing the material behavior taking into account a large number of parameters (*e.g.*, chemical composition or aging duration). Microstructural analyses supported the understanding of physical mechanisms at the origin of a change in behaviour with thermal aging. Finally, microstructural observations were used as a basis to develop consistent models aiming at accurately reproducing behaviors acquired in experimental tests. In order to explain the source of discrepencies between these models and experimental observations, the basics of aging characterization are set out in the next parts. Then, empirical models to follow thermal aging kinetics are explained and a succinct description of mechanical models developed in earlier studies is given to draw up new ways of improvements.

1.2.1 Kinetics of spinodal decomposition and G-phase precipitation

Spinodal decomposition of ferrite was identified by [Fis53] as the formation of an α′-phase, which is rich in chromium, inside the α-phase. Embrittlement of the ferritic phase and by extension of duplex stainless steels has longly been attributed to the separation of the two phases. The progress of decomposition is characterized by the growth of α′ islets and wavelength of spatial fluctuation of Cr atoms between α and α′ phases which increases with aging. Previous studies using atome probe tomography [Dan04, Par11, Par15, Bad18] showed that the decomposition kinetics is highly dependent on the molybdenum content and that the decomposition has not yet reached a coalescence regime after a reasonable operating time (*ca.* 60 years).

Besides spinodal decomposition, G-phase precipitation is also observed in components of the primary circuit [Aug90, Par15, Bad18]. G-phase contribution to thermal aging effects is still to be proven. Some authors claimed that its contribution to ferrite embrittlement was negligible [Chu90, Li13b] while other studies suggested the opposite conclusion [Aug90, Mil90, Bad18]. Nonetheless, an interaction between spinodal decomposition and G-phase growth has been demonstrated [Par15, Bad18] and recent studies are more likely to support their major contribution [Bad19, Kon22].

Figure 1.3 presents atome probe tomography (APT) reconstruction illustrating the two previous processes occuring in the α-phase during thermal aging. Each view corresponds to a 45 x 45 x 10 nm volume integrated along the third direction to produce a 45 x 45 nm image that is representative of the 3D atomes distribution. Figure 1.3 (a-b) displays a significant evolution of the chromium distribution from an almost random distribution of atoms in the ferritic lattice to the formation of two distinct phases: a first Cr-rich phase (α′) and a second Cr-depleted phase (α). APT reconstructions also emphasize the formation of G-phase inclusions (Figure 1.3 (c-d)). After thermal aging, Ni, Si, Mn and Mo atoms (constituting the G-phase crystallographic system) form small clusters in the ferritic matrix [Bad18].

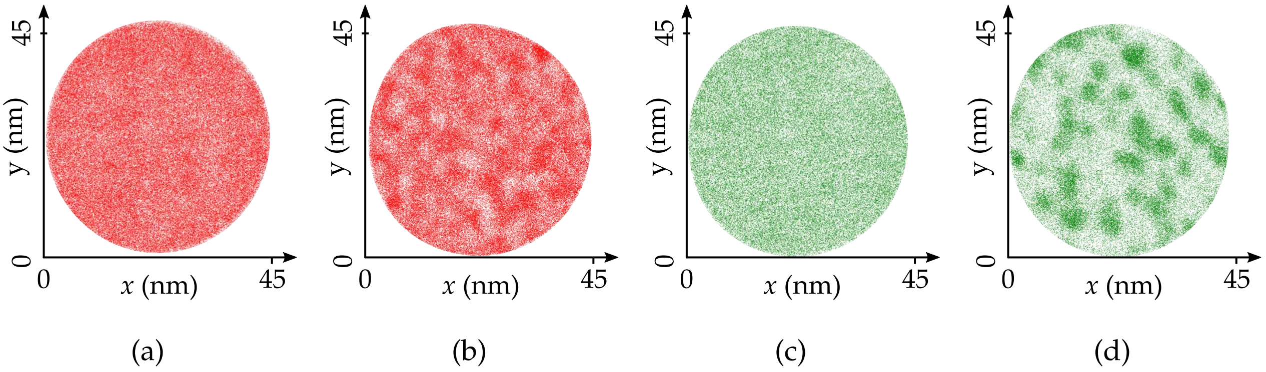

Figure 1.3: Spinodal decomposition and G-phase precipitation with aging observed using APT in a small ferrite volume of a molybdenum-bearing duplex stainless steel. The volume displayed is 45 x 45 x 10 nm^3. (a) As-received distribution of Cr atoms. (b) Cr atoms distribution after 100000 h at 350°C. (c) As-received distribution of Ni, Si, Mn and Mo atoms. (d) Distribution of Ni, Si, Mn and Mo atoms after 100000 h at 350 °C. Image courtesy of Badyka [EDF R&D/MMC]

As the mechanisms leading the transformation are thermally activated, accelerated aging is possible by subjecting the material to temperatures higher than 323°C (of the hot leg of the circuit) [Par11]. This allows in-service component state to be reproduced and to evaluate further the change of mechanical properties with thermal aging. Despite its discussed involvment in duplex stainless steel embrittlement, G-phase displays different properties when samples are subjected to accelerated thermal aging above 350°C [Nov09, Bad18]. As a precaution, this limit temperature was selected for accelerated aging.

1.2.2 Characterization of thermal aging effects

The presence of cast components defects is the source of potential failure in CDSS. They are inherent to the forming process. The expertise of manufacturers allows the presence of these defects such as shrinkage cavities or blowholes to be limited but they are still likely to be present. Defects are thus tolerated if the utility can justify that in-service conditions will not result in an unstable propagation of cracks initiating from these defects [Min10, LD15]. An unstable propagation may however be promoted by CDSS embrittlement induced by thermal aging. Hence, mechanical characterization is conducted to follow the behavior change with aging as part of the safe operation assessment. Because it is the most direct method to ensure that the material withstand mechanical constraints to which it is subjected ductile tearing resistance was measured on compact tension (CT) specimens [Pok06, LD15]. Multiple specimen sizes were considered to account for the large microstructural properties and subsequent lack of representativeness of standard sized specimens. They were the first evidence of the effect of thermal aging on the mechanical behavior of CDSS. Nonetheless, the number of specimens and the multiplication of tests needed to account for microstructural effects required more representative material than available. To address ductile tearing tests execution complexity and restrictions in available amounts of material, Charpy impact tests were intensively used as a substitute and relations between ductile tearing resistance parameters and Charpy impact energy were developed [LD15]. The latter constitute an effective method to determine CDSS mechanical properties change with thermal aging [Mag82, Tra82, Bon90, Cho91, Chu92, Sah09, LD15, Col22]. At temperatures close to in-service conditions (*ca.* 300°C) and depending on the chemical composition, the Charpy toughness may decrease by a factor of 10 [Bon90, DG98]. The toughness change with aging has a similar kinetics as that of spinodal decomposition in considered time periods but the material will tend towards saturated mechanical properties while spinodal decomposition is endless [Par15]. Yet, an asymptotic behavior is unlikely to be reached in a realistic operating time. Figure 1.4 illustrates the kinetics of room temperature Charpy impact energy drop with aging duration. According to the time-temperature superposition principle, the reported change is also representative of in-service conditions.

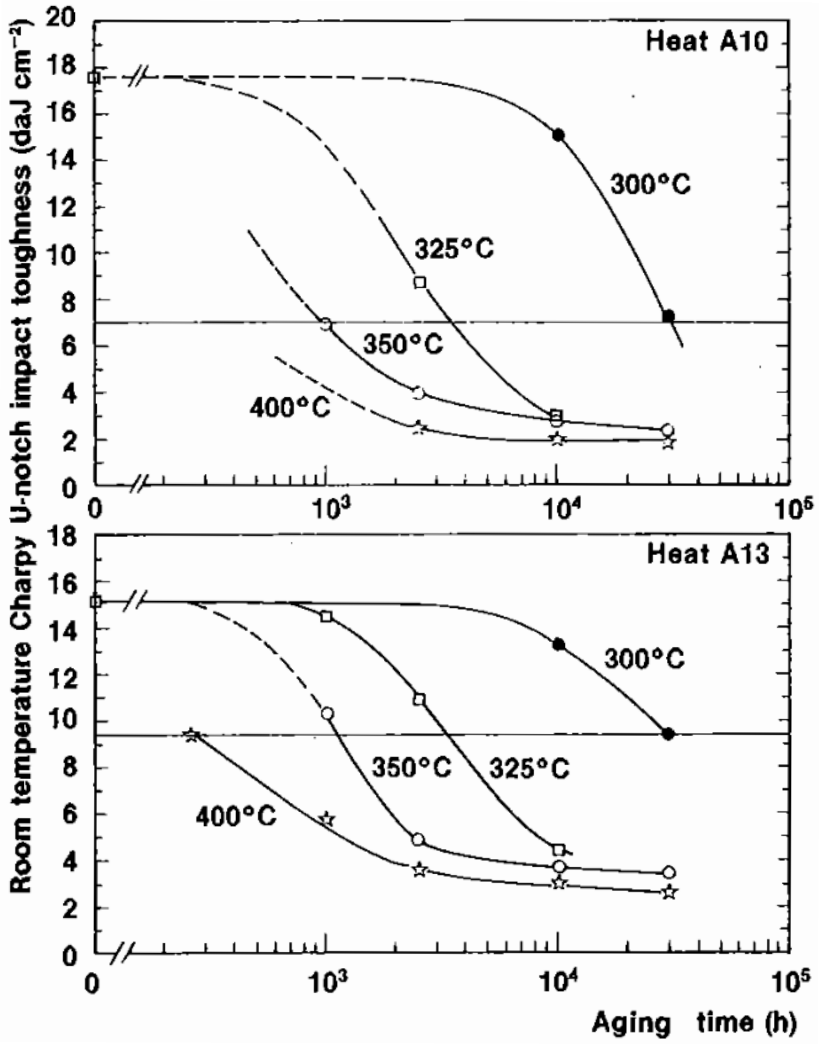

Figure 1.4: Room temperature Charpy impact toughness change with thermal aging at different temperatures for two different alloys denoted A10 and A13 [Bon90].

Thermal aging also impacts other mechanical properties that are conventionally measured. Since the microstructural transformation induces an embrittlement, hardness is indicative of the aged state [Kaw97, Che00, Tan03, Li13a, Jan14, Liu18, Huo19, Zha19b]. In particular, the ferritic phase hardness measured by nanoindentation is directly correlated to aging duration. Tensile tests are another way to extract mechanical data. Again, stress-strain curves are influenced by thermal aging. For instance, the changes of yield stress or hardening parameters are followed [Bug00, Mci00]. Such mechanical characterizations are fully integrated in current EDF programs to monitor thermal aging. They include samples extracted from real parts that endured in service conditions or from dedicated ingots subjected to accelerated aging. Such approaches are costly in the amount of material used and available resources are limited especially for real component samples. With this in mind, some less indirect methods to evaluate the α-phase changes have also been developped. For example, Tane *et al.* [Tan03] measured the elastic constants of the ferritic phase by means of resonant ultrasound spectroscopy and a micromechanical model to highlight their dependence to aging time at 400°C. Other authors also demonstrated a correlation between mechanical and electrochemical behavior [Cha10, Huo19] or changes of Volta potentials between the two phases using Kelvin probe and magnetic force microscopy [Ör17].

EDF programs rely mainly on Charpy impact tests and ductile tearing tests from which empirical J-Δa laws are extracted. They provide necessary data to estimate the energy that is required to initiate crack propagation from a defect. Particular precaution is given to establish a representative statistics (*i.e.,* specimen size, geometry and number of tests to perform) given the material peculiar microstructure. Further, a huge monitoring campaign making use of the Seebeck effect [Cos97, Kaw02] is conducted. Tests making use of the effect consist in measuring the material thermoelectrical power (TEP), *i.e.,* its ability to generate an electric flux under an applied thermal gradient. The TEP is defined as the ratio between the applied thermal gradient and the resulting electrical gradient. As the Seebeck effect is related to the crystal network and therefore to the steel microstructure, any change such as the spinodal decomposition and the precipitation of G-phase will modifiy the material TEP. From these observation, charts are built to assess a component aged state (locally). The benefits of such method are its simplicity and non-destructive aspect. It may be applied directly on operating components. Yet, as any structural change may modify the TEP (*e.g.,* plastic yielding), it should be ensured that a difference of power is the result of aging only.

1.2.3 Modeling thermal aging

From the previous observations, EDF developped an integrity assessment program of CDSS components of the main primary cooling system. The necessity to estimate fracture toughness for a variety of configurations including different chemical compositions and aging durations conducted to the development of predictive empirical formulae. The impact energy estimated from aforementionned laws is compared to fracture mechanics calculations relying on a Finite Element (FE) model of the components. The computations are carried out on the basis of a reference crack size (extracted from experimental observations on manufactured cast elbows) and a mechanical behavior defined from a master curve determined experimentally. The input law for such computations is highly simplified and suffer from experimental uncertainties related to parameters identification in tensile tests of CDSS [Mic94, Leo13]. Consequently, multiple studies were conducted with the aim to develop a reliable model based on an accurate description of CDSS deformation mechanisms [Ver97, DG98, Bug00, Mci00]. The setting up of embrittlement kinetics are detailed hereafter before introducing the micromechanics based models that were already suggested. A critical review of their hypotheses and limitations is also proposed.

1.2.3.1 Mechanical property changes

As previously discussed, impact toughness properties evolve between initial and saturated values as a function of the aging duration and material parameters. The change of mechanical properties results from a modification of the ferritic phase microstructural properties. A strategy from PWRs utilities to estimate the kinetics of embrittlement was to set up database of impact resistance properties as functions of time for different CDSS grades [Sla83, Bon90, Cho90, Pum90]. From these data, empirical models of the kinetics were built. For instance, the decrease of the Charpy impact energy C_V was estimated as function of time and temperature [Cho91]:

$$\log_{10}(C_V) = \log_{10}(C_{Vsat}) + \beta(1 - \tanh[(P - \theta)/\alpha]) \tag{1.1}$$

where $\beta = (\log_{10}(C_{Vint}) - \log_{10}(C_{Vsat})/2$, C_{Vint} is the reference impact energy at room temperature, C_{Vsat} the saturated impact energy at room temperature, θ and α experimental constant linked to C_{Vsat}. P is the aging parameter describing the time-temperature superposition based on a reference temperature T_{ref}.

$$P = log_{10}[t] + \frac{Q}{R}\left(\frac{1}{T_{ref}} - \frac{1}{T}\right) \tag{1.2}$$

where R is the gas constant and Q the apparent activation energy dependent on the alloy composition and aging temperature.

The studied material property changes with aging can be linked to similar transition curves. The dependence of the activation energy to aging temperature of mechanical properties, for instance the Charpy impact energy, shows however that the origin of their changes is not trivial and that basic mechanisms do not all have the same activation energy for a given aging temperature. As an illustration, Novy and Badyka [Nov09, Bad18] reported a list of multiple values of activation energy for spinodal decomposition and G-phase precipitation. Hence, the evolution of mechanical properties may be seen as a macroscopic signature of inner mechanisms at the origin of the thermal embrittlement. The experiment for characterizing mechanical properties changes must then cover a wide range of parameters to be accurate for the wide diversity of cases met.

1.2.3.2 Mechanical behavior modeling

Proposed laws for estimating CDSS behavior are all based on the observation that the material microstructure is constituted of two phases with a specific spatial arrangement. Figure 1.5 depicts its appearance on an optical micrograph similar to the ones used in previous studies to apprehend the phases morphology. Austenite appears as colonies of more or less homogeneous shapes ranging from lath-like and elongated to more globular islets clusters. The two phases layout is complex at first sight and pragmatic simplifications must be made to propose a mechanical description. All models rely on micromechanics hypotheses and an homogenization scheme to correlate the resulting macroscopic behavior to experimental data. Microstructural features are included in the lowest layers of the model and are different for all proposed models. Yet, the microstructural description constitutes the most important part as it provides the distribution of mechanical fields in each phase at the origin of components failure. Additionally, a good agreement with macroscopic curves is always reached in a certain extent which commands attention to a consistent description of local fields. During his Ph.D. thesis work, Bugat [Bug00] has reviewed all the developments on CDSS micromechanical models at that time. It is noteworthy that nearly all models addressing this very specific kind of material were associated to PWR lifetime studies and most of them issued from internal projects at EDF. As the microstructure is uncommon, only limited data are available and the following review focuses on these studies only.

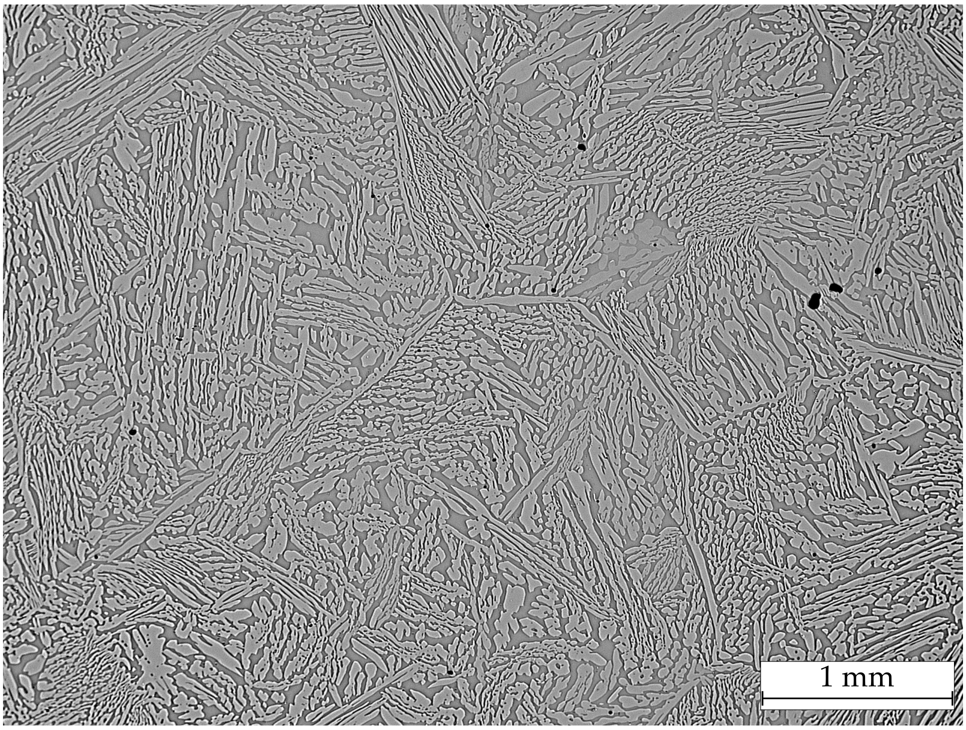

Figure 1.5: Optical macrograph of a CDSS. The dark phase is ferrite and the bright phase is austenite. Some void casting defects appear as black globular shapes.

Multiple paths have been explored to develop a micromechanical model in these previous studies. A simple model has been introduced with a Voigt rule of mixture by Verhaeghe [Ver96] to evaluate the stress in ferrite during cyclic tests. Verhaeghe *et al.* [Ver97] have proposed a damage growth law based on the previous stress in the α-phase. Devillers-Guerville [DG98] considered a random distribution of damage nucleation based on experimental measurements. None of these two references included any crystallographic data in their models. Nonetheless, the Verhaeghe *et al.* [Ver97] model takes material parameters into account such as the distance between laths and the crack length during loading. On her side, Devillers-Guerville [DG98] extended a Gurson-Tvergaard-Needleman ductile damage model to the formation of cracks in ferrite instead of matrix-inclusion debonding. Using this model, an experimental crack nucleation rate was used to predict the macroscopic response. Despite a good correlation with experimental ductile tearing tests, no heterogeneity nor crystallographic data were included. Yet, damage heterogeneity is characteristic of CDSS (and was noticed in early works *e.g.*, by Joly [Jol92]) in accordance with the coarse microstructure. Mcirdi [Mci00] used her experimental stress measurements to include ferrite orientation in experimentally determined damage growth. She proposed a law based on the stress along twin plane normal in the ferritic phase in accordance with observations in the tested and longly aged material.

Because local fields are hardly accessible, the microstructure was put aside or greatly simplified in all the previous models. With the aim of predicting the macroscopic behavior, emphasis was put on damage growth. Still, the material peculiar properties related to its microstrucure were already well known and could be easily observed from usual experimental tests. Accordingly, the previous models were deemed not predictive enough as they did miss parameters related to the microstructure itself. Bugat [Bug00] proposed a micromechanical approach for modeling the mechanical behavior at scales he deemed relevant and to subsequently predict fracture. He introduced an explicit definition of an intermediate scale (called the "bi-cristal" *i.e.,* the "dual crystal" in english) using a crystal plasticity based FE model represented in Figure 1.6. Such approaches have been widely used to model representative volumes elements for different types of materials from composites and porous materials [Fri12, Sha18], or multi-scale microstructures [Bar01, Dia05, Mat06, Que11, Ser18, Cha21]. The scale definition results from Joly [Jol92] observation that the two phases are interlocked in each other. Introducing a new scale in the micromechanical model allows for a more realistic description of stresses and strains inside the phases by taking explicitely into account crystallographic and morphological aspects. The level of stress in embrittled ferrite and the incompatibilities at the phase boundary giving rise to crack initiation observed in the aforementioned works could in theory become accessible. Bugat [Bug00] used this two-scale transition along with a damage model to predict the macroscopic response of tensile specimens. Its damage law introduces a nucleation rate at the intermediate scale that allowed the experimental measurements of Joly [Jol92] to be reproduced. At the macroscale, an effective stress depending on crack coalescence and crack shape parameter was computed. Large scatter was observed in the simulations depending on the orientations sampling as is the case in experimental tests. However, multiple discrepencies between observed and simulated ductility changes still remained unexplained.

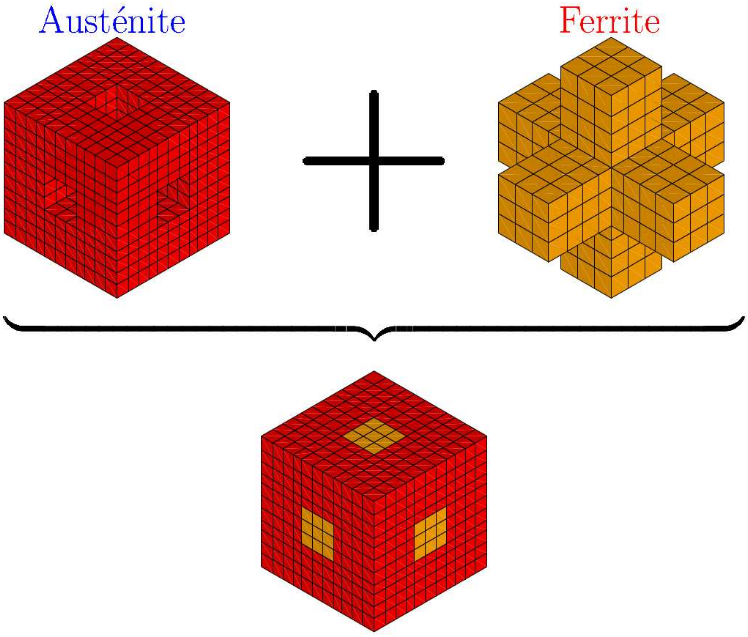

Figure 1.6: Explicit description of an intermediate scale between macroscopic and microscopic of CDSS microstructure introduced by Bugat [Bug00]. This scale is intended to reproduce an homogenized behavior representative of a small volume as presented in Figure 1.5

As of today, Bugat's model is still the most reliable and physically founded description to the micromechanical behavior of main primary loop components. Beside some discrepancies with experimental data, it includes some limitations and modeling choices that were necessary at that time but deemed restrictive in current studies. For instance, there is no scale explaining the high heterogeneities observed in large specimens. Such specimens display highly uneven surfaces related to an anisotropic behavior at the millimetric scale that has not been described. At the intermediate scale describing the dual-phase layout, various morphologies are observed. Figure 1.5 illustrates an apparent anisotropic morphology at a millimetric scale and Messiaen [Mes97] gave a glimpse in the complex three-dimensional features of the microstructure that is sometime largely elongated and sometime more random. Both micrographs and EBSD acquisitions presented phase morphologies differing significantly from the introduced cross-shaped unit cell. Regarding the description of each phases, a coarse crystallographic description has been adopted and an average austenite-ferrite orientation relationship has been chosen. Last, quantitative measurements of local stresses and strains in both phases to probe the model predictions are still missing.

1.3 Proposed approach

In front of the industrial challenge to predict more accurately CDSS mechanical behavior with aging, we propose to extend the approach introduced by Bugat [Bug00]. A general scheme to model the CDSS behavior under monotonic loading is introduced to reach failure predictions. We demonstrate that one must fully characterize microstructural features to explain experimental observations and measurements. The microstructure response to mechanical loadings is analyzed by correlating the unveiled features to full-field measurements at a consistent scale. The measurements provide quantitative data at the microstructural scale in CDSS that are relevant to assess the significance of each material property extracted from the microstructure analysis. Based on the acquired experimental data, a multiscale micromechanical model is proposed. The calibration of its constitutive parameters using full-field measurements is also discussed.

In Chapter 2, we report an accurate description of microstructural features using recent improvements in experimental characterization. In light of the component history, different microstructural features are described. The goal is to reproduce them faithfully inside a relevant model. Tools dedicated to the characterization of the microstructure from crystallographic data are introduced. The complete description aims to explain the mechanical response of dual-phase steels qualitatively. In particular, a new hierarchical decomposition of the microstructure is given by linking orientation and morphological features describing the different scales.

The mechanical characterization at the different scales for four aged states is presented in Chapter 3. We explain the effects of thermal aging on the mechanical response through macroscopic tensile tests and associated difficulties justifying the use of a model. *In situ* tensile experiments are carried out to confirm the aging-dependent deformation mechanisms in each phase. The resulting crystallographic and morphological effects on the mechanical behavior are unveiled through microstructure full-field measurements.

Regarding the development of a micromechanical model for CDSS, a new homogenization method based on the previous results is proposed in Chapter 4. It consists of a two-step upscaling/downscaling from the laths scale to the Representative Volume Element (RVE) scale, including an intermediate structure. We introduce an original mesoscale representative model built from meaningful crystallographic and morphological features to evaluate stresses and strains in the two phases of the material and the incompatibility at their interfaces. It also integrates necessary parameters taking into account the aged state. A calibration of intermediate scale constitutive parameters is performed based on available data. Finally, a microstructure generator enabling the full-field simulation of CDSS mechanical fields is presented.

Chapter 2

Microstructural characterization

It is well established that the macroscopic mechanical behavior of materials is conditioned by their microstructural properties. For instance, the size, shape and texture of crystals in steel alloys are first order parameters in the prediction of their behavior. In forming processes involving solid state transformations, the final texture results from the parent phase texture and the symmetries involved in the mechanisms giving rise to the child phase. Similar conclusions can be drawn regarding crystal shapes. Child phase morphology is therefore inherited from parent orientation and the induced crystallographic consistency between the two phases. Consequently, understanding the material microstructure is of prime importance for predicting macroscopic response under mechanical loadings. In this part, it is proposed to make use of rich data acquired by Electron Backscatter Diffraction and to demonstrate that CDSS microstructure presents four distinctive scales that are relevant to understand deformation mechanisms. The nanoscale where ferrite undergoes spinodal decomposition is left aside because data are not easily characterized in the upper scales, so that ferrite properties will be considered dependent on aging. These scales, their size and textures are inherited from physical mechanism occuring during the forming process. Identification of properties required to build a consistent multi-scale description of this microstructure are presented accordingly.

2.1 Selected material

The slabs settled on for the whole study were took off an 80 kg, cross-shaped ingot (Appendix A), cast alongside the “EK” elbow that has been previously studied [Jol92, Ver95, Bug00]. The alloy is a molybdenum-bearing CF8M (AFNOR Z3CND19-10M) grade stainless steel classifying among CDSS alloys that are the most sensitive to thermal aging. The cast composition was specifically developped to match the chemical composition of "E" type elbows from reactors already in service. Only the sulfur contents is adjusted (drastically lowered) to avoid the appearance of MnS type inclusions. Chemical compositions of the actual industrial component reported in [Bug00] and the ingot available for the study are given in Table 2.2 and compared to the specifications for CDSS given by official PWR design rules (RCC-M) [AFC18]. The primary focus being on homogeneous equiaxed solidifaction areas, samples were cut off far from the ingot borders (to target a specific macrostructure described in Section 2.2) using electrical discharge machining (EDM).

Material	C	Si	Mn	S	P
Target [AFC18]	≤ 0.040	≤ 1.50	≤ 1.50	≤ 0.015	≤ 0.030
Cruciform	0.032	1.04	0.80	0.0007	0.025
EK	0.033	1.07	0.88	0.004	0.018
Material	**Cr**	**Ni**	**Mo**	**Cu**	**Co**
Target [AFC18]	≥ 18.00	≥ 9.00	≥ 2.25	≤ 1.00	≤ 0.20
	≤ 21.00	≤ 12.00	≤ 2.75		Aimed: 0.10
Cruciform	20.9	10.4	2.68	0.17	0.02
EK	21.14	9.67	2.51	0.16	0.05

Table 2.1: Measured chemical composition (wt.%) of the EK elbow analysed by L. Devillers-Guerville [DG98] and S. Bugat [Bug00] and of the cross-shaped (cruciform) ingot from which samples were cut off.

Four slabs were subjected to accelerated thermal aging. Aging times at 350°C are distributed between as-received and saturated mechanical properties according to the previously introduced law (see Section 1.2.3.1). The aging times are in increasing order 0 h, 1000 h, 2500 h and 10000 h respectively corresponding to a mean operating time of 0h, 67300 h, 168000 h and 673000 h for the cold leg and 0h, 4530 h, 11300 h and 45300 h for the hot leg.

2.2 Elaboration

Duplex steels acquire their name from their dual-phase microstructure. At ambient temperature, body centered α-ferrite and face centered γ-austenite coexist. This is ideally suited for achieving specific corrosion and mechanical properties (in particular an acceptable ductility) by combining complementary features of both phases [Sol82, AA09, Cha09, Cha12, Kny13]. The two phases in the final product can present varied properties depending on the alloy chemical composition and cooling conditions (Figure 2.1). According to the iron-chromium-nickel ternary system given in Figure 2.1 (a), the coexistence of the two phases is possible only for a precise range of chromium and nickel contents [Sch39, Lip80, Bro91]. Combination of different Cr/Ni ratios with complex thermal cycles can lead to very different solidification structures and properties of the two phases. Figure 2.1 (b) from [Dav81] illustrates this variety with micrographs of duplex morphologies evolving with the distance to the weld bead in 308 austenitic steel weldments. One can relate both sub-figures because chemical compositions in multipass welding processes are highly heterogeneous (due to macro- and micro-segregations) and may fall within the four domains depending on location in bulk. Nonetheless, we should add that cooling rate dependencies also control the final morphologies to a great extent.

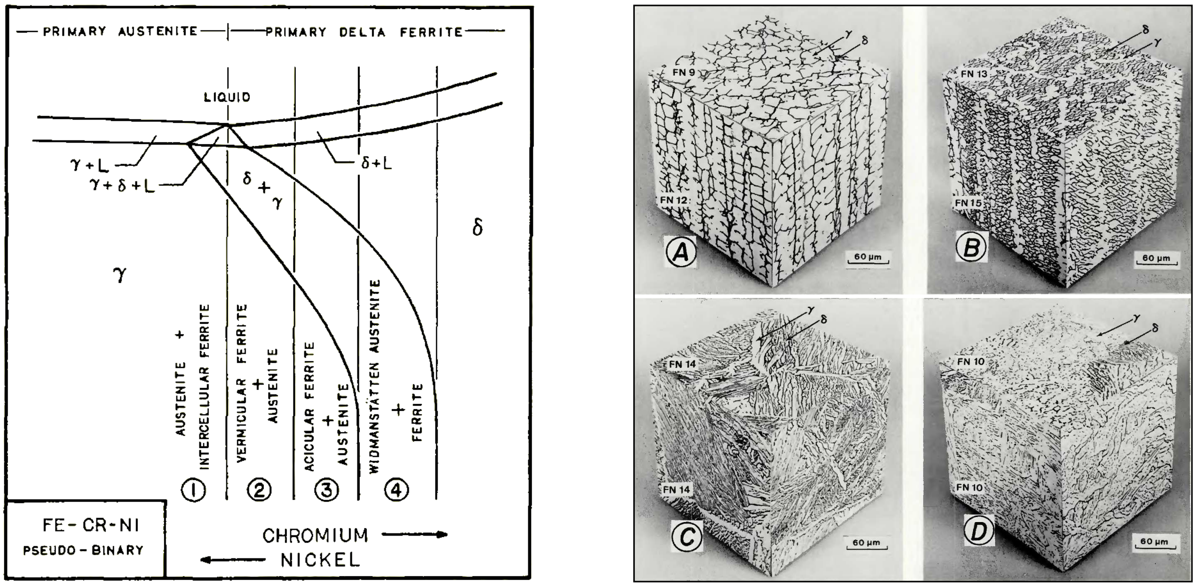

(a) (b)

Figure 2.1: Different solidification paths and morphologies for duplex stainless steels. (a) Schematic Fe-Cr-Ni ternary diagram slice for a given Fe content showing solidification paths for different Ni/Cr ratios [Lip80]. (b) Duplex morphologies obtained at different distances (*i.e.*, for different cooling conditions) from a weld bead in an austenitic steel [Dav81]. Micrograph Ⓐ is in the weld bead (first pass) while Ⓓ is the farthest from the bead.

Existence domain for this type of alloys can be extended by the means of α stabilizing elements (Cr,Mo,Si) or γ stabilizing elements (Ni,Mn) depending on the type of primary solidification. In the case of primary cooling circuit components, solidification sequence starts with a complete liquid to δ-ferrite (improperly called α-ferrite in the following for simplification) transformation. Then, a solid transformation occurs in which γ-austenite partially develops in the parent α-ferrite grains. The resulting microstructure is close to the Widmanstätten network described in early studies of austenitic weldments (Type Ⓒ from Figure 2.1 (b)) [Lip80, Dav81]. Austenite accordingly appears as colonies of near homogeneous morphology in a ferritic matrix. To aim for a final ferrite content that is directly related to the sought-after mechanical and corrosion resistance properties, a final heat treatment is performed (Figure 2.2). It is also commonly mentioned that austenite and ferrite orientations are closely related through Kurjumov-Sachs orientation relationship [Kur30] which is a distinctive feature discovered in steels involving martensitic transformations and analytical work considering displacive transformations [Bow54, Mac54, Wec59]. However, some authors argue that the Widmanstätten network is owed to the migration of Cr and Ni at the transformation interface and that no evidence about displacive transformation can be found [Leo82]. Regarding the timescales involved during the forming process of Figure 2.2, it would make sense to argue that diffusion mechanisms may occur. Still, studies proved that this type of diffusional controled transformation involves orientation relationships [Sta05]. Bugat [Bug00] came to the same conclusion on CF8M centrifugally cast components by making use of EBSD measurements but he also noticed significant gaps that remained unexplained. Similarly, pole figures given by Verhaeghe [Ver95] display a visible spread with austenite orientations distributed in an arc of a circle pattern. Given that some relationships are involved between the two phases, such a spread must have a significant effect on morphology and presumably on the local behavior at α/γ interface. Despite the unknown effects on the local mechanical behavior, it was chosen in first studies to average orientation relationships to KS [Ver95, DG98, Bug00, Mci00]. This amounts to consider that the ”average anisotropy“ of crystal behaviors prevails over the geometrical effects and local inter-phase slip transmissions even though these properties were not quantified. Austenite orientation spread and its relationship with the morphology observed on metallography pictures has therefore an unknown effect on local deformation mechanisms. Besides, it seems to introduce severe anisotropic features at a millimetric scale. Consequently, such a property needs to be studied in depth.

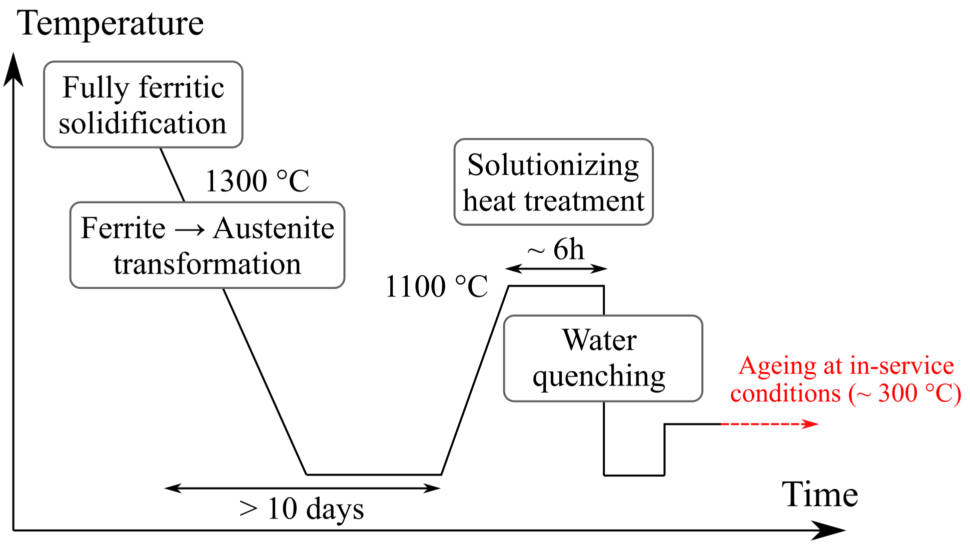

Figure 2.2: Solidification sequence endured by ”E“ elbows and the studied ingot.

Components of the primary circuit are an assembly of pipes, elbows and fittings for which two distinct forming processes where used. While elbows and fittings are statically air cooled, pipes are centrifugally cooled. Devillers-Guerville [DG98] mentioned that the solidification sequence is the same for the two processes. Centrifugally cast process gives larger elongated basaltic shape to primary ferrite grains. The shape is aligned with the pipes radial direction and ferrite crystallographic axes [Jol92, DG98, Bug00] but equiaxed grains still form at the core of the component. Static cooling also provides elongated but smaller basaltic grains near components edges. Core macrostructure is however characterised by randomly oriented equiaxed ferritic grains [DG98]. Figure 2.3 (a) and (b) illustrate the heterogeneity of a static cast pipe macrostructure. On account of the mold complexity and components size, various macrostructures are observed in the final product. For instance, proximity with a mold cooler induces higher thermal gradient resulting in a larger columnar zone (Figure 2.3 (b)). Broadly speaking, from the external skin to the core of the part, grains are respectively fine equiaxed, long and fine basaltic and fine equiaxed.

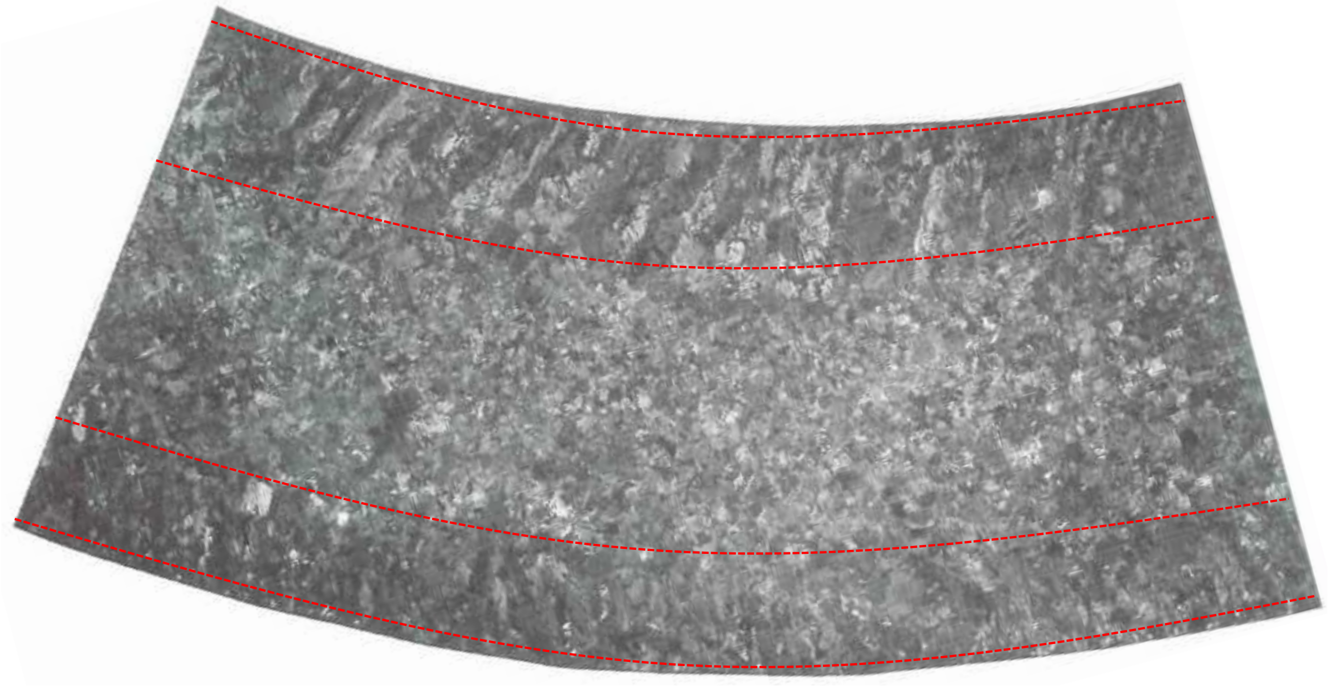

(a)

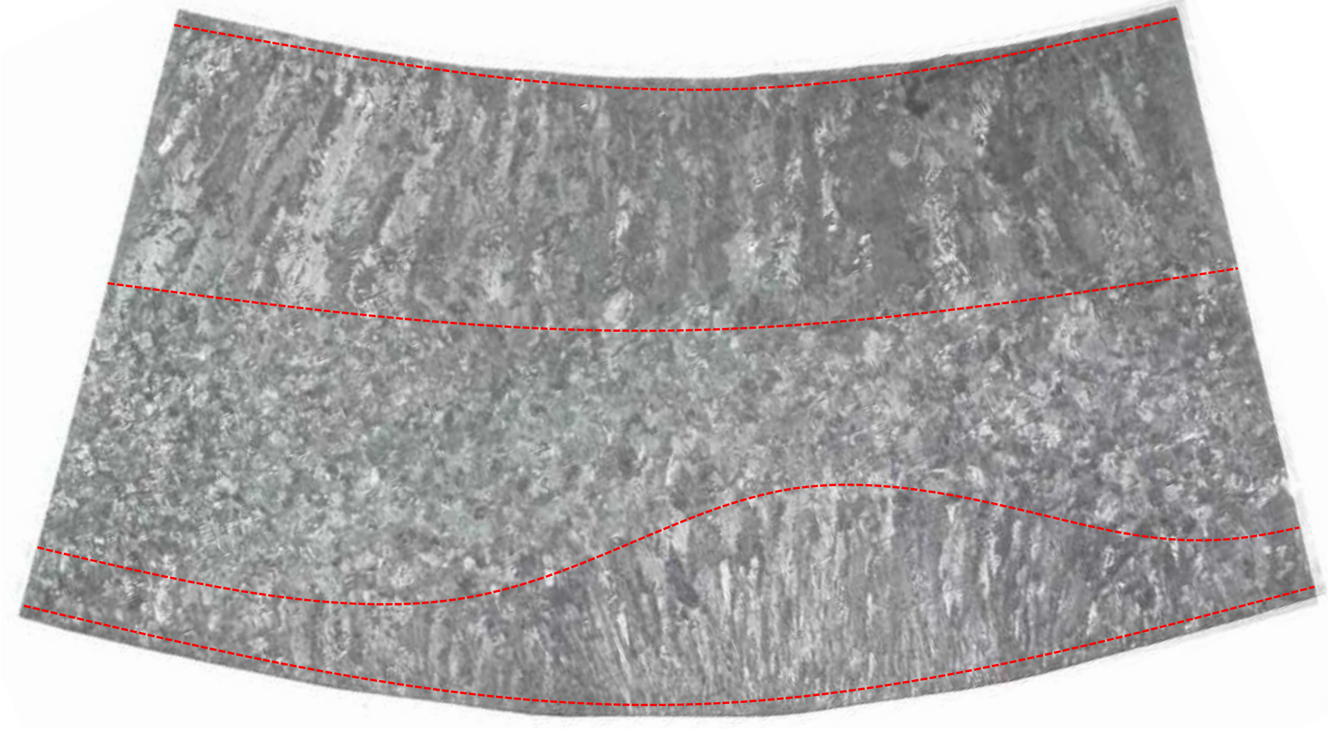

(b)

Figure 2.3: Solidification macrostructure highlighting various distinct solidification steps during static casting process. Contrast levels are the reflection of primary ferrite grains orientations. Areas presenting different solidification structures are delimited with red dashed lines. (a) Standard solidification macrostructure. (b) Solidification macrostructure near a mold cooler. A significant area is impacted by the modified thermal gradients resulting in a visibly larger columnar surface.

The observed locally anisotropic morphology (in the form of colonies as described by Bugat [Bug00] or simply refered to as lath packets in the following) is of course dependent of the primary ferrite grains morphology. However, it is difficult to correlate morphology with preceding metallography pictures without having a precise crystallographic descriptions on these surfaces. Nevertheless, these packets display properties that are seemingly not inconsequential regarding the material mechanical behavior. Metallic alloys presenting lath-like arrangements (martensitic, bainitic or perlitic steels) show great inhomogeneities in the mechanical fields at the relevant scale [Lin14, Mor16, Kum19a]. In these materials, inhomogeneities are at the origin of strain localization and therefore damage evolution. In the present case, the analogy with other structures can be drawn further. From the previous micrographs, one could compare the layout of the two phases in a packet as a bi-material layered composite in which one of the constituting material is becoming stiffer with age. Given the apparent scales of the lath packing (close to millimetric), the inhomogeneities have a considerable potential to manifest at the components scale but are yet unknown. Accordingly, additional data are acquired using EBSD acquisitions in the following. These data are processed with the aim of understanding the morphology of both phases and conclude on their relation with orientation. The homogeneous equiaxed ferrite grain area is used as a starting point but the carried out methodology can easily be extended to more complex solidification areas.

2.3 Insights in CF8M microstructure using EBSD acquisitions

Reproduced from: **M. Mollens, S. Roux, F. Hild and A. Guery, 2022**. Insights into a dual-phase steel microstructure using EBSD and image-processing-based workflow. *Journal of Applied Crystallography*, 55(3):601–610. ISSN 1600-5767. doi: 10.1107/S1600576722004265

2.3.1 Introduction

Understanding microstructures is of key importance to predict mechanical properties in advanced system components. In nuclear power plants, the prediction of the behavior of primary coolant system pipes is mandatory. These components undergo severe thermal and mechanical loadings in their in-service environment [Bet96, JG00]. Long-term microstructural changes are likely to degrade material properties by modifying deformation mechanisms and stress distributions under loadings [Ver97, Bac16, Wan16].

For polycrystalline materials, the size, shape, and organization of individual crystals are keys to optimizing the macroscopic constitutive laws and, in the present case, to understanding their changes with aging. In such characterizations, electron backscattered diffraction (EBSD) has known a tremendous surge of interest from the nineties on with the development of digital cameras allowing for fast acquisitions of diffraction patterns, and increased computer power driving SEM systems. EBSD offers noteworthy properties such as complete characterization of each phase, very high resolution images for strain analyses [Wil06, Bri18, Shi19, Wan21], recent and forthcoming promising advances (*e.g.*, Transmission Kikuchi Diffraction (TKD) [Sne16]), and ultra fast characterization [Wan21]. Remarkable efforts have been achieved in serial sectioning alongside collection and assembly of 3D EBSD data [Gro06, Bur16, Guy16, Ech20, DeM21], and dedicated software [Bac11, Gro14]. However, handling and interpreting such results may become very complicated in the case of complex microstructures. Besides, such experimental data feed models of growing complexity to account for realistic microstructures [Bug99, Mci00, Pan11]. Most of the time, quantitative parameter extraction requires the processing of images coming from different acquisition techniques where EBSD plays a significant part. With this feature in mind, numerous image processing toolboxes were automated and made user-friendly [Sch12].

Image processing based on any scalar information extracted from crystallographic orientations cannot be objective in the sense that it depends on the chosen reference frame, whereas the *frame indifference* property should be a prerequisite to all crystallographic data processing routes. Generalization of necessary tools used in basic image processing for segmenting phases to standard EBSD data is therefore of great interest. Dedicated post-processing procedures were developed to significantly improve the accuracy of orientation measurements by applying proper filters to crystallographic data [Hum01, Che10, Hie19] or directly to EBSD patterns [God04, Wri15]. The quaternion orientation formalism adopted in many EBSD processing codes is well suited for this development and will be used along with some plotting functions available in the MTEX Matlab toolbox [Bac10]. Quaternions have been used extensively in monitoring of systems involving orientations (*e.g.*, aerospace, robotics) for their computer friendly encoding of rotations. They have also been used in image processing [Che15, Xu15] to handle color properties even though 3D rotations or deformations have no physical meaning in color spaces. For example, it would be irrelevant to encode colors in inverse pole figures as used for orientations. Hence quaternions are convenient beyond their physical relevance, but for orientations, the latter aspect allows for the formulation of a distance between orientations that is objective, and does not suffer from any singularity (as would be the case with Euler angles).

The present paper intends to illustrate a workflow composed of dedicated tools to classify and segment crystal indexing data on materials with complex microstructure layouts. One emblematic example of such materials is cast dual phase stainless steel, out of which elbow pipes and connections of pressurized water reactors are made. This material will be used in the following analyses to illustrate the discussion. Its microstructure covers a very broad range of scales with characteristic features ranging from 1-10 µm up to several millimeters. The microstructure is ideally suited for achieving specific strength and corrosion resistance requirements [Sol82, Cha09, Cha12]. However, this material suffers from thermal aging over the years, and becomes slowly more prone to damage and microcrack initiation, which contribute to an increase of the risk of failure [Bon90, Cho91, Chu92, LD15]. The complex spatial organization of austenitic and ferritic phases (crucial for the material properties) is challenging to illustrate orientation processing.

The outline of the article is as follows. first, the material and its peculiar microstructure are introduced in Section 2.3.2 to highlight distinctive scales that are relevant for mechanical models. The formalism for handling crystal orientations and associated image analysis tools based on previous observations are defined in Section 2.3.3. A direct application to the studied material and subsequent morphological analyses are shown in Section 2.3.4. The benefits of the introduced methods on the case of interest are discussed in Section 2.3.5 alongside some proposed improvements.

2.3.2 Material and microstructure

The material of interest is CF8M alloy, which is a cast dual phase stainless steel used in the primary loop components of French pressurized water reactors. It consists of two constitutive phases, namely, ferrite and austenite in a 25/75 wt% ratio. Its remarkable microstructure exhibits elongated austenite laths of about 10 to 50 µm width embedded in a ferritic matrix (Figure 2.12).

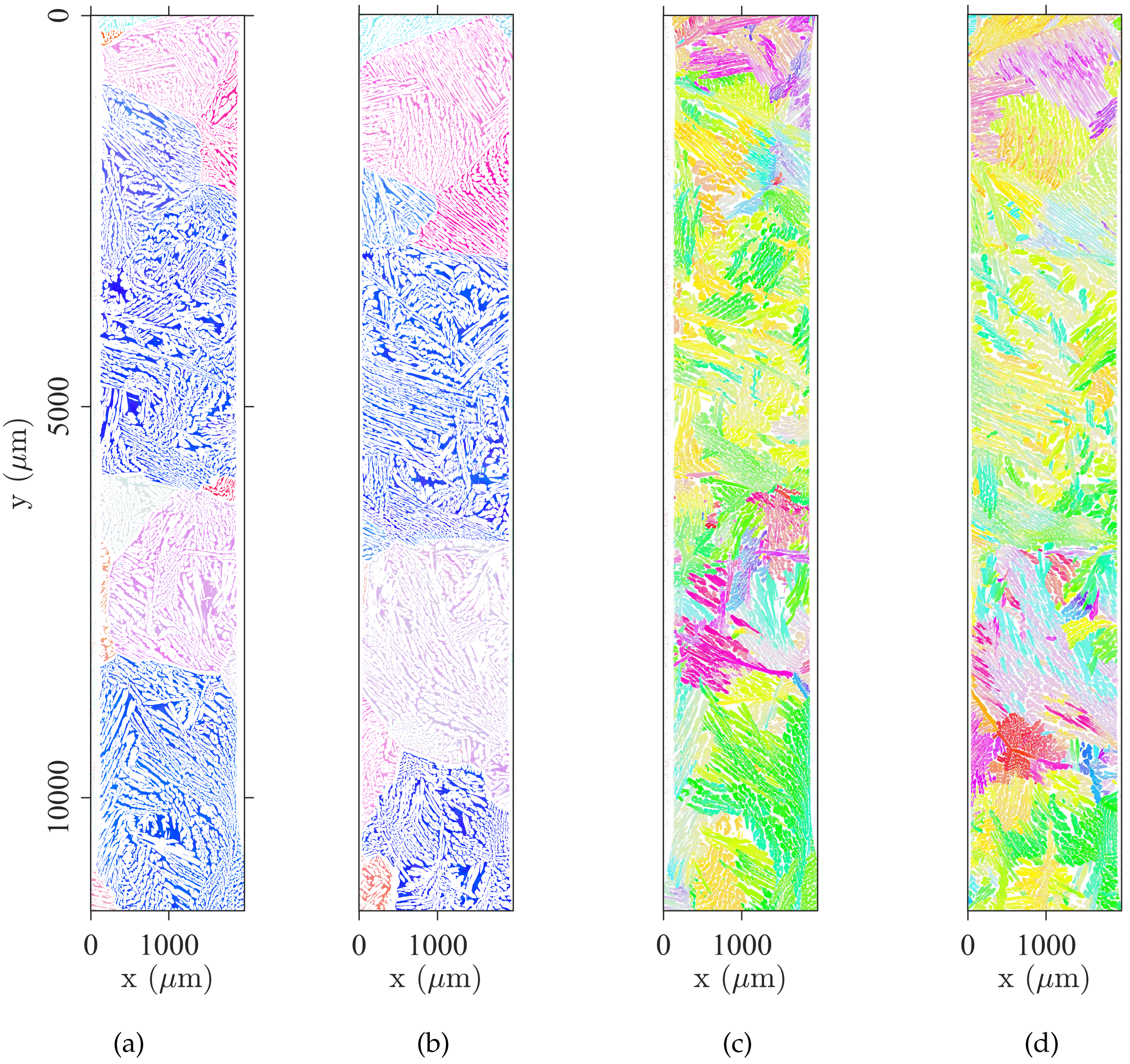

(a) (b) (c) (d)

Figure 2.4: Microstructure of CF8M dual phase stainless steel captured on both side of a 1 mm thick specimen[1]. Orientations are colored according to the standard inverse pole figure (IPF) color scheme for cubic systems. (a) and (c) Large ferritic grains obtained from primary solidification. Only the α-phase is displayed. A majority of grains are present on both faces. (b) and (d) Austenitic lath network growing within ferritic grains. Some laths clusters can be found on both sides but the layout is obviously more complex.

Looking at the solidification path is instrumental for reading orientation maps of this material and identifying the different scales. A schematic description of the main steps is given in Figure 2.5. The chemical composition is such that solidification starts with a liquid to an α-phase transformation resulting in a standard assembly of millimeter-size polygonal grains. The polygonal grain shape is easily observed at room temperature (Figure 2.5(a)).

A second and quite unusual solid/solid phase transformation from ferrite to austenite takes place further along the cooling process. Two growth configurations have been identi-

---

[1] The present figure is an enriched version of the figure inserted in the paper that only depicts one face of the sample.

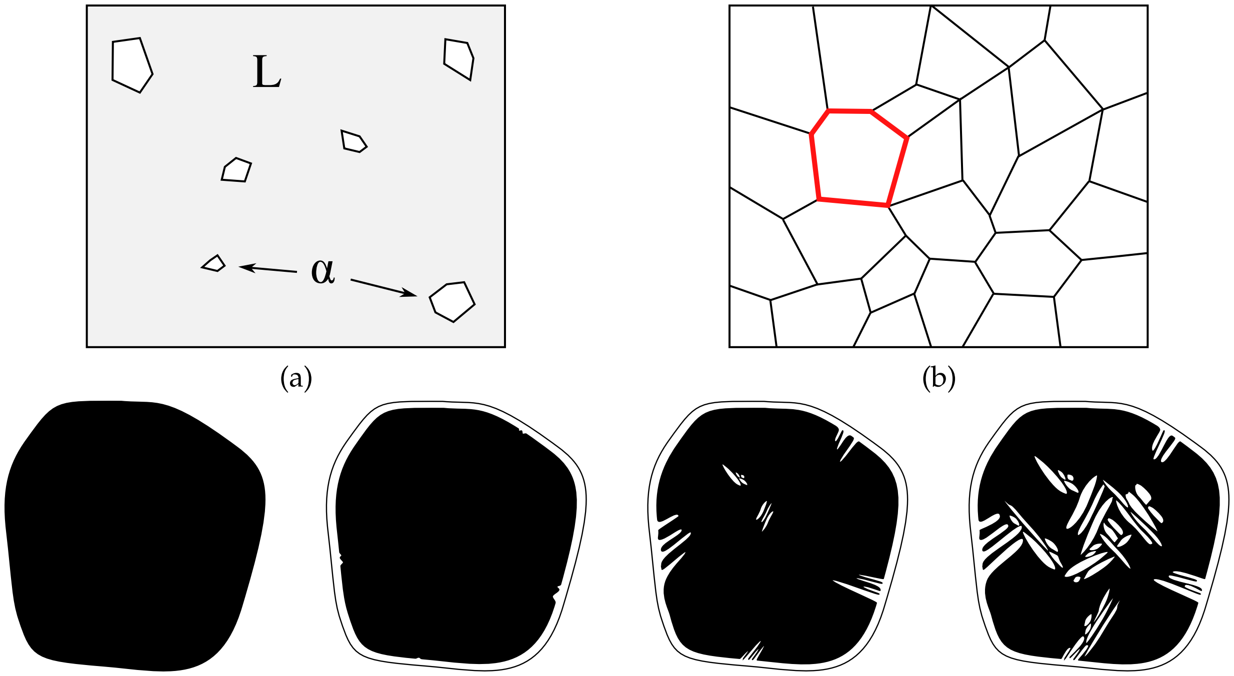

(a) (b)

(c) (d) (e) (f)

Figure 2.5: Schematic representation of solidification mechanisms of CF8M duplex stainless steel. The two primary phase transformations occurring during cooling are illustrated. Understanding the physical mechanisms will further help to guide the classification and segmentation methods. (a) First phase transformation from liquid to α-ferrite. (b) Common polygonal ferritic grain network resulting from full solidification. (c) Initial primary ferritic grain taken from (b). (d) Austenite (in white) starting to grow at ferritic grain boundaries. (e) Austenite growth forming laths. (f) Ferrite-austenite nested layout

fied on crystallographic orientation maps for the second phase. First, nucleation is likely to occur where the disordering energy is high (*i.e.*, at ferritic grain boundaries and most likely at triple points where three grains meet). Being schematically planar, primary ferritic grain boundaries are replaced by a thin continuous austenite lath (whose thickness is of order of hundreds of µm). Secondary austenite laths grow from these boundaries and into the ferritic grain to form the observed nested layout. Austenite laths give rise to clusters constrained by variant selection mechanisms [Kun12, DJ17, DeM21] resulting in preferential morphological and crystallographic parameters inside a cluster. Groups of austenite laths with similar orientation are easily observed (Figure 2.5(b)).

The macroscopic mechanical modeling, which is a motivation for such study, leads to identifying four scales in this microstructure. The first (smallest) scale is the monocrystalline austenite lath with constant crystallographic orientation (or the ferritic interlayer). The second scale with meaningful mechanical parameters is associated with the austenite lath clusters characterized by constrained morphological and crystallographic parameters. The third scale is delimited by the primary ferritic grains layout in which clusters are nested. The fourth mechanical scale is the representative volume element of ferritic grains. The aim of multiscale models is to retrieve spatial boundaries of each intermediate scale, and to endow them with appropriate mechanical features. The smallest scale is easy to delineate. The larger scale is a theoretical extension of the layout given by primary ferritic grains. Hence, only the two intermediate scales have undetermined boundaries. In the following, it is proposed to retrieve these boundaries by considering crystal orientations.

2.3.3 Classification of EBSD data

Phase identification from optical or SEM images in metals has been a major task for a long time [Tam78, Fis81, Osm00], and still benefits from the latest advances in computer power and classification algorithms [Duc13, Azi18] to exploit the relationships between quantitative phase morphology and mechanical behavior. Such images are acquired from a wide range of imaging systems including EBSD. However, scalar fields of such images do not integrate crystal symmetries and consequently do not do justice to the physical meaning of crystallographic orientations. Hence, suited extensions of classification and segmentation operators in the crystallographic orientation space need to be introduced.

Similarly, grain boundary identification using indexed EBSD data has been the focus of substantial efforts [Gro06, Bac11, McM13]. More advanced processing of crystallographic orientations may also give access to underlying properties of complex microstructures. For instance, parent grain reconstruction has been a major focus in the past years [Cay06, Ger12, Wan19]. Between these two cases lie microstructures for which morphological parameters are visible but require some processing to be properly quantified. In the case of CF8M, each phase transformation leaves remarkable features that are unveiled by the crystal orientation maps. These features guide the maps processing. For example, spatial boundaries of primary ferritic grains are easily identifiable by separating phases and focusing on ferrite in the spatial orientation maps. Regarding austenite, smooth orientation gradients seem to be correlated with the evolution of morphological properties.

In light of the CF8M microstructure, suited tools must be developed. The two-phase orientation maps of Figure 2.12, colored using a standard Inverse Pole Figure (IPF) coding, unveil the aforementioned microstructure scales. Large EBSD maps only include a small number of ferritic grains owing to their millimeter sizes. Hence, ferrite orientations correspond to few distinct clusters randomly distributed in the orientation space. Austenite orientation maps are much more complex and exhibit clusters with homogeneous or continuously varying crystallographic orientations. Their representation in the orientation space results in large and diffuse clouds of scattered points. At the intermediate scale, each lath cluster corresponds to a similar orientation (and thus, in the orientation space, the corresponding points are grouped into a narrow region), while distinct lath clusters appear as distant sets of points in the orientation space. Thus, the boundaries of these clusters will be retrieved by processing ferrite and austenite maps hierarchically in compliance with the above described nested microstructure layout.

Supplementary analysis that was not in the paper

By observing the two phase maps obtained from EBSD acquisitions, the result of the different steps of the solidification process introduced in Figure 2.1 can be apprehended. In particular, distinctive features of the microstructure are explained with the help of orientation maps. Ferritic grains equiaxed morphology at the core of the components is due to the homogeneous thermal field and the absence of other external driving forces (unlike the centrigal cast case). Dendritic growth of α-nuclei result in a common polygonal grain network partially retained on the ferrite orientation map. Austenite growth is more complex and involves the quite unusual BCC to FCC transformation at a solid state.

The striking feature unveiled by EBSD maps is the spatial distribution of austenite. First, nucleation is likely to occur where the disordering energy is high (*i.e.,* at ferritic grain boundaries and most likely at triple points, in a Voronoi sense, where more than two grains meet). Being schematically planar, primary ferritic grain boundaries are replaced by a thin continuous austenite lath (whose thickness is of order of hundreds of µm). This lath orientation is not necessarily homogeneous since a single ferritic grain is connected to multiple other grains. Hence the lath rather displays multiple orientations rising from all the triple points belonging to the grains. Junctions between these different orientations are thus present in the planes describing the boundary between former ferrite grains. Secondary austenite laths grow from these boundary laths into the ferritic grain to form the observed nested layout. They form clusters presumably constrained by variant selection mechanisms [Kun12, DJ17, DeM21] resulting in preferential morphological and crystallographic parameters inside a cluster. Groups of austenite laths with similar orientation are easily observed.

When considering a unique phase, its orientation maps contains a large fraction of missing data (which correspond to the other phase). Processing is thus difficult as it has to accommodate this missing information. Thus some kind of "inpainting" will be needed, and it is important that such inpainting does not misrepresent the actual microstructure, and preserve frame indifference (inpainting a rotated map (with an arbitrary rotation), or rotating the inpainted map, should be equivalent). For this aim, a *dilation operation* is introduced. Further, *classification* and *segmentation* of orientations are needed. Here, ideas inspired from standard methodologies such as K-means [Har79] or "connected component" algorithms [DS99] will be used. However, for these different processing operations (dilation, K-means, connected components) one must properly extend their formulation to account for the fact that rather than "gray levels" (*i.e.,* scalars), crystal orientations are to be considered, and hence a fair definition of distance between two orientations for instance is essential. It is the purpose of the following sections to provide such a suited extension.

2.3.3.1 Representation of crystal orientations

A rotation in the 3D space is conveniently represented by a unit vector $\boldsymbol{d}$ giving the rotation axis and an angle θ. Encoding rotations into unit quaternions

$$\boldsymbol{q} = \cos(\theta/2) + \sin(\theta/2)(d_1\boldsymbol{i} + d_2\boldsymbol{j} + d_3\boldsymbol{k}) \tag{2.1}$$

where $\boldsymbol{i}$, $\boldsymbol{j}$ and $\boldsymbol{k}$ are the basic quaternions, offers a very powerful formalism to handle rotations including composition, but also interpolation, average and elegant account of symmetries [Fra88, Mor04].

The "distance" $\mathrm{d}(\ldots)$ between two quaternions $\boldsymbol{q}_1$ and $\boldsymbol{q}_2$ is defined as the angle of rotation $\boldsymbol{r} = \boldsymbol{q}_1\overline{\boldsymbol{q}_2}$ (where the over-line denotes conjugation) transforming $\boldsymbol{q}_1$ into $\boldsymbol{q}_2$. The cosine of the half angle of rotation of $\boldsymbol{r}$ is provided from its real part $\Re(\boldsymbol{r})$

$$\mathrm{d}(\boldsymbol{q}_1, \boldsymbol{q}_2) = 2\arccos(\Re(\boldsymbol{q}_1\overline{\boldsymbol{q}_2})) \tag{2.2}$$

When dealing with crystal orientations, it is essential to account for their symmetries. Again, quaternions offer a simple solution to select as a crystallographic orientation $\boldsymbol{g}$ associated with the quaternion $\boldsymbol{q}$ its representative in the "fundamental region" [Fra88], considering all transformations of the crystal symmetry class $\mathcal{S}$

$$\boldsymbol{g} = \boldsymbol{q}^*_S\boldsymbol{q} \qquad \text{where} \qquad \boldsymbol{q}^*_S = \underset{\boldsymbol{q}_S \in \mathcal{S}}{\mathrm{Argmin}}\,(\mathrm{d}(\mathbf{1}, \boldsymbol{q}_S\boldsymbol{q})) \tag{2.3}$$

where $\mathbf{1} = (1, 0, 0, 0)$ denotes the unit quaternion.

In turn, the "distance" $\mathrm{d}(., .)$ between quaternions is easily extended to define a distance $\mathrm{d}_{\mathcal{S}}$ between *orientations*. Accordingly, the distance between two orientations $\boldsymbol{g}_1$ and $\boldsymbol{g}_2$ is the minimum magnitude of the disorientation angle between them, after due consideration of their symmetry

$$\mathrm{d}_{\mathcal{S}}(\boldsymbol{g}_1, \boldsymbol{g}_2) = \min_{\boldsymbol{q}_S \in \mathcal{S}} \mathrm{d}(\boldsymbol{g}_1, \boldsymbol{q}_S\boldsymbol{g}_2) \tag{2.4}$$

Quaternion mapping of orientations also grants easy interpolation. Using linear interpolation (Lerp) between two quaternions, the average orientation between $\boldsymbol{g}_1$ and $\boldsymbol{g}_2$ with a weight ω and $(1-\omega)$, respectively, reads

$$\overline{\boldsymbol{g}} = \frac{\omega\boldsymbol{g}_1 + (1-\omega)\boldsymbol{g}_2}{\|\omega\boldsymbol{g}_1 + (1-\omega)\boldsymbol{g}_2\|} \tag{2.5}$$

Last, encoding orientations into an axis-angle representation grants a consistent space for representing orientations and misorientations [Fra88, Kra17], and to understand how they are distributed in this space. With the aim of keeping consistency with the quaternion formalism introduced herein, orientation $\boldsymbol{g}$ will be represented as a 3D vector $\boldsymbol{v}$, as given by the imaginary part of the associated unit quaternion $\boldsymbol{q}$, $\boldsymbol{v} = \Im(q) = \boldsymbol{d}\sin(\theta)$.

2.3.3.2 Dilation

The EBSD technique provides a map of $\boldsymbol{g}(\boldsymbol{x})$ for all analyzed pixels $\boldsymbol{x}$ in the region of interest (ROI). It is convenient to decompose this map into elementary ones, $\boldsymbol{g}_i(\boldsymbol{x})$, restricted to a single phase i (here ferrite and austenite).

Identifying orientation clusters that are meaningful in the spatial maps requires to fill empty regions (*i.e.,* occupied by the complementary phase) without changing the orientation distribution. To retrieve the transformed parent phase orientations, one can make use of the resulting child phase properties or extrapolate the residual parent phase map. The first method, often referred to as "parent grain reconstruction" [Cay06, Ger12, Wan19], assumes a unique orientation relationship between parent and child phases, and tries to optimally recover the parent orientations through a dedicated algorithm. Since the only required inputs for the method are the parent and child phases, symmetry groups and an *a priori* guess of the orientation relationship between both crystallographic frames, the reconstruction is carried out even when the second phase transformation is complete. Despite its common designation, the method may also be applied to compute a child phase orientation that would result from transforming the remaining small ferrite islets.

The approach selected in this paper is to make direct use of the crystallographic data given by the residual parent phase. Then, the only assumption is a certain amount of regularity in the parent phase distribution (the shape of grains) and a close-to-uniform orientation distribution inside a single grain. Recovering a full map is achieved using a *dilation* operator assigning the mean orientation of the neighborhood to empty pixels, which is applied incrementally until all empty pixels are filled (Algorithm 1). The neighborhood is defined by a prescribed structuring element W (taken as a 3×3 cross shape in the present algorithm). In order to preserve high magnitude orientation gradients, pixels in the window W that are too far from the mean (according to a chosen threshold) are set aside and the mean is computed again. The higher the threshold level, the more boundaries, which are to be highlighted by the process, will be smoothed. Conversely, a threshold meeting EBSD pattern registering accuracy would limit the number of pixels taken into the average and thus "sharpen" the filled pixels. In the following, a threshold of 2.5° was chosen because it was larger than the small orientation gradients that were observed in some austenitic laths, and thus no boundary smoothing was expected to occur.

Algorithm 1 Orientation map dilation algorithm

```
Require: $W$                                                    ▷ Structuring element
Require: $G$                                  ▷ Spatially defined set of orientations
Require: $\epsilon$                                                          ▷ Threshold
  for $\{\ \boldsymbol{x} \mid G(\boldsymbol{x})\ isempty\}$ do
      $\boldsymbol{m} \leftarrow G(\boldsymbol{x})$
      $\boldsymbol{m}' \leftarrow \langle G(\boldsymbol{y}) \rangle_{(\boldsymbol{y}-\boldsymbol{x} \in W)\ \&\ G(\boldsymbol{y})\ notempty}$   ▷ Compute mean orientation on indexed pixels in window
      while $\boldsymbol{m}' \neq \boldsymbol{m}$ do
          $m \leftarrow m'$
          $\boldsymbol{m}' \leftarrow \langle G(\boldsymbol{y}) \rangle_{(\boldsymbol{y}-\boldsymbol{x} \in W)\ \&\ \mathrm{d}(G(\boldsymbol{y}),\boldsymbol{m})<\epsilon}$      ▷ Update mean to significant pixels
      end while
      $G(\boldsymbol{x}) \leftarrow \boldsymbol{m}$
  end for
```

2.3.3.3 Erosion

Similar to scalar images, an *erosion* operator is defined in the orientation space to make small structures disappear and separate larger ones. Typical structures of grains are spherical or elongated clouds in the orientation space and irrelevant data are isolated points. Hence, a consistent binary image A of the orientation space where 0 corresponds to an empty cell and 1 to a non empty one are introduced. A regular grid is instrumental to perform the morphological erosion. The eroded data set G_e is defined from a given data set G as

$$G_e = \{\inf_{\boldsymbol{y} \in W}(G(\boldsymbol{x}+\boldsymbol{y}) - w(\boldsymbol{y})), \forall \boldsymbol{x} \in X\} \tag{2.6}$$

where $\boldsymbol{X}$ is the set of coordinates in the rotation space corresponding to G, and W a subspace where $w(\boldsymbol{x})$ is defined. The grid should be defined according to the quaternion distance metric to avoid distortions. In this framework, the neighborhood is controlled by the grid cell size.

2.3.3.4 Connected components

For the studied material, each phase orientation has a specific layout in the orientation space, which is preserved by the previously introduced dilation operator. Appropriate tools are to be introduced in order to group orientations sharing similar properties using suitable criteria. According to solidification mechanisms, ferritic grains are scarce, even on large EBSD maps (as their size is millimetric) and correspond to scattered and distinct dense clusters. Hence, an algorithm that can efficiently identify a small number of distinct (and significant) point clouds was used.

A connected component algorithm was selected. It is a simple clustering algorithm assigning a label to each group of adjacent elementary cells in a given space, where cells correspond to a space discretization. Different spaces may be considered, but because a very similar orientation characterizes each ferritic grains, cells correspond to a discretization of the orientation space. Connectivity of a group of cells is controlled by the cell size. From adjacent pixels in a unique ferritic grain, one may study the distribution of "distance", d, of their respective orientations. The standard deviation of this distribution is chosen to set half the cell size. The advantage of this procedure is that it is not necessary to set the number of components arbitrarily beforehand.

For data sets including a significant number of grains, it is necessary to add a contribution of the distance in the specimen physical space (*i.e.,* to differentiate two distinct grains having close crystallographic orientation). This step is, for example, achieved by segmenting the label map obtained from the connected component algorithm in the real space.

2.3.3.5 Gradient

It is needed to rely on the physical meaning of quaternions to establish a meaningful gradient operator for orientations. The latter should rest on crystallographic rotation angles to highlight grain and sub-grain boundaries, smooth transitions occurring in a grain to accommodate local constraints, and spurious isolated orientation variations due to badly indexed pixels. Accordingly, the previously introduced crystallographic distance becomes a natural descriptor of a crystallographic variation "intensity" and a significant gradient operator is defined as

$$TV = \lim_{|\boldsymbol{dx}|\to 0} \frac{\mathrm{d}(G(\boldsymbol{x}), G(\boldsymbol{x}+\boldsymbol{dx}))}{|\boldsymbol{dx}|} \tag{2.7}$$

which is translated into a finite difference version for crystallographic orientation maps

$$TV \approx \max_{\boldsymbol{e}} \left[\frac{\mathrm{d}(G(\boldsymbol{x}), G(\boldsymbol{x}+a\boldsymbol{e}))}{a} \right] \tag{2.8}$$

where $\boldsymbol{e}$ is a unit vector in the 2D plane.

The determination of crystal orientations from acquired Kikuchi patterns can be locally troublesome. Thus, raw indexed data suffer from badly or not indexed pixels. To maximize the classification algorithms efficiency, denoising orientation data with the appropriate filters is helpful. For this, the introduced total variation operator can be derived in relevant filters. Interesting tools have already been published and implemented in MTEX [Ber16a, Hie19] *e.g.,* half-quadratic filter that keeps consistency in grain boundaries and strain induced gradients.

2.3.3.6 K-means classification

Austenite orientations require to process large elongated clusters. Thus, a clustering algorithm that is able to separate data into distinct clusters based on statistics is needed. In the present case, it was chosen to rely first on a centroid-based algorithm, namely, K-means because it efficiently partitions large data sets [Har79], and is therefore instrumental for understanding uncommon γ-phase orientation distributions. The K-means algorithm (Algorithm 2) assumes a known cluster number. From an initial guess of the cluster centroid positions, their coordinates are updated to reduce the variance of all data in a cluster until stationarity is reached. By making a direct use of the crystallographic orientation metric, point clouds spread near a boundary of the fundamental region are fully recovered by taking crystal symmetries into account. The main drawback is that this algorithm is sensitive to noise, and strongly depends on the number of clusters and their initialization. Yet, it constitutes a powerful tool for manually scanning relevant data to be extracted from the full data set. In particular, K-means outputs are later used for a specific segmentation detailed in Section 2.3.4.2.

Algorithm 2 K-means for crystallographic orientations

```
Require: $G$                                          ▷ Set of $N$ orientations
Require: $k \geq 1$                                   ▷ Number of desired clusters
Require: $\epsilon$                                   ▷ Convergence criterion
  $C \leftarrow \{c_1, ..., c_k\}$                    ▷ Initialization of centroids
  $s_n = \mathrm{Argmin}_k \, \mathrm{d}_{\mathcal{S}}(g_n, c_k)$   ▷ Assign orientation $n$ to the closest centroid
  while $convergence\ criterion > \epsilon$ do
      $c_k \leftarrow \langle g_n \rangle_{c_n = k}$  ▷ Update centroid $k$ to mean of data labeled $k$
  end while
```

2.3.4 Microstructure analysis through processing of EBSD maps

2.3.4.1 Processing ferrite orientation

Splitting the two phase maps favors a clearer reading of their layout and unveils the three smaller scales but leaves some locations empty. As intermediate scale boundaries are identified through distinct crystallographic gradients, empty pixels of each map must be filled as seamlessly as possible. For this purpose, an iterative nonlinear average "inpainting" procedure was developed. An empty location gets assigned the mean orientation of its neighborhood ignoring empty pixels and orientations whose distance is too far from the mean according to a prescribed threshold as above discussed. In the case of CF8M steel, applying this procedure to the ferrite orientation map (Figure 2.6) highlights primary α-grain boundaries. Although ferrite represents only about 25% of the map, 75% must be filled with the procedure, thus giving a significant weight to badly indexed pixels. Consequently, some noise originating from automated EBSD indexing gets amplified by the algorithm (as highlighted by green points in Figure 2.6(d)) but the grains remain identifiable.

A similar dilation algorithm was implemented and tested by Wright *et al.* [Wri06] to replace some badly indexed pixels. The major difference with the proposed algorithm lies in the orientation attributed to bad pixels. Instead of an average operator, bad pixels are assigned the orientation of a neighboring pixel until all pixels belong to a grain. The neighboring pixel is chosen using a minimum grain size and a confidence index [Fie97] criterion. Results obtained by Wright underline the significant influence of the initial spatial distribution of reference pixels (*i.e.*, pixels that are correctly indexed in the phase of interest). To test the robustness of the proposed dilation step, simulated "scarce" data were extracted from the presented ferrite orientation map. In Figure 2.7(a) and (c), ferrite phase pixels were removed at random with a proportion of respectively 60% and 90%. As a result, the dilation step recovers most of the ferritic phase, as is judged from the angle distance between the dilated maps starting from the entire set of ferritic pixels and the randomly depleted cases shown in Figure 2.7(b) and (d). Grain boundaries are more fragile, and are observed in those differences, but the most striking feature is the robustness of the procedure.

2.3.4.2 Generation of Parent Phase from Child Phase

Parent grain reconstruction algorithms have been extensively developed over recent years. In the following, the method proposed by Niessen *et al.* [Nie22] and implemented in MTEX was used. The algorithm starts from an initial guess of the orientation relationship between the two phases and then optimizes it iteratively. Austenite orientations are then clustered into the number of possible child variants given by the computed relationship, and the local parent orientations are determined through a voting scheme. As an initial guess, the Pitsch orientation relationship [Pit59] gave the best fit at convergence and was

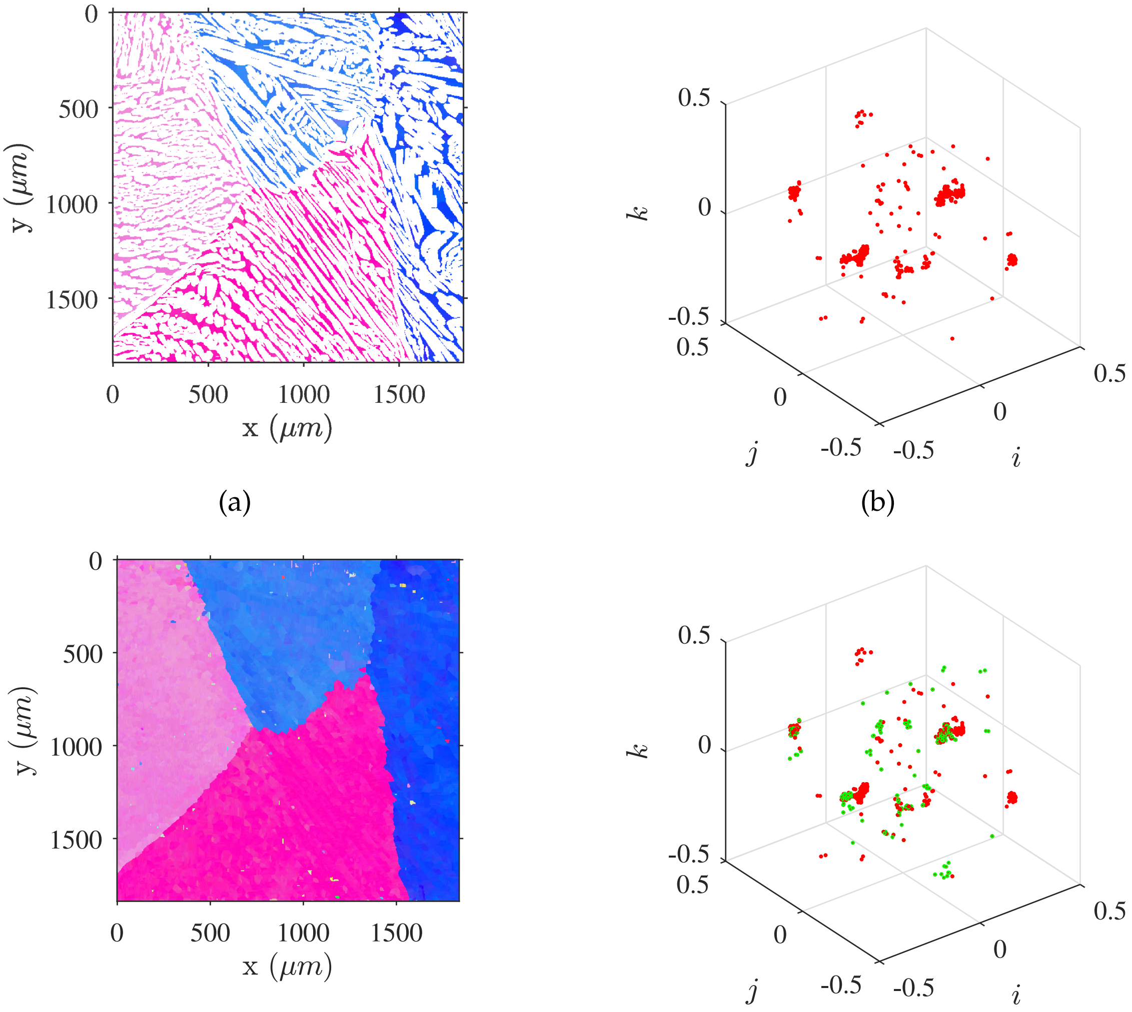

(a)

(b)

(c)

(d)

Figure 2.6: Illustration of the ferrite orientation map dilation process. (a) Measured ferrite orientation map. (b) Corresponding orientations plotted in the orientation space. (c) Dilated ferrite orientation map revealing the boundaries of the primary ferrite grains. (d) Dilated map orientations plotted in the orientation space. Green points refer to empty pixels on the initial map that are filled by the dilation process

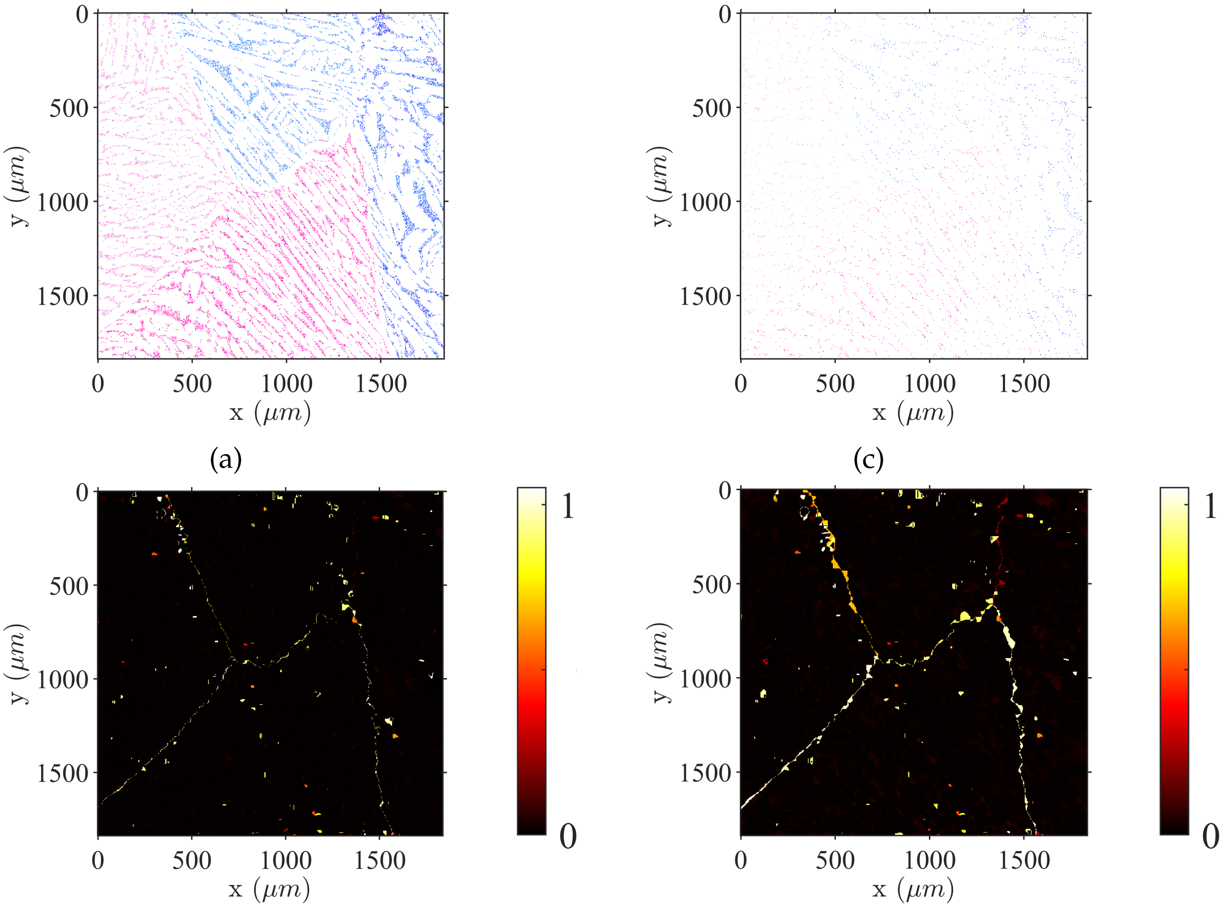

(a)

(c)

(b)

(d)

Figure 2.7: Influence of the initial spatial distribution of correctly indexed pixels on the dilation process. In both test cases, a random selection of ferritic grain pixels was removed, namely, 60% in case (a) and 95% in case (b). The angular distance of orientation (in degrees) between the dilated map obtained from the full set of ferritic pixels, and the depleted cases are shown in sub-figures (c) and (d), respectively for 60% and 95% depletion.

therefore used to reconstruct the ferrite orientation map of the CF8M alloy.

Figure 2.8 shows the reconstructed map of ferrite as provided by the parent grain reconstruction algorithm (Figure 2.8(a)) and the crystallographic distance (Figure 2.8(b)) with the raw dilated map of Figure 2.6(c). A majority of points (*i.e.,* 97%) belonged to a child variant after reconstruction. The two ferrite maps are very close to each other, showing the high quality of the proposed algorithm, and the relevance of the Pitsch orientation relationship. It is interesting to observe that the areas where the orientation difference shown in Figure 2.8(b) exceeded 5°, correspond to prior ferrite grain boundaries, and where, very early on in the cooling process, thin and continuous austenite linings nucleated.

The difficulty for the present algorithm to detect correctly the boundaries is presumably explained by the exceptional propagation of the austenite phase in this material. Not only did austenite appear along ferrite grain boundaries, but it also propagated on both sides of this boundary keeping a similar orientation. This feature means that the orientation relationship cannot be obeyed in both ferrite grains, and hence on one side the Pitsch relationships had to be violated. This effect prevents the reconstruction algorithm from properly identifying the faulty ferritic grain. By continuity, it inherited the neighboring grain's orientation. Inside the parent grains where a good agreement with the computed orientation relationship was found, the difference with dilation was rational and stayed below 5°. The precise accommodation of the phases during the casting process still remains unclear, so that no conclusion was drawn on whether small changes of the austenite orientation could be attributed to a transmitted small rotation in the prior ferrite phase or to a rotation of the child phase occurring at a later stage. In this regard, the differences between the two processes inside the parent grains, albeit small, may be an interesting observation deserving further investigations.

Several approaches may be considered to detect isolated clusters considering local orientation density to overcome the influence of outlying points and noise. Density-based clustering using the DBSCAN algorithm was shown to provide satisfactory results for relatively small sets of orientations [Joh20]. In the present case, large EBSD sets (up to four million points) prevent from computing the crystallographic distance matrix for all orientations in a decent computation time. The connected components algorithm is well-suited for such a configuration because checking if adjacent cells are connected is straightforward. The computation time is drastically reduced to a very small cost as compared to DBSCAN. However, orientation clusters lying on an edge of the fundamental zone will be cut if points spread

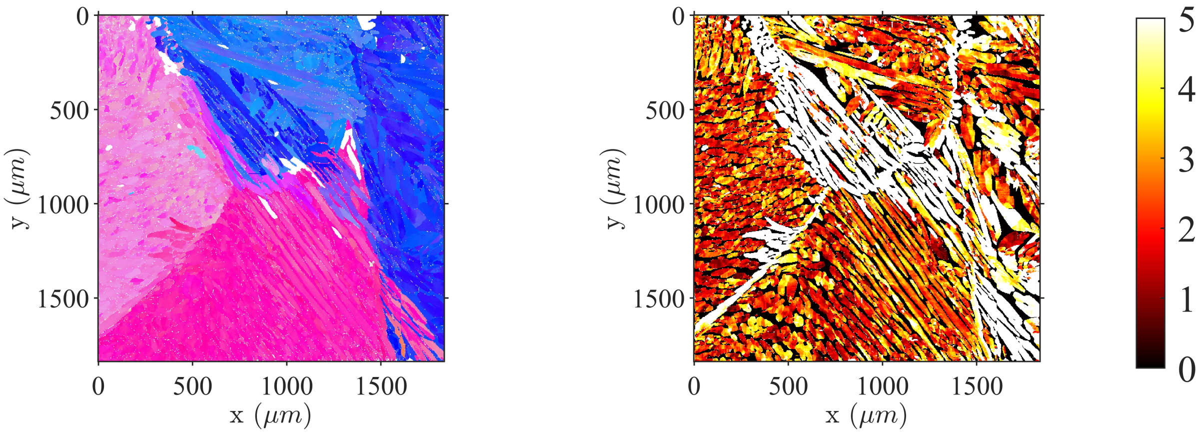

(a)

(b)

Figure 2.8: Comparison between recovered ferrite maps using dilation and parent grain reconstruction methods. (a) Ferrite orientation map computed with the parent grain reconstruction method described by Niessen *et al.* [Nie22]. (b) Angle (in degrees) with dilated map of Figure 2.6(c)

apart from this boundary. To assign equal weight to each sub-area and avoid metric distortions, the grid must be uniform. For the sake of simplicity, a standard voxel sampling of parameter $\boldsymbol{t}$ was chosen although it is known that it is not the most appropriate choice [Yer10] (the earlier introduced "distance" between voxels is not strictly uniform). However, the angular distances between orientations considered herein are assumed to be much greater than the heterogeneity of the inter-voxel distance. The labeled clusters identified with the connected components algorithm are depicted in Figure 2.9(a-b). Cells containing less than thirty orientations are associated with noise and assigned to label 0. An additional cleaning step is performed by deleting those bad pixels and running the dilation process again (Figure 2.9(c-d)).

Processing austenite orientation

It is meaningless to classify austenite orientations on a full EBSD map including several ferritic grains. Crystallographic orientation distributions of the γ-phase are strongly related to the primary α-grain from which it originated. This feature is highlighted by plotting the child orientations relatively to the parent grain crystallographic frame (*i.e.*, plotting the misorientation $\tilde{\boldsymbol{g}} = \boldsymbol{g}_{parent}^{-1}\,\boldsymbol{g}_{child}$ in the orientation space). An example is given in Figure 2.10 corresponding to the ferritic grain attributed to the purple label in Figure 2.6. Each point was colored using a default inverse pole figure color map to highlight the γ-phase features. Its orientations are gathered in so-called Bain groups but showcase continuous transitions

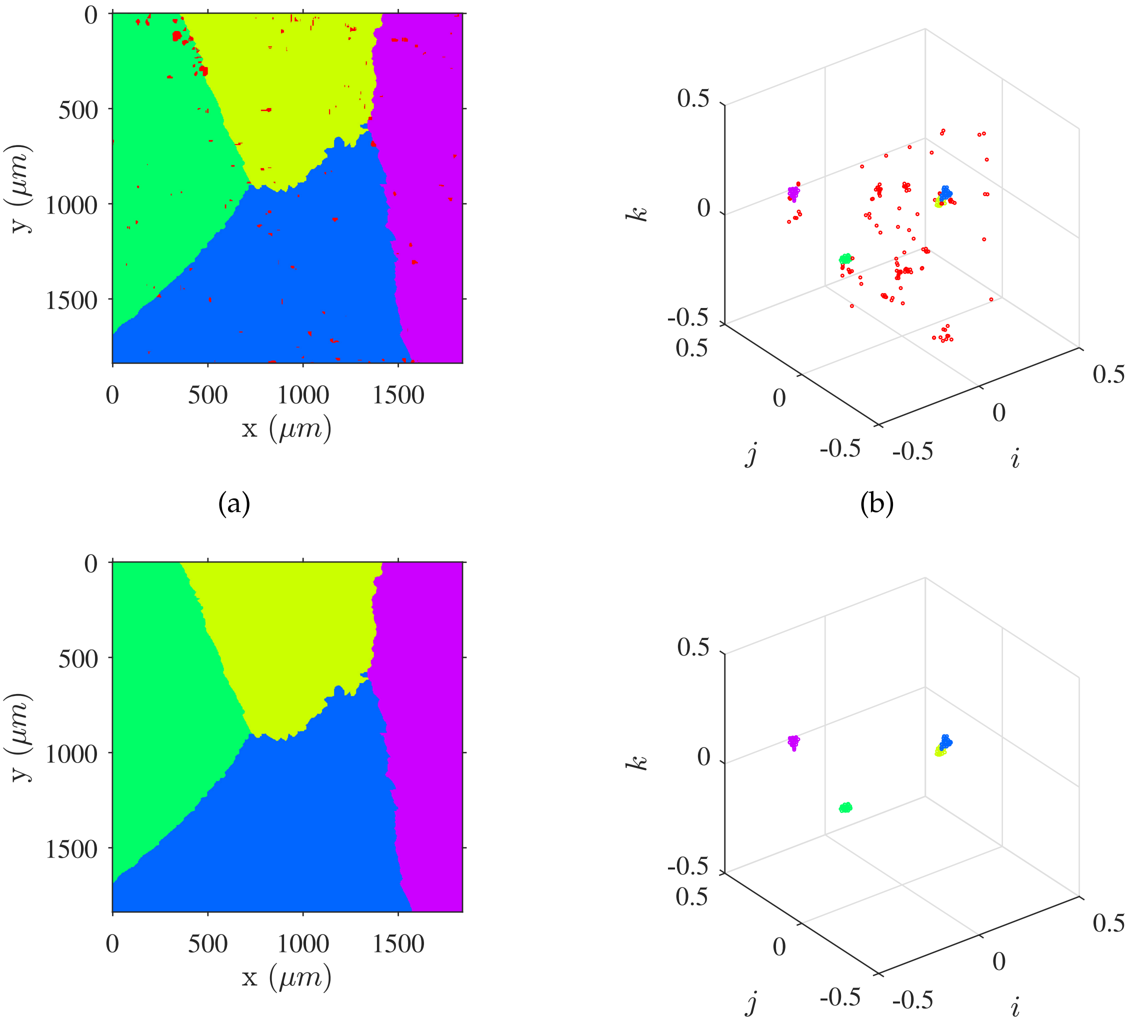

(a)

(b)

(c)

(d)

Figure 2.9: Illustration of ferrite orientation clustering using the connected components algorithm. (a) Labels attributed using the connected components algorithm in the orientation space. (b) Orientation colored according to cluster labels in the orientation space. (c) Label map after inpainting. (d) Dilated ferrite orientations after inpainting

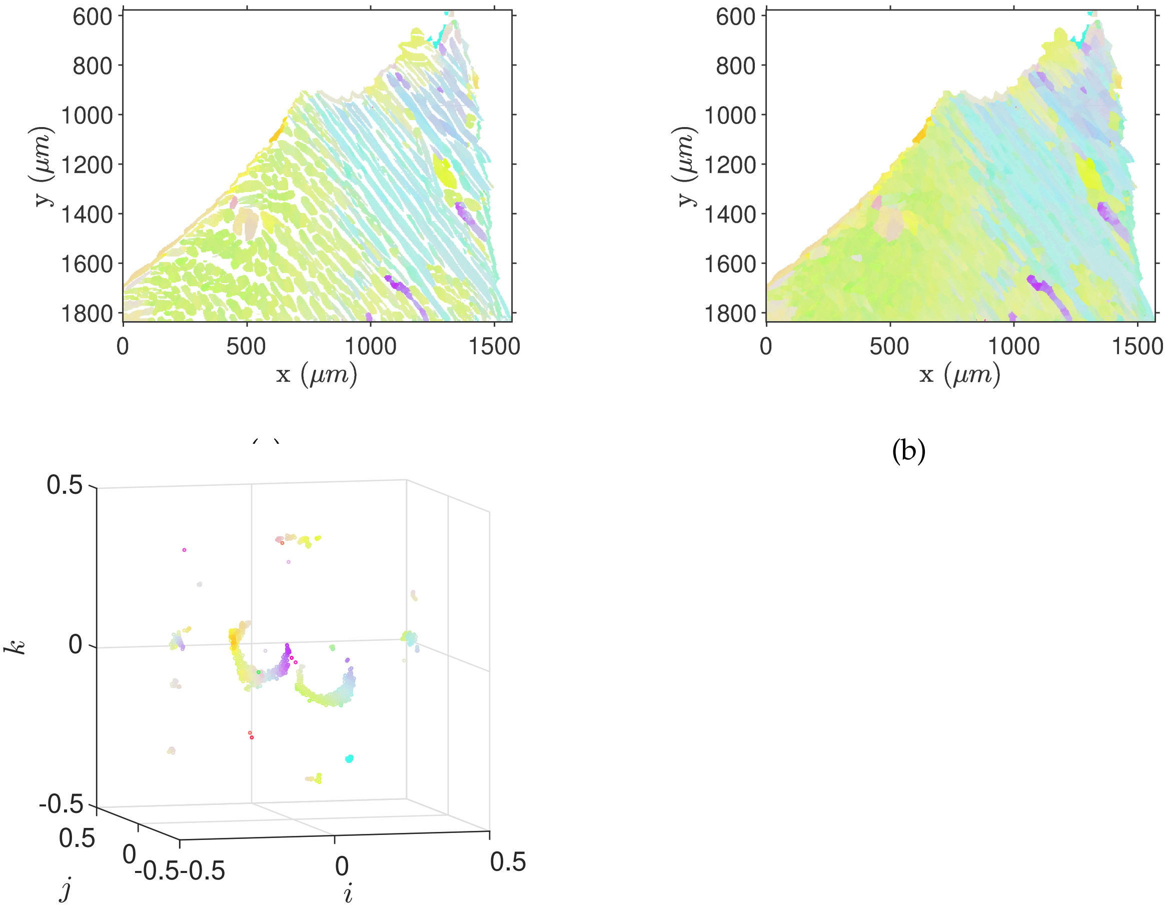

(b)

(c)

Figure 2.10: Illustration of the austenite orientation map dilation process in a single ferritic grain. (a) Measured orientation map. (b) Dilated orientation map. (c) Dilated orientations plotted in the ferrite crystallographic reference frame.

between commonly reported orientation relationships (OR) (*e.g.*, Kurdjumov-Sachs (KS), Nishiyama-Wassermann (NW) and Pitsch (P)). These Bain groups correspond to the union of symmetrically equivalent orientation relationship representatives (*i.e.*, variants) that are close to one another. The continuous aspect manifests itself through smooth crystallographic gradients between variants belonging to a Bain group and morphological gradients on the orientation maps.

There is an intrinsic issue in reading quaternion plots in this case because orientation clusters are not distinct but rather large and elongated. Thus, a K-means tool was used to automatically search for centroids and significant orientation groups in the map. The clustering algorithm was helpful to selecting points that illustrate the continuous aspect of the orientation spread. Clusters identified on the data set of Figure 2.10 are given in Figure 2.11 for five centroids randomly initialized inside the cubic fundamental region. This segmentation clearly depicts the majority of orientations spreading around one Bain group (orientations gathered in clusters 1, 3 and 5 of Figure 2.11(a-b)). Few remaining points are either on the other two Bain groups (far from usual orientation relationships) or badly indexed (clusters labelled 2 and 4 of Figure 2.11(a-b)). The segmentation also points out the continuity between the three major clusters. Clusters 1, 3 and 5 seem to be connected as represented in Figure 2.11(b).

The continuous path between different ORs was highlighted before in FCC to BCC transformation paths [Cay10, Cay20], and in the reverse transformation [Sta05, DJ17] occurring in the present material. The continuous aspect is strongly believed to be explained by the accommodation of elastic strains in the parent matrix during the $\alpha \rightarrow \gamma$ phase transformation [Cay13] since continuous OR variation accompanies continuous morphological features. The studied dual phase steel has the particularity to have continuous orientation variations over long characteristic lengths compared to primary ferrite grain sizes. Thus, this feature is likely to influence the local mechanical behavior and should be preserved in the segmentation step. Strict segmentation of the presented data proved to be inadequate for describing this BCC to FCC transformation feature.

The consistency in the orientation groups computed by K-means was recovered by measuring the smallest distance between all pairs of points in different groups. One way around computing the full distance matrix between points in two groups G_{k_1} and G_{k_2} is to evaluate the distance matrix for a single orientation g_{k_1}, and to find the orientation in the second group corresponding to $\min_{g_{k_2} \in G_{k_2}}(\mathrm{d}(g_{k_1}, g_{k_2}))$. Carrying out the computation this way and the other from G_{k_2} to G_{k_1} iteratively allows for the determination of the closest points in the two groups in a very small number of steps. If the distance between the two closest orientations is less than a given threshold, the two groups are merged; otherwise they correspond to distinct orientation clusters.

Figure 2.11(c-d) depicts the application of the merging algorithm on the spatial map and in the orientation space. Three clusters remained after merging clusters 1, 3 and 5 of Figure 2.11(a-b) into a unique one labelled 1 in Figure 2.11(c-d). These three clusters roughly correspond to the three Bain groups where continuity in the orientation spread is now preserved. According to Figure 2.11(c), a majority of austenite orientations belongs to a single Bain group, but exhibits a significant orientation spread greater than 10°.

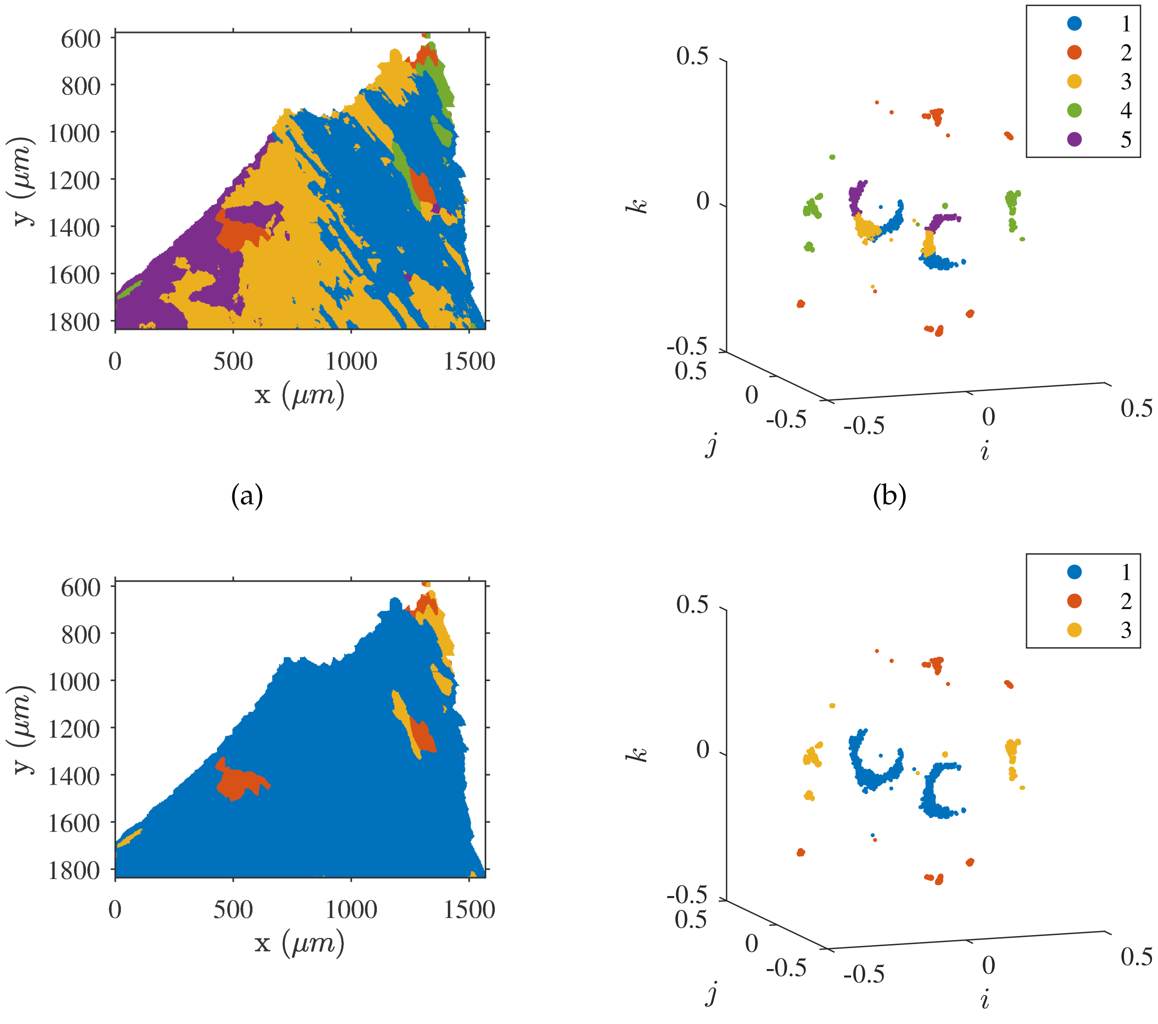

(a) (b)

(c) (d)

Figure 2.11: Clustering of austenite crystallographic orientations in a single ferritic grain using K-means with $k = 5$ before and after merging adjacent groups. (a) Computed clusters illustrated on orientation map. (b) Same clusters in the orientation space. (c) Retained classification after merging adjacent clusters. (d) Merged clusters represented in the orientation space

2.3.5 Conclusion

The use of an image processing inspired workflow accounting for crystal orientation data proved to be useful in reading the complex microstructure of a CF8M dual phase steel. The chosen hierarchical approach using different classification and segmentation steps emphasized different specific features of the studied microstructure. The parent ferritic grain structure was fully retrieved from the combined dilation-erosion, and classification using a connected components algorithm. The structure of austenitic laths was determined from similar techniques. However, the K-means algorithm intended for clustering orientations connected to distinct orientation relationships with the parent phase turned out to be insufficient. Regrouping the obtained clusters based on their minimum distance allowed for the restoration of continuity in austenite orientations. Assuming that the BCC to FCC phase transformation was predominantly displacive (*i.e.*, diffusionless), the precipitation of austenite at former ferritic grain boundaries resulted in high strain energies. A unique relationship that tended to minimize lattice distortions could not be followed in two α-grains that were randomly oriented with respect to each other. Accommodation was thus carried out while the precipitate moved farther from the boundary during the cooling process, thereby resulting in smooth morphological and crystallographic orientation gradients in the γ-phase.

This work demonstrated the benefit of using classification and segmentation techniques adapted from image analysis procedures on crystallographic data. The introduced tools may be useful in various cases from manual investigations to fully automated processing of microstructures giving a better understanding of the studied material. In the present case, the knowledge of the different scales and their properties was needed for a better understanding of the alloy behavior. The relationship between relative phase orientations and laths morphology is one key ingredient to develop a consistent mechanical model. Besides, the recovered domain geometries (*i.e.*, primary ferrite grains, laths packet) will be used to identify different constitutive laws using full field measurements together with the analysis of their microstructure. 3D reconstruction will also be considered by generalizing the presented algorithms in the third (missing) dimension.

Addition to the paper conclusion

The previously introduced segmentation technique emphasizes continuity in the austenite orientation layout. Adding a spatial connexion component in the segmentation is insufficient since some laths packets display smooth transitions or cross former grain boundaries indifferently. Proving a relationship between discrete crystal and morphological orientations with the previous method would require arbitrarily breaking this continuity, making the comparison with existing relations a difficult task. Consequently, a sampling of Bain groups that is physically relevant needs to be introduced. In the following, it is proposed to look at existing relationships and to propose a coherent sampling of austenite orientations lying on Bain groups.

2.4 Link between laths crystal orientation and their apparent morphology

Reproduced from: **M. Mollens, A. Guery, D. Loisnard, F. Hild and S. Roux, 2022**. Link between BCC-FCC orientation relationship and austenite morphology in CF8M stainless steel. *Submitted*

2.4.1 Introduction

It is well established that the macroscopic mechanical behavior of materials is conditioned by their microstructural properties. For instance, the size, shape and texture of crystals in steel and alloys are first order parameters in the prediction of their mechanical response [Kim81, Han04, Bou06, Ver17]. In forming processes involving displacive (*i.e.*, diffusionless) transformations, the final texture results from the parent phase texture and the symmetry involved in the displacive mechanisms giving rise to the child phase [Bun84, Bat00]. Similar conclusions are drawn regarding crystal shapes. The child phase morphology is therefore inherited from parent orientations and the induced crystallographic consistency between the two phases.

Several components of the primary coolant system in nuclear power plants are made of alloys involving complex phase transformation, and they are of fundamental importance to ensure safe operations. In their in-service environment, they undergo severe thermal and mechanical loadings for an extended time duration [Bet96, JG00]. The temperature they are subjected to leads to slow microstructural transformations resulting in a modification of their mechanical properties. Hence the impact of thermal aging on the risk of failure must be predicted accurately to support their integrity demonstration for long term operation [LD15]. The material these parts are made of exhibits a very peculiar dual-phased microstructure (*i.e.*, formed from an α ferrite (BCC) to a γ austenite (FCC) transformation) that is responsible for its specific corrosion and ductile fracture resistance. This microstructure presents identifiable properties in a broad range of scales from millimetric polygonal parent grains to the atomic scale where thermal aging occurs. When building a consistent multiscale model, careful investigations of the microstructure are to be carried out. Understanding its dual-phase layout and crystallographic relationships is required to control the deformation mechanisms occurring during the component lifetime. At first sight, both should be deduced from the crystallographic orientation relationship (OR) between the two phases, based on prior knowledge of the parent phase. Numerous and rigorous experimental and numerical works have proven the link between ORs, crystallographic properties and morphology in martensitic steels in which displacive transformation (from γ austenite to α ferrite) occurs. Morito *et al.* [Mor06] have listed a series of historical works on this issue, and more recent studies continue to tackle the complex mechanisms of martensite transformation with interpretation of experimental observations [Bau19, Ram20] and numerical simulations [Eng08, Tat08, Mal12, Zha21]. Materials presenting the reverse transformation were also studied but to a much lesser extent.

Tools commonly used for an accurate determination of crystallographic parameters may not be suitable for coarse microstructures. In particular, transmission electron microscopy is not appropriate for the considered material, as it cannot safely be scaled up to reach the characteristic scale of the grains. Consequently, mostly Electron BackScattered Diffraction (EBSD) analyses will be used in this paper as they allow for crystallographic measurements with the necessary accuracy over large surfaces.

The outline of the paper is as follows. First, observations regarding the specific microstructure properties are extracted from EBSD measurements in Section 2.4.3. To address the complexity associated with the material forming process, a specific post-processing of EBSD maps is introduced for determining preferential directions of austenite (Section 2.4.4). Results are then confronted to different theoretical models proposed in the literature. Last, previously reported observations are discussed in Section 2.3.5 together with perspectives toward future studies.

2.4.2 Experimental Procedures

The studied material is a cast dual-phase CF8M stainless steel. The samples were taken from an 80 kg cast ingot (≈ 6.4 dm^3) using electrical discharge machining (EDM) far from external surfaces to avoid inhomogeneous zones. The ingot was cast, then air cooled for approximately 15 days before being heat-treated at 1120°C for 6 h and 20 min, and then water quenched. The corresponding composition is given in Table 2.2 for the major chemical components. For SEM observations and EBSD acquisitions, the samples were mechanically polished up to 0.1 µm grain size and then processed with an oxide polishing solution. Acquisitions were carried out on a Mira3 SEM from TESCAN, and diffraction patterns were indexed using “OIM Data Collection”. All EBSD maps have a 3 µm step size. The open source Matlab MTEX toolbox [Bac10] was used for its very convenient and flexible plotting features.

Table 2.2: Measured chemical composition (wt.%) of the ingot from which samples were extracted.

C	Si	Mn	S	P	Cr	Ni	Mo	Cu	Co
0.032	1.04	0.80	0.0007	0.025	20.9	10.4	2.68	0.17	0.02

2.4.3 Observations

The material obtained from the casting process has two phases resulting from the partial ferrite to austenite transformation, and the solutionizing heat treatment recovering some of the transformed ferrite during the first cooling step. The analyzed specimens have roughly a 25/75 vol.% ratio for ferrite and austenite, respectively. The resulting microstructure is shown in Figure 2.12. The orientation map of the α-phase reveals the geometry of primary grains with distinct areas of uniform orientation. Conversely, the γ-phase exhibits elongated lath colonies with homogeneous or smoothly varying crystallographic orientations.

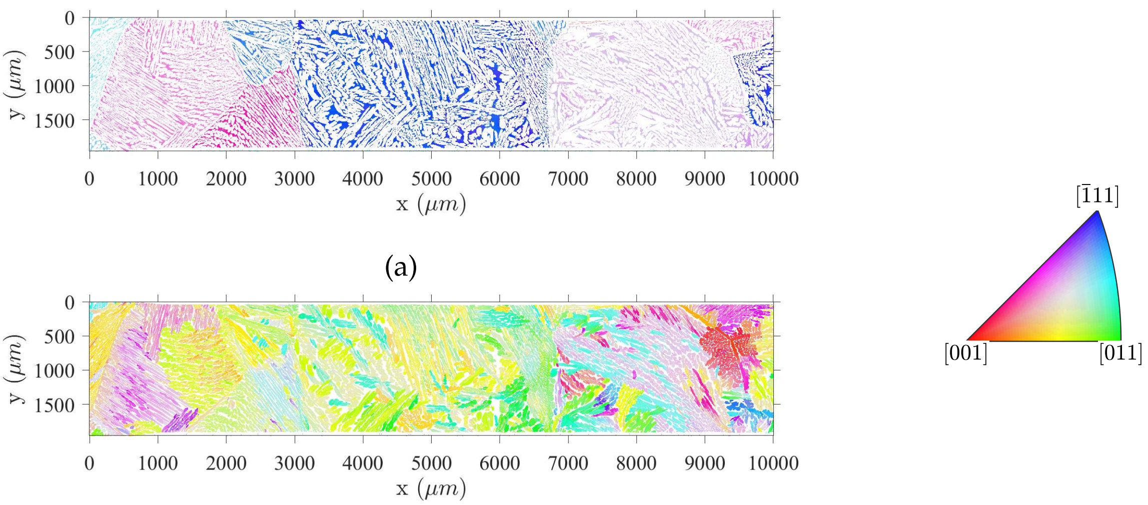

(a)

(b)

Figure 2.12: Microstructure of CF8M dual-phase steel. (a) α-phase map displaying large ferritic grains resulting from the first phase transformation. (b) Austenitic lath network growing within ferritic grains.

2.4.3.1 Primary ferrite grain inner structure analysis

In order to quantify possible links between parent and child orientations, and their correlation with the laths morphology, it is necessary to first estimate the primary phase orientation where laths have grown from. The remaining α-phase is then utilized to recover the primary grain geometry using, for instance, a crystallographic orientation based inpainting process [Mol22b]. The recovered orientation map displays millimeter-size polygonal grains resulting from the first phase transformation (*i.e.*, liquid to solid). Hence, at each pixel coordinate $\boldsymbol{x}$ of the map, the austenite orientation $\boldsymbol{g}_\gamma(\boldsymbol{x})$ can be connected to its parent phase orientation $\boldsymbol{g}_\alpha(\boldsymbol{x})$ (*i.e.*, the misorientation $\boldsymbol{m}(\boldsymbol{x}) = \boldsymbol{g}_\alpha^{-1}(\boldsymbol{x})\,\boldsymbol{g}_\gamma(\boldsymbol{x})$ can be measured.

Commonly mentioned orientation relationship (ORs) in BCC $\leftrightarrow$ FCC phase transformation include Bain (B) [Bai24], Kurdjumov-Sachs (KS) [Kur30], Nishiyama-Wassermann (NW) [Nis34, Was35], Pitsch (P) [Pit59] and Greninger-Trojano (GT) [Gre49]. Experimentally, measured ORs are more than 9° away from B, and most of the time related to KS and NW [Ver09]. These two ORs actually result from experimental observations using X-ray diffraction in the FCC $\rightarrow$ BCC case. P and GT ORs were identified using transmission electron microscopy (TEM) approximately 20 years later. Some authors mentioned that ORs in BCC $\rightarrow$ FCC transformations were far less discussed even if some relatively recent studies on meteorites [Bun03, He06, Nol08, Yan10] and various metallic alloys [Sta05, Fuk11, Rao16, DJ17, Hag20, Cai21] have appeared.

Let us consider that these ORs are defined by the set of parallel planes and directions given in Table 2.3 (and not reduced to a single rotation operator, since a non-zero strain is needed to accommodate the crystal atomic spacing). Then, the misorientation is the rotation that maps the crystal directions $\boldsymbol{d}_\alpha$ of the child phase to their parallel relatives $\boldsymbol{d}_\gamma$ in the parent frame. The misorientation obeying $\boldsymbol{d}^1_\gamma || \boldsymbol{d}^1_\alpha$ and $\boldsymbol{d}^2_\gamma || \boldsymbol{d}^2_\alpha$ is such that $\boldsymbol{d}^1_\gamma = \boldsymbol{m}_{\alpha\to\gamma}\boldsymbol{d}^1_\alpha$ and $\boldsymbol{d}^2_\gamma = \boldsymbol{m}_{\alpha\to\gamma}\boldsymbol{d}^2_\alpha$. The axis-angle representation associated with the parallelism conditions is given in Table 2.3.

Table 2.3: Orientation relationships commonly referenced between FCC and BCC lattices. Both parallelism conditions and axis-angle pairs are given. The latter corresponds to the pair having the smallest rotation angle of all the symmetrically equivalent operators

OR	Plane	Direction
Bain	$(001)_\gamma \parallel (001)_\alpha$	$[110]_\gamma \parallel [100]_\alpha$
KS	$(111)_\gamma \parallel (110)_\alpha$	$[\bar{1}10]_\gamma \parallel [\bar{1}11]_\alpha$
NW	$(111)_\gamma \parallel (110)_\alpha$	$[\bar{1}10]_\gamma \parallel [001]_\alpha$
		$[11\bar{2}]_\gamma \parallel [\bar{1}10]_\alpha$
P	$(110)_\gamma \parallel (111)_\alpha$	$[001]_\gamma \parallel [\bar{1}10]_\alpha$
		$[\bar{1}10]_\gamma \parallel [11\bar{2}]_\alpha$
GT	$(111)_\gamma \parallel (110)_\alpha$	$[\bar{12}, 17, \bar{5}]_\gamma \parallel [\bar{17}, 17, 7]_\alpha$

Data obtained from a single ferritic grain are shown in Figure 2.13. Figure 2.13(a) displays austenite orientations (colored using the standard inverse pole figure code for cubic symmetry) grouped in lath packets with uniform or smoothly varying crystal orientations. These packets are also characterized by a preferred morphology. The comparison with all symmetrically equivalent child orientations (*i.e.*, so-called variants) predicted for KS (Figure 2.13(b)) and the distance distributions with some reference ORs in Figure 2.13(c) highlights the spread of crystal orientations. This phenomenon has already been observed in numerous studies [Nol04, Cay10, Yar14, DJ17, Hay20] but its origin is still unclear. Cayron *et al.*have built different physically based models [Cay10, Cay13, Cay15] by considering that there may be an optimal OR from which the transformation starts. As a consequence, the strain induced in the parent matrix would rotate the child phase nucleus along a specific direction producing an intermediate state between commonly cited ORs. Yet, the classical phenomenological theory of martensite crystallography (PTMC) [Bow54, Mac54, Wec59] has been widely accepted because of its flexibility regarding its input parameters and the agreement of some of its predictions with experimental observations [McD92, Chr02]. Interesting discussions have arisen with PTMC proponents claiming that the continuous orientation spread was attributed to diffusion regarding the very long recovery treatments involved in the studied materials [Bha11]. However, it was argued that similar pole figures could be obtained with the same material in as-quenched conditions [Cay11]. In addition, some recent analyses [Hay20] provide measurements of OR distributions that are interpreted within the PTMC framework.

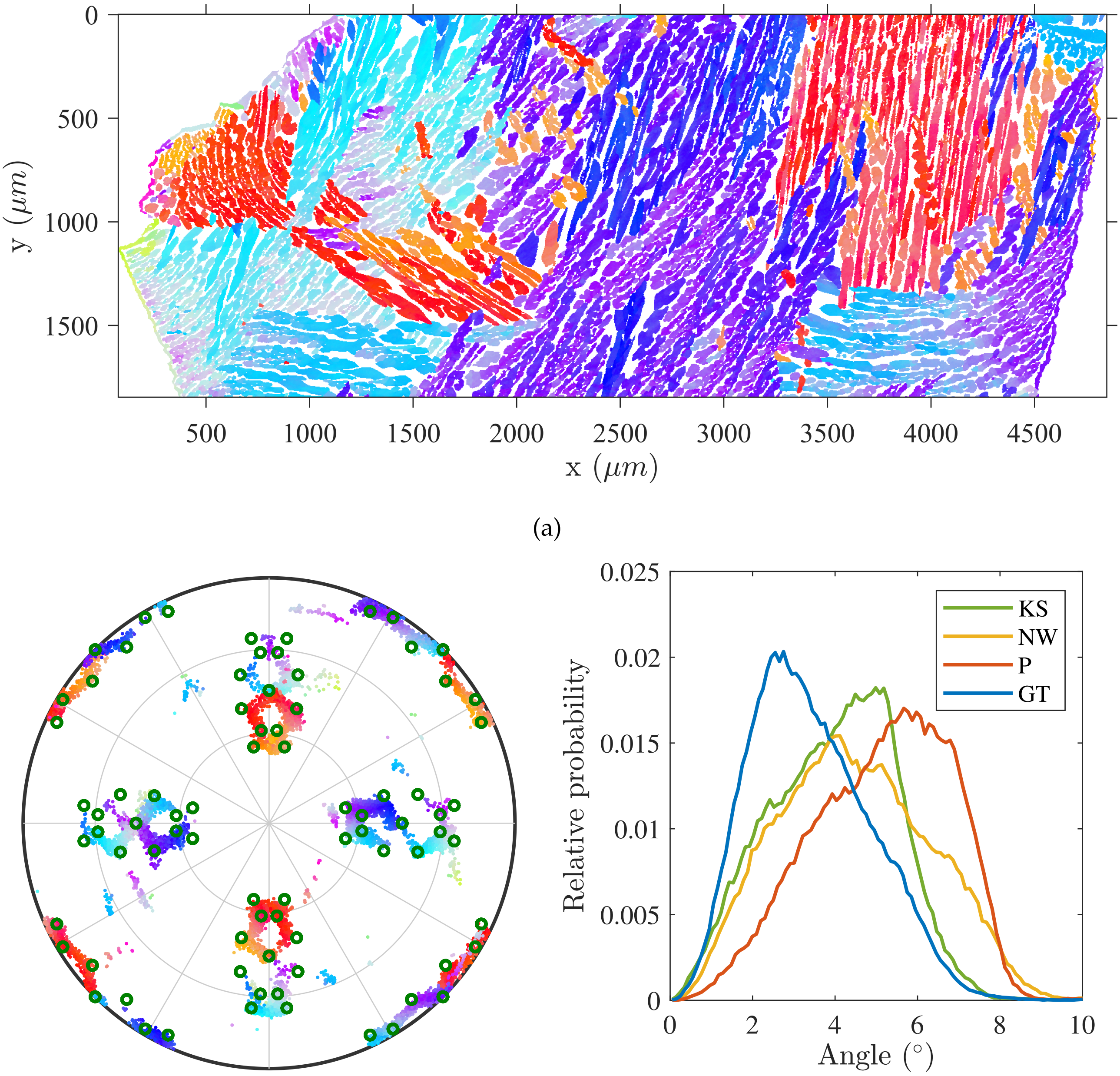

(a)

(b)

(c)

Figure 2.13: Austenite orientation in a single ferritic grain. a) Spatial orientation map (IPF colored); b) [111] pole figure in the ferrite crystallographic frame clearly displaying the γ-orientation spread in a single ferritic grain. The orientations are colored using the inverse pole figure color coding convention to relate to Figure 2.13(a). The exact KS variants are plotted in green to highlight the continuous feature. Only 1% of measured points of the data present on the spatial map are shown in the pole figure; c) Histograms of distance to some reference ORs in FCC ↔ BCC systems emphasizing that there is not a single representative OR in the CF8M alloy.

The material of interest for this study could bring interesting new observations to the discussion. Indeed, this alloy has been subjected to a long solutionizing heat treatment propitious for triggering diffusion-based mechanisms and exhibits a broad range of morphological features from sharp lath shaped patterns (associated with Widmanstätten growth) to more incurvate and globular ones. Moreover, locally measured OR in a single cluster may vary over a long characteristic length along with morphological changes. This morphological "gradient" is rather linked to a transition between OR variants than to genuine crystallographic distance to a fixed OR. A specific post-processing procedure of orientations was developed to reveal this aspect.

Instead of considering the crystallographic distance over the symmetry group, it was chosen to rely on an image processing based interpretation of the distribution of OR variants. Stereographic projections normal to the principal cubic directions of these variants show a nearly circular pattern (Figure 2.14(a)) the approximate expression "Bain circles" originates from. Knowing the Bain circle (*i.e.,* the Bain variant) on which lies an experimental γ-orientation $\boldsymbol{g}_{child}$, according to its parent α-orientation $\boldsymbol{g}_{parent}$, one may parameterize the angular position θ of $\boldsymbol{m} = \boldsymbol{g}_{parent}^{-1} \cdot \boldsymbol{g}_{child}$ (*i.e.,* the associated misorientation) on a circle centered on the Bain variant (Figure 2.14(a)). This step was achieved by projecting the quaternion vector representing $\boldsymbol{m}$ onto the plane normal to the Bain variant, and computing its polar angle with respect to an arbitrary direction. Hence, knowing $\boldsymbol{g}_{parent}$ allows one to reduce the description of $\boldsymbol{g}_{child}$ to two parameters, namely, the Bain variant and θ. The angle θ computed for austenitic orientations shown in the ferritic grain of Figure 2.13(a) are plotted on a [100] spherical projection in Figure 2.14(b).

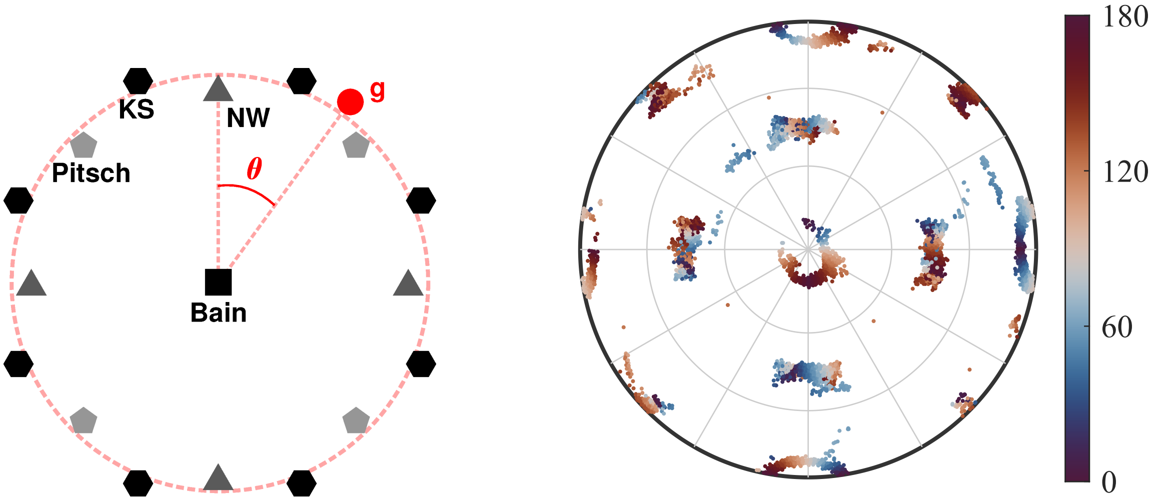

(a) (b)

Figure 2.14: Parameterization of γ-orientations according to their distribution about their corresponding Bain variant in a single primary ferrite grain. (a) Schematic representation of θ parameterization for a single Bain variant. The angle is taken between the orthogonal projection $\boldsymbol{g}$ and an orthogonal vector taken among three basis vectors of the ferrite grain crystallographic frame. Thus, only θ variation is symptomatic of a spread or orientations around Bain groups. (b) [100] pole figure of γ-orientation in the α-grain reference frame. Orientations are colored according to the value of θ.

Interestingly, the “circles” observed from the present EBSD analysis and shown in Figure 2.14(b) seem to display a quasi continuous distribution about each Bain variant. As shown in Figure 2.15(a), many different laths are encountered around each Bain variant, at different (but close) specific distances to Bain OR. The θ parameterization depicted in Figure 2.15(b) reveals an important feature of the γ-orientation distribution. In the ferrite reference frame, the continuous orientation around Bain circles correlates well with their morphology as observed on spatial maps. In some Bain groups (delimited by black lines on the spatial maps), the θ range is close to 180°, which reflects a transition from a near horizontal lath shape to a near vertical lath shape on the 2D section given by the EBSD maps. A 180° θ range also means that multiple ORs are crossed around a Bain group. In other words, a single spatial Bain group may contain multiple variants of a single OR, smoothly connected with orientation gradients.

The θ parametrization is only relevant for orientations lying on (or close to) the circles, considering a sensible tolerance regarding the EBSD measurement accuracy. In this example, a small number of regions is far from all Bain variants (distance greater than 15° in Figure 2.15(a)). A detailed analysis shows that they are close to the primary α-grain boundaries. Still, the analysis of misorientation and morphology at primary α-grain boundaries is relevant. During solidification, the second phase transformation (from α to γ) is likely to nucleate at grain boundaries and even more at triple points. This observation is supported by optical micrographs reported by Stanford and Bate [Sta05] showing the as-quenched fixed microstructure of brass with a similar microstructure and solidification path. Further, the surfaces describing primary ferrite grain boundaries are replaced by a "thickened" austenitic surface with same primitive shape from where the inner laths grow since they are sharing the same orientation on the spatial maps. Hence, if γ-laths grow from ferrite grain boundaries, hints on the solidification mechanisms should be found in these regions. In addition, the austenitic microstructure in the inner primary ferrite grain may result from a transition to that starting at its boundaries as the previously highlighted smooth transitions seem to always start or end there.

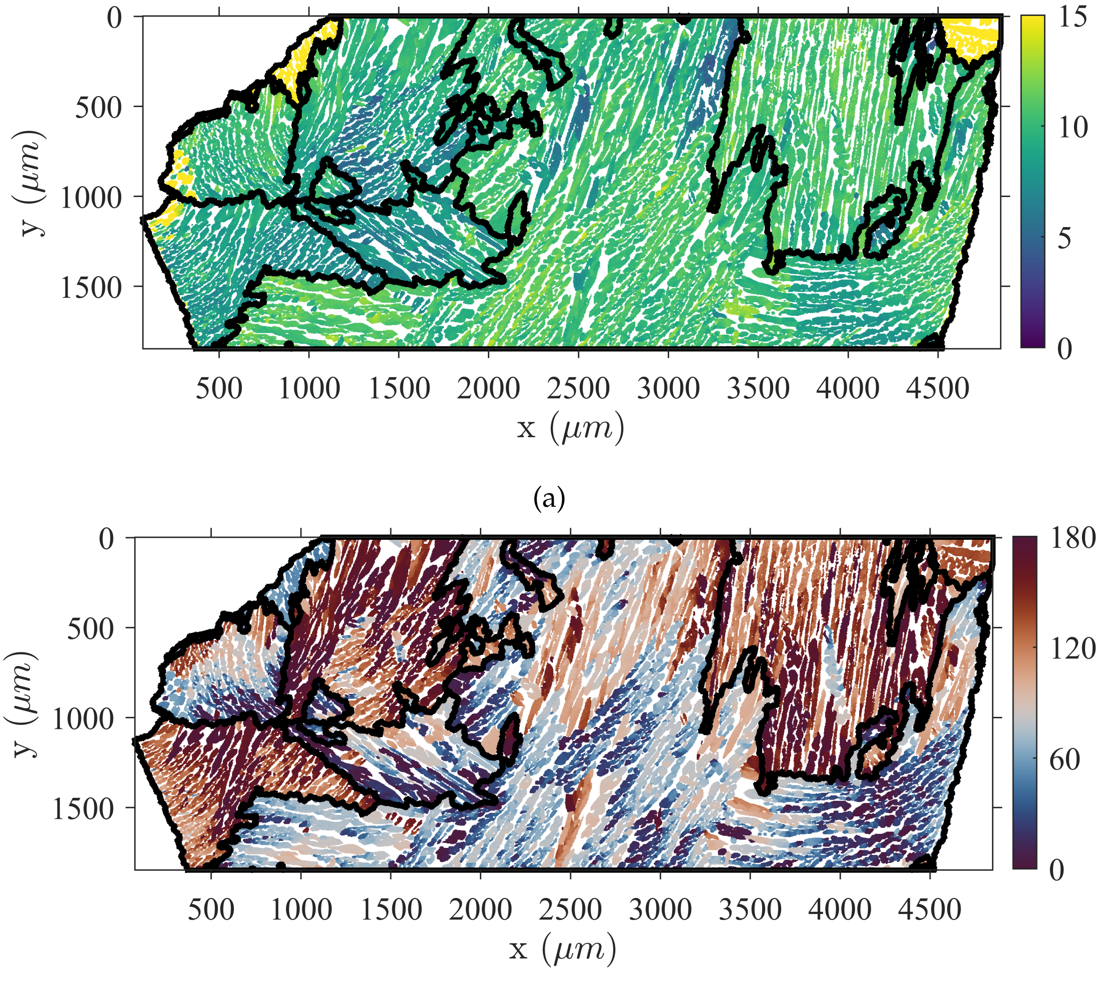

(a)

(b)

Figure 2.15: Illustration of the variant crossing phenomenon. (a) Crystallographic distance (in degrees) to Bain OR. Frequently reported KS and NW ORs are at 11.07°and 9.74°, respectively. The depicted map is spread over a greater extent. The black boundaries delimit neighboring Bain groups. (b) Spatial map colored according to the value of θ. This subfigure shows that the orientation may cross multiple variants of a given OR in a single Bain group by preserving a spatial continuity at this scale (*i.e.,* θ varies more than 7.54°, which is the smallest $\Delta\theta$ separating two variants in the cited ORs.

2.4.3.2 Primary ferrite grain boundaries neighborhood analysis

Two types of boundary configurations are distinguished from the EBSD maps. *Almost-coherent* boundaries (*i.e.,* low angle grain boundaries) and *incoherent* boundaries where the disorientation is high (more than 10°). In almost-coherent boundaries, Bain groups from both sides of the boundary are close or may cross each other. Consequently, there is a good agreement between orientations in both grains hinting that, at the present scale, the laths are crossing the original ferrite grain boundary. Figure 2.16 shows such an example. With a disorientation angle of 6.86°between the two ferritic grains, the morphology and crystal orientations are preserved on both sides of the boundary. The pole figures in Figure 2.16(b,c) illustrate the small gap between the two sides given the accuracy of orientation measurements. More importantly, they demonstrate that in each grain, austenite orientations lie on the Bain circle given by its ferrite orientation, meaning that a slight rotation occurs in the vicinity of the boundary to comply with this observation.

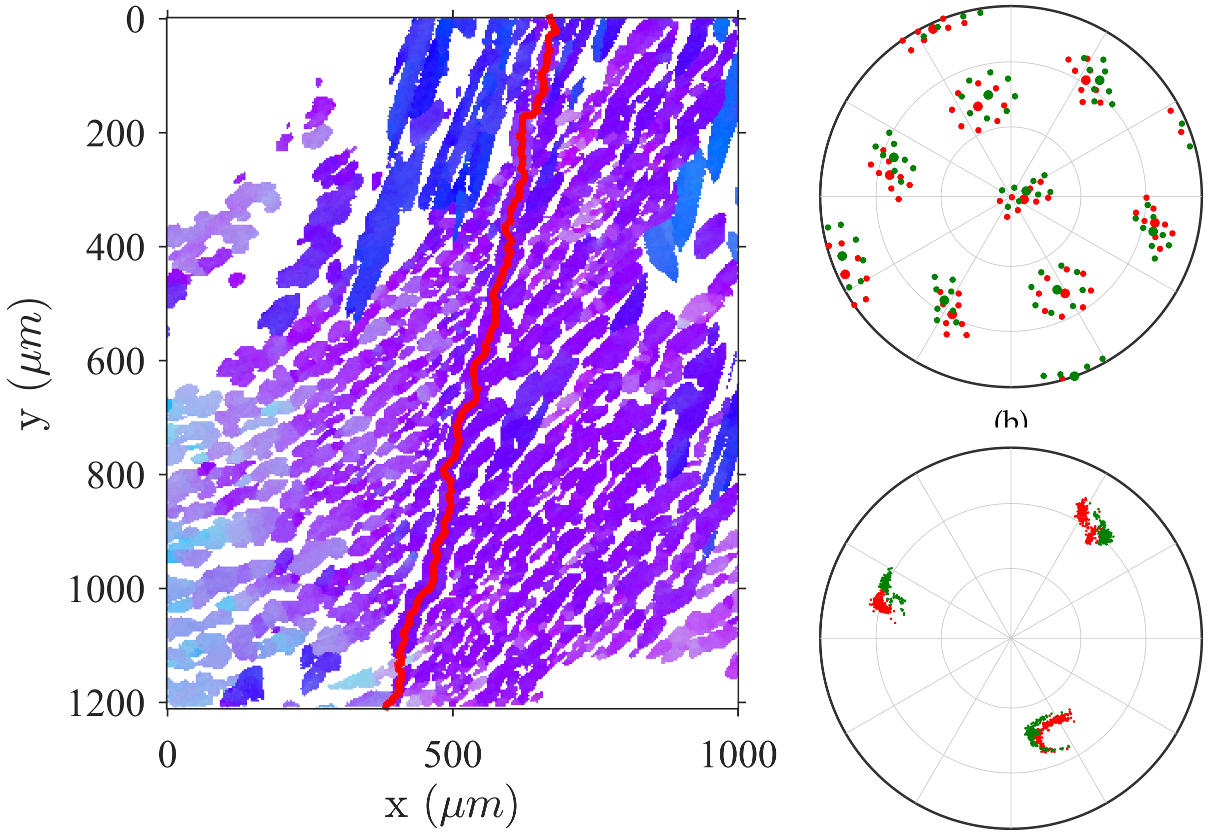

(a) (c)

Figure 2.16: Orientation and morphology for an almost-coherent grain boundary. (a) Spatial plots of orientations using an inverse pole figure based color coding. The primary α-grain boundary is plotted in red. Morphology and orientation of austenite appears similar on either side of the boundary. (b) [100] pole figure of the simulated KS and B variants given the primary α grain orientations. The red points correspond to the left grain, and green to the right one. (c) [100] pole figure showing actual γ-orientations measured in both grains using the previous color coding.

The second type of boundaries, coined incoherent, corresponds to a large disorientation angle boundary illustrated in Figure 2.17(a). Since the child phase predominantly starts growing from these boundaries, severe accommodation should occur to grow on the side where its orientation does not lie on the corresponding Bain group. Yet, the crystallographic orientation is preserved across such boundaries at the cost of a loss of coherence with the parent lattice. Figure 2.17(b) corresponds to the predicted [100] directions according to Bain and KS ORs for the two parent grains. Figure 2.17(c) reveals the actually measured [100] directions being far from the predicted ones for the top grain (red points in Figure 2.17(b,c)) and more coherent with the Bain zone predicted for the bottom grain. However, in the incoherent grain, austenite takes the shape of laths with a different morphological orientation possibly adapted to the top grain orientation.

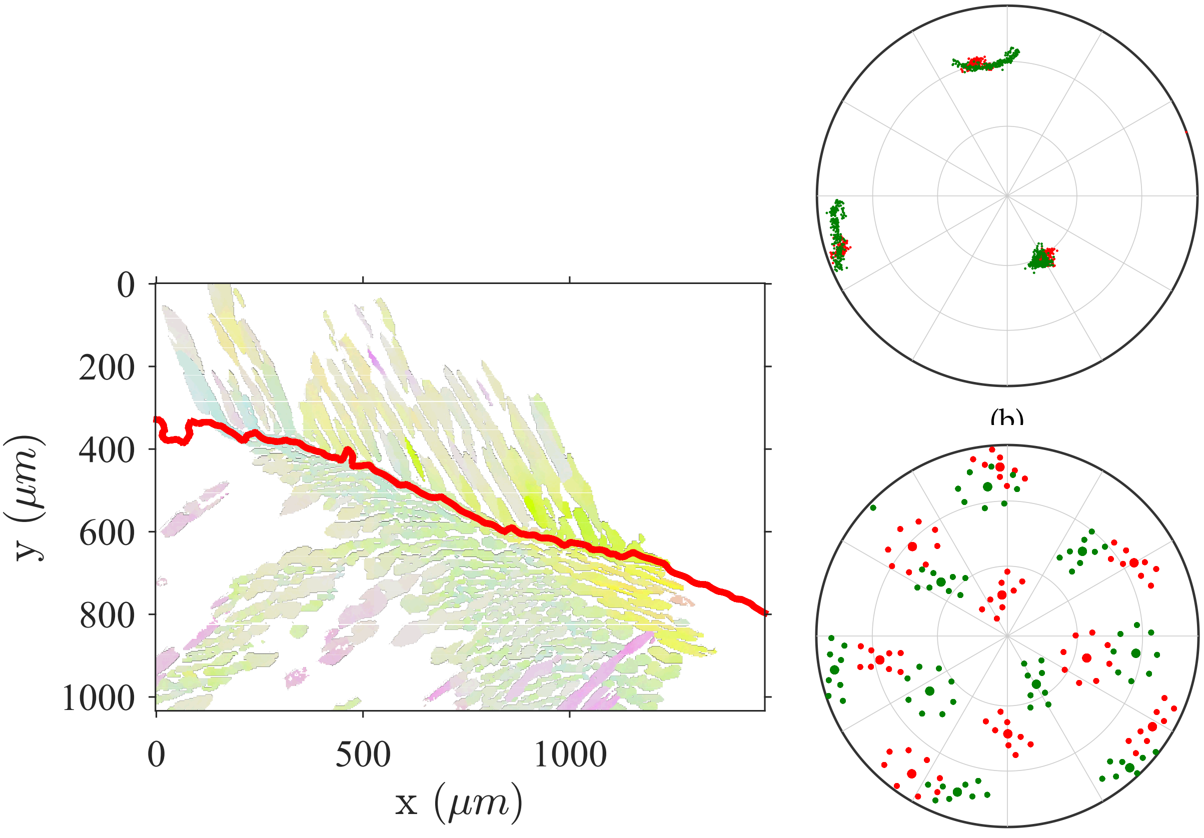

(a)

(b)

(c)

Figure 2.17: Orientation and morphology for an incoherent boundary. The disorientation between the two primary α-grains is 41.1°. (a) Spatial plots of orientations using an inverse pole figure based color coding. The primary α-grain boundary is plotted in red. Only the crystallographic orientation is preserved on both sides of the boundary. In the incoherent grain, a lath shape is also preserved with a different morphological orientation. (b) [100] pole figure of the simulated KS and B variants given the primary α-grain orientations. The red points correspond to the left grain, and green to the right one. (c) [100] pole figure showing the preservation of γ phase orientations in the two parent grains even if it is far from a stable configuration given by standard ORs.

2.4.4 Lath plane determination

2.4.4.1 Method

The determination of the plane of the lath of lath-shaped austenite crystals (*i.e.*, the so-called habit plane) is of great interest to study the local mechanical behavior. Lath clusters have near uniform or smoothly varying crystallography and morphology. Assuming that these orientations result from a unique mechanism linked to preferential growth directions, there must exist a limited number of configurations to which a relevant homogenized mechanical behavior may be attributed. However, if austenite islets are largely extended, their boundaries locally display large fluctuations. This property is likely to be inherited from the long solutionizing heat treatment and prevents from using the standard habit plane determination methods associated with TEM measurements [Oka92, Zha95, Luo06], requiring an accurate and unbiased definition of phase boundaries. Therefore, one may only rely on average measurements to determine the laths extension. If the lath packet average direction can be extracted in the observation plane, the method introduced by Hoekstra *et al.* [Hoe78] is practical.

Considering a single configuration, the lath normal is fully described by a unique direction in the parent frame or by two directions in the lath plane. The trace of a lath in a cross-section as observed on any imaging technique is somewhere between an acicular and globular shape. Figure 2.18 illustrates that the preferential direction of the lath cross-section, in the observation plane, corresponds to a linear combination of the two vectors defining the lath plane. To completely determine the plane, another projection is required. For the same plane, one may determine a second non collinear vector by finding a similar layout in a ferrite grain having a different orientation (Figure 2.18(b)). The parent crystallographic direction corresponding to the lath normal is then retrieved by finding a vector that is orthogonal to the two in-plane vectors.

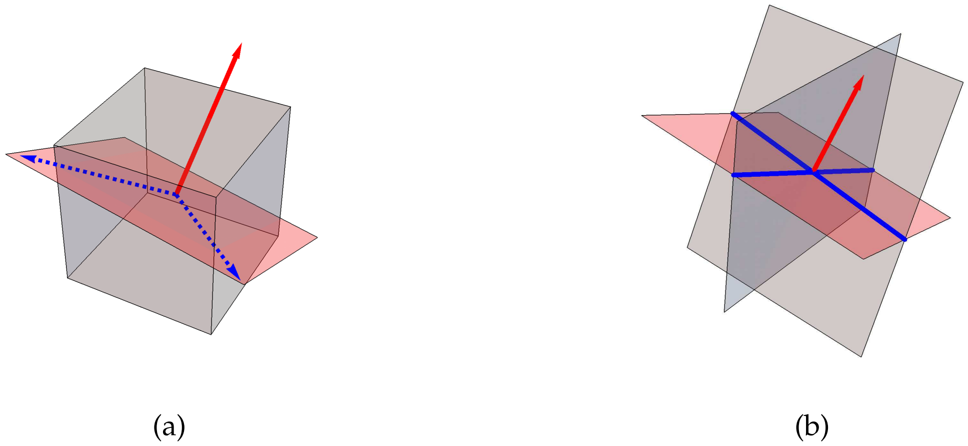

Figure 2.18: Illustration of the geometrical configuration of laths. (a) Illustration of fixed configuration. The lath plane (in red) is fully described by its normal (plain red arrow) or by two non-collinear vectors in the plane (dashed blue arrows). (b) Illustration of two cross-sections (blue lines) of the lath plane given by two random observation planes (grey planes). Any cross-section of the lath plane has a principal direction in 2D that is a basis vector of the lath plane in the parent frame. At least two (non collinear) cross-sections are required to fully determine the normal.

It is worth noting that there is not a single configuration in the parent frame. Otherwise, all lath cross-sections would appear identical in a single ferrite grain. Conversely, the different cases are likely to be selections of different variants of a single or multiple ORs. First, it may be postulated that a single OR is followed and check for the consistency of this assumption. Each child orientation is attributed to the closest child variant predicted by the OR, and lath clusters are associated with contiguous areas belonging to the same variant. According to the previous observations, each child cluster should have near uniform crystallography and morphology (*i.e.*, preferential orientation). Hence, an EBSD map can be processed hierarchically to compute i) the ferrite grains, ii) the child variant clusters, and iii) the mean morphological orientation. If two clusters for each child variant are found in a different configuration (*i.e.*, in two ferritic grains that have different orientations), the lath normal can be computed in the parent crystallographic frame (as explained in Figure 2.18(b)). However, the mean orientation computation will suffer from all the experimental inaccuracies of EBSD maps (definition of phase boundaries according to the imaging technique, natural fluctuations of boundaries). Thus a large enough statistical sampling is needed to retrieve the lath normal for each cluster. The pseudo-code for retrieving the lath normals for a given OR from the measured orientation map in the studied CF8M alloy is given in Algorithm 3.

The chosen OR defines the subsets of the orientation map in which the morphological properties are estimated. Each child orientation is attributed to the closest predicted ones

Algorithm 3 Lath normal computation from EBSD maps

```
Require: $F$                                  ▷ Spatially defined set of $\alpha$-orientations
Require: $A$                                  ▷ Spatially defined set of $\gamma$-orientations
Require: $\boldsymbol{m}$                                  ▷ Chosen orientation relationship
$G_f \leftarrow (g_f(n))_{n=1..N_g}$                        ▷ Set of $N_g$ grains from $F$
for $i = 1..N_p$ do                ▷ Browse the $p$ predicted variants according to $\boldsymbol{m}$
    for $j = 1..N_g$ do                              ▷ Browse every $\alpha$-grain
        $C_p^m \leftarrow$ Orientations in $g_f(j)$ belonging to the $i$-th variant cluster according to $\boldsymbol{m}$
        $\boldsymbol{v} \leftarrow$ Mean morphological orientation from $C_p^m$
        $\boldsymbol{h}(j) \leftarrow$ Corresponding crystallographic orientation of $\boldsymbol{v}$ in parent frame
    end for
    $H(i) \leftarrow$ best perpendicular vector to set $\boldsymbol{h}$
end for
```

considering the local parent orientation and the OR. The mean morphological orientation of each resulting clusters is computed using the structure tensor $\boldsymbol{n} \otimes \boldsymbol{n}$, where $\boldsymbol{n}$ is the mean pixelwise normal vector at the boundary. Its minor eigen vector corresponds to the projection of the mean lath normal in the observation plane while its major eigen vector relates to the direction of extension of the laths in the packet. Likewise, the "best" perpendicular vector to a set of vectors $\boldsymbol{v}$ is conventionally defined as the minor eigen vector of $\boldsymbol{v} \otimes \boldsymbol{v}$.

2.4.4.2 Application

The above construction was tested for all "classical" ORs (*i.e.*, B,KS,NW,P,GT). The Pitsch OR appears to provide the most consistent agreement between predicted austenite lath morphology orientation and crystallography. In order to take advantage of a significant statistical distribution, a total surface of 140 mm^2 was used to compute the normals of the twelve child variants predicted by the OR. The different steps are illustrated on the microstructure shown in Figures 2.13, 2.15 and 2.19. Figure 2.19(a) shows variant clustering of austenite orientations performed in every ferrite grain according to the Pitsch OR (12 variants). The resulting clusters qualitatively encompass a uniform morphological orientation.

The $[111]$ pole figure (Figure 2.19(b)) reveals how the sampling of child orientations given by the variant clustering fragments the continuous aspect introduced in Figure 2.14. Once the sampling is performed, each variant cluster is processed to compute the principal axis of the laths corresponding to the cross-section between the lath plane and the observation plane (Figure 2.19(c)). For all processed ferrite grains, this direction is stored as a crystallographic orientation in their frame. Once the sampling is complete, each variant cluster is processed to compute the principal axis of the laths corresponding to the cross-section between the lath plane and the observation plane (Figure 2.19(c)). For all processed ferrite grains, this direction is stored as crystallographic orientation in their frame. These directions should theoretically all lie on a plane but some deviations are observed. Laths are not strictly planar and some clusters are not well determined. These differences introduce artifacts in the principal direction computation. To take into account such errors, the lath plane normal is computed as the "best" (as above defined) perpendicular vector to the set of computed principal directions. As an example, the set of directions and the resulting lath normal for the 12th cluster are shown in Figure 2.19(d).

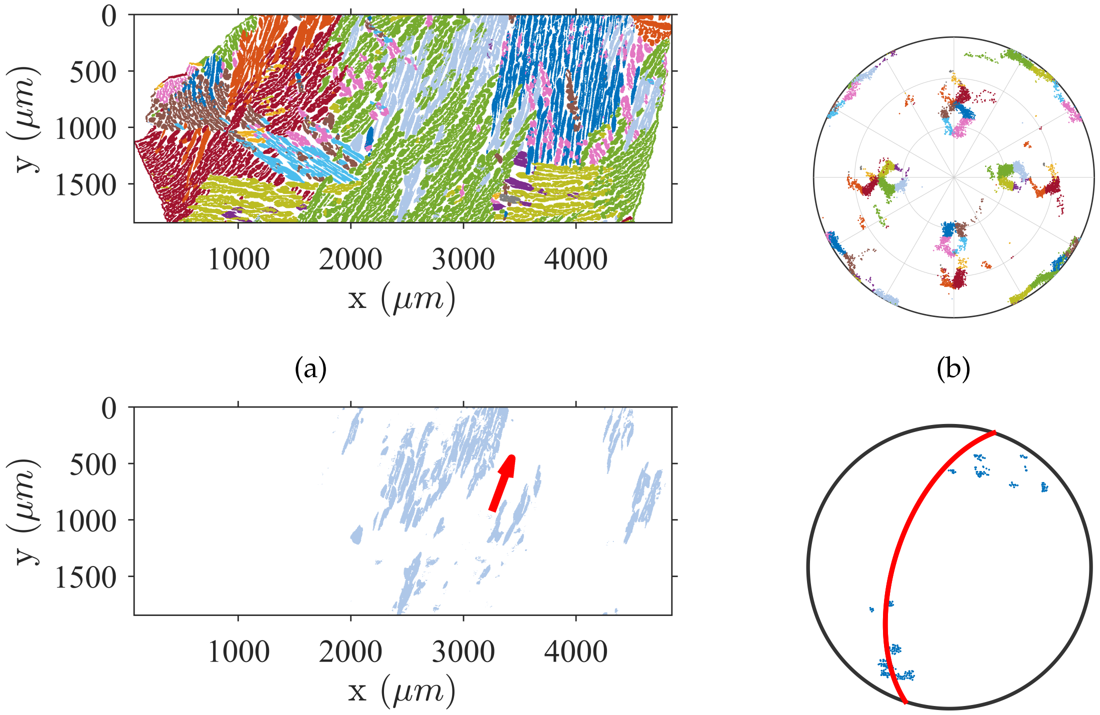

(a) (b)

(c) (d)

Figure 2.19: Illustration of the different steps involved in computing the laths normal for the Pitsch OR. (a) Austenite orientations colored according to their affiliations to the twelve variants given by the Pitsch OR. (b) [111] Pole figure revealing the resulting sampling of the continuous orientation clusters. (c) Principal direction computed from pixels belonging to the 12th clusters. (d) Spherical projection in the parent frame of principal directions for the 12th variant computed in all processed ferritic grains (blue points) and the resulting "mean" plane trace (red line).

The average lath plane pole in the α-frame is given by the direction $\{-0.996, 1.275, 2.366\}$ at about 1 ° from the rational plane $\{\bar{4}, 5, 9\}$ and 4.1° apart from the invariant direction $\{\bar{2}, 1, 1\}$ given by the Pitsch OR. The proximity with the latter direction is illustrated in Figure 2.20 by plotting the differences with the computed plane directions and variants of the $\{\bar{2}, 1, 1\}$ direction given by Pitsch OR. The standard deviation of the twelve computed poles is 4.45 °. This value seems reasonable compared to the 2° read on the precisely defined twinned planes studied by Hoekstra *et al.* [Hoe80].

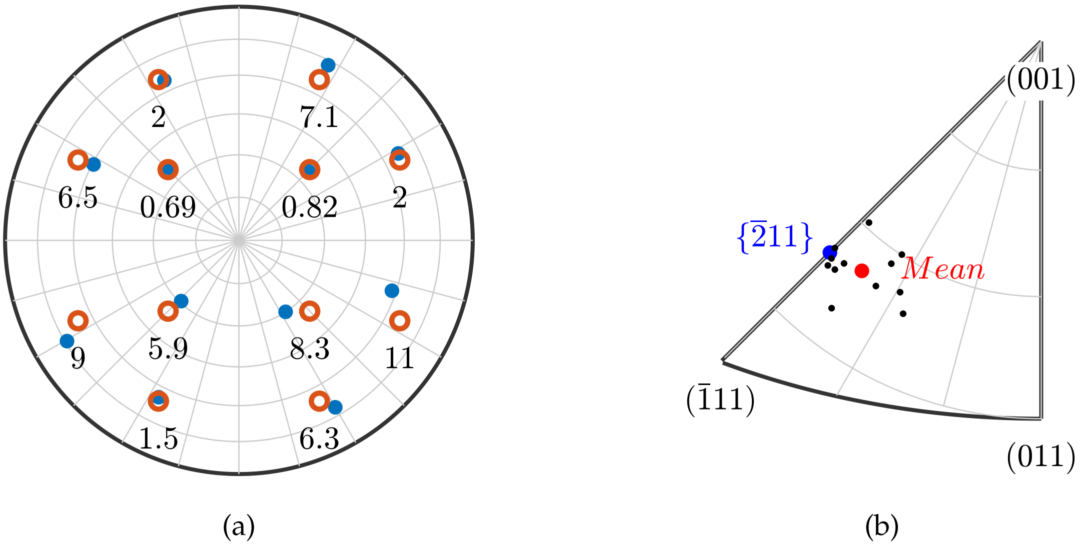

Figure 2.20: Comparison between Pitsch invariant direction and computed lath normals in the parent frame. (a) Element-wise variant comparison. The computed directions are plotted as blue points, and $\{\bar{2}11\}$ equivalent directions as red circles. The angular error between both directions is indicated for each variants in degrees. (b) Comparison between the equivalent average pole and direction. The twelve computed poles are represented as black points. The average distance between measured and computed poles is 4.1°

2.4.5 Discussion

According to Section 2.4.3, the CF8M alloy microstructure in the core of the industrial part is organized hierarchically as follows:

- Large equiaxed ferritic grain network resulting from the liquid to solid phase transformation. Each grain is wrapped by a thin austenite border whose orientation lies on the Bain circle of one of the neighboring grains.
- Lath packets that are either attributed to a local selection of a Pitsch OR variant or to an extension of the γ-orientation that have grown from prior ferrite grain boundaries. Their morphology is inherited from variant selection or induced crystallographic consistency between the two phases.
- Austenite laths themselves described by their crystal orientation and their affiliations to a Pitsch OR variant.

The above reading provides a meaningful description of the microstructure from a mechanical point of view. At the observation scale, laths are nearly homogeneous crystals described by their own elasticity and plastic slip under mechanical loadings. Lath packets can be modelled by periodic layered domains alternating between two different mechanical behaviors. Ferritic grains constitute an additional intermediate domain between lath packets and a representative volume that allows one to distinguish packets growing with similar γ-phase orientations on both sides of a prior grain boundary. The mechanical behavior of lath packets is different since the α-phase is oriented differently. Additionally, the laths morphology is most likely different on both sides to accommodate different growing environment. The dedicated workflow to characterize these morphologies is relevant only for orientations belonging to a Bain group since it relies on a variant segmentation.

While the method may first appear of poor accuracy compared to historical results achieving 1° errors [Hoe80], the results obtained with the present method appears to be conclusive in the study of CF8M only using a series of 2D EBSD maps. Interfaces between the two phases at small scales display large fluctuations. At higher scales, a preferential direction of the laths is more readable but is to be measured in a similar manner as the one presented herein. Moreover, the studied slabs are likely to be chemically heterogeneous. Such large ingots exhibit a significant range of cooling rates and high mechanical constraints are present. The redistribution of residual stresses during solutionizing combined with diffusion mechanisms add more possible distortions from theoretical habit planes. The theoretical habit plane between the two phases is most likely deformed by the forming process. As a result, the observed gap between theoretical invariant directions and experimentally measured ones is reasonably small (Figure 2.21) and attributed to experimental deviations of the habit plane and to the long solutionizing treatment.

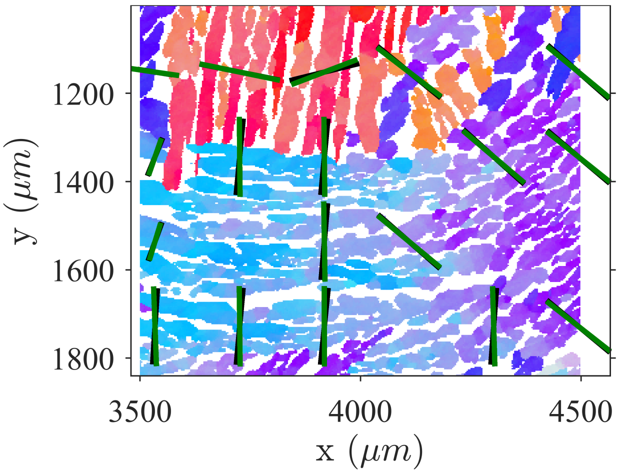

Figure 2.21: Sampling of the lath normal projection in the observation plane for the computed (black lines) and invariant $\{\bar{2}11\}$ (green lines) directions. The figure illustrates the very small difference between both directions compared to local fluctuations of lath boundaries.

2.4.6 Conclusion

Mappings of child orientations on the specimen space and in the parent crystallographic frame allowed to read into the mechanisms occuring in the forming process. The inner structure of primary ferrite grains is for the most part replaced by austenite laths packets growing from their former boundary. Their growth is constrained by the parent grain volume and the simultaneous growth of other packets resulting in a complex layout. It was shown that the lath packets were reasonably segmented according to their distance to Bain OR and to Pitsch OR variants. Laths falling far from any Pitsch variant and consequently from the Bain OR displayed degenerated morphology resulting from an accomodation of the FCC structure growing inside a BCC structure having an incompatible orientation. Some of the packets belonging to distinct Pitsch variants depict the particularity to be spatially connected. This manifests through smooth crystal and morphologic orientation gradients over long characteristic lengths. The morphological orientation was connected to the Pitsch relationship where child orientation belongs to this OR. A specific method was developed to connect the apparent lath morphology to the local Pitsch variant from the EBSD acquisitions. It enabled for the determination of lath normals in a microstructure with complex layout. The success of the method proved that austenite islets are close to a lath shape. In the present case, it also provided a multiscale segmentation of the microstructure with consistent subsets that are meaningful for understanding the mechanical behavior of the studied dual phase steel. This process however required the parent phase orientation map, which was supported by recent literature results on parent grain reconstruction. This step was made easier in the CF8M alloy because of the retained parent phase [Mol22b].

The Pitsch OR yielded the best results for the lath properties determination, while it is not the most frequently cited OR in FCC-BCC systems. Over the set of twelve computed orientations for lath normals, an uncertainty of about ± 2° was reached. This level was deemed precise enough considering the performance of Hoekstra's method [Hoe78] for a material having exactly defined twinned boundaries. Moreover, multiple factors may lead to a spread in the locally measured morphology in such large microstructures (*e.g.*, varying thermal gradients, chemical segregation or stress accommodation). Hence, an averaging methodology such as the one conducted herein is desirable.

Addition to the paper conclusion

Based on the assumption that the description of the microstructure in existing mechanical behavior models remained poor compared to experimental observation, an in-depth study using EBSD images has been carried out. The preceding part introduced a segmentation of the microstructure relying on the account of morphological and crystallographic aspects in the two phases. The different boundaries delimiting the scales and the properties linking them can be computed and characterized from EBSD data. In view of the laths morphology, the lath cluster scale suggests that significant anisotropy at a near millimetric scale is to be expected. Indeed, each scale is embedded into the one above but lath packet scale (in between ferritic grain scale and lath scales) has largely scattered characterisitc lengths. Packets also inherits some transversely isotropic properties from the lath morphology. It is assumed that this property is of great importance in the distribution of strains inside the material. Otherwise, it would mean that crystallographic effects *i.e.,* slip transmission between phases prevails over morphological effects. The parameters describing laths and laths clusters scales are missing from existing models and the scale transition rule considered so far does not hold. In spite of these observations, the dual-phase microstructure layout could be sufficiently interlocked to be mechanically homogenized at a ferritic grain scale. However, this would imply that mechanical loadings induce diffuse strains inside the microstructure *i.e.,* that the described properties does not create weak points. Yet, it is known from the study of aging mechanisms that the gap between austenite and ferrite mechanical properties is increasing over time which is likely to be detrimental to the diffuse nature of strains inside each phase.

In the chapter that follows, mechanical tests are conducted to capture the microstructural effects. The knowledge from characterizations gathered so far is used to interpret the behavior resulting from conventional mechanical tests and more advanced *in situ* tensile tests. As agreed with the features described in this chapter, a convenient framework is developed to arbitrate the significance of each microstructural properties by reading acquired mechanical fields and extract significant modelling parameters.

Chapter 3

Mechanical characterization

The study of the microstructure suggests a high complexity of the mechanical fields. The differences in the apparent moduli of the two phases, the distinct deformation mechanisms in each crystal system, and the laths atypical morphology necessarily influence local mechanical fields. Due to a lack of experimental data, simple models have been proposed in the past. However, almost no local mechanical data have confirmed their relevance. In this chapter, we study the local mechanical behavior to create a model based on our observations. First, the macroscopic behavior in tension is characterized to quantify the effects of thermal aging. A second step presents an implementation of *in situ* tests combined with full-field measurements adapted to the microstructure scales. Last, we use local fields to explain the effect of microstructure and thermal aging on the strain fields. The next chapter will use these observations to construct a multi-scale model.

3.1 Macroscopic characterization

The monitoring of CDSS mechanical behavior changes with aging has shown a significant statistical scatter of tensile properties for a given material but also for similar microstructure morphologies having different chemical compositions or aging conditions [Mic94]. Tensile tests have played a lesser role in studying thermal aging effects, but the extent of research programs on nuclear power plants allowed for substantial databases to be created over the last decades. Because relationships between tensile and impact resistance properties were drawn in internal programs (*e.g.*, see [Leo13]), such simple mechanical tests proved helpful in evaluating CDSS thermal embrittlement. Furthermore, tensile tests are used to ensure that new cast components meet mechanical property requirements [AFC18].

For instance, yield stress σ_y, ultimate tensile strength (UTS) σ_m and elongation at break $A\%$ of replacement cast elbows must be greater than 210 MPa, 480 MPa, and 35%, respectively. Tensile tests additionally provide input laws in structural computations aiming to ensure the integrity of main coolant pipings in their environment [LD15].

The effect of thermal aging embrittlement on ferrite on macroscopic tensile properties causes a tensile strength increase and a ductility loss but no apparent yield stress σ_y change [Mic94]. Figure 3.1 (a) illustrates the tensile behavior and aging effects on a CF8M alloy with similar ferrite proportion and molybdenum content as the one presently studied. The results were obtained on conventionally sized cylindrical specimens featuring a gage length of 20 mm and a 5 mm diameter. Under stable conditions, tensile properties were estimated within an approximate 20% confidence range. Drastically different aging states also sporadically lead to similar tensile properties. Only the average properties lead to stable results. That is to say, a substantial number of tests are required to evaluate the tensile properties using small specimens accurately. Despite the scatter of experimental data and the large microstructure, conventional stress-strain curves of unaged and aged material are conveniently approximated by empirical power laws (*e.g.*, Ramberg-Osgood type models) as shown in Figure 3.1 (b). The study of thermal aging effects is thus made more accessible by following the change of a reduced number of parameters. Assuming sufficient statistics, a good correlation with Charpy impact test data can also be drawn from Figure 3.1 (c). However, the necessity to multiply the number of tests to reach stable tensile properties is restrictive. For instance, the amount of material available when receiving new components is limited, and only very few samples can be extracted to assess that the component falls within the normalized tolerances. Depending on the local microstructure, some samples may present non-admissible properties. However, there is no evidence for explaining specific tensile properties without acquiring precise microstructural data, which is costly. Thus, considerable deviations in the measurements should be anticipated.

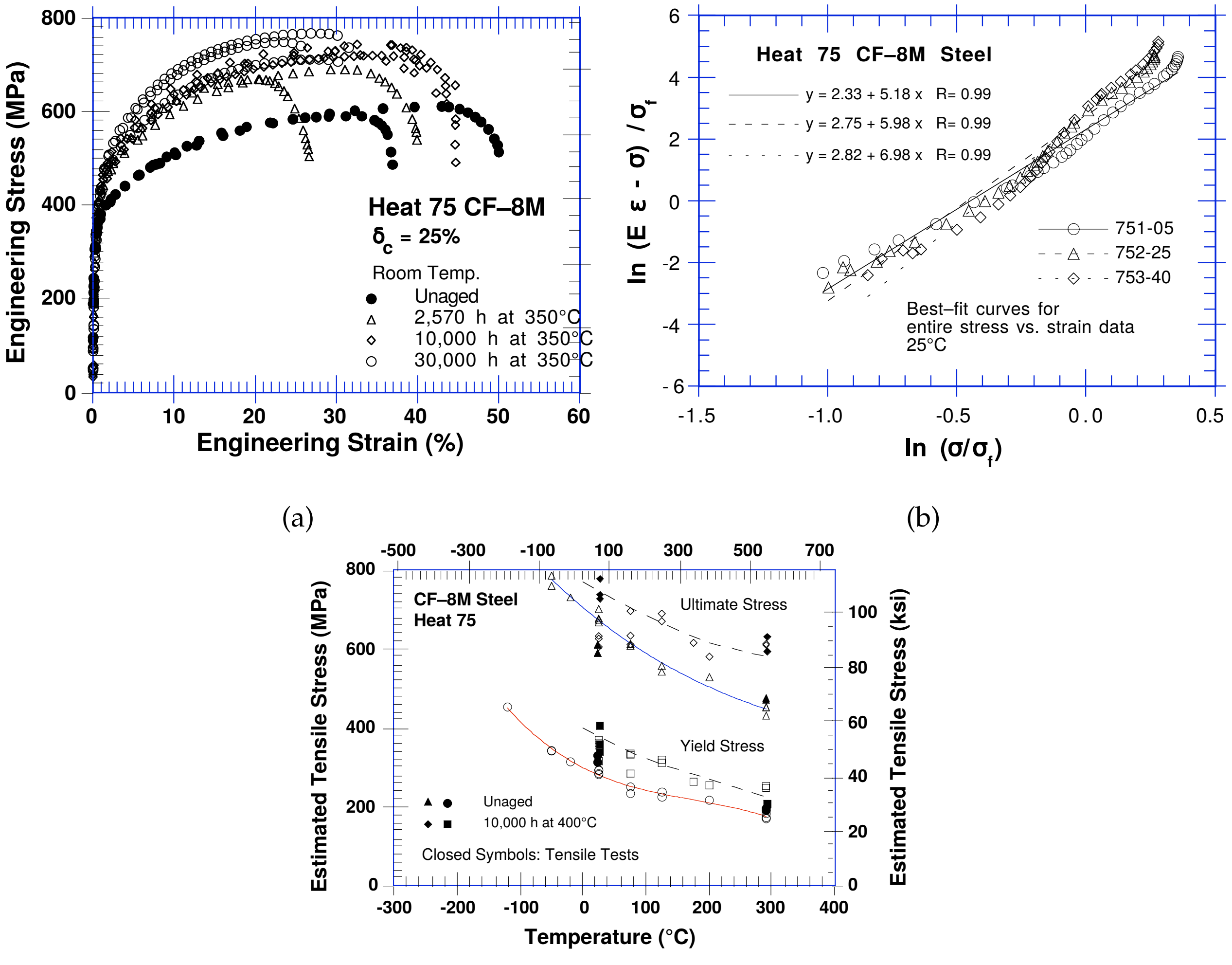

(a)

(b)

(c)

Figure 3.1: Change and prediction of the tensile response of a CF8M alloy for different aged states (extracted from [Mic94]). (a) Stress-strain curves of four aged states at 350°C. (b) Plastic stress flow as compared to a power law. (c) Comparison of yield and ultimate stresses predicted from Charpy-impact data and tensile tests at different testing temperatures.

The tensile behavior of the studied material was characterized by testing standardized specimens (see Appendix A.3) used at EDF. Four aged states are included in the protocol to consider ferrite embrittlement effects. Specimens associated with the four aged states are designated P1, P2, P3, and P4, corresponding to accelerated aging times of 0h, 1000h, 2500h, and 10000h at 350°C, respectively. More details on the specimen geometry and position in the cast ingot are given in Appendix A. Figure 3.2 presents the resulting raw stress-strain curves. Most tests were carried out until fracture, but two were interrupted prematurely (P1-2 and P2-1) to perform surface analyses with small amounts of plastic strains. The specimens have a 42 mm long cylindrical gage length. Their relatively small diameter (6 mm) compared to microstructural features of CDSS highlights the tensile properties scatter. However, such specimens are not undersized compared to the equiaxed zone of cast components (about 50 mm). Thus, it is not meaningless to understand the scattering in the present conditions. Figure 3.2 also displays tensile data scatter. For instance, the overlap of the tensile curves between two distant aging states is common. The range covered by tensile curves acquired in the EDF database for the same chemical composition, and aging temperature emphasizes that tougher and weaker tensile behavior were characterized. Assuming that a representative volume element at a 10 to 100 mm scale can be found, such inhomogeneities are not likely to be reproduced. Thus, it is assumed at this stage that the interlaced γ-phase does not homogenize the millimetric scale of ferritic grains. A small number of α-grains introducing strong crystallographic texture at the specimen scale is selected in each sample. In light of the microstructure morphology that has been previously described, local ferrite orientations can be favorable to an apparent strength of the specimen or to fast localization on a weaker zone.

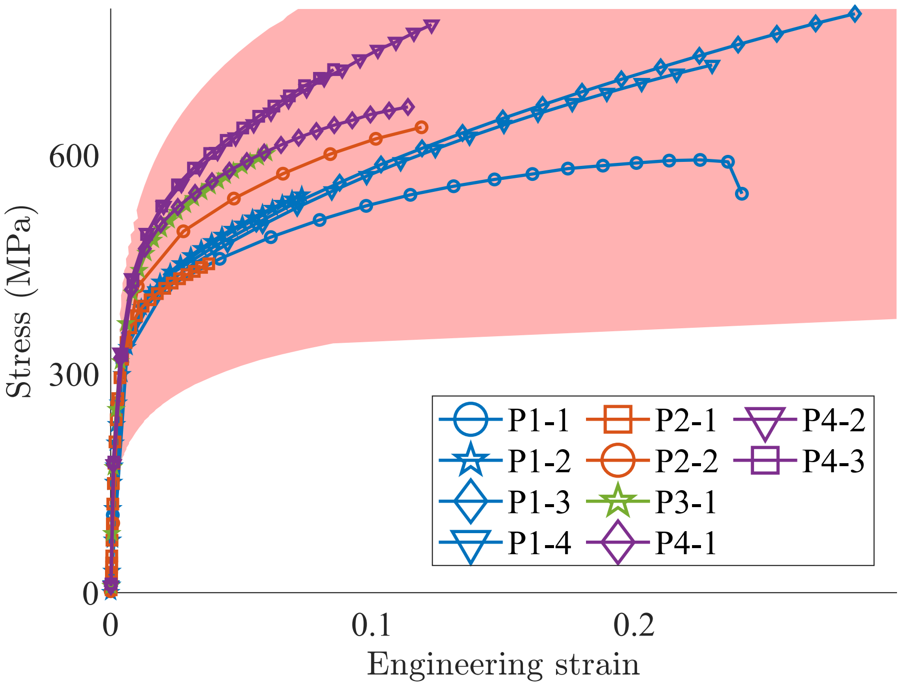

Figure 3.2: Tensile behavior at room temperature for different aging states measured from TC6 samples cut from the studied ingot. The red envelope corresponds to extrema of the whole EDF database on CF8M tensile tests having the present material chemical composition and the same aging temperature of 350°C. Aging state designation and EDF specimen references are detailed in Appendix A.5.

A specific experimental setup has been designed to obtain more precise knowledge of the spatial distribution of ferritic grains. The basic principle is to perform EBSD acquisitions on a device that allows the specimen to be rotated along its axis of revolution. However, it is necessary to adapt the measurements and to perform small adjustments to deal with the non-flat surface and the huge specimen size for an SEM. First, the EBSD technique requires a good surface finish to reveal diffraction patterns. While polishing a flat surface is straightforward with widespread, dedicated laboratory machines, cylindrical specimens require specific setups. A dedicated tool was developed earlier in the context of fatigue sample preparation. A lathe has been adapted to rotate a sample in contact with a small band of polishing paper wrapped around a cylinder. The crossed cylinder-to-cylinder contact and a combined rotation-translation motion allow an entire cylindrical surface to be polished. Starting from the available device, a specific polishing sequence was developed to reach surface conditions compatible with EBSD requirements. The second difficulty lies in the registration of diffraction patterns. To acquire diffraction patterns at a position located at θ degrees about the specimen axis, the sample is placed so that the tangent plane to the cylindrical surface below the incident electron beam is approximately at 70°. Figure 3.3 (a) illustrates the geometrical configuration for acquiring an orientation map ribbon at a position indexed by the angle, θ, about the specimen axis of revolution. The depth of focus in the SEM is sufficient to acquire diffraction patterns at small angular variations $d\theta$ by recalibrating the computed observation plane for each pattern. The ferrite orientation map given in Figure 3.3 (b) is an example of a ribbon that was acquired at a fixed position. In the end, the whole surface was characterized by conveniently sampling the whole specimen circumference.

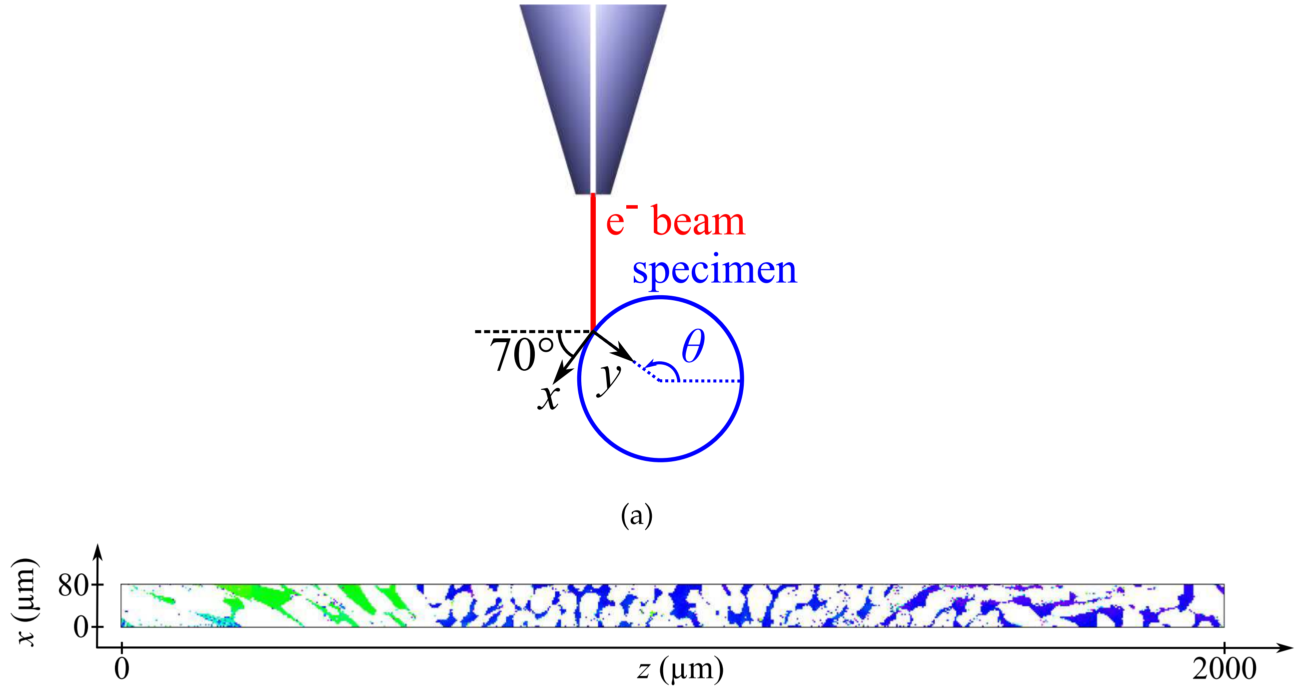

(a)

(b)

Figure 3.3: Schematic view of the setup for acquiring EBSD maps on cylindrical specimens. (a) Geometrical configuration. (b) Example of ferrite orientation map (IPF colors) extracted from an EBSD “ribbon”. The map width of 80 µm corresponds to $d\theta$ = 2.4°.

The goal of these experimental characterizations is twofold. As previously discussed, it provides insights into the microstructure layout of a specific specimen and, therefore, its potential structural behavior. The second objective is to model and simulate these tests at the scale of ferritic grains and to predict the properties of interest (*e.g.*, σ_y, σ_m, $A\%$) and their scatter. In particular, interactions between ferritic grain and lath packet scales are not easy to apprehend. Coupled with a full-field measurement technique, the crystallographic data acquired at this scale could enable a precise understanding of the microstructure-induced strain fields and infer whether an appropriate mechanical behavior at the ferritic grain scale can be identified or not. This question was investigated during the master internship of L. Moreau [Mor21] on CDSS tensile specimens. The current experimental device carrying out EBSD acquisitions on cylindrical specimens is only partially automated. Hence, limited data could be acquired on the circumference in an appropriate amount of time. A reconstruction strategy has been developed according to available data. Using the dilation algorithm of Section 2.3.3.2, the boundaries of ferrite grains in each ribbon acquired on the surface are determined and approximated as a straight line. Then, the grains are repositioned on the surface according to their angular position. Figure 3.4 presents the grain layout after reconstruction on one of the tested unaged specimens (2274-P1-TC6-1), where each color corresponds to a ferritic grain in one ribbon (the grain continuity in adjacent ribbons is not shown here). As only surface data are acquired, grains are extruded in the specimen bulk over a small length. This figure clearly highlights the small number of grains in the specimen gage length and thus in the whole considered volume.

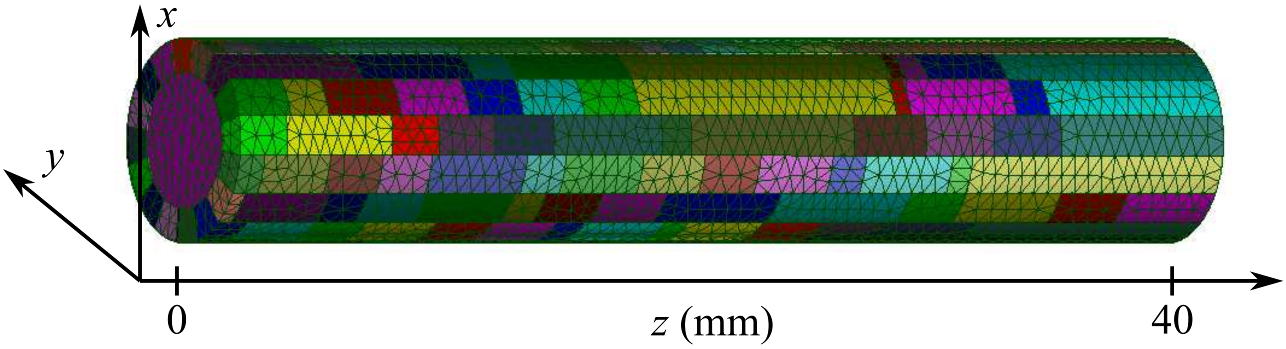

Figure 3.4: Reconstructed specimen using 16 ribbons distributed on the specimen circumference.

Finite element computations were carried out with the objective of illustrating the anisotropic effects induced by this large grain distribution. Each ferritic grain is given an equivalent crystal plasticity behavior using the Méric-Cailletaud (fully detailed in Section 4.1.1) law [Mer91b, Mer91a] even though it is not representative of the α-γ interlaced behavior. It should, however, be representative of the inhomogeneities observed on the rough surfaces of tensile specimens. The grain layout in the bulk of the specimen being unknown is assigned to the mean isotropic behavior resulting from tensile tests performed on the same specimen. Figure 3.5 corresponds to the computed longitudinal strain field for the MC law using the parameters of an FCC single crystal [Shi18a]. Such simple computations emphasize the amplitude of inhomogeneities in strain levels likely to result from the TC6 specimens. Such a small number of ferritic grains is undoubtedly localizing the strain in the weaker zone that ensues from ferritic grain size or “soft” grain directions (relative to the local stresses) and producing the kind of anisotropy observed on the tensile properties extracted from the database.

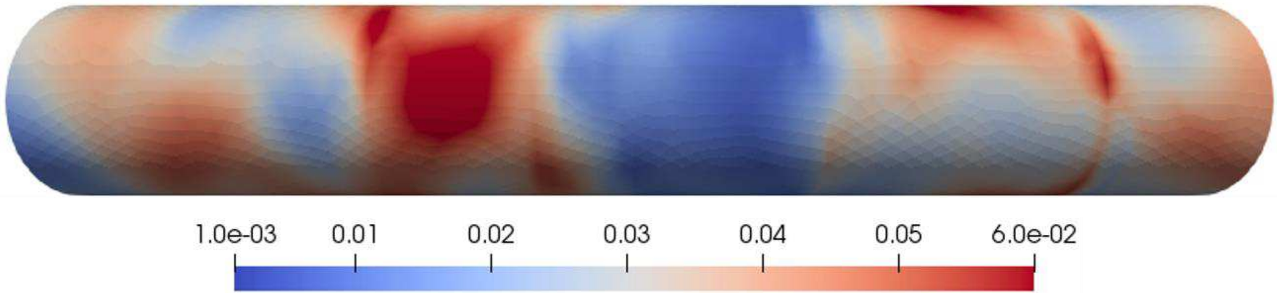

Figure 3.5: Longitudinal strain on the reconstructed specimen at 0.3 % prescribed macroscopic strain resulting from an MC contitutive behavior at the ferritic grain scale.

This section proposes an experimental technique for acquiring crystallographic data responsible for the scatter of tensile properties. However, the mechanisms governing early damage or high apparent ductility are certainly more complex, given the microstructure layout. Subscale inhomogeneities of CDSS are most likely not reproduced by a homogeneous anisotropic behavior at the ferritic grain scale. In particular, local mechanical fields may be dependent on the orientation relationship and morphological properties observed inside a single α-grain. In order to quantify these strain inhomogeneities and how they interact at different scales, more accurate observations need to be performed. Further, this technique may provide the necessary data to measure and model a tensile test on the cylindrical specimen geometry used at EDF. Up to now, the strain partitioning inside ferritic grains is unknown. In this regard, it is proposed to directly observe the elementary deformation mechanisms in both phases and measure the resulting mechanical fields using advanced tools.

3.2 *In situ* characterization

3.2.1 Inherent significance of *in situ* mechanical tests in material characterization

Thanks to automation, SEM is more accessible than ever. Its expansion has supported further progress in characterizing materials from surface observations. In the field of mechanics of materials, electronic microscopy offers many methods to understand and qualify deformation mechanisms over a broad range of scales. For instance, the availability of dedicated tools to test materials inside an SEM, *i.e.*, to perform *in situ* mechanical tests, allows for accurate observations of microstructural effects. Grain boundaries, inclusions or pores influence on slip systems activation or crack nucleation and propagation is observed during loading [Veh79, Plu97, Ma10, Sha13, Bar15, Fra15, Hé17, Jia18, Kum19b, Zha20]. Figure 3.6 shows an example of direct observations of different features at the origin of fatigue cracks using *in situ* mechanical tests in a Zircaloy-4 (nuclear grade).

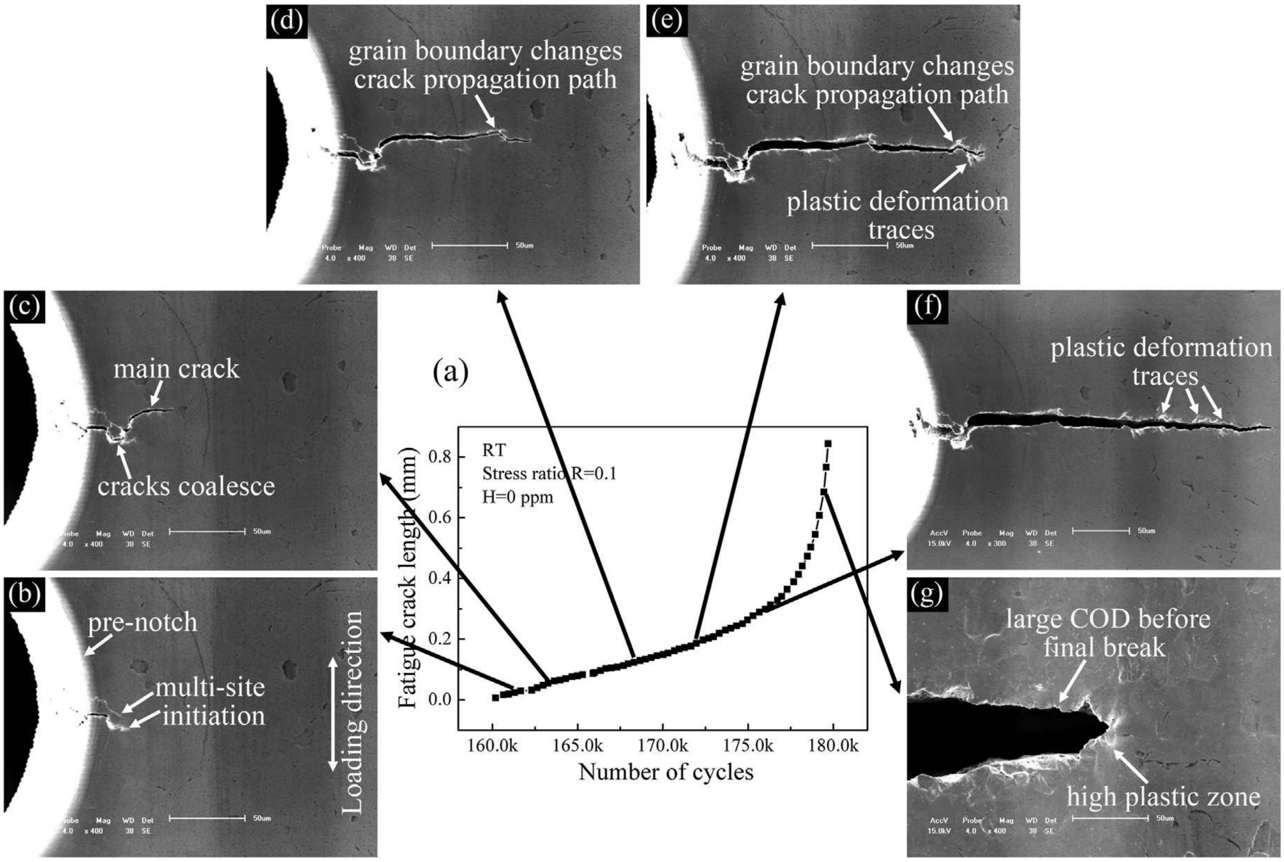

Figure 3.6: Influence of microstructural features on crack path observed from SEM images during an *in situ* cyclic test on a Zircaloy-4 sample (reproduced from [Zha20]).

Different deformation regimes can be identified from a micromechanical point of view, and microstructural features can be engineered from these observations. Simultaneous acquisition of crystallographic data with EBSD increases the information breadth of such experiments. Coupled with advanced measurement techniques, *in situ* mechanical tests in an electronic microscope are a great tool for acquiring rich multiscale experimental results to be confronted with mechanical models for identification and validation purposes. To this end, global schemes coupling generated models, microstructure reconstruction from real data using either destructive or non destructing techniques and experimental measurements were extensively used altogether [Hé06, Gue14b, Tas14b, Tas14a, Shi17a, Shi17b, Cha21].

Despite its widespread use and improvements that followed, SEM imaging still presents some constraints inherent to the electromagnetic environment and fundamental operating principles. Therefore, metrological aspects in an SEM are somewhat limited, and the sources of these limitations must be understood to get the most out of SEM images in quantitative measurements. Moreover, the combined use of SEM standard imaging techniques and EBSD implies dealing with different artifacts as the specimen is positioned differently in the two acquisition modes. Assessing SEM capability of acquiring data in the chosen conditions is then mandatory to ensure consistent interpretation of observations. Properly treating SEM artifacts allows for performances as remarkable as mapping microstructure and strain maps of nanoscaled specimens consistently in the same frame to be reached [Ver22].

3.2.2 Deformation mechanisms of CDSS

3.2.2.1 Deformation mechanisms of as-received alloy

The understanding of intermediate and large-scale deformation mechanisms can only be achieved after a detailed description of the elementary mechanisms in each phase and their interactions in the complex microstructure layout that has been described. The material is composed of two phases represented by different cubic lattices. Inelastic deformation modes in crystals can be decomposed into two contributions: an elastic distortion of the crystal lattice and a "plastic" deformation. The "plastic" deformation may occur either by the activation of slip or by twinning and does not distort the lattice. Slip activation is a multi-scale phenomenon starting with the motion of dislocations and resulting in the selection of gliding planes that do not change the crystal orientation. A synthetic view of slip systems in FCC and BCC is given in Figure 3.7. Twinning is associated with a collective motion of atoms. Hence it is characterized by a local change in the lattice orientation.

The main plastic deformation mode in FCC lattices is slip [Gro63, Jao65, Mar99]. It is triggered along {111}<110> systems and is homogeneous for low strain levels [Ver95]. With increasing strain, regularly spaced bands form. They may further localize the strains. Twinning may also occur in FCC crystals under high strain levels along {112}<110> systems [Jao65].

In BCC lattices, the two previous inelastic deformation modes are also present. However, dislocation motions giving rise to slip result in more complex layouts. Slip may occur on multiple atomic planes (*e.g.*, {110}, {112} and {123}) but only in the <111> direction [Hut64, Mit68, Jac91]. Twinning occurs more commonly in BCC crystals but is likely to result from slip [Lag93]. Twins in BCC lattices only form on the {112}<111> systems.

The dual-phase layout of CDSSs inherits from the two-phase slip mechanisms. Slip is

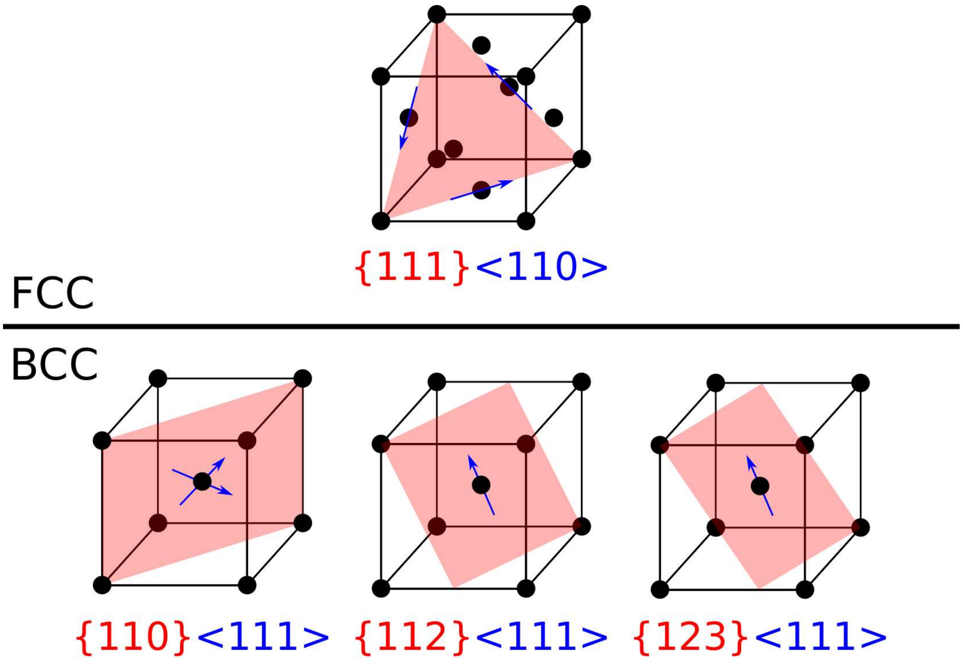

Figure 3.7: Main slip systems active in FCC and BCC crystallographic lattices.

relatively easy to trigger in austenite, and plasticity is likely to occur in that phase first. The low Stacking Fault Energy (SFE) allows for planar glide to occur on multiple planes of the {111}<110> systems without triggering cross slip [Ver95]. Joly [Jol92] and Verhaeghe [Ver95] note that slip in the γ-phase is homogeneous on a large scale for low strains and progressively concentrates into bands with increasing strains. Further, Verhaeghe [Ver95] and Bugat [Bug00] note that slip transmission at phases interface is not always spontaneous, which results in a higher dislocation density at phase interfaces in austenite.

Figure 3.8 (a-b) displays deformed austenite near a former ferrite grain boundary on an unaged *in situ* sample loaded to 4% strain. Two austenitic orientations are found on either side of the α-boundary. γ-islets are representative of other deformed islets in inner ferritic grains with single or multiple slip bands in a single lath corresponding to {111} planes. These bands are regularly spaced (0.4 µm from each other). Thus the strain in austenite can be considered homogeneous at the lath scale [Bug00]. However, the former α-grain boundary, which a thin austenite layer has replaced, seems to localize the strains significantly in multiple areas. Such a phenomenon may result from a geometrical effect of this austenitic layer that represents a soft binder between two areas strengthened by the dual-phase composite effect. However, both cases do not present slip or twinning that are observed using electron microscopy. Verhaeghe [Ver95] explains that transmission of slip from austenite to ferrite is difficult to highlight. Austenite accumulates too much damage in thin TEM samples before transmitting the strain to the second phase. Nonetheless, larger *in situ* samples display slip transmission at interphase boundaries that can be locally observed with electron microscopy. Interestingly, studies have identified a slip transmission mode in equivalent alloys using electron microscopy with slip bands in γ-iron crossing α-islets with no deviation [Zha19b]. However, there is no evidence of an orientation relationship that would result in parallelism of slip planes in the two phases. Hence, the conclusion that bands do not deviate may not be accountable when considering the phase morphology. Laths and more globular shapes constituting the microstructure are easily cut close to a boundary, and it is common to observe relics of small phase islets at the surface whose contribution to the mechanisms in the observed plane is insignificant.

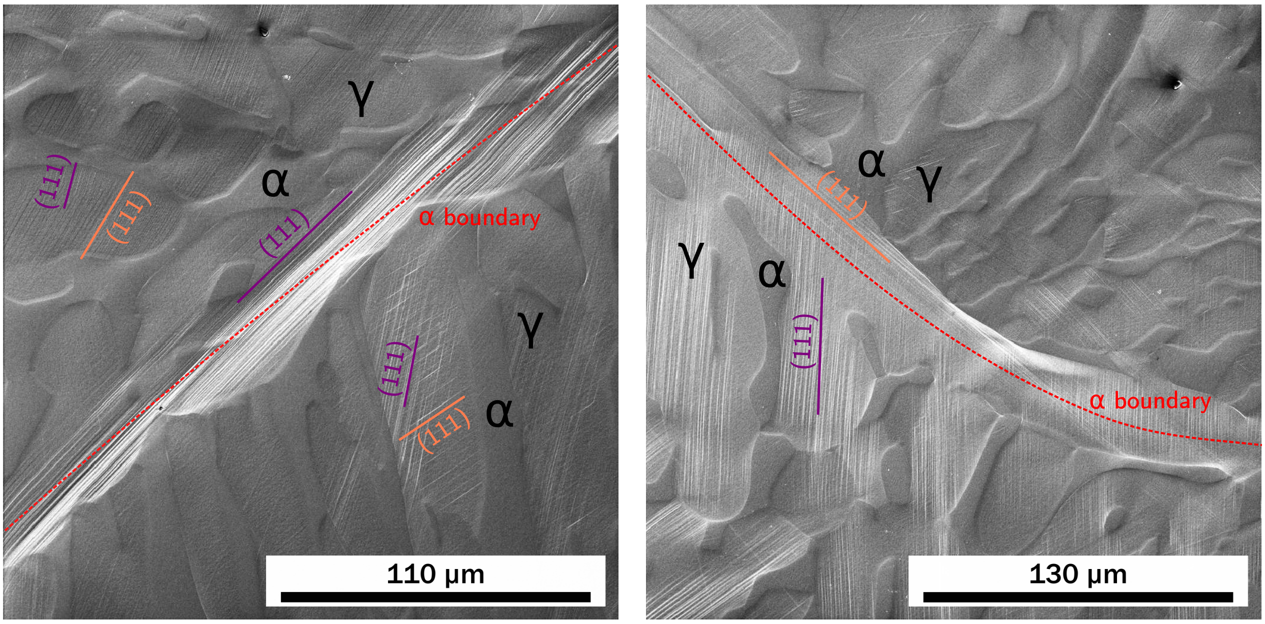

(a) (b)

Figure 3.8: Deformation mechanisms near former α-phase boundaries in the as-received material (P1) as observed on SE images. For both images, the loading direction is horizontal. (a) Illustration of a primary ferritic grain boundary displaying significant strain in the common $(111)_\gamma$ slip planes. (b) Illustration of a primary ferritic grain boundary showing $(111)_\gamma$ slip plane activity similar to the surrounding austenite laths.

Figure 3.9 (a) shows a transmission from austenite to a ferrite lath inserted between two γ-laths. Continuity of slip band traces corresponding to (111) planes in γ-iron is ensured by similar slip bands in ferrite along (110) planes. These bands connect from one phase to the other on both sides of the ferritic lath while displaying similar properties (number and spacing). Nonetheless, slip in ferrite is not easily observed in an SEM for moderate macroscopic plastic strain levels. Figure 3.9 (b) illustrates the difficulty of transmission of slip from austenite to ferrite. The first phase is significantly deformed with visible slip bands corresponding to (111) plane traces in the whole region. Relatively thin α-islets show resistance to the surrounding deformed phase. (112) slip band initiation is visible, but propagation is rapidly stopped near the boundary. The constraints result in larger slip bands and activation of more slip planes in austenite close to ferritic boundaries. However, increasing plastic strains compel slip to be transmitted in ferrite in the as-received material [Bug00, Zha19a] but austenite presents substantially damaged areas before reaching "homogeneous" slip activation in the parent phase.

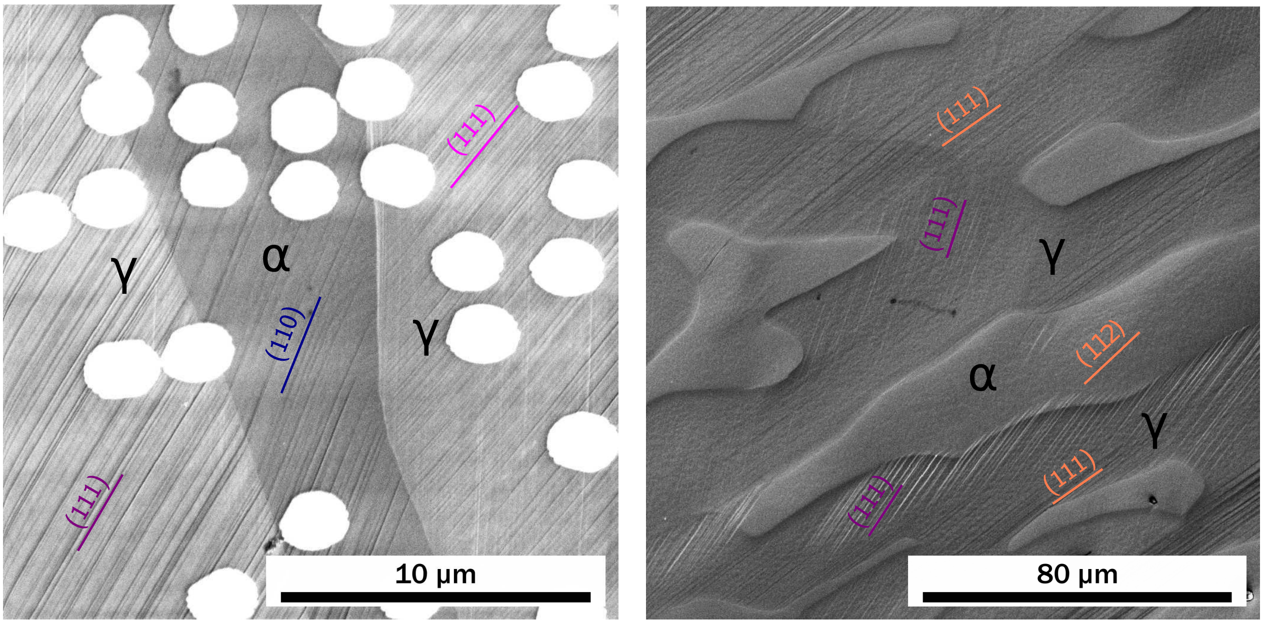

(a) (b)

Figure 3.9: Deformation mechanisms of the inner primary ferrite grains in the as-received material (P1) as observed on SE images. For both images, the loading direction is horizontal. (a) Illustration of slip transfer at an α-γ boundary. $(110)_\alpha$ slip bands originate from $(111)_\gamma$ slip bands. The white dots are deposited for measurement purposes in the next section. (b) Illustration of slip transfer in small ferritic islets surrounded by austenitic laths. $(111)_\gamma$ slip planes are transferred into ferrite resulting in $(112)_\alpha$ slip activation that is rapidly stopped near the boundary.

Summary of unaged deformation mechanisms

- Plastic deformation triggers first and predominently in austenite by planar slip along {111}<110> systems
- Ferrite deformed by planar slip in <111> directions possibly along multiple slip planes
- Strain is homogeneous in the two phases at lath scale

- Slip incompatibilities, differences in triggering mechanisms and geometrical effects make slip transmission from austenite to ferrite difficult
- Geometrical effects inherited from the morphology may influence strain localization

3.2.2.2 Deformation mechanisms of aged alloy

As γ-phase microstructures are not impacted by thermal aging, the fundamental mechanisms giving rise to observable slip bands in austenite are not expected to be modified. Only the interaction with embrittled ferrite in the present microstructure layout will likely modify deformation mechanisms at laths and higher scales. Verhaeghe [Ver95] confirmed from TEM acquisitions that dislocation motion activities in austenite for aged and unaged material are equivalent. As aging increases ferrite strength, strain levels in austenite for a given "macroscopic" strain are expected to be higher. More mechanical constraints are thus present in austenite resulting in a higher frequency of cross-slip occurrences. Figure 3.10 (a) illustrates the occurrence of slip in the γ-phase for the P4 (aged 10000h at 350 °C) material. The specimen was *in situ* deformed at 2%. For a similar macroscopic loading, bands in austenite appear coarser than in the unaged case due to the hardened neighboring ferrite. These bands consistently correspond to (111) slip plane traces. Moreover, incompatibilities at interphase boundaries are the source of higher constraints. Cross-slip is often encountered at such boundaries in austenite and is easily recognizable from the "arrow" pattern created by slip steps on the observed surface. Figure 3.10 (b) depicts an orientation configuration where strains produce a cross-slip front expanding in austenite with imposed strain rather than being transmitted to the surrounding ferrite. Furthermore, some former ferritic boundaries are localizing the strains in the same way as the unaged material.

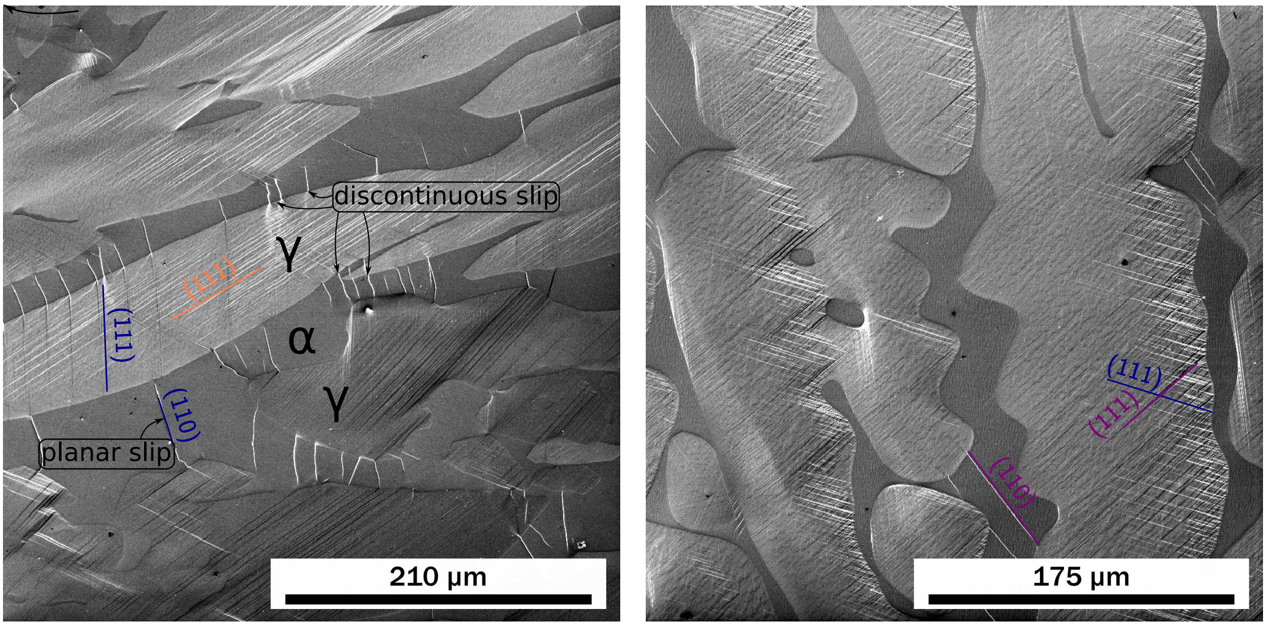

(a)

(b)

Figure 3.10: Deformation mechanisms in the 10000h/350°C aged (P4) material as observed on SE images. For both images, the loading direction is horizontal. (a) Representative mapping of the deformation mechanisms in longly aged CDSS. Austenite is still deformed along (111) planes. Both planar and discontinuous slip are present in ferrite. (b) Illustration of interphase boundaries blocking slip transmission in ferrite. High constraints induce cross-slip in austenite close to the boundary.

In ferrite, aging generates obstacles to dislocation motions. The creation of α/α' boundaries and the precipitation of G-phase contribute to pin edge dislocations that were able to move freely in the as-received material [Ver95]. As a consequence, deformation is completely different in the aged material. Figure 3.10 (a) illustrates planar and discontinuous slip corresponding to the main deformation mechanisms observed in ferrite. Discontinuous slip is dissociated from cross-slip because the first mechanism corresponds to a continuous deviation of the active slip plane while the second deviation occurs punctually and periodically. Discontinuous slip is observed in numerous locations as long as a considerable fraction of surrounding austenite is plastically deformed. By nature, the orientation of a discontinuous slip line is not trivial. The local combination of active planes may result in different apparent traces on the deformed surface at the lath scale. Nevertheless, our observations emphasized inclination toward the shortest path linking the two closest γ-laths. Occurrences of planar slip are also regularly found in aged ferrite. Figure 3.11 (a) depicts multiple active system for a single FCC crystal orientation. In most cases, the slip bands are distinct, straight, and accurately match $(110)_\alpha$ traces. When multiple systems are active in a single lath, they do not seem to interfere. The striking feature for both deformation mechanisms in aged ferrite is loss of homogeneity *i.e.*, highly localized phenomena. Moreover, increasing strains will further localize glide on already active zones. Pioneer authors who demonstrated the effects of ferrite embrittlement also noted a gradual increase of twinning in iron-chromium alloys [Mar64, Lag67]. No trace of twinning has been observed in the ferritic phase in the present case yet.

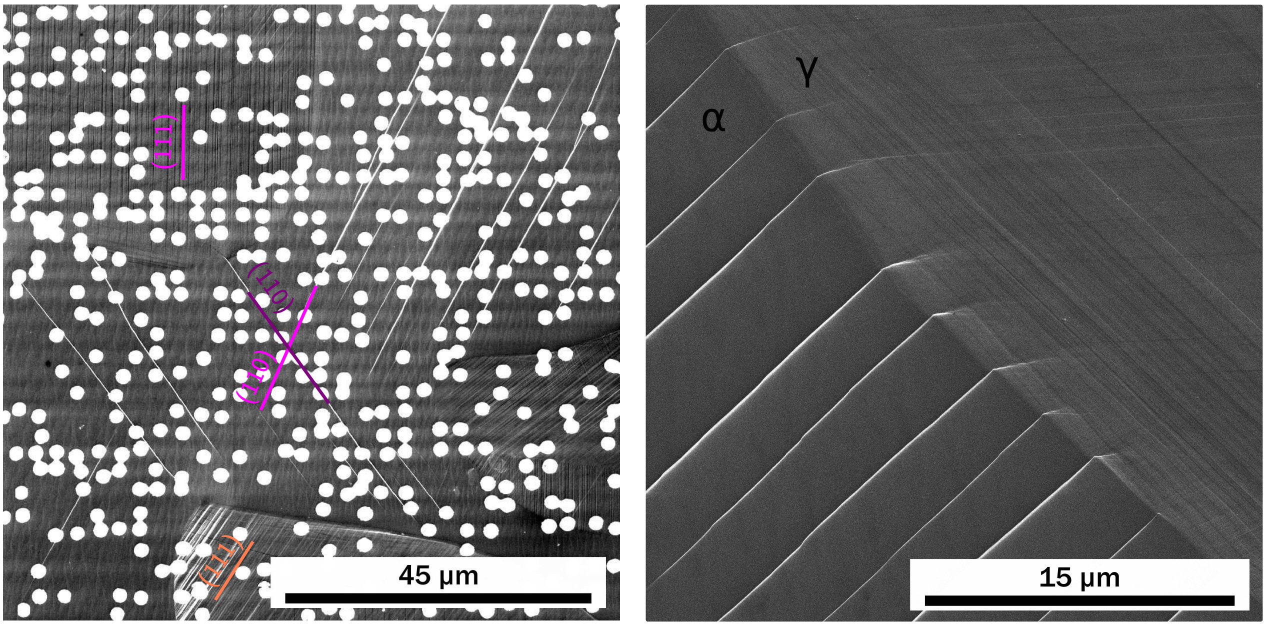

(a) (b)

Figure 3.11: Illustration of slip transmission at γ/α interfaces in the 10000h/350°C aged (P4) material as observed on SE images. For both images, the loading direction is horizontal. (a) Illustration of double planar slip activation in ferrite where the alignment with the load seems to favor this deformation mode. Slip bands are relaxed immediately after crossing the austenitic boundary. (b) Focused view of the transmission of $(110)_\alpha$ slip band in austenite. The gliding plane is forced into the γ-phase but rapidly stopped after the boundary by newly activated slip systems.

Additionally, α-γ slip transmission is also impacted by thermal aging. While Verhaeghe [Ver95] argues that plastic strains still initiate in austenite first, the transmission of slip from close-packed directions in both phases is not significantly present as it is in [Ver95]. Conversely, many slip lines encountered in ferrite end in austenite and are relaxed by triggering a new mechanism. Figure 3.11 (b) illustrates a nearly periodic network of $(110)_\alpha$ slip bands being absorbed by activation of vanishing cross-slip in the second phase at the interface. Slip planes triggered in austenite are usually not following those already active. A similar mechanism is found at the edge of discontinuous slip lines reaching γ-boundaries. While it is difficult to apprehend the starting point of glide in the observed 3D volume, it cannot be assumed that plastic strains initiate in austenite in the present material. TEM acquisitions [Ver95] also show that every occurrence of slip (discontinuous or planar) in ferrite blocks the transmission of dislocations in this phase. Each following dislocation motion induced by an increase of the load forces them to move along existing slip planes. Subsequently, these dislocations are piled up and transmitted at γ-phase interfaces where the slip band in ferrite ends.

Summary of deformation mechanisms in aged alloy

- Ferrite embrittlement induces more occurrence of cross-slip along {111}<110> systems in austenite despite the fact that the main deformation mode remains planar slip
- Ferrite deforms either by planar or discontinuous slip
- Deformation is less homogeneous than in the unaged case in austenite at lath scale and highly localized in ferrite
- Less occurrence of smooth slip transmission was observed at the studied strain levels
- Geometrical effects inherited from the morphology are still influencing strain localization

Different forms of slip along preferential slip systems constitute the main deformation mechanisms in the two phases of the studied material. No representative occurrences of twinning were found, which agrees with previous studies. Nonetheless, the lath structural effect may lead to relatively complex configurations that significantly evolve with thermal aging. It may be argued that more structural effects ensue from lath packets and ferritic grain scales, but they are not easily observed nor deduced from the present observations. Presently, the transition between apparent changes in the mechanical behavior at larger scales and the previous observations was conducted in a single step even though such mechanisms are not taking into account the distinct scales introduced in Chapter 2. It is proposed to capture such effects by making use of full-field measurements and to infer the role of each mechanical scale. These measurements will also provide valuable quantitative data to calibrate a model at the different microstructural scales.

3.2.3 Experimental setup and associated SEM-DIC performances

3.2.3.1 Microscope and tensile device

The experimental setup associated with *in situ* tensile tests carried out in this study is shown in Figure 3.12. The tested specimens (Figure 3.12 (a)) have a 10 mm long gage length. After polishing the sample surface, their section varies between 2 mm x 0.6 mm and 2 mm x 0.8 mm. The *in situ* tensile device (Figure 3.12 (b)) is designed to fit in the TESCAN MIRA 3 SEM (Figure 3.12 (c)) used throughout the study and allowed images in both flat and tilted configurations to be acquired.

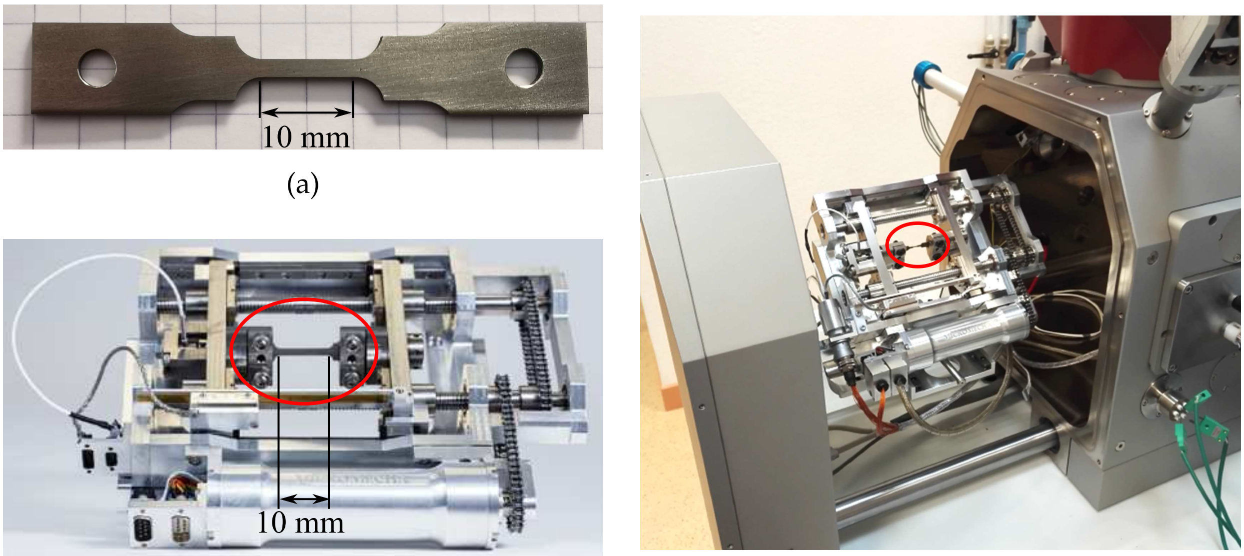

(a) (b) (c)

Figure 3.12: Experimental setup used for *in situ* characterization. (a) *In situ* tensile specimen. (b) Tensile device used for performing *in situ* tests. (c) Tensile device to be mounted in the SEM chamber.

3.2.3.2 Protocol

The following protocol is used to characterize microstructures, measure mechanical fields, and correlate both data types for each specimen. To meet the surface finish conditions required by EBSD measurements, specimens are polished on both sides. The two faces are subsequently characterized by serial EBSD acquisitions (Figure 3.13 (a)). Once crystallographic data are acquired, a speckle pattern, mandatory for the full-field measurements, is deposited onto one of the surfaces (Figure 3.13 (b)). The pattern is deposited using a dedicated auxiliary microscope (a QUANTA 400 from FEI), limiting the accuracy of large field observations. Consequently, the 8 x 2 mm pattern is uniformly split into 100 µm x 100 µm regions scanned individually. Passing between each pattern is carried out by physically moving the sample with the SEM stage. More details on the benefits of enhancing surface contrast with a speckle pattern are given in the next section. Last, the test is performed by incrementally prescribing a macroscopic strain. A strain rate of $10^{-4}s^{-1}$ is prescribed for the transition between each load step. Three Regions Of Interest (ROIs) are followed at each load step (Figure 3.13 (c)). The ROI position is adjusted to keep a 100 µm overlap between them to be able to correlate measured fields over the whole specimen gage length. The image size is 4096 × 4096 pix corresponding to a physical surface of 2187 µm^2 *i.e.,* a pixel size of 0.534 µm. The sample is positioned at a working distance of 18 mm (the smallest allowed by the setup). The electron beam acceleration voltage is set to 30 kV, and the beam spread is adjusted to have a theoretical 10 nm probe size. Images are acquired after waiting long enough to minimize the effects of relaxation. It is noteworthy that the waiting time is significant in the plasticity domain when considering such large areas, and the effects of relaxation may still be measured after one hour. To avoid increasing the experiment duration, a ten-minute interval was adopted between each load increment and image acquisition. This choice will be shown to have no detrimental effects on measurements.

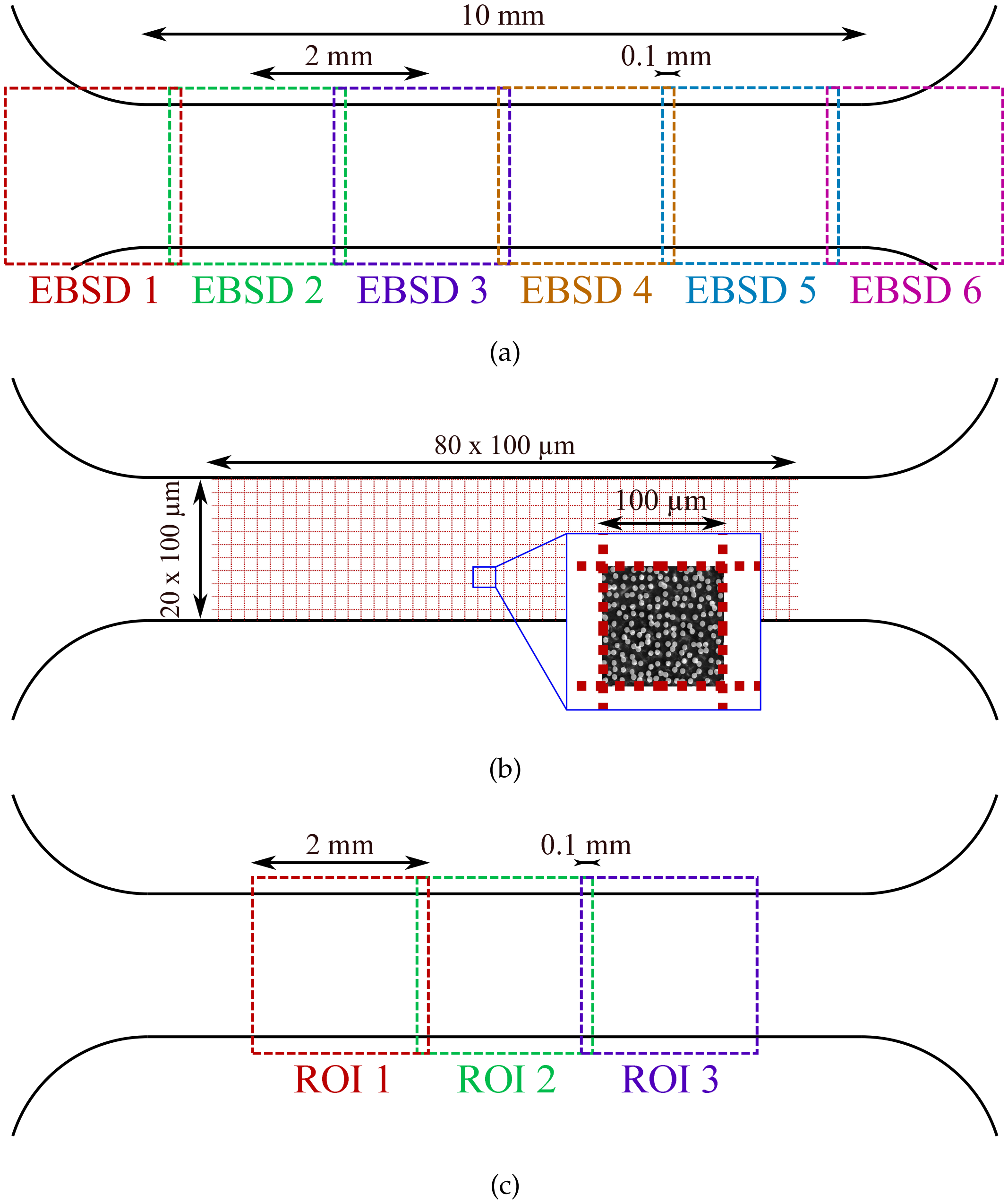

Figure 3.13: Illustration of the three SEM preliminary steps enabling for the measurement of mechanical fields. (a) Acquisition of six 2 × 2 mm EBSD maps (3 µm pixel size) with a stitching area on each side of the specimen. (b) Deposition of a speckle pattern of circular dots 1.5 µm in diameter. (c) Acquisition of three 2 × 2 mm BSE images with a small overlapping region at each loading step.

3.2.3.3 Synthetic surface pattern deposition

The methodology developed from now onward is based on the application of global regularized DIC described in Appendix B and used for multiple purposes throughout the present study. Resolving the displacement field ensuring the assumed gray level (GL) conservation in image correlation techniques, requires image contrast. In the framework of digital images, high gray level gradients are beneficial to measurement quality (*i.e.*, to have a low displacement uncertainty) [Rou06, Pan10]. However, natural contrast on sample surfaces is often inadequate. In some cases, contrast variations in the "deformed" image are not associated with displacement fields. For example, this variation may happen in electronic microscopy images where gray level images are composite, including chemical, crystallographic and topography data. Consequently, artificial contrast is often obtained by depositing specific patterns onto the sample surface. The deposition method mostly depends on the desired measurement resolution and image acquisition technique. While simple painting techniques provide satisfactory results for measurement with optical imaging [Cra13, Lio14], electronic imaging is often more challenging. Consequently, numerous methods of varying complexity, cost, and processing time were used. Recent reviews have classified existing methods based on their benefits and complexity [Kam11, Don17]. In the present study, the electron beam lithography technique developed at EDF was used [Gue14b]. The electron beam of an SEM is handled to scan a thin polymeric layer uniformly deposited onto the sample surface where we want the pattern to be drawn. The exposed locations of the polymeric layer are then removed in a solvent. Last, a small nanometric metallic layer is deposited, and the rest of the polymeric layer is removed in a more powerful solvent. This last step leads to removing the polymer and metallic layers on the whole unexposed surface, leaving the pattern drawn untouched.

The benefit of electron beam lithography is its average 10 nm resolution and its ability to write custom-made patterns generated beforehand. When planning to deposit a speckle for running DIC algorithms, the technique offers the possibility to precisely map the speckle pattern features with scanning electron microscope accuracy. Furthermore, the intrusiveness may be controlled by the convenient design of the pattern density to allow for local observations during the test as the deposition leaves the specimen surface undamaged. Nonetheless, the technique is challenging to master and requires considerable initial investments limiting its usage to specific applications.

The pattern was optimized based on multiple considerations. The metal deposited is gold since its high atomic number provides a good contrast with the substrate surface in electron imaging. The pattern unit feature was chosen as a disk because it provides the best contrast gradient over the feature surface ratio (among elementary geometrical shapes). In light of the deformation mechanisms presented in Section 3.2.2, the size of each disk and the distance separating them were prescribed to resolve displacements at the austenitic lath scale *i.e.,* three to five dots should cover the lath thickness. Thus, the disk diameter was chosen to be 1.5 µm, and the average distance between them was set below 10 µm. Last, the microstructure should be distinguishable in the acquired image. This requirement comes from the necessity of performing local investigations of the deformation mechanisms during the test and further relating the microstructure in SEM images to orientation maps not acquired in the experimental conditions. Figure 3.14 shows the deposited speckle pattern to perform full-field measurements on CDSS *in situ* tensile specimens. Figure 3.14 (a) corresponds to a reference image in the chosen conditions. The field of view is set to approximately 2.2 mm to capture the whole specimen width (2 mm). The pixel size is selected to resolve each disk with four to five pixels resulting in a 4096 × 4096 pix definition with the 2.2 mm field of view. The resulting images satisfy both conservation of the microstructural features and the resolution of the speckle pattern with an appropriate size. Figure 3.14 (b) and (c) present the deposited speckle features at a smaller scale. Quantitative assessments of the measurement quality with these images are presented in the forthcoming parts.

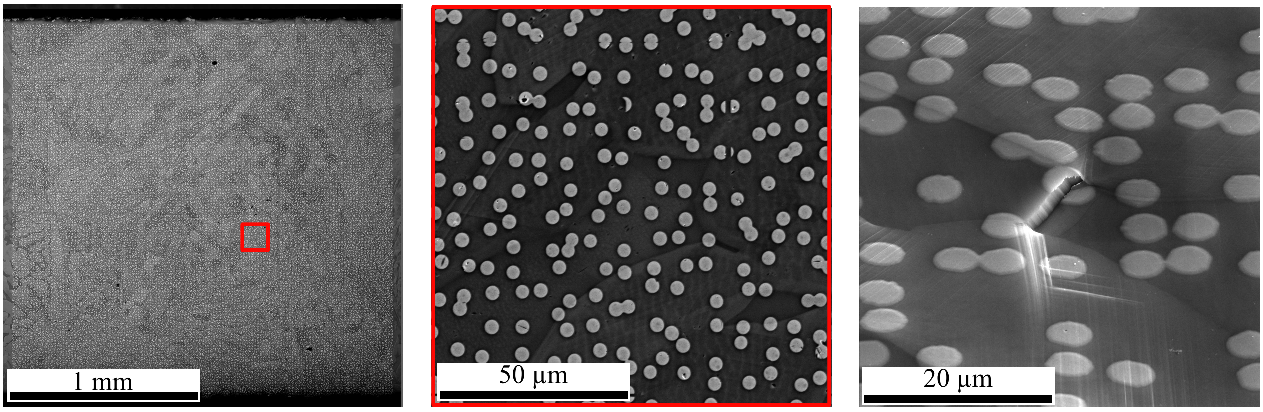

(a) (b) (c)

Figure 3.14: Deposited speckle pattern using electron beam lithography inside an SEM. (a) 2mm x 2mm pattern deposited over the complete *in situ* specimen width. (b) Zoom on the speckle pattern where each dot appears as a sharply defined disk. The area corresponds to the red square in sub-figure 3.14(a). (c) Illustration of the good adhesion between gold disks and the substrate surface where large deformations occur.

3.2.4 Capturing large areas with an SEM

3.2.4.1 Distortions associated with millimetric SE-BSE maps

Standard imaging techniques in SEMs produce contrasted images of a sample positioned perpendicularly to the electron beam. Two types of detectors are usually operated. Secondary Electron (SE) detectors acquire electrons that are pulled off from sample atoms. These electrons originate from the specimen surface, and the resulting image contrast mostly depends on topography. Back-Scattered Electron (BSE) detectors capture electrons from the electron beam sent back by elastic interactions with the sample. Such electrons usually come from deeper depths under the characterized surface than SE. Hence, the contrast in BSE images carries information about element nature (atomic number) and relative orientation of crystals with the electron beam (channeling contrast). Image distortions in SEMs and identified sources were investigated [Sut06, Nol07, Pł09, Shi18b, Lun18]. Among these sources, let us mention long time drifts associated with electrical systems, beam control accuracy with a slow scan direction error and spatial distortions. Since distortions are highly dependent on working conditions (sample nature, magnification, imaging technique, or acquisition time), many authors have proposed a solution to account for them [Gue14b, Shi18b, Mar19, Ton21]. Their combined contribution appears somewhat difficult to decorrelate. In this case, a unified correction technique, as introduced in [Mar19], seems to be the most appropriate.

In light of the characteristic lengths of the CF8M microstructure, large millimetric images must be acquired. Under these circumstances, the electron beam is highly deflected, and the assumption of perpendicularity with the observed surface no longer holds. Hence, spatial distortions are amplified and likely to prevail over other sources. Images are acquired for more than half a day after setting up the sample in the microscope to lower drift effects. Only the beam control accuracy (slow scan drift error) among significant distortion sources remains unknown.

Guery *et al.* [Gue14b] highlighted a certain regularity in spatial distortions that allows images to be corrected with a reduced basis of polynomial functions, for example. Hence, one can assume that the information about spatial distortions is included at the boundaries of acquired images. In particular, the displacement field necessary to stitch two overlapping images is typical of these image artifacts. The correlation of overlapping areas on undeformed specimens was carried out to evaluate such spatial distortions. These regions correspond to the same spatially translated area without introducing mechanical deformation.

Therefore, deviations of the displacement field from a rigid body motion are associated with image distortions. Figure 3.15 illustrates a representative correction field on shared regions (Figure 3.15 (a)) between adjacent images. The correlation is achieved via global DIC on a structured mesh with 10 pix element size. The favorable acquisition condition without mechanical deformation of the images is sufficient to compute the displacement field without mechanical regularization. As the translation between two ROIs is performed by moving the microscope stage, there is a significant average component in both $\boldsymbol{x}$ and $\boldsymbol{y}$ directions related to specimen alignment and stage accuracy. Nonetheless, there is an additional deviation of the displacement field components U_x and U_y from their average $\overline{U}_x$ and $\overline{U}_y$, as illustrated in Figure 3.15 (b) and (c). The maximum amplitude is in the $\boldsymbol{x}$ direction and approximately corresponds to 4 pix ($\approx$ 2 µm). Despite appearing small, BSE image distortions are corrected using an image of a standard grid acquired in the *in situ* tensile test conditions. A fixed correction field interpolated with a fourth-order polynomial basis (such as the one described in [Gue14b]) is performed. The maximum displacement amplitude given by the correction is less than 10 pix (= 5.3 µm).

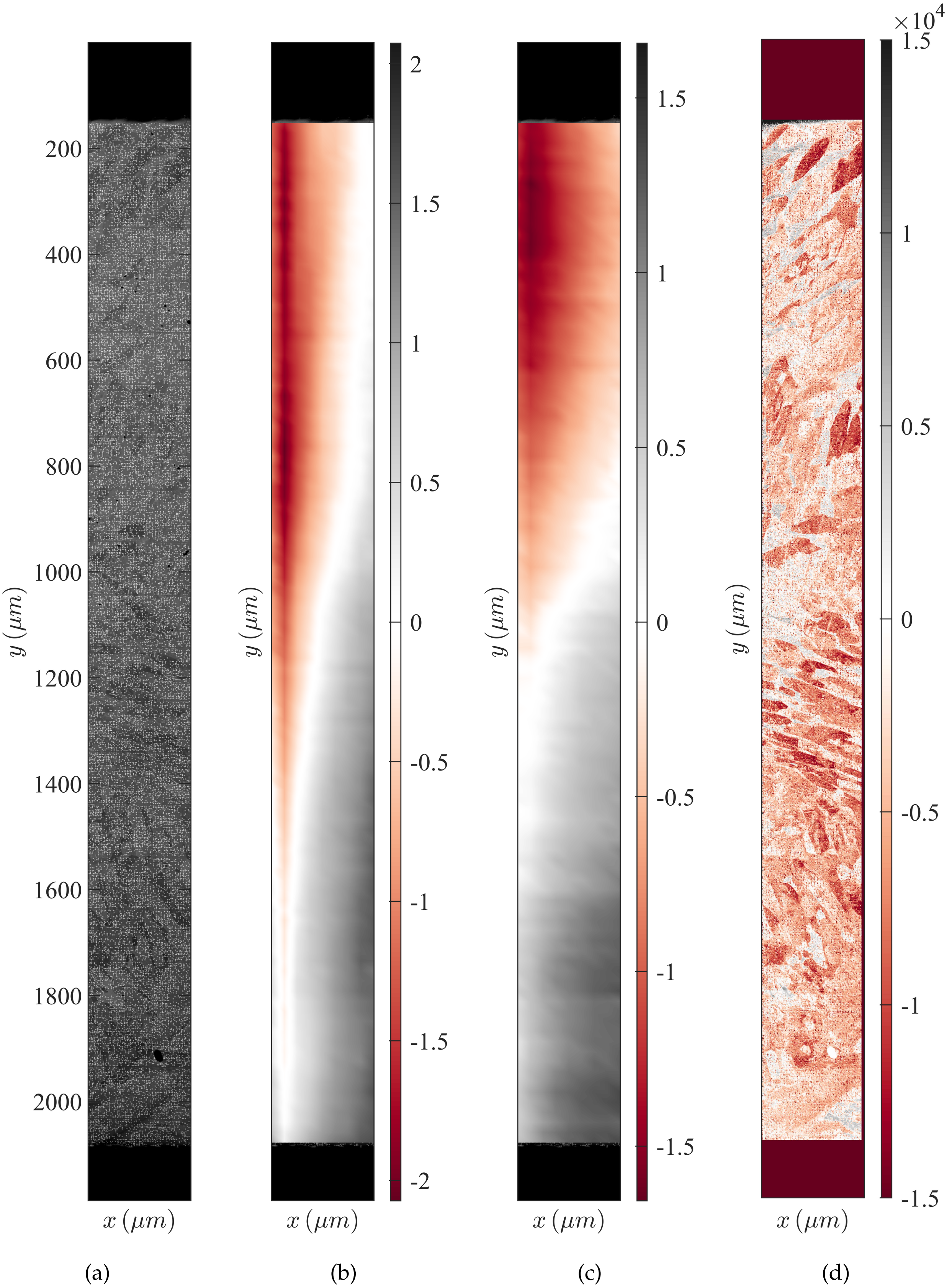

Figure 3.15: Example of spatial distortions of BSE images. Correction fields are obtained by correlating the overlapping area of two adjacent BSE images. (a) Overlapping area (left side). (b) Deviation from the average $U_x - \overline{U}_x$ (µm) ($\overline{U}_x = 2.9$ µm). (c) Deviation from the average $U_y - \overline{U}_y$ (µm) ($\overline{U}_y = -18.6$ µm). (d) Residual (GL).

The correlation residual emphasizes the gray level dependence on the channeling effect in BSE-type images (Figure 3.15 (d)). Besides image distortions that are corrected by displacement fields, moving the sample induces a change in the electron beam incident angle in local crystallographic frames (Figure 3.16 (a)). This modification manifests itself in gray level variations related to crystal parameters (phase and orientation in the specimen frame). Consequently, the morphology of the grains is likely to appear on the residual because of this effect. Accommodations of local strains by the activation of slip (which does not change the lattice orientation) and small crystallographic network rotations follow the loading of a specimen. One can then expect the channeling effect also to occur during these tests. It is proposed to carry out Brightness-Contrast Correction (*b.c.c.*, see Appendix B) to quantify gray level variations due to this phenomenon. We will also show that channeling contrast variations will not introduce bias in resolving the displacement field.

Introducing *b.c.c.* on a coarse mesh (40 pix element size) reduces the Root Mean Squared (RMS) from 8.5% to 4.9% of the total dynamic range (2^{16}-1 GL). The final residual depends on the channeling contrast changes and can be corrected. The relaxation algorithm allows one to reach a good registration of electron images, including these crystallographic effects. In the present case, it is also beneficial to implement the gray level correction locally. Thus, gray level variations associated with each grain are accurately captured (Figure 3.16). Reducing the element size for the brightness-contrast correction improves the correlation quality steadily without deteriorating the converged kinematics. Figure 3.17 illustrates that the correlation residual becomes much more uniform when increasing the number of degrees of freedom during GL relaxation. Despite this increase, the displacement field is still computed in a reasonable number of iterations without introducing any unphysical bias. Figure 3.18 depicts the difference between displacement field amplitudes computed with and without *b.c.c.* and its change with the element size. The amplitude is defined as $\|\boldsymbol{U}\| = \sqrt{U_x^2 + U_y^2}$ and the difference reads $\|\Delta \boldsymbol{U}\| = \sqrt{(U_x^{ini} - U_x^{BCC})^2 + (U_y^{ini} - U_y^{BCC})^2}$ where U^{ini} is the displacement field computed without correction and U^{BCR} the one with correction. Figure 3.18 (b-d) proves that only minor changes in the displacement field are introduced by *b.c.c.* compared to the initial case (Figure 3.18 (a)). In the end, the gray level correction expressed as a linear combination of brightness and contrast fields distinctly outlines microstructural features. The residual associated with the computation of the displacement field can then be estimated and the contribution of channeling contrast quantified.

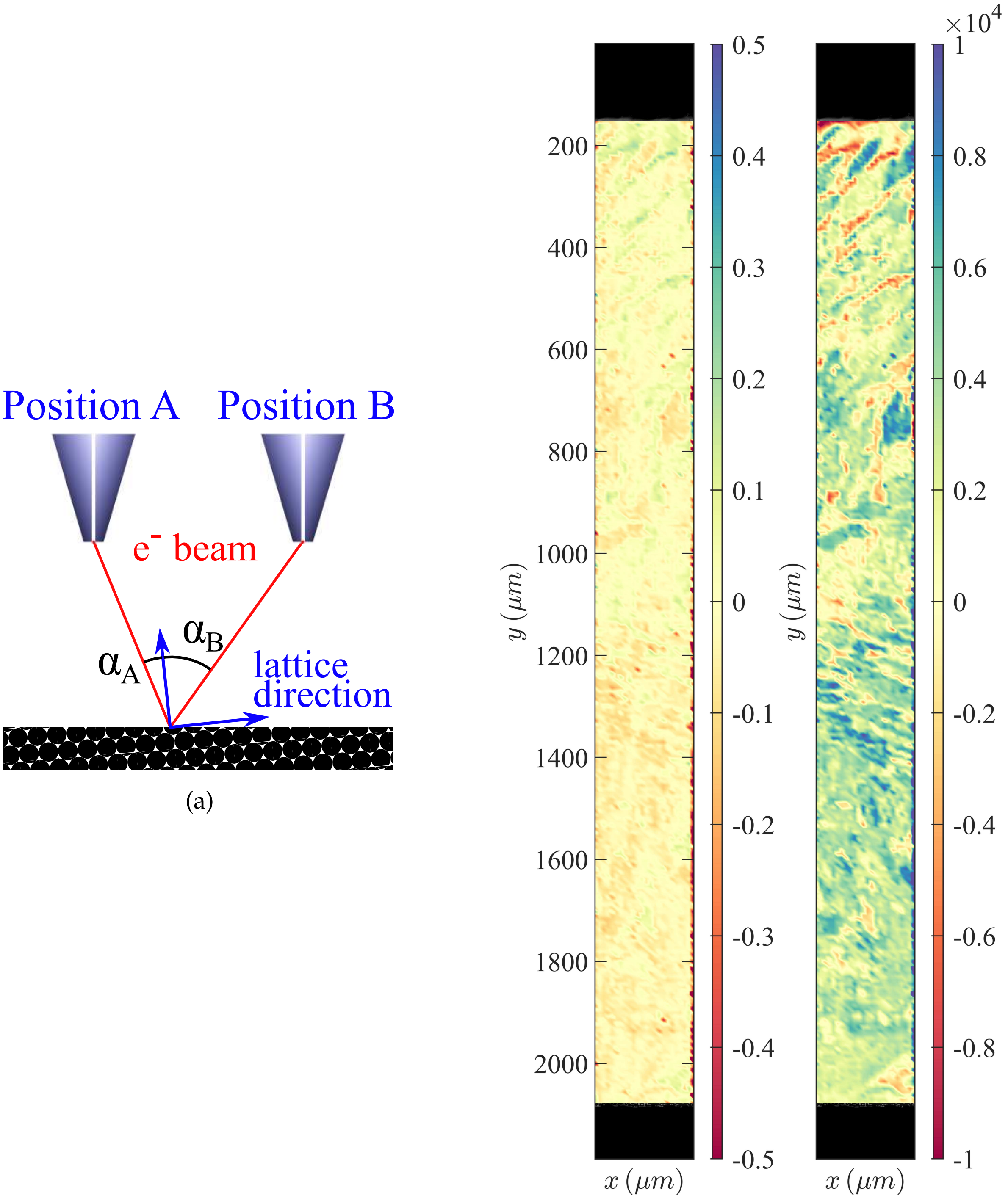

(a)

(b)

(c)

Figure 3.16: Origin and correction of brightness and contrast variations between two translated images. (a) Difference in channeling contrast from two scanning positions. (b) Contrast correction (in GL) for the best case (element size of 10 pix). (c) Brightness correction (in GL) for the best case (element size of 10 pix).

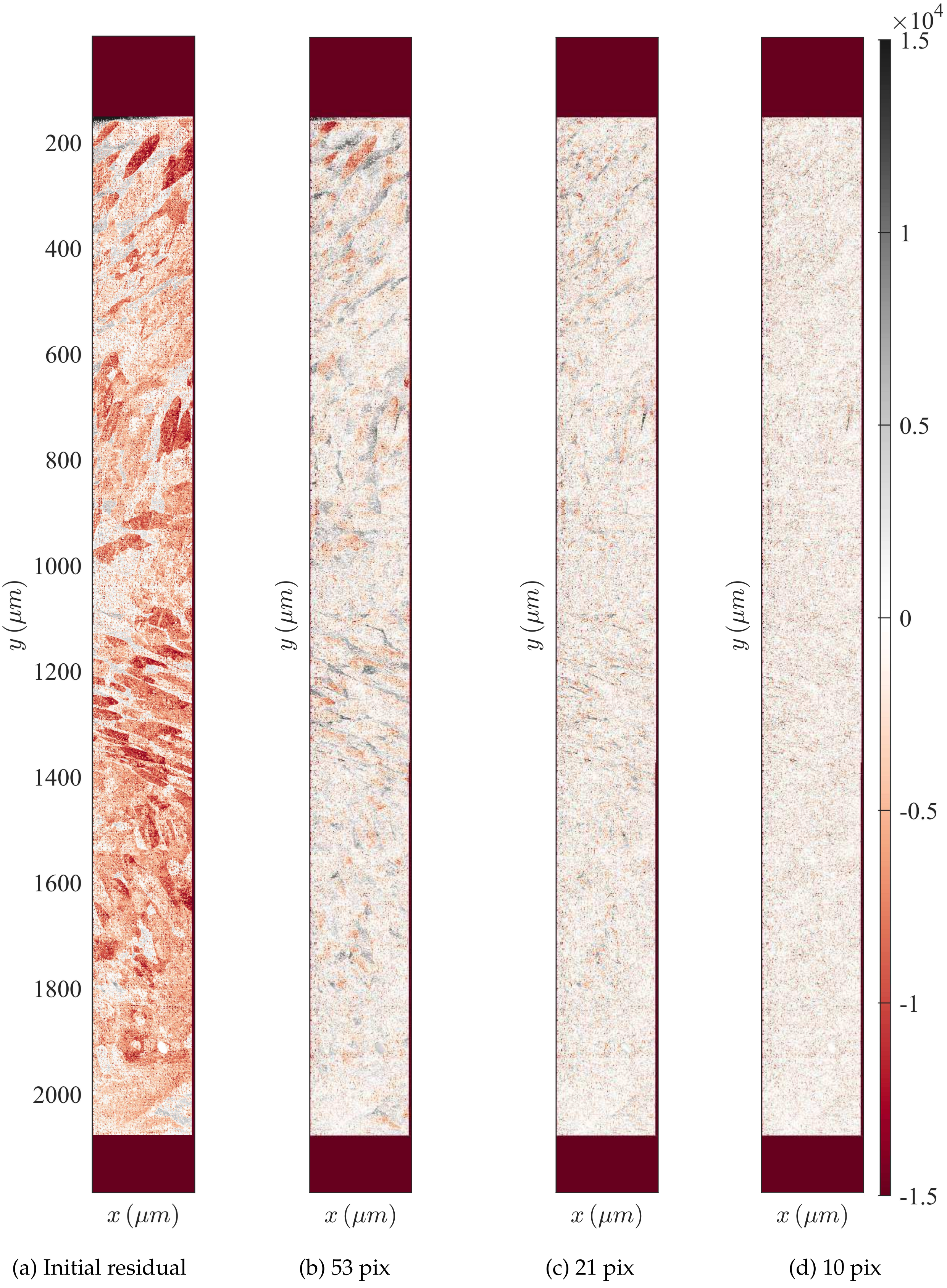

(a) Initial residual (b) 53 pix (c) 21 pix (d) 10 pix

Figure 3.17: Change of GL residuals with a decreasing element size.

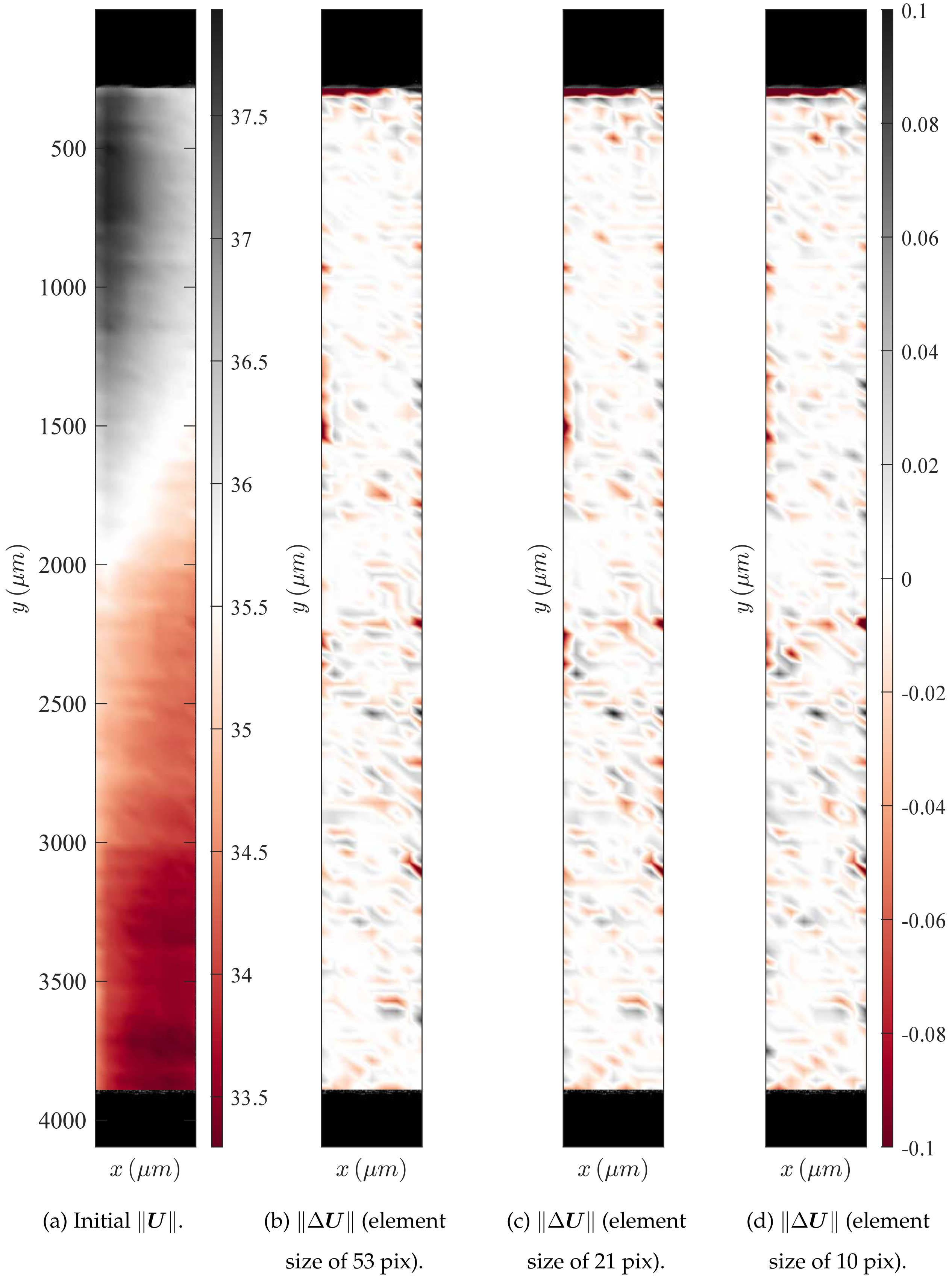

(a) Initial $\|\boldsymbol{U}\|$.

(b) $\|\Delta\boldsymbol{U}\|$ (element size of 53 pix).

(c) $\|\Delta\boldsymbol{U}\|$ (element size of 21 pix).

(d) $\|\Delta\boldsymbol{U}\|$ (element size of 10 pix).

Figure 3.18: Comparison of displacement field amplitudes computed with and without *b.c.c.* for different element sizes. All fields are expressed in pixels.

3.2.4.2 Distortions associated with millimetric EBSD maps

EBSD uses the same acquisition procedure as standard SEM images. Only the specimen positioning and the treatment of electron signals are different. Consequently, EBSD images suffer from the same artifacts as BSE images detailed in the previous parts. Intending to acquire large data maps, assessing the ability of EBSD to map crystal orientations at a millimetric scale consistently is derivable. In the manner of BSE images in the previous section, maps of crystallographic data are acquired by assembling multiple 2 mm x 2 mm areas with overlapping regions (see Figure 3.13 (a)). Information about EBSD images spatial distortions lies at their boundaries. Consequently, data were correlated from two overlapping maps to assess the distortions of EBSD maps. The procedure involving DIC in the case of BSE images is used. However, EBSD maps are acquired before speckle deposition (see Section 3.2.3.2). One can only use crystallographic data to correlate overlapping regions between two adjacent maps. As the rotation angle carries the “distance” information, the scalar rotation angle map as the observable was chosen. However, the rotation angle information is rather poor compared to the sharply defined features of speckle contrast in BSE images. A successful correlation is ensured by prescribing a regularization length of 30 pix (90 µm).

Figure 3.19 presents the correlation of the area depicted in Figure 3.19 (a) considering the angle map of the two alloy phases. Similarly, there is a large rigid body motion to correct alongside variations about the average (Figure 3.19 (a,c)). Apart from an isolated high amplitude in the x direction (at the top of the image), variations are less than 1 pix (3 µm). Besides, this local rise in variation seems related to spurious diffraction pattern indexing of some small microstructural features. Over their region of overlap, both images are very well correlated, as can be judged from the residual (Figure 3.19 (d)). Local high residuals at phase boundaries are noticed. This observation results from the difficulty of EBSD in delivering reliable indexing at grain boundaries (when no specific data analysis is made in the diffraction patterns [Shi21]).

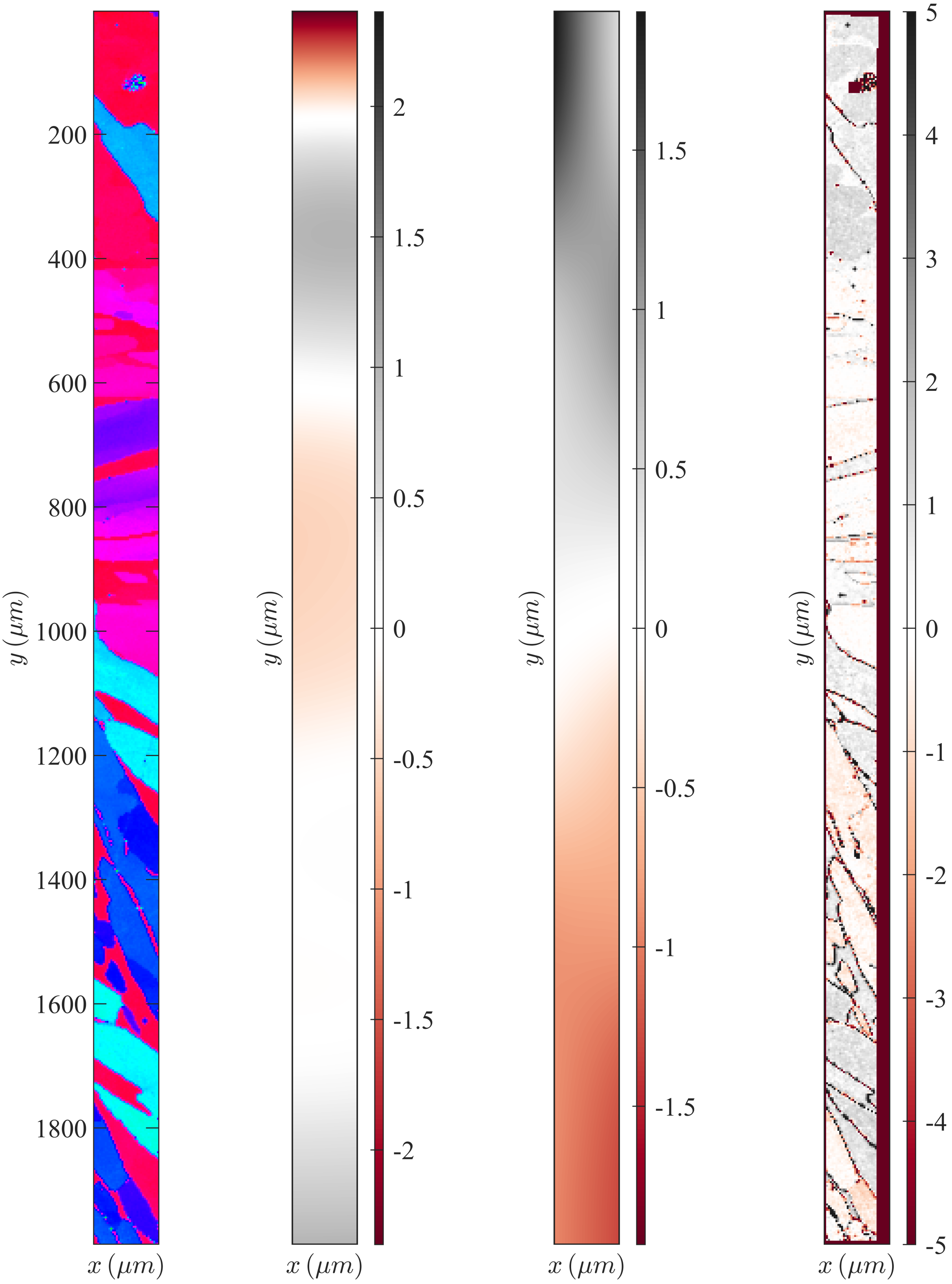

(a)

(b)

(c)

(d)

Figure 3.19: Example of spatial distortions of EBSD images. Correction fields are obtained by correlating the rotation angle of two adjacent EBSD maps. (a) Overlapping rotation angle map (left side). (b) Deviation from the average $U_x - \overline{U}_x$ (µm) ($\overline{U}_x = 16.5$ µm). (c) Deviation from the average $U_y - \overline{U}_y$ (µm) ($\overline{U}_y = -1.4$ µm). (d) Residual (°).

The same correlation was conducted considering only the austenitic phase maps to ensure that the previous spurious point is not linked to badly reconstructed EBSD maps. The rotation angle has no information about the phase distribution, and similar angles are found at the phase boundaries. The child phase provides the highest density of boundaries (*i.e.,* contrast) that are meaningful for correlating the two ribbons. Selecting one over two phases adds information about the phase map in the angle map. The correlation result using this second approach is shown in Figure 3.20. The new angle map is displayed in Figure 3.20 (a). The average components in x and y directions remain the same with a minimal measured difference (0.08 µm in x direction and 0.05 in y direction). The variation amplitudes in y direction are identical. However, the fluctuations in U_x are reduced. Still, a concentrated negative displacement $y \approx 700$ µm is observed. However, variation amplitudes are very low (less than 1 µm). It may be explained by the specific laths morphology in the middle of the image aligned along the x axis. Poor contrast variations result from this rotation angle map, as emphasized by the high residuals at the grain boundaries. Hence, sub-pixel displacements in the x direction should not be given too much credit. One can consider that the average component in both directions is sufficient to provide excellent stitching.

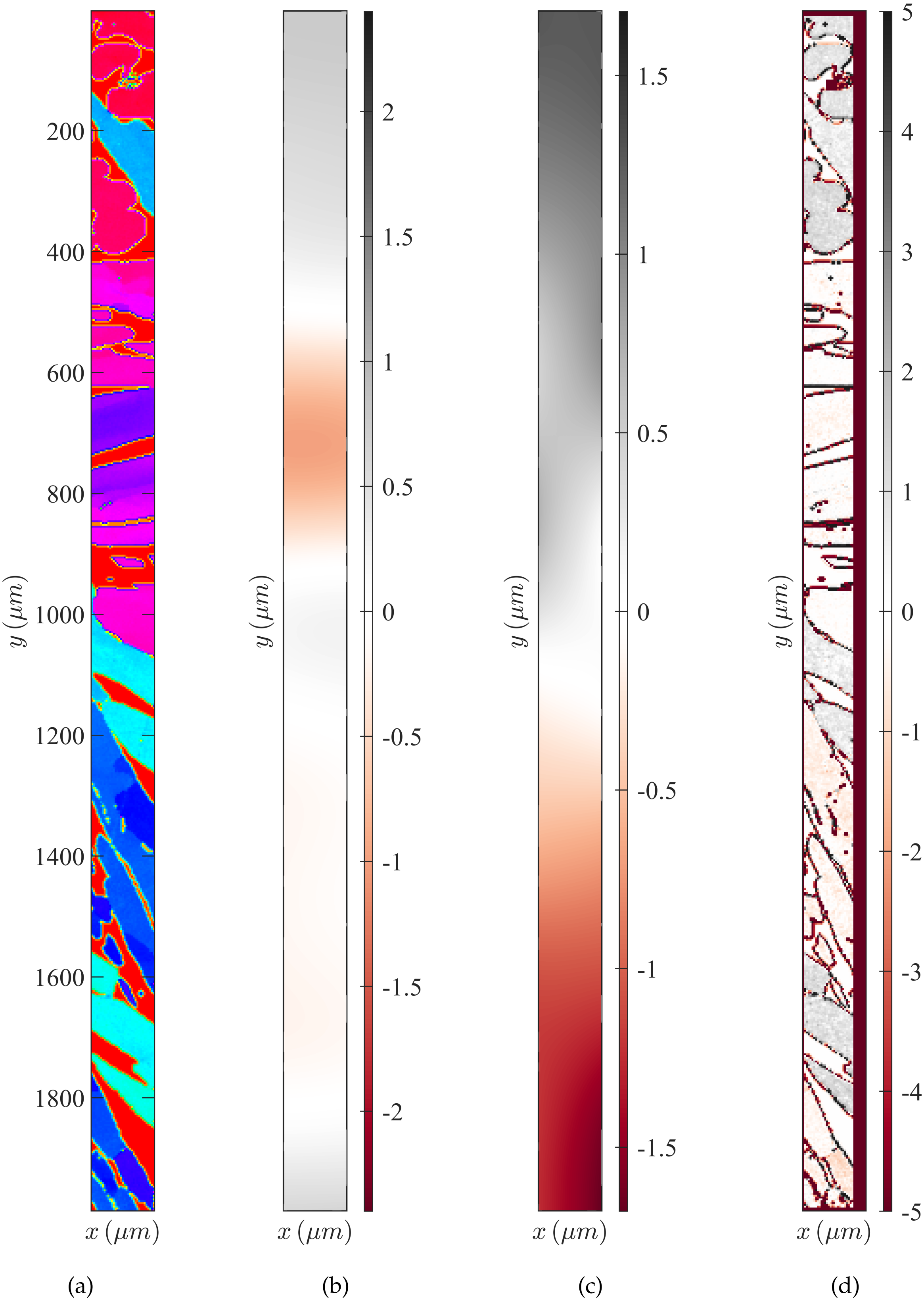

(a) (b) (c) (d)

Figure 3.20: Example of spatial distortions of EBSD images. Correction fields are obtained by correlating the rotation angle of two adjacent EBSD maps considering only the austenitic phase. (a) Overlapping rotation angle map (left side). (b) Deviation from the average $U_x - \overline{U}_x$ (µm) ($\overline{U}_x = 16.6$ µm). (c) Deviation from the average $U_y - \overline{U}_y$ (µm) ($\overline{U}_y = -1.4$ µm). (d) Residual (°).

The overall correction on EBSD images appears relatively low, especially considering the pixel size of 3 µm. Consequently, it is considered that spatial distortions are negligible in this imaging modality, and EBSD images can be stitched with a regular rigid body motion basis to map full *in situ* specimens.

3.2.4.3 Backtracking EBSD images to BSE images frame

The last correction to ensure consistent field measurements at the microstructure scales comes from the correlation between different imaging modalities. For the two considered imaging techniques, experimental acquisition conditions are different. In BSE images, the sample is positioned so that its surface is normal to the incident beam path. To acquire diffraction patterns, the sample must be tilted with respect to the beam direction. Different geometrical transformations thus describe distortions. In addition, samples and images processed in the present study are of exceptionally large dimensions, therefore prone to significant artifacts, which are detrimental to image quality. A more general approach to link BSE and EBSD images has been adopted. The main idea is to correlate the grain boundaries of the two imaging techniques. This physical information is present in both, although an easy and objective definition of boundaries is not trivial in BSE images. In the latter modality, gray levels result from channeling (relevant for distinguishing different phase orientations) but also chemical contrast and topography. In the present case, the deposited speckle also introduces high chemical contrast variations that are beneficial to DIC for images obtained from the same modality, but makes the determination of grain boundaries more difficult. A direct way to avoid the speckle would be to acquire an image before deposition, but it proved unsuitable as speckle deposition is performed outside of the SEM. That means that the sample needs to be removed and reintroduced in the microscope between acquiring a raw reference image and another one with the deposited speckle. The operation of an SEM is sensitive to its electromagnetic environment, and tests emphasized that one cannot obtain the same exact images after taking out and reintroducing a sample in the vacuum chamber. In particular, the image scaling and channeling contrast are not preserved and show great sensitivities. Consequently, the images used for full-field measurements must be kept to correlate the two imaging techniques.

Under these circumstances, an image processing to recover and isolate phase contrast in these images was set up. First, the disk centers and radii are accurately detected using a Circle Hough Transform (CHT) [Yue90] algorithm that has been implemented (Figure 3.21).

The disks detected with the circle finding algorithm in the image sample of Figure 3.21 (a) are highlighted with red marks in Figure 3.21 (b).

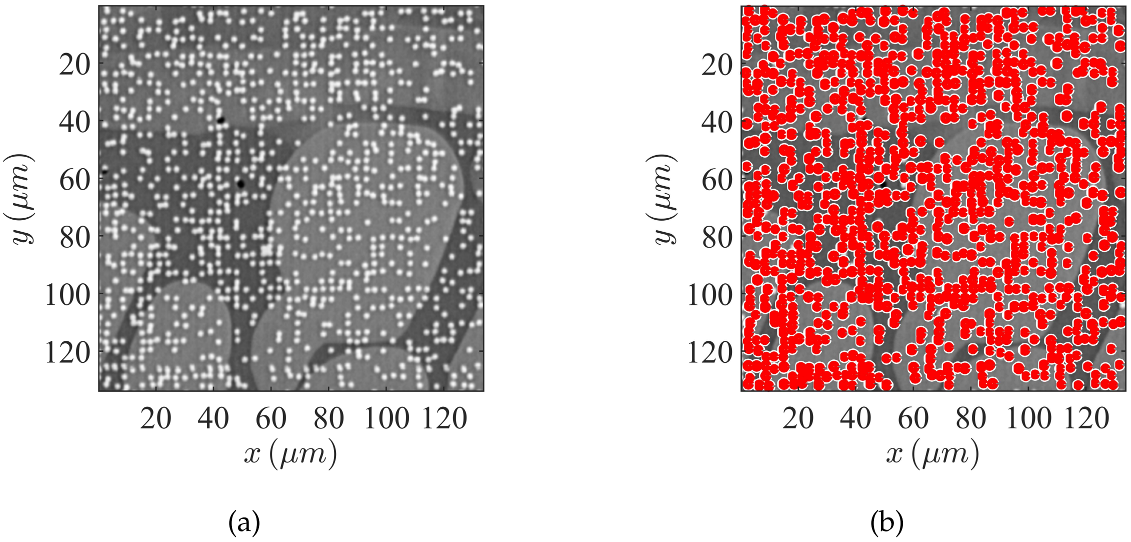

(a)

(b)

Figure 3.21: Illustration of speckle detection using Hough Circle Transform. (a) Sample of an original image used for mechanical field measurement. (b) Speckle disks detected as circles by the CHT algorithm.

A mask is created from the computed circle parameters to remove pixels corresponding to speckle disks. The deleted pixel values are replaced by a local background level obtained using a median filter on the initial image with a 50 pix window size (Figure 3.22 (a)). One can notice that spurious high gray levels remain due to the circle detection algorithm. The latter does not remove fragments of gold particles initially corresponding to a packed stack of disks or disks with irregular shapes. Thanks to their low spatial density, these bad pixels can further be filtered using an incremental Gaussian filter scheme, and phase contrast from BSE images can be restored (Figure 3.22 (b)). Figure 3.23 illustrates the correction on a full BSE image, excluding areas not corresponding to the specimen surface. A typical BSE image used for full-field measurements is shown before restoration of phase contrasts (Figure 3.23 (a)), and after restoration in Figure 3.23 (b).

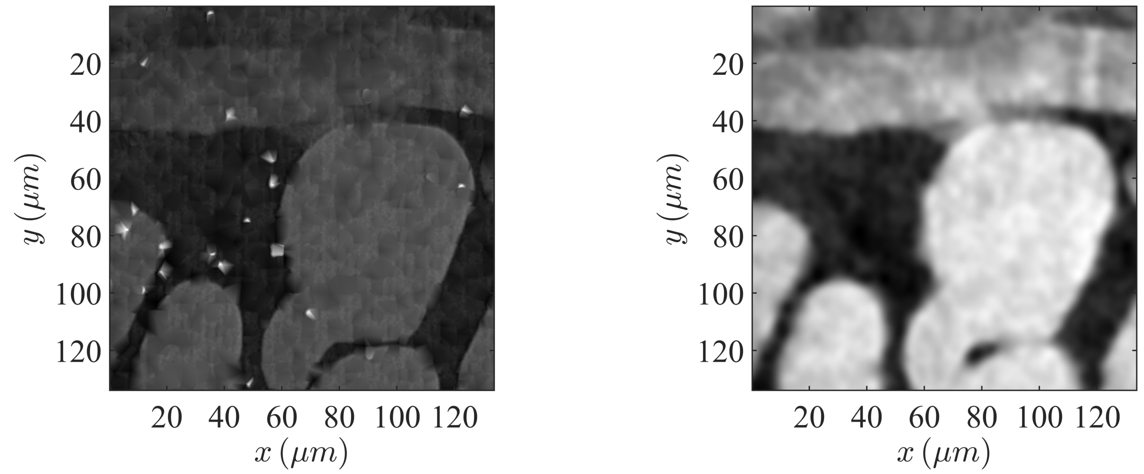

(a)

(b)

Figure 3.22: Illustration of speckle replacement in BSE images. (a) Replacement of disk gray levels by a long range median value of unprocessed image. (b) Filtering of remaining high gray levels that were not masked after the circle detection algorithm.

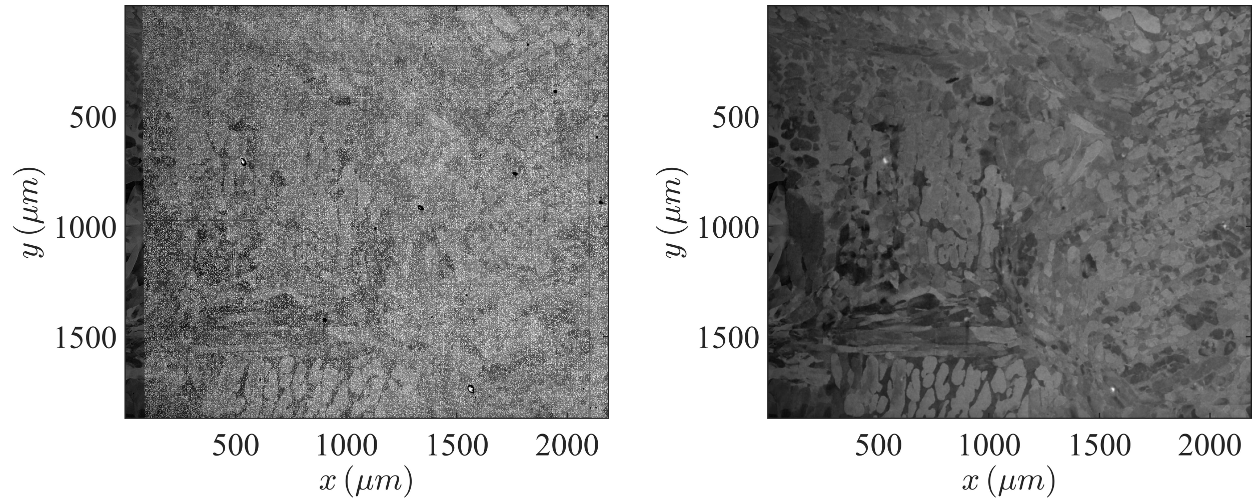

(a)

(b)

Figure 3.23: Example of restored image displaying mostly phase and channeling contrast. (a) Original BSE image including the speckle. (b) Restored image with speckle removed.

Once restored, BSE images used for DIC purposes globally depict distinct phase contrasts that can be correlated with the phase maps from EBSD acquisitions. A straightforward computation of the gradients in the two image types provides data to locate grain boundaries. A Gaussian filter is applied to the boundary images to make the correlation easier. An example of a pair of images used for correlating BSE and EBSD grain boundaries is given in Figure 3.24. Despite a satisfactory restoration procedure, grain boundaries may locally appear attenuated in BSE images because of other factors contributing (mostly channeling contrast) (see, Figure 3.24 (a)). At the same time, the EBSD map provides a clear definition (Figure 3.24 (b)). In this context, global regularized DIC proved to be a powerful tool (because of its robustness) to compute the correction field between the two types of images. The global minimization scheme undeniably helped overcome high uncertainties of boundary definitions in BSE images. With such a method, both rigid body motions and imaging technique-induced distortions were corrected. Figure 3.25 illustrates the initial position (Figure 3.25 (a)) of boundaries deduced from the BSE map (considered as the reference frame after the correction introduced in Section 3.2.4.1) and the position after the correction computed with DIC (Figure 3.25 (b)). The correction allows for a quasi-perfect match between the two images with respect to the lowest resolution of microstructural features given by the pixel size of EBSD images.

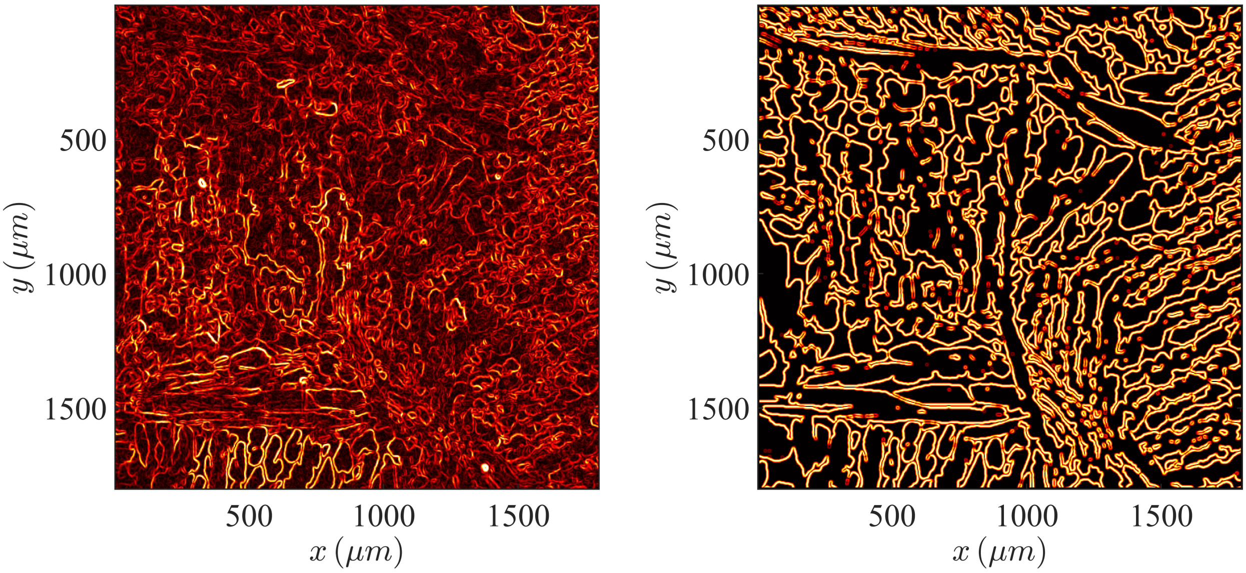

(a)

(b)

Figure 3.24: Pair of images used to backtrack EBSD grain boundaries onto BSE frame. (a) Gradient of restored BSE image. (b) Gradient of EBSD phase map.

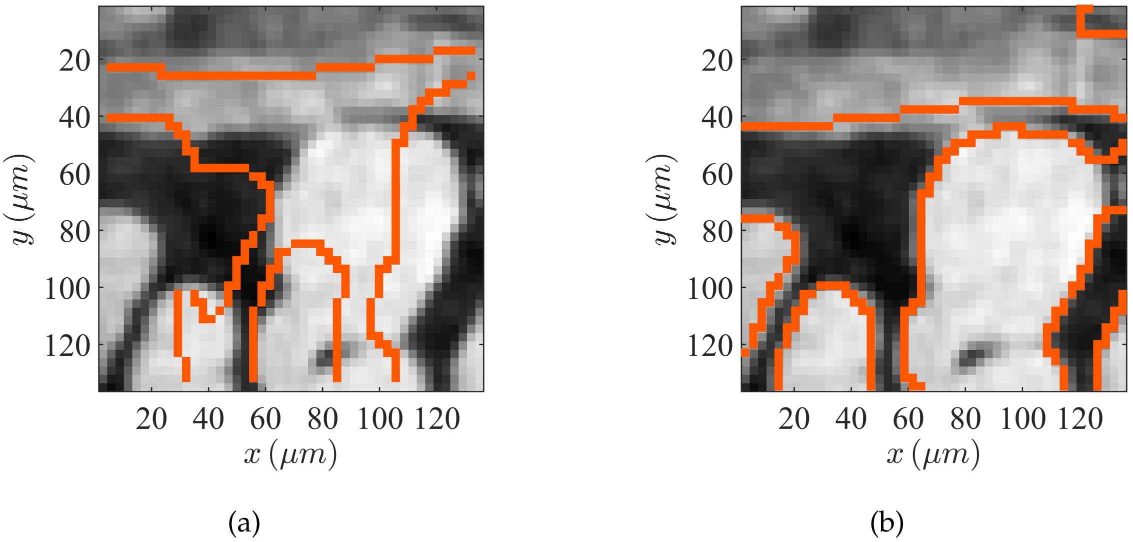

Figure 3.25: Correction of EBSD position using DIC on the phase boundary map. (a) Initial EBSD boundary (red pixels) according to the global specimen frame inside the microscope. (b) Corrected EBSD boundaries with the computed displacement field.

Figure 3.26 presents a typical correction field mapping an EBSD map onto the corresponding BSE frame. The deviation to the average of the components (*i.e.,* the rigid body translation between the two images) highlights significant distortions while they looked relatively negligible in Section 3.2.4.2. Such differences emphasize that stitching EBSD maps when mapping large areas should be achieved cautiously, mainly when small microstructural features are present. The correction includes an isotropic stretch of the image combined with parallax correction and occasionally presents an asymmetry changing the layout of the two distortions mentioned above. The asymmetry is likely attributed to a difference in the alignment of the sample in the two imaging techniques. Figure 3.26 (a,b) demonstrates how the robustness of the global DIC algorithm allows the fuzzy grain boundaries definition to be overpassed in the backtracking procedure. The computed correction fields finally allow for a very good match of the two imaging modalities over the whole domain.

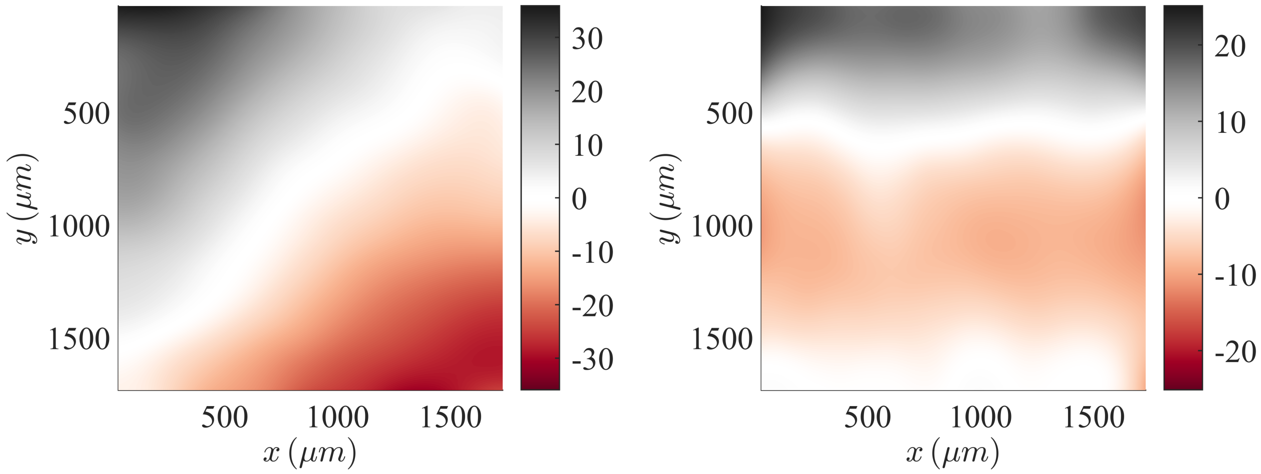

(a) $U_x - \overline{U_x}$ (μm) ($\overline{U_x} = 50.4$ µm) (b) $U_y - \overline{U_y}$ (μm) ($\overline{U_y} = -13.7$ µm)

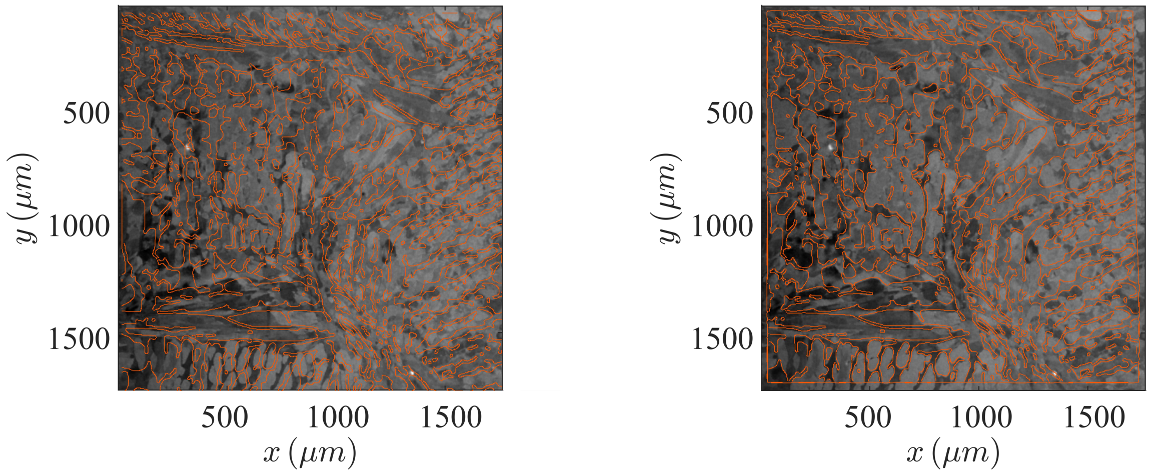

(c) (d)

Figure 3.26: Typical correction displacement field of a full EBSD map. (a) Deviation to average in the $\boldsymbol{x}$ direction (µm). (b) Deviation to average in the $\boldsymbol{y}$ direction (µm). Restored BSE images superimposed with EBSD grain boundaries before (c) and after (d) backtracking.

3.2.4.4 Measurement resolution

Once correlated to the BSE images frame, EBSD images convey crystallographic data in the frame where displacement fields are measured. Thus, objects identified on EBSD maps (*e.g.*, laths, laths packets, or primary grains) can be used to build meshes for DIC purposes. Such a mesh is illustrated in Figure 3.27. The measurement accuracy should be sufficient to resolve the strain fields resulting from the mechanisms analyzed in Section 3.2.2 at the smallest scales described in Section 2.3.2. One way to assess the measurement uncertainty is to correlate two images acquired in the same condition without loading. Figure 3.28 shows such an evaluation from a typical case in the chosen experimental framework. The residual associated with 2 mm × 2 mm (4096 pix × 4096 pix) images is depicted in Figure 3.28 (a).

The computed difference between the reference and back-deformed images is conveniently associated with Gaussian noise and an additional component presumably related to the bottom of the image (Figure 3.28 (b)).

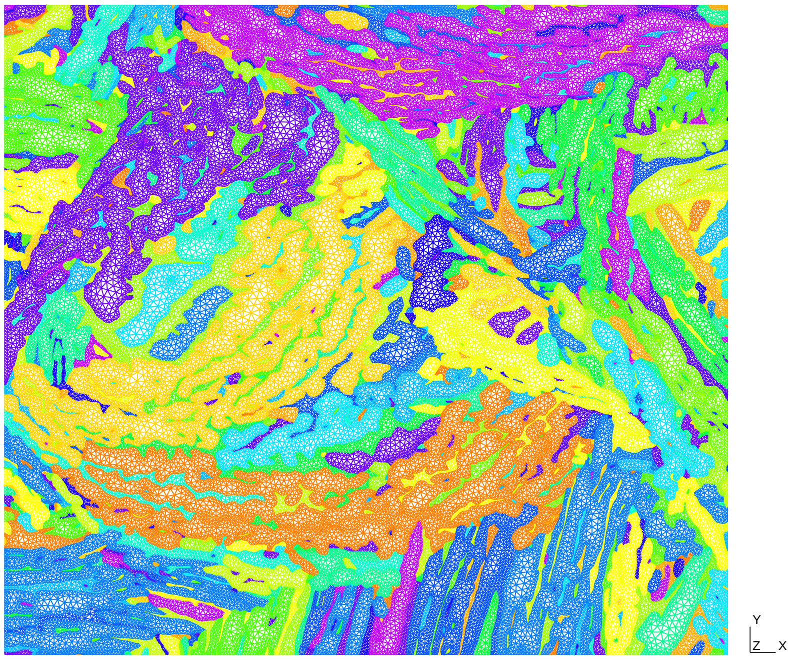

Figure 3.27: Example of 2D mesh fitting microstructure features as measured with EBSD. The mean element size is 10 pix (≈ 5.34 µm) and the covered area is approximately 2 mm × 2 mm.

The displacement field resulting from the correlation of the two images differs distinctly from a random distribution. Figure 3.28 (c,d) highlight artifactual displacements with smooth variations along the scan direction and much more irregular variations in the perpendicular direction. Such effect results from scan drift errors in the slow scanning direction (previously introduced) and of unknown amplitude (the scan direction is vertical). However, they differ from literature cases as they do not systematically cross the whole image and sometimes locally vanish. They constitute the limiting factor in measurement accuracy and control the measurement uncertainty of about one pixel (0.5 µm). The inherent accuracy of global DIC approaches would be much lower. It is noteworthy that the current pixel size results from a compromise to avoid new developments on existing scan drift correction algorithms that consider no error in the fast scan direction (because this hypothesis does not hold on the present image scale). An uncertainty of 0.5 µm is deemed sufficient to resolve local displacements resulting from CDSS microstructural features. This assumption is confirmed in the analysis of the strain maps in Section 3.3.

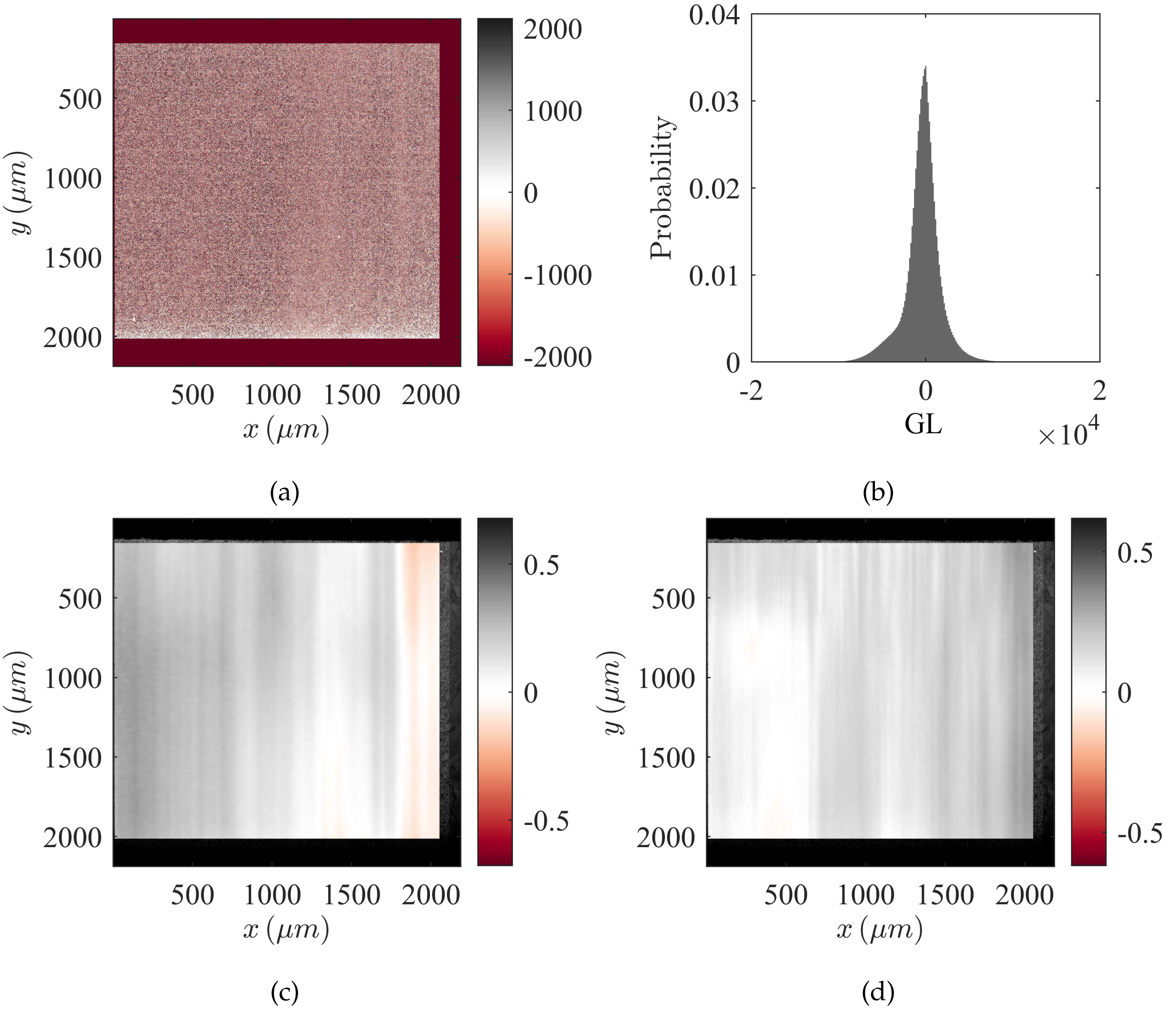

(a) (b)

(c) (d)

Figure 3.28: Artifactual displacement measurement from 2 mm × 2 mm BSE images. The fast scan direction is $\boldsymbol{y}$. (a) Gray level residuals from a pair of undeformed images acquired simultaneously. (b) Histogram of the GL residuals. Displacements in the slow x (c) and fast y (d) scan directions (in µm).

As phase contrast in BSE images is still present and likely to vary with channeling effects during loading, a detailed observation of the correlation residuals was carried out. A demonstration of the ability to account for gray level variations induced by channeling contrast with the current DIC framework has been illustrated (Section 3.2.4.1). *b.c.c.* at a local scale (in comparison with microstructural features) allows to sort out the DIC error due to displacement field calculation only and to quantify gray level variations due to channeling and topography changes during the *in situ* tests. Figure 3.29 illustrates that this correction still stands during a test up to 5% macroscopic strain and significant out-of-plane displacements on the last increments. The RMS gray level residual change over the whole test with and without the corrections are shown in Figure 3.29 (a). The RMS residual is found to be much lower and stable during the test when using *b.c.c.*. Figure 3.29 (b) shows that grains pop out in the GL correction field carried out by *b.c.c.* between the initial and last images of the test on the unaged material (P1 ROI 3). This is evidence that the variations in the residual without *b.c.c.* are due to topography and channeling contrast effects and that they can be conveniently quantified and corrected. After correction, the residual is much closer to a random distribution related to the imaging technique used herein (Figure 3.29 (c)).

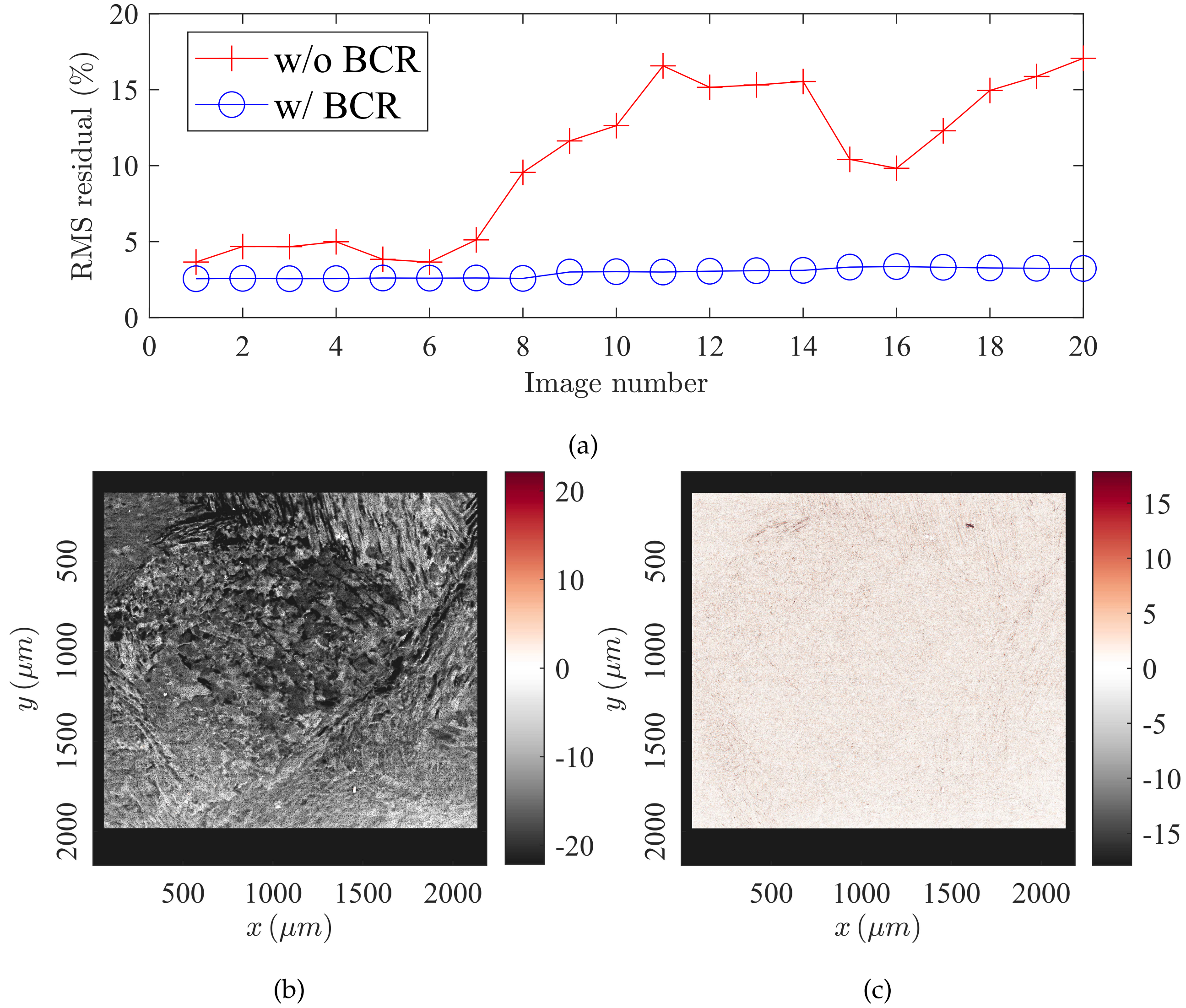

(a)

(b)

(c)

Figure 3.29: Gray level evolution of BSE images during *in situ* tensile tests. (a) Evolution of RMS residual expressed as a percentage of the image dynamic range (2^{16}-1 GL) along the test. (b) Gray level correction expressed as a percentage of the total image dynamic range (2^{16}-1 GL) using *b.c.c.* between the first and last image. (c) Residual of correlation between first and last image with *b.c.c.* expressed as a percentage of the total image dynamic range (2^{16}-1 GL).

3.3 Understanding CF8M deformation mechanisms using EBSD and full-field measurements

3.3.1 Overview

The previous sections were dedicated to setting up a reliable framework for analyzing deformation mechanisms in the CF8M alloy using full-field measurements. Knowing microstructural features from Chapter 2 and the deformation mechanisms observed at the smallest scale of interest for this study (Section 3.2.2), we made a point to convey this information to the BSE image frame that carries the mechanical data thanks to DIC. The following discussion aims to explain crystallographic and morphologic influences on the redistribution of small-scale strains. We will use highly resolved measured strain maps acquired at the ferritic grain scale (from 1 to several millimeters). How this influence is affected by thermal aging is apprehended by testing three different aging states (as-received, aged for 1000h, and 10000h at 350°C corresponding to P1, P2, and P4 designations). For the three specimens, displacement fields are captured on three adjacent ROIs. Each ROI allows for the measurement of displacements as small as 0.5 µm on 2 mm × 2 mm images (Section 3.2.3.2).

Figure 3.30 illustrates the change of the average tensile behavior for each observed ROI on the three specimens. The stress is computed from the initial measured specimen section, and the resulting force is measured throughout the test. DIC is used to assess the average strain in the tensile direction. Resolving standard features and differences among the different aged states confirms the high merit of full-field measurements. The embrittlement with aging is revealed in such small-scale specimens through the change of tensile hardening. Using DIC, we measure similar behavior along gage lengths for each aged state. One ROI of the unaged specimen still shows much lower strains at failure (but equivalent maximum stress), while ROI 1 in the 10000 h aged specimen displays perceptible ductility. A specific crystallographic configuration may be responsible for the stiffer apparent elastic modulus of the unaged sample. In particular, the distribution of primary ferritic grains may play a significant role due to their relatively large size. A shift in the initial mean displacement would probably provide a more convincing result and is plausible, given the complexity of conducting *in situ* tests. If this shift is present, it occurs in all the fields and will not affect the strain maps studied later. Therefore, the data are kept as received. Full-field measurements exploited for extracting the previous tensile behavior give access to much richer mechanical data. In the following sections, data provided by DIC are utilized to explore strain mechanisms at the microstructural scales for the different aged states.

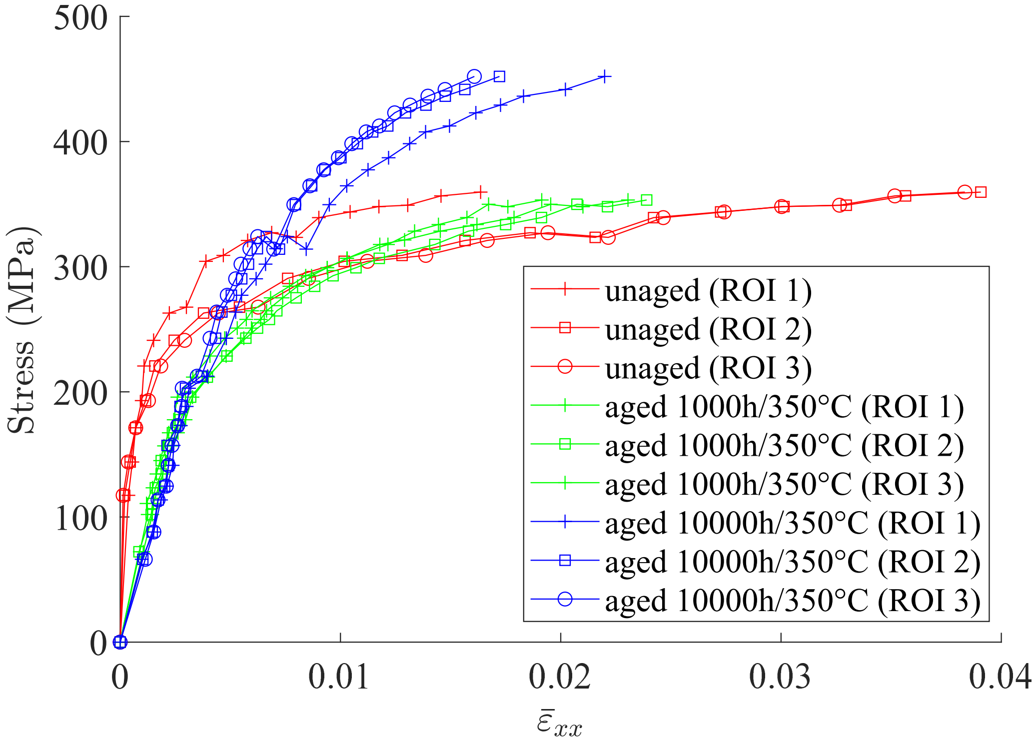

Figure 3.30: Change of average strain in the tensile direction as a function of the engineering stress for each analyzed ROI.

3.3.2 As-received behavior

Figure 3.31 presents the strain map resulting from the three ROIs that were analyzed next to the α- and γ-crystallographic orientation maps. The x (tensile) scale is identical in the three maps. The global view displays similar strain patterns across the gage length apart from a large area between $x = 5000$ µm and $x = 7000$ µm deformed to a much lesser degree. These strain patterns appear as long rectilinear (or slightly curved) strain bands or serrated bands. Looking closer at these strain patterns, the three ROIs were investigated and delimited with laths packets and ferritic grain boundaries used to create the correlation mesh. The first crucial observation is the “stability” of deformation mechanisms at the specimen scale. The strain patterns appear very early in the test and get more intense continuously during the test without changes other than their magnitude (Figure 3.32). The strain development process may differ between regions with different crystallographic properties (*e.g.*, specific clusters may concentrate most of the strain increments after a certain macroscopic strain level). This observation suggests that strain is simply scaled by the macroscopic (plastic) strain. Hence, an accurate prediction of plasticity mechanisms is instrumental for understanding the asymptotic tensile behavior of these tests.

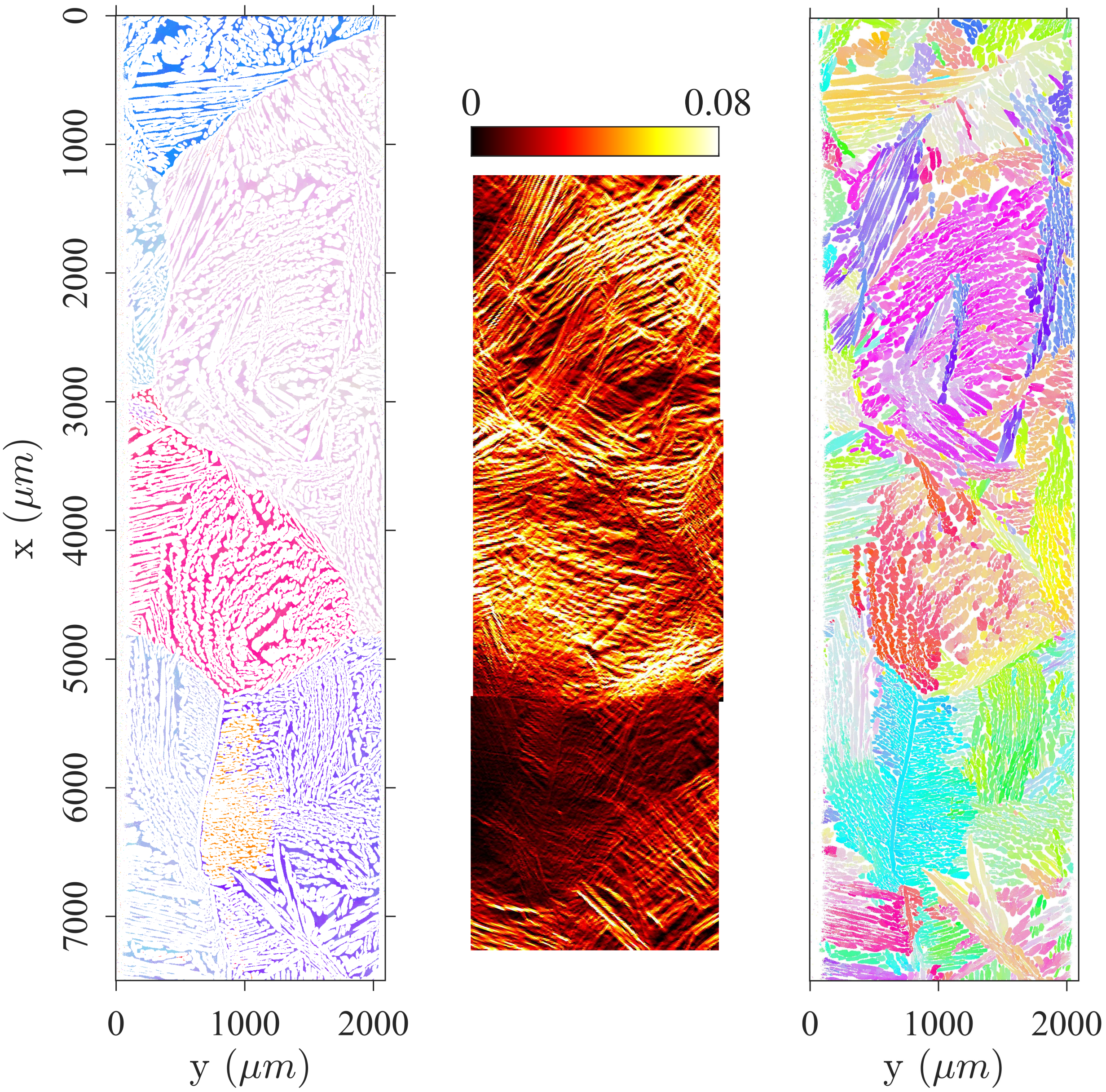

Figure 3.31: Overview of the as-received aged state (P1). From left to right: ferrite orientation map, measured ε_{xx} strain field at 4% macroscopic strain, and austenite orientation map. The loading direction is vertical.

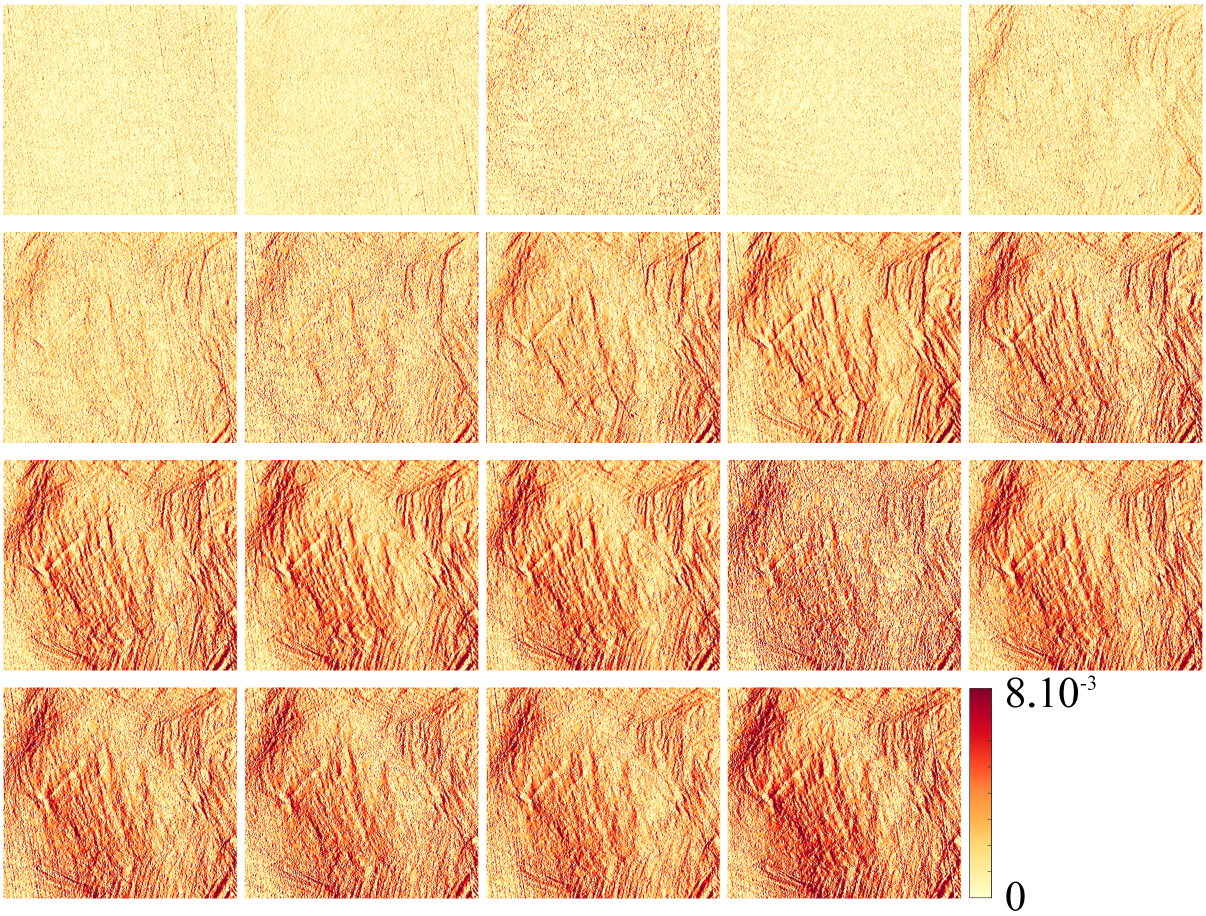

Figure 3.32: Incremental strain maps measured on ROI 2 from first to last load step. Mean strain is increasing in the reading order. The colormap is the same for all incremental fields.

Figure 3.33 highlights evidence of the different mechanisms that initiate in the unaged material. The as-received material deformation mechanisms reveal strain concentrations in the softest phase (*i.e.*, in austenite). Plastic strains first occur in this phase by activating single or multiple planar slip bands. Ferrite appears drastically less deformed with rare slip bands in SEM observations, but slip system activation is observed in TEM acquisitions [Ver95]. The resulting strain map (Figure 3.33 (a)) consists of clusters with an almost homogeneous strain distribution. In a distinct cluster, strain bands localizing the deformation are enclosed in nearly unstrained bands. For the most part, band alternation (highly strained and unstrained) is consistent with α- and γ-phase maps. Additionally, strain fields draw a remarkable correlation between areas of constant strain band orientation and lath packets. It is noteworthy to add that strain bands in austenite are often the result of the activation of multiple slip planes at the measured scale. The measurement resolution is not sufficient here to resolve strain bands corresponding to localized glide planes, and activation of multiple slip planes is nearly always observed (see Section 3.2.2). At the lath cluster scale, bands are not always as regularly defined as a lath. Their morphology appears related to lath packet orientation with respect to the loading direction.

The strain band orientation can be classified into two categories. They roughly correspond to Voigt and Reuss composition of two materials :

- In Reuss, iso-stress configuration, austenite is easily deformed as it is softer than ferrite. Consequently, γ-laths localize most of the strain. The link with orientation maps is easily drawn as strain bands follow austenitic lath orientations. When a packet meets this configuration, it mainly presents one orientation for the bands (Figure 3.33 (b) case ①). A homogeneous lath orientation is what initially defines a lath cluster. As austenite activates multiple slip systems more easily than the BCC system of ferrite, γ-laths are homogeneously deformed in the loaded direction by triggering multiple planes. Such an observation agrees with the conclusion drawn in Section 3.2.2.1 stating that strains in austenite are homogeneous at the lath scale. One may notice, however, that the in-plane lath growth direction is often close to a $(111)_\gamma$ plane trace, which makes the distinction between these two directions difficult experimentally. Remarkably, high strain levels in this configuration may locally trigger strain bands whose orientation differs from that of laths morphology but still coincide with a $(110)_\alpha$ slip plane trace (Figure 3.33 (b) case ②). In essence, these bands localize strains but also cross ferrite.

- In the Voigt case, austenite and ferrite are equivalently strained. This case is observed when the loading direction is nearly orthogonal to the lath packet normal. In this configuration, ferrite is constrained to yield. It follows that strain bands oriented along the two phases slip systems appear. In that case, bands are finer since they result from slip localization in the two phases and not from a uniform strain in the laths. Their direction is consistent with BCC and FCC slip plane traces depending on the local crystallographic properties. Figure 3.33 (b) case ③ corresponds to this second layout. Multiple strain bands are observed, and coincidence with slip plane traces is difficult to assess because disruptions are likely to be created by the competition of slip activity in both phases.

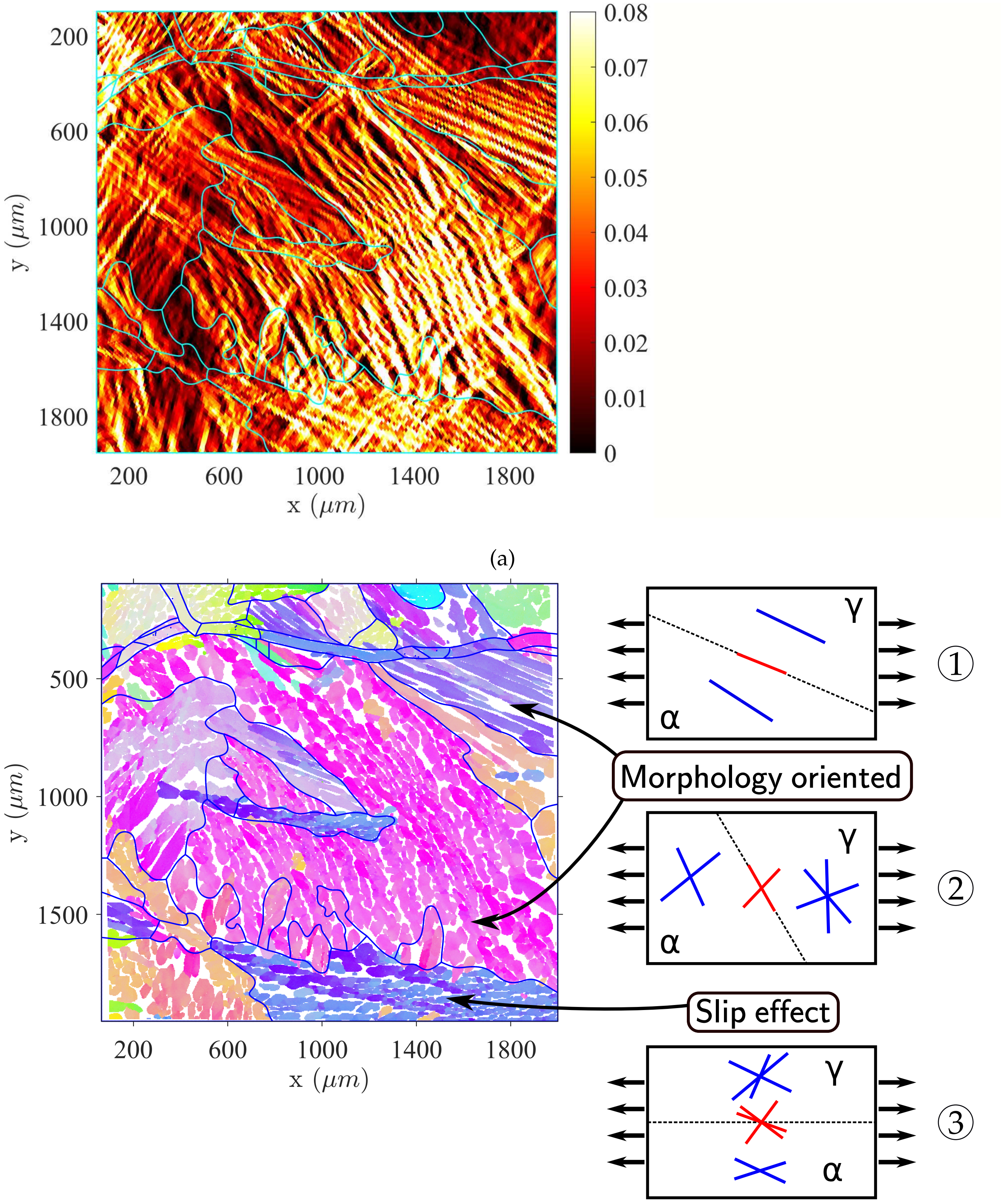

(a)

(b)

Figure 3.33: Microstructure correlated deformation mechanisms in the as-received material (ROI 1). (a) Green-Lagrange strain in the tensile direction (ε_{xx}) and lath packet boundaries (cyan lines). (b) Austenite orientation map with lath packets delimited in blue and schematic drawing of the observed features. Observed strain bands (red lines) are compared to lath orientation (dashed line) and closest slip plane traces (blue lines) in the two phases.

To further illustrate this effect seemingly linked to the microstructure morphology, the longitudinal strain map of ROI 2 is shown in Figure 3.34. While multiple packets are deformed in accordance with lath growth direction (*e.g.,* Figure 3.34 (b) case ①), a large packet (Figure 3.34 (b) case ②) has a remarkable behavior. At first sight, lath growth looks orthogonal to the tensile direction. This layout has already been described and resulted in a much simpler strain distribution from previous observations. A closer look, including crystallographic data processing from Section 2.4.4 reveals that laths normal is nearly out of the plane with a 2:1 ratio with in-plane components explaining their singular aspect. That is, ferrite is largely extended in this packet observation plane and is close to the iso-strain configuration described above. Hence, the strain bands result from slip localization in both phases, not from the lath morphology, although it appears clearly on the present strain field that the bands are parallel to $(111)\gamma$ slip planes. This particular example emphasizes the importance of in-depth knowledge of lath morphology.

Apart from lath packet properties, former ferritic grain boundaries present some interesting properties to localize strains at the present scale. Section 3.2.2.1 showed that these former boundaries (replaced by a thin austenitic layer) were locally prone to high slip activity. These boundaries are also characterized by the coherency of γ-orientations on either side of the layer (Section 2.4.3.2). Data acquired on the single specimen look insufficient to conclude on induced strains at the present scale. Nonetheless, Figure 3.34 (b) case ③ highlights such configuration as an “incoherent” boundary exhibiting high localized strains.

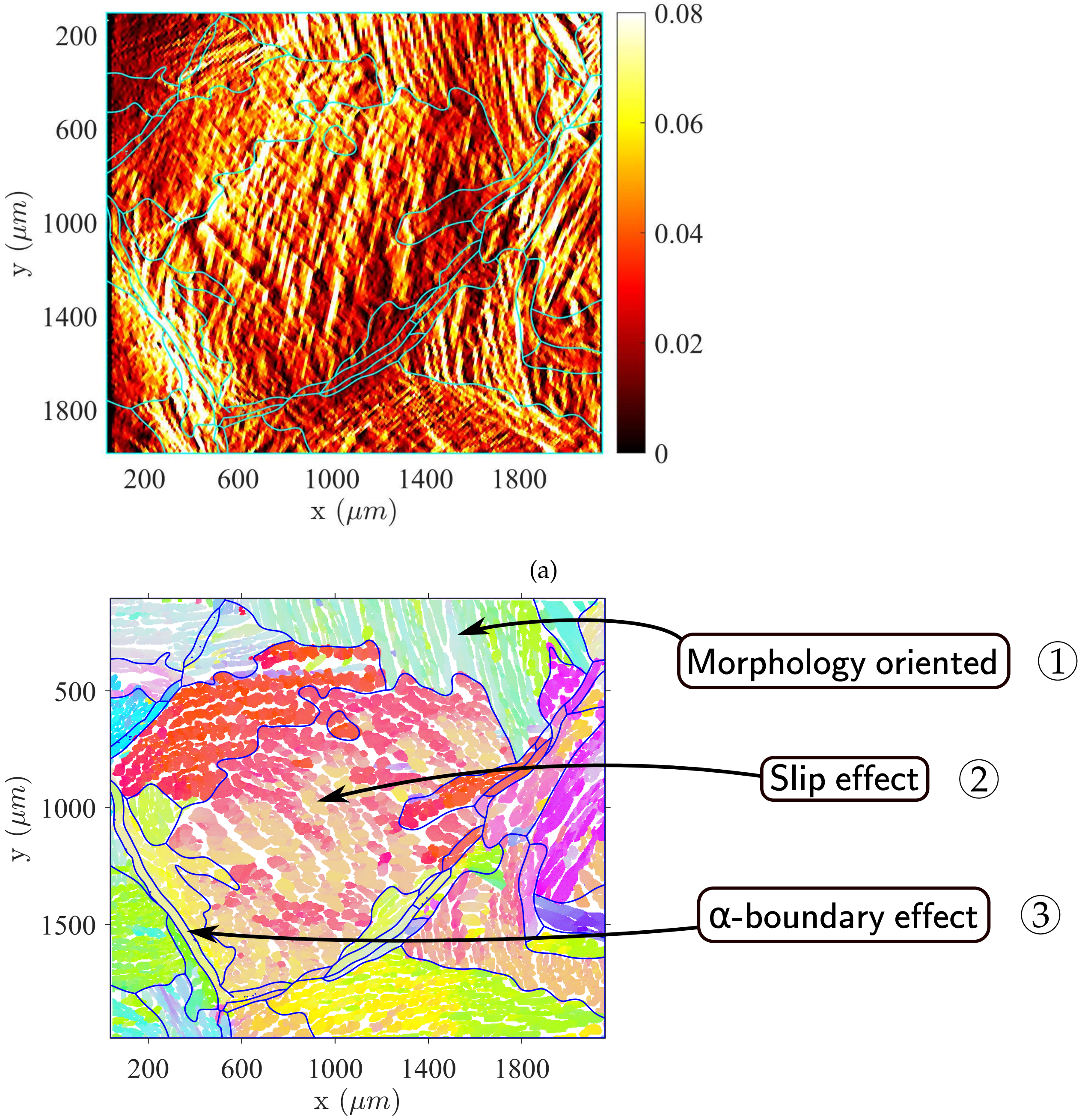

(a)

(b)

Figure 3.34: Microstructure correlated deformation mechanisms in the 10000 h aged material (ROI 2). (a) Green-Lagrange strain in the tensile direction (ε_{xx}) and lath packet boundaries (cyan). (b) Austenite orientation map with lath packets delimited in blue. Different strain layouts depending on crystallography and lath morphology are indicated.

We conducted the previous analyses by focusing on significantly strained areas. Still, large zones, just like ROI 3, remain undeformed. It was already stated that plastic deformation initiates in austenite (Section 3.2). However, initiation is not homogeneous in the specimen volume meaning that the ability of this phase to be “easily” deformed is relative to other austenitic regions. In particular, a good correlation exists between high values of macroscopic Schmid factor in austenite and deformed areas. Figure 3.35 highlights the visible match between the two observables on the ROI 3. The longitudinal strain map (Figure 3.35 (a)) is cut in half. The two vast lath packets at the top right-hand corner of the image display high resistance even though their austenitic phase ratio seems high. Conversely, the bottom left-hand corner is highly strained. The two extreme strain levels are in accordance, respectively, with low and high Schmid factor values (Figure 3.35 (b)). This may imply in the present case that lath clusters may be homogenized as grains whose strength is associated with austenite crystallography. Since the lath packet size is consistent with the specimen dimension, local stress is essentially uniform, and the computation of the Schmid factor is a reliable estimate. Consequently, the latter is a relevant criterion for plasticity initiation in the unaged material.

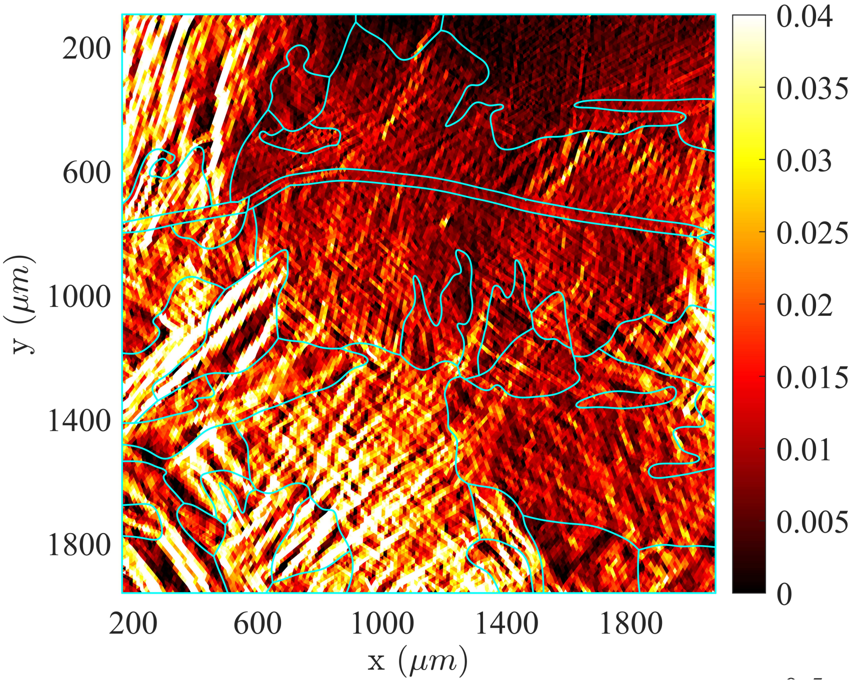

(a)

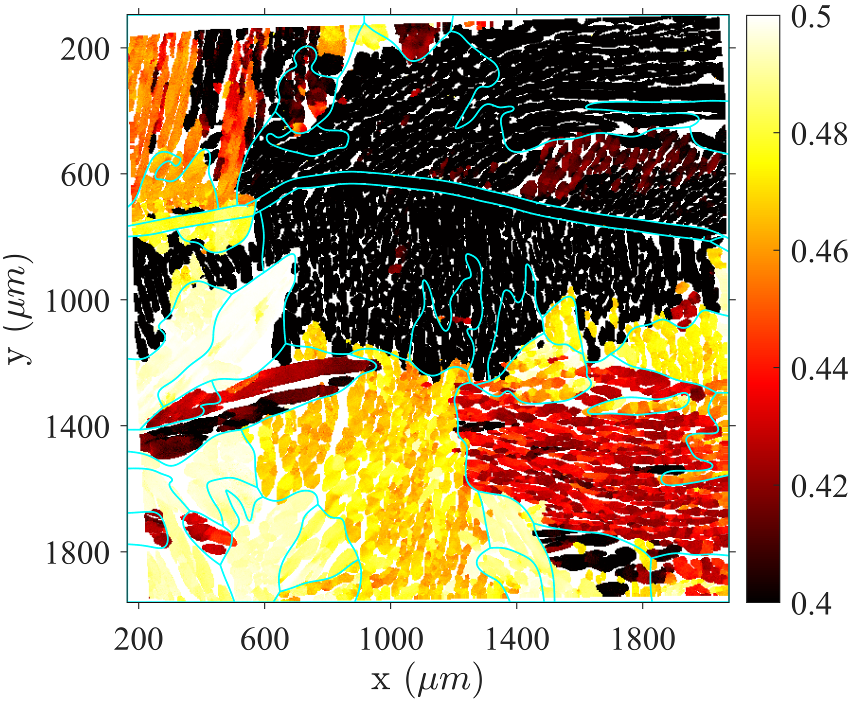

(b)

Figure 3.35: Correlation between strain localization and macroscopic Schmid factor in the as-received CF8M. (a) Green-Lagrange strain in the longitudinal direction (ε_{xx}). (b) Maximum Schmid factor for the $\langle 111 \rangle_\gamma$ direction considering uniaxial stress.

In general terms, crystallography and laths morphology dictate the unaged CF8M tensile behavior. The austenite crystallography provides a good insight into lath cluster resistance in agreement with the large γ-volume fraction. Strains predominantly manifest themselves in the form of bands whose distribution and orientation result from the lath morphology (*i.e.*, α-γ orientation relationship) relatively to the loading direction. Depending on the local configuration, the strain distribution is driven either by the lath morphology (loading direction close to the lath normal) or by slip plane directions in the two phases (shear strain state in both phases). However, the long-term resistance may differ for the two cases at high strain levels since the latter configuration generates more localized strains in ferrite. The last point has not been investigated as considerable out-of-plane displacements detrimental to DIC measurements accuracy arise at high strain levels. Likewise, proximity between loading and laths normal/growth directions is not quantified. Yet, we may address/discuss all these points with the help of a consistent model.

3.3.3 Aged for 1000 h at 350°C

The first striking feature of the entire ε_{xx} strain map (Figure 3.36) measured on the specimen aged for 1000 h at 350° C is the presence of multiple isolated and large strain bands corresponding to former α-grain boundaries. At this stage, it is unclear whether their onset is due to the specific crystallography/morphology of the specimen or an aging effect. Still, multiple occurrences may be favorable to the latter hypothesis. Furthermore, the strain patterns found in the as-received sample appear more disrupted, even though some similar microstructure morphologies are found. Although no apparent Schmid factor discrepancy was found, a higher frequency of barely deformed clusters is also visible.

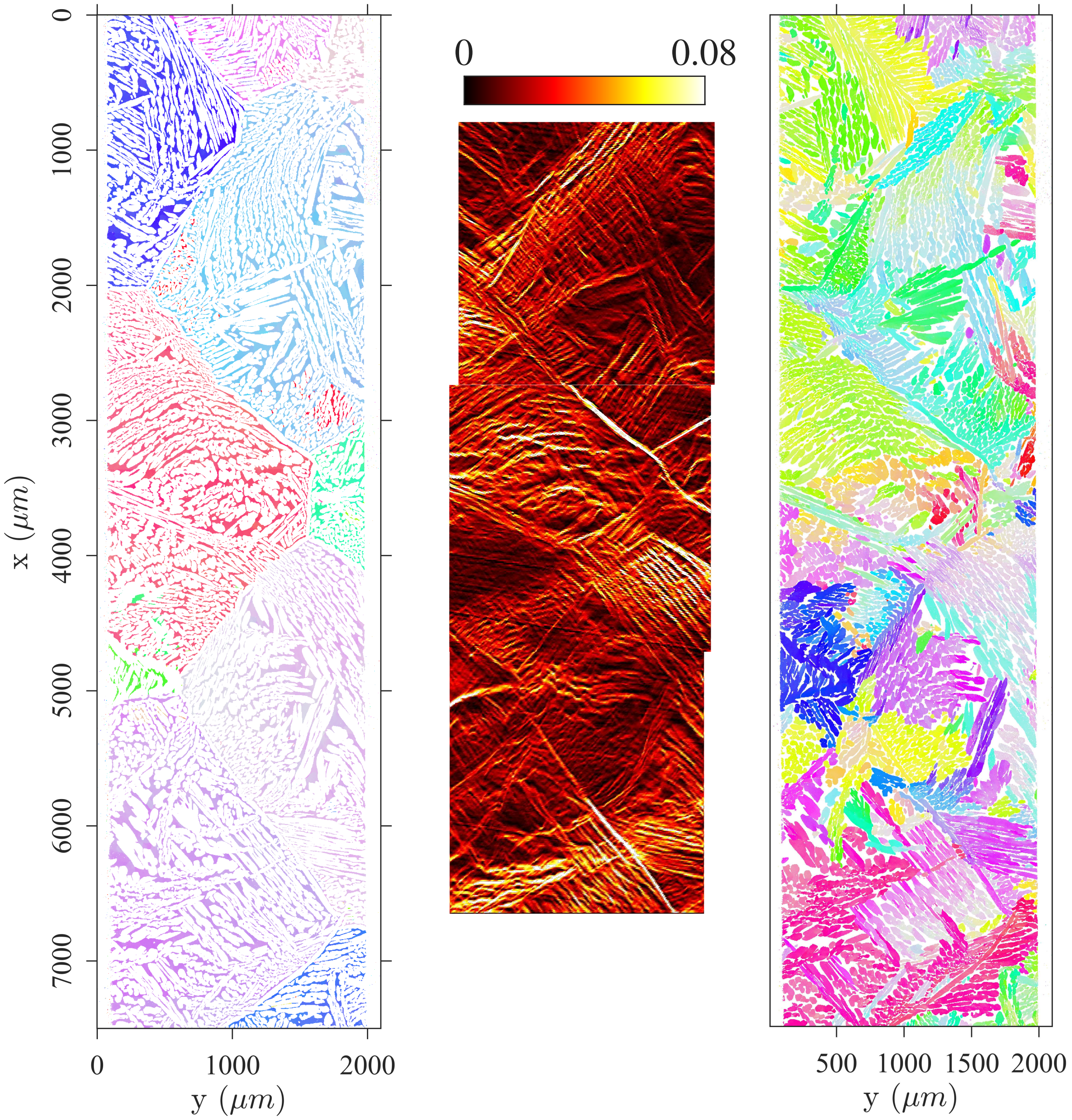

Figure 3.36: Overview of the 1000 h/350° C aged (P2) state. From left to right: ferrite orientation map, ε_{xx} strain field at 2.5% macroscopic strain, and austenite orientation map. The loading direction is vertical.

Equivalently to the previous unaged specimen, the strain field is in excellent agreement with measured crystallographic and morphologic orientations. We retrieve the marked layering at the lath scale following the iso-stress layout and the crossed slip strain bands of the second layout. These patterns are still homogeneous at higher scales. Consequently, the lath packet boundaries shown in Figure 3.37 (a) provide a good discretization of the different local strain layouts. Therefore, the observed strain bands still follow the lath morphology (*e.g.*, Figure 3.37 (b) case ①) or slip planes from the two phases depending on the configuration of the packet with respect to the load direction. The corresponding strain levels in bands are low as compared to the unaged state, whereas former α-grain boundaries (Figure 3.37 (b) case ②) reach very high values. Similar strain values were not observed in the as-received specimen. Figure 3.37 (b) case ③ constitutes a rare observation as the microstructure results from a nearby triple junction of α grains. However, clues and knowledge of the microstructure allow us to understand it. There are remnants of different ferritic orientations found on the α-orientation map (sparse green pixels from Figure 3.36 at x = 4200 µm and y = 200 µm). Moreover, the child phase grows with more constraints close to triple junctions, the lath morphology is no longer obeyed, and austenite looks disordered. No indication of lath-oriented strain bands is found at this location. Instead, we observe bands oriented in $(111)_\gamma$ slip planes. The previous comment further confirms that the grain morphology is decisive in the resulting strain pattern.

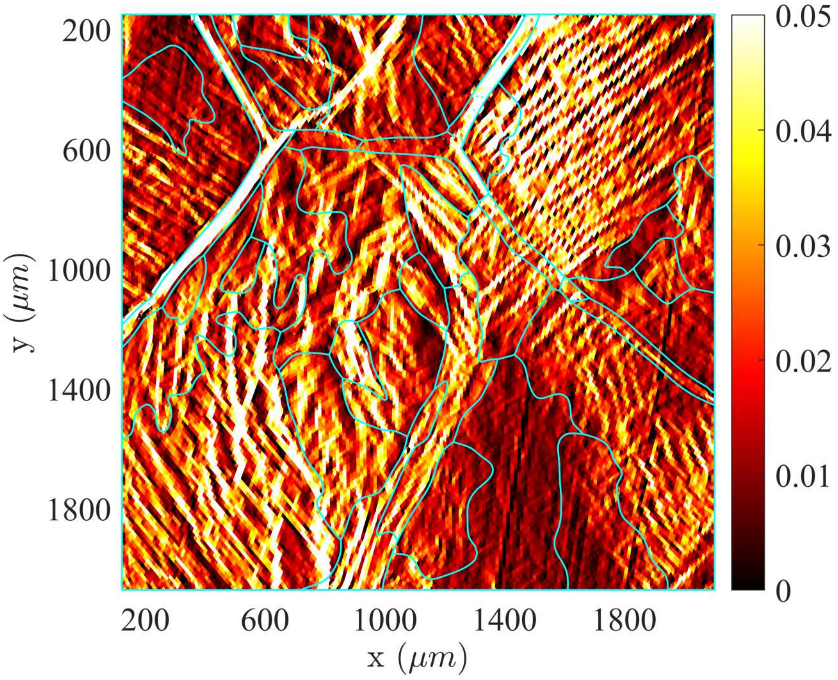

(a)

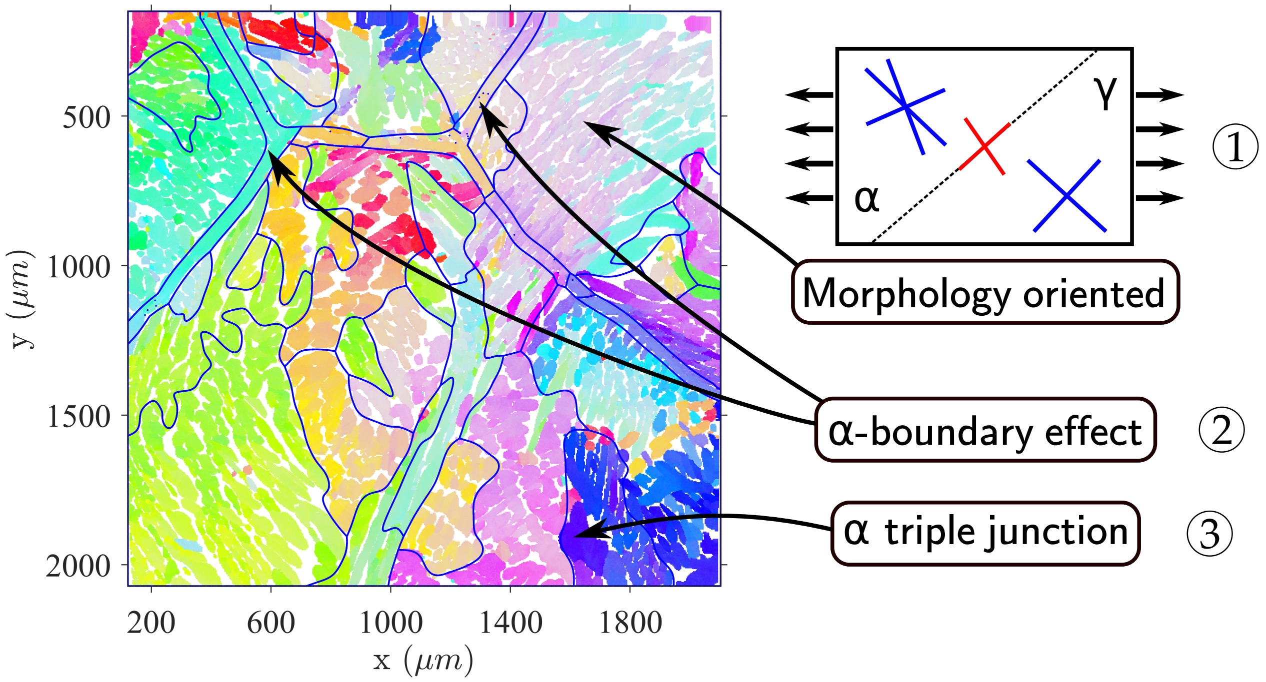

(b)

Figure 3.37: Microstructure correlated deformation mechanisms in the material aged for 1000h at 350° C (P2 ROI 2). (a) Green-Lagrange strain in the longitudinal direction (ε_{xx}). (b) Austenite orientation map and schematic view of observed strain bands (red lines) as compared to morphology (dashed line) and closest slip plane traces (blue lines) in the two phases. Other microstructure induced strain distributions are highlighted.

Aside from the appearance of strain bands at former ferritic grain boundaries, strain patterns inside lath clusters express similar deformation mechanisms as unaged specimens.

The slightly higher hardening (Figure 3.30) is thus probably related to the strain distribution between the two phases. However, our measurement resolution makes measuring accurate strains in the two phases difficult.

3.3.4 Aged for 10000 h at 350° C

The last *in situ* tensile test was carried out on an aging state corresponding to a long-term operation. The observation of local deformation mechanisms on this specimen in Section 3.2.2.2 unveiled severe and localized slip activity in ferrite. The strain field resulting from highly embrittled ferrite is displayed in Figure 3.38. A few confined areas are highly strained. Strain bands rapidly reach high values and concentrate at some former α-boundaries. In particular, the boundary at x = 2200 µm forced the interruption of the tensile test as this single austenitic layer accommodated the whole plastic flow in further loading steps. The measured mechanical field, including the boundary mentioned above, is depicted in Figure 3.39. The longitudinal component of the Green-Lagrange tensor in Figure 3.39 (a) maps the strain distribution around this boundary. The observations made for previous specimens regarding the morphology of strain bands persist. Figure 3.39 (a) cases ① and ③ illustrate the standard strain layout previously described. However, the α-boundary concentrates the majority of longitudinal strain (Figure 3.39 (a) case ②) of ROI 1.

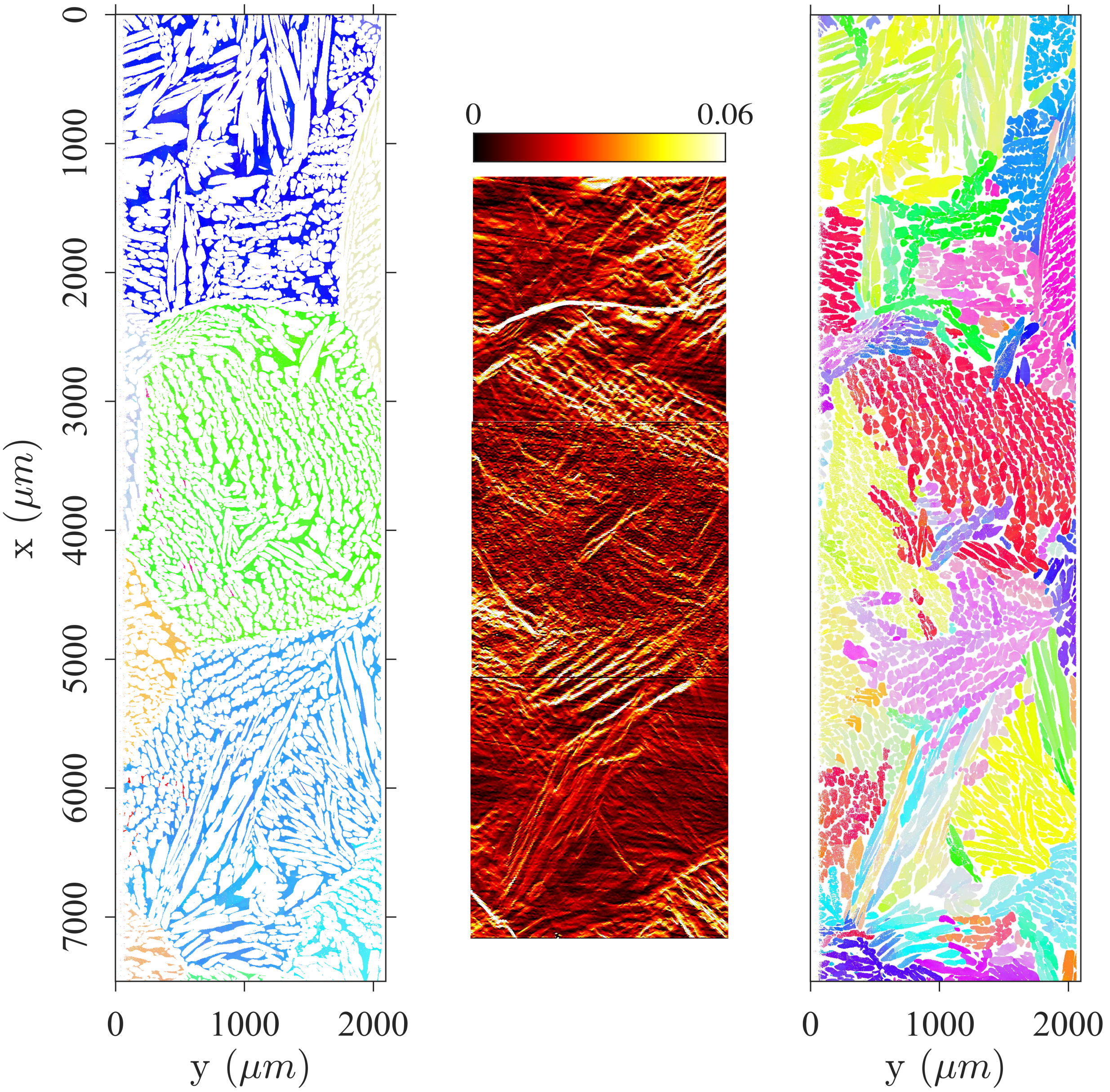

Figure 3.38: Overview of the 10000 h aged (P4) smaple. From left to right: ferrite orientation map, ε_{xx} strain field at 2% macroscopic strain, and austenite orientation map. The loading direction is vertical.

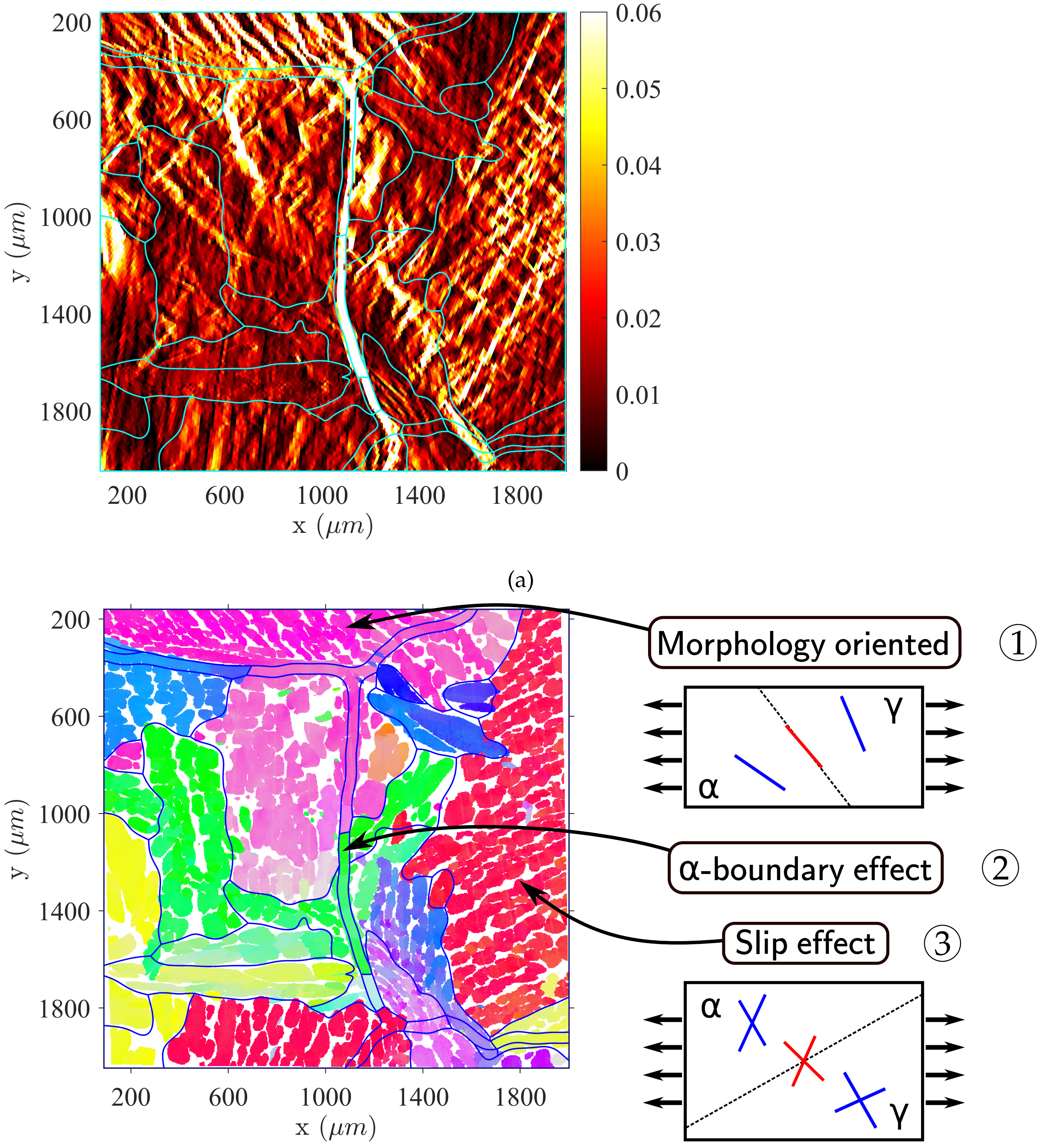

(a)

(b)

Figure 3.39: Microstructure correlated deformation mechanisms in the material aged for 10000h at 350°C (P4 ROI 1). (a) Green-Lagrange strain in the tensile direction (ε_{xx}). (b) Austenite orientation map and observed strain bands (red lines) as compared to morphology (dashed line) and closest slip plane traces (blue lines) in the two phases.

Apart from the standard layouts, significantly deformed lath clusters are dispersed compared to the unaged case, and isolated strain bands appear more frequently. Such bands appear not as sharply defined as those arising from austenite slip activity and result from the sudden activation of slip (planar or discontinuous) in ferrite. This phenomenon prevents homogeneous strains in other lath packets. The high constraints dissipated by the activation propagate bands across laths. The highly localized property of slip in ferrite induces such a small displacement jump that they cannot be resolved everywhere with the present measurement technique. A final point concerns the growing importance of ferrite crystallography with aging, which may explain the selection of deformed lath packets. While the austenite volume fraction predominantly imposed the plastic strain activation for the as-received material, the embrittled ferrite orientation controls the susceptibility to deformation of lath clusters. For instance, Figure 3.40 illustrates this effect at an incoherent grain boundary separating two distant ferritic orientations. As described in Section 2.4.3.2, γ-orientations growing in place of the former α-grain boundary are preserved on both sides. Only the morphology is adapted as a consequence of the non-standard orientation relationship on the incoherent side. Hence, austenite orientation-guided plasticity, as described in Figure 3.35, would result in intense strain bands on both sides. However, Figure 3.40 (b) case ① shows a separation of strain intensity on the two sides of the α-boundary. One could argue that the different morphology layout due to the incoherent boundary growing mechanisms explains this difference. However, such differences are not meaningful in the case of the as-received specimen where austenite crystallography is principally driving slip activity (Figure 3.35).

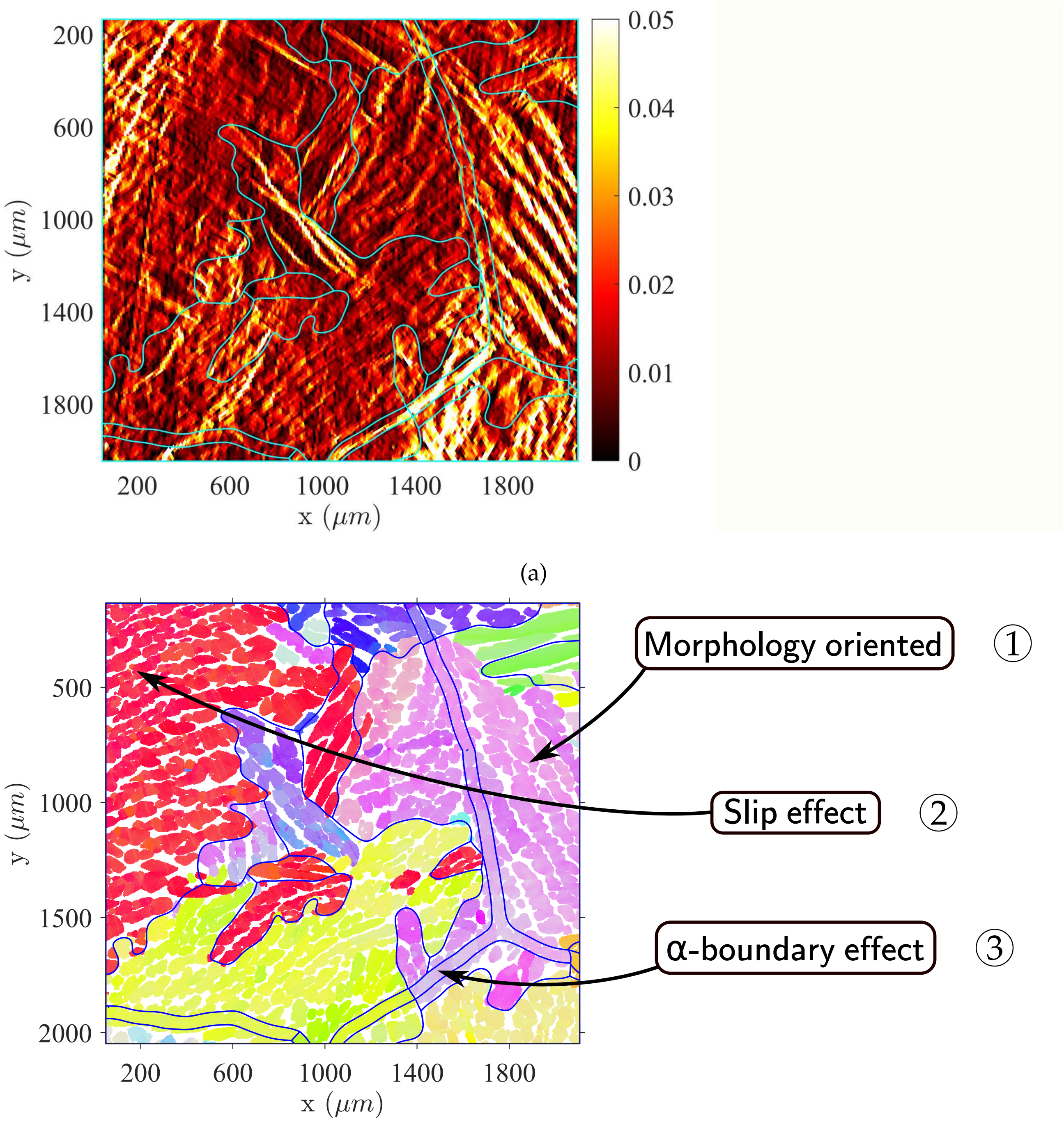

(a)

(b)

Figure 3.40: Microstructure correlated deformation mechanisms in the material aged for 10000 h at 350°C (P4 ROI 2). (a) Green-Lagrange strain in the tensile direction (ε_{xx}). (b) Austenite orientation map and observed strain mechanisms.

3.4 Discussion

The measured strain maps revealed the deformation mechanisms at lath packets and ferritic grain scales. The strain distribution in both phases is undoubtedly conditioned by the crystallography and morphology of the two phases. The austenite microstructure mainly drives the local strain distribution for the as-received material. Hence, many packets are deformed, and the strain is diffuse over the whole specimen. Ferrite properties are likely to play an increasing role with aging. It follows that more parameters control the susceptibility of lath packets to be highly strained. Although the analysis of the measurements did not explicitly emphasize new parameters, α-phase Schmid factor, slip transmission between the two phases, and local volume fraction may intuitively take part in the strain mechanisms of the aged material. The former ferritic grain boundaries also showed high slip activity and localized strains for the two aged states.

In light of the crystal plasticity mechanisms at the origin of the measured strain bands, deformation is homogeneous in austenite laths, resulting in strain bands consistent with lath morphology. Some more complex layouts forcing high slip activity in ferrite result in thinner bands that are more difficult to resolve with DIC, even though they seem in agreement with slip plane traces. The fact that aging is prone to triggering more localized deformation mechanisms in ferrite makes understanding aging effects more uncertain due to poor statistical sampling of microstructure and strain states. Moreover, the interpretation of strain fields with EBSD images is limited at the lath scales regardless of the images resolution. The microstructure presents features at this scale that are inherently three-dimensional, and laths are reasonably well defined at an intermediate scale but not well apprehended locally. This ambiguous definition comes from the fact that “laths” are not strictly lath-shaped. It is then difficult to read the strain components of each phase as the measured bands may appear on small α/γ islets revealed in EBSD maps. In reality, they reflect the behavior of a coarser structure lying below. Figure 3.41 illustrates an irregular match between strain peaks and the austenitic phase map. While some alternation between high and low strains coincides with α-γ boundaries, other cases are not as clear. Low values may belong to ferrite insertions that are too small or undefined at this depth (because of the local globular aspect of the laths) but endows the same composite behavior nonetheless. The profile also emphasizes the difficulty of accurately resolving the strains in the ferritic phase at this scale, which hampers to highlight the role of aging on local strain distributions.

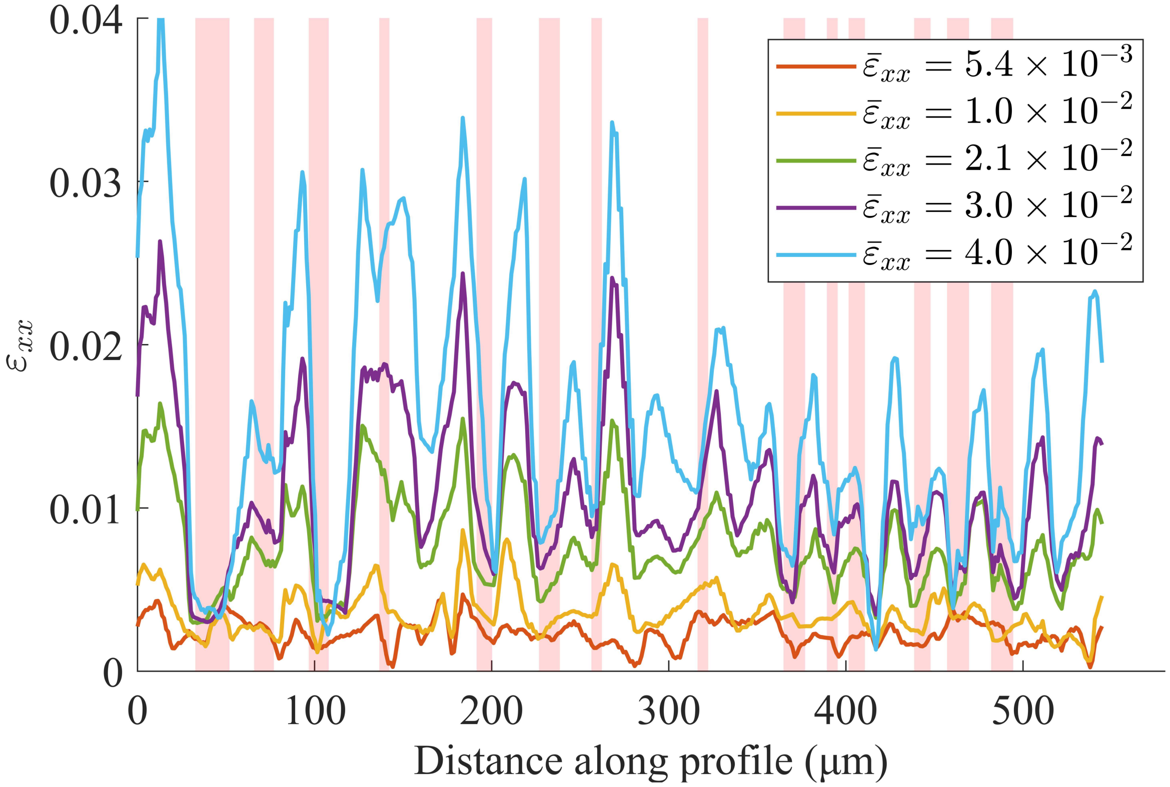

Figure 3.41: Evolution of a strain profile in the in-plane lath normal direction. The profile corresponds to Figure 3.37 (b) case ① lath packet. Areas corresponding to ferrite on the EBSD image are colored in red.

The difficulty in accurately correlating strain levels to spatial phase maps is even truer for the unaged state. Figure 3.42 shows the strain fields separated by phase for the unaged specimen. The strain is relatively diffuse compared to the aged case, as it is easily transmitted between the two phases at many locations. Part of the measured strain appear in the two phases (Figure 3.42 (a,b)). As a result, the precise strain distributions in the two phases are not representative with the current measurement resolution (Figure 3.42 (c)). However, a larger density of high strains in austenite are noted in agreement with the patterns observed in the field measurements. In the aged case, the full-field measurements offer an interesting spatial correlation (Figure 3.43). The contrast in behavior is stronger than in the unaged state. Thus, intense stresses appear early in the ferrite. Areas where thin ferrite laths are “pinched” between two austenite islets give rise to stress relaxation by the deformation mechanisms studied earlier. Some of the places where this mechanism has been observed are circled in blue in Figure 3.43 (a,b). This relaxation is visible as it propagates into austenite with a strain pattern typical of localized phenomena. Other thick austenite laths experience localized strains at the interface with ferrite. As seen in Section 3.2.2.2, it corresponds to a complex slip transmission that gives place to cross-slip. The particular case of aged specimen depicts larger ferrite laths than the unaged and 1000h/350° C aged states. The microstructure may be sensibly different because of the position of the specimen in the cast ingot. It follows that strains in ferrite were more accurately measured in this particular case with the same measurement uncertainty. Figure 3.43 (c) highlights that strain levels reach undoubtedly higher values with aging.

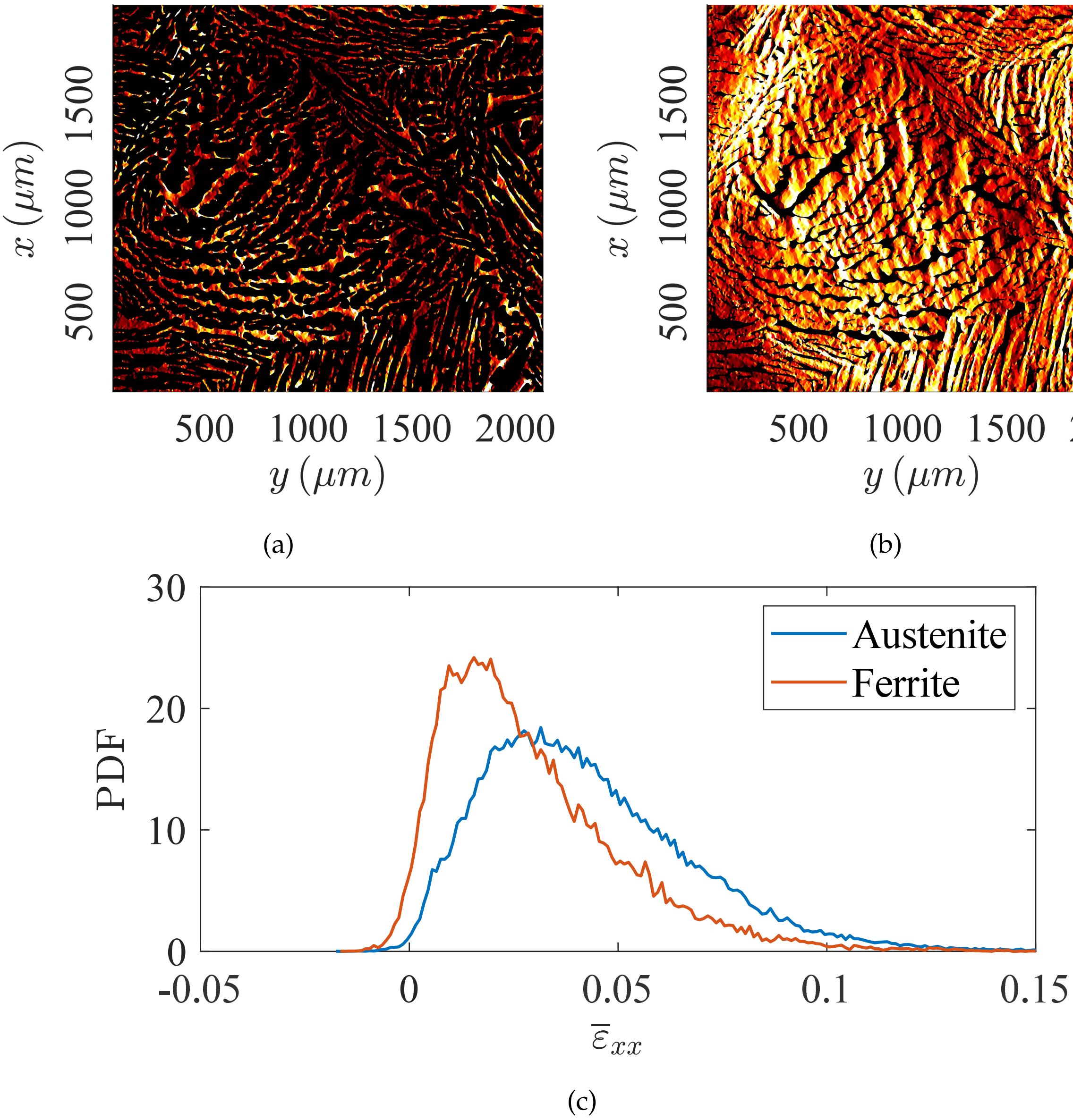

(a)

(b)

(c)

Figure 3.42: Strain partitioning between the two phases in the unaged state (P1 ROI 3). (a) Strain field at 4% macroscopic strain in ferrite. (b) Strain field at 4% macroscopic strain in austenite. (c) Strain Probability Density Functions (PDF) in the two phases.

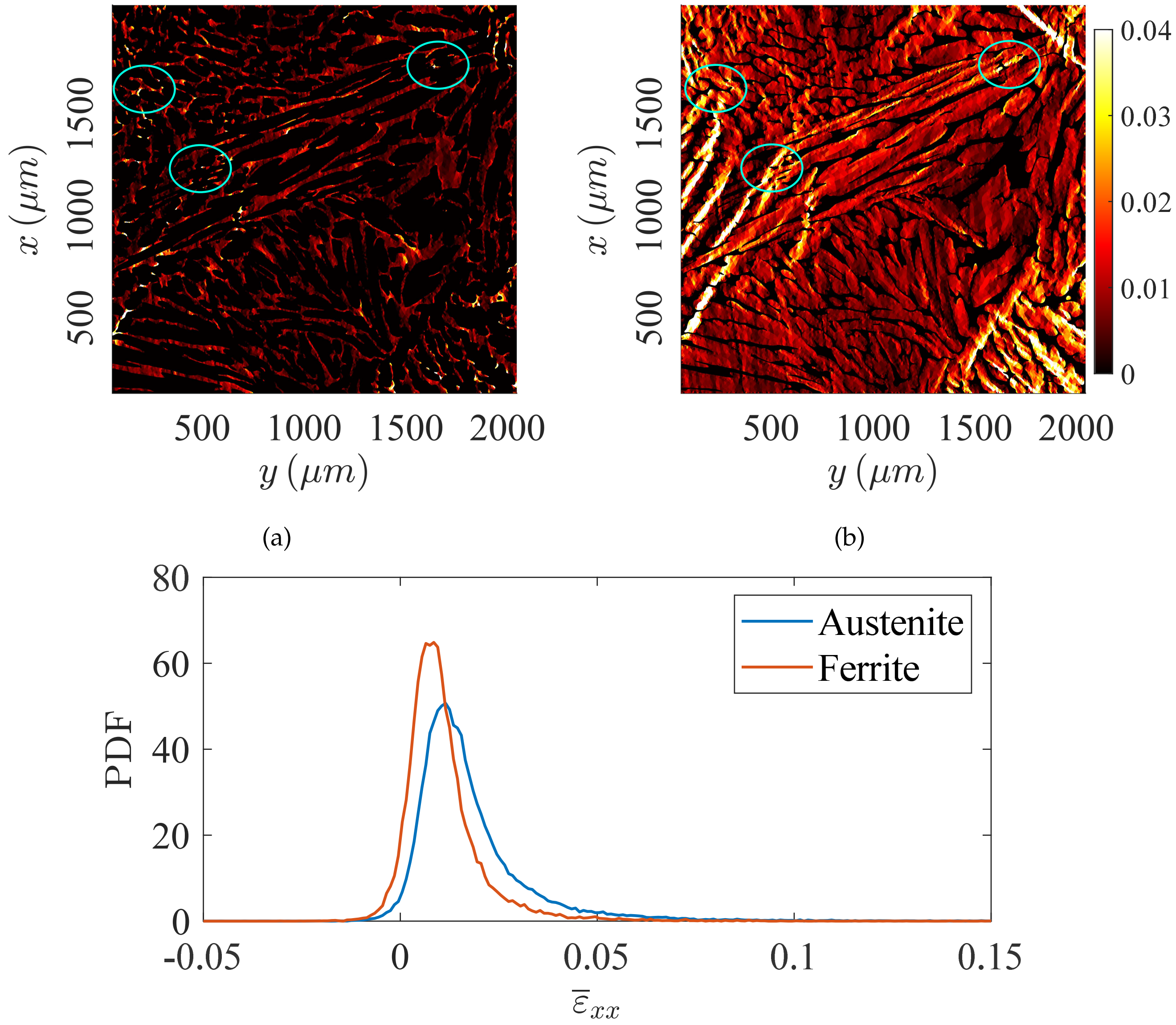

(a)

(b)

(c)

Figure 3.43: Strain partitioning between the two phases in the aged state (P4 ROI 3). Constricted ferrite islets where high stresses are presumably reached and then dissipated are circled in cyan. (a) Strain field at 2% macroscopic strain in ferrite. (b) Strain field at 2% macroscopic strain in austenite. (c) Strain PDF in the two phases.

Overall, the interlocked microstructure layout controls the strain levels in both phases. Since this layout prevents the deformation from a single phase alone, the slip activation gap between the two phases is essential in inducing strain localization. In the unaged material, the gap is small; thus, the strain distribution is diffuse because it can be accommodated in multiple locations. In the aged material, ferrite dislocation mobility is restrained. Consequently, part of the macroscopic strain is transferred to austenite compared to the unaged state, and deformation in ferrite is more and more localized. Hence, the presumably higher stress in ferrite should lead to earlier localization, as shown in the previous figures (3.42

and 3.43). The statistics resulting from large strain mappings are deprived of spatial components of measured strains. They show that spatial correlation is critical to understanding the strain levels in the two phases and apprehending aging. Figure 3.44 points out that these distributions are well-defined and smooth at all loading steps. The distributions in the aged state seem to widen more rapidly with increasing macroscopic strain increments. The bifurcation of strain distributions follows loading increments, but the asymptotic standard deviation change rate will likely increase with aging time (Figure 3.45). However, the increase is barely sensitive, and each phase measured individual strain change does not include valuable data concerning the lath morphology acquired in Section 2.4. For all these reasons, interpreting the measurements alongside a microstructure model would add a significant contribution. In the following, such a model is proposed to better understand the mechanical fields at play and their change with aging.

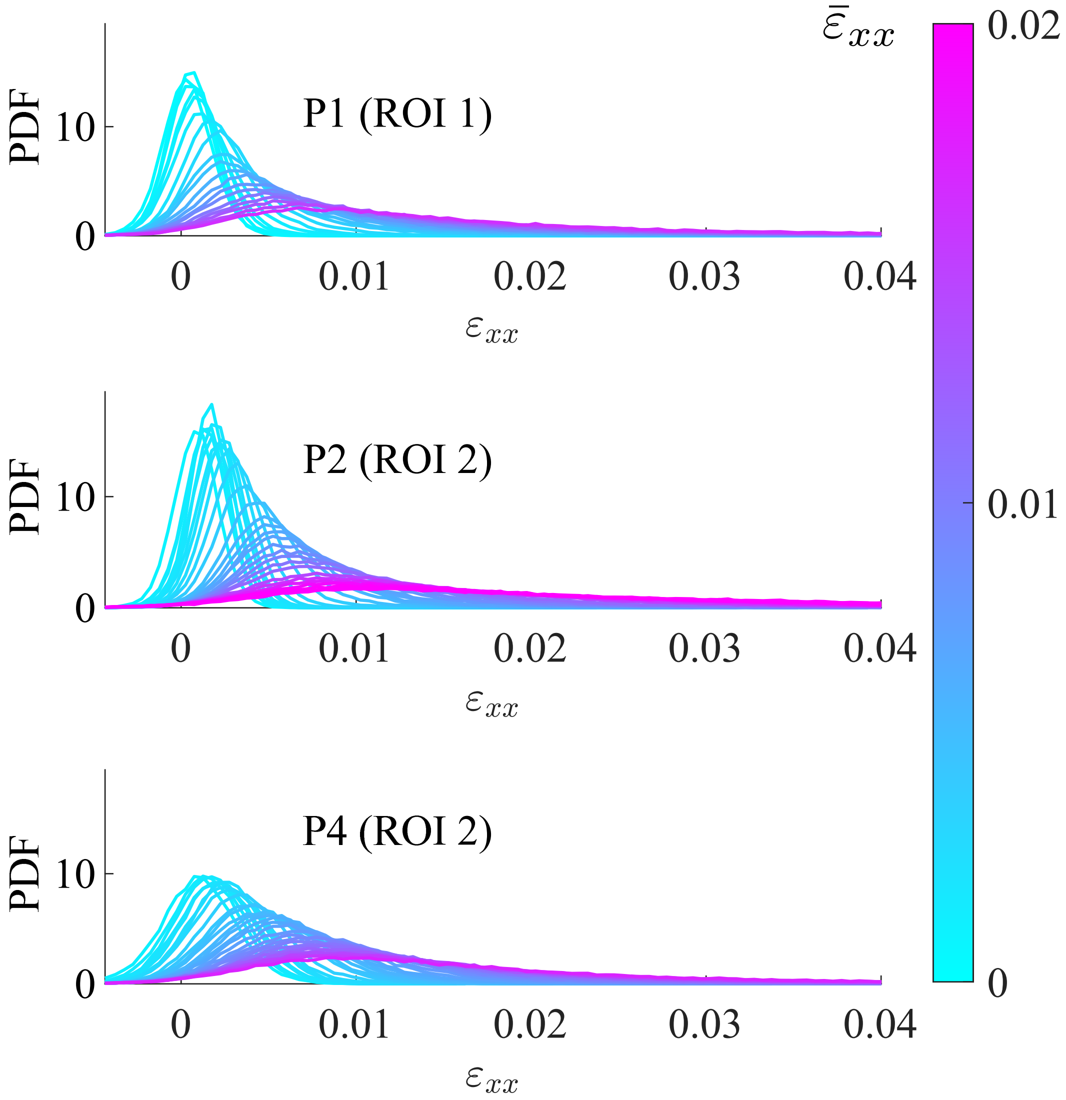

Figure 3.44: Evolution of the tensile direction strain distribution for the three aged states.

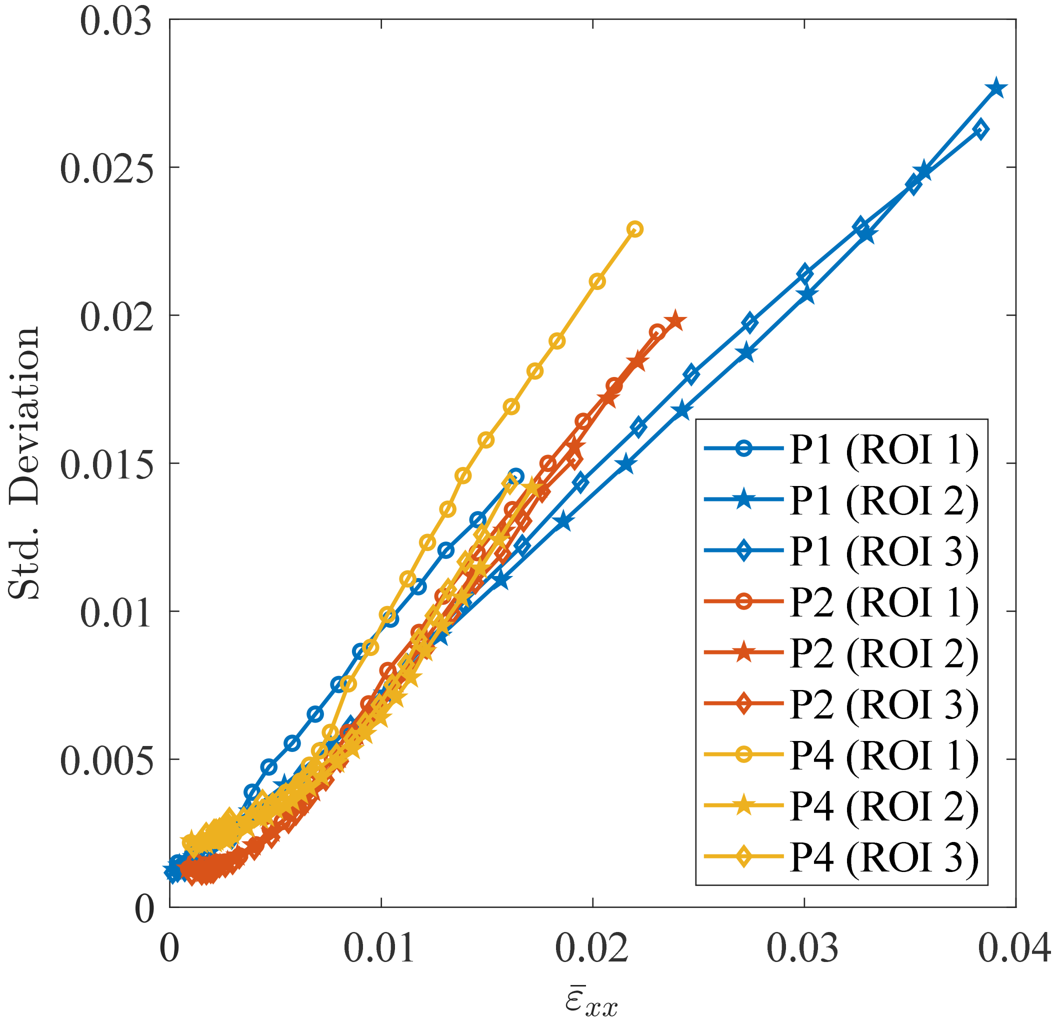

Figure 3.45: Evolution of the standard deviation of tensile direction strain distributions for all observed ROI.

Chapter 4

Modeling the mechanical behavior of CDSS

The following chapter deals with the derivation of a mechanical model aiming at accurately describing the mechanical behavior of CDSS. Important microstructural scales detailed in Chapter 2 are to be introduced in the model to describe mechanical fields in each phase correctly. The role of phase morphology on local responses has been investigated using full-field measurements in Chapter 3. We have shown that combining unitary inelastic deformation mechanisms in each phase with microstructural features gives rise to complex strain fields. The model should thus include the crystal plasticity effects. In particular, the impact of crystal orientations and their relationship effects on mechanical fields is part of the modeling approach. It is thus expected that a faithful definition of monocrystalline behavior combined with a consistent description of the microstructure morphology will provide realistic results. Correspondingly, the approach is a straight continuation of observations from preceding chapters. The general workflow taking into account currently available experimental data and the microstructure description of Chapter 2 is given in Figure 4.1. First, the field measurements are used as basis to estimate, “at best”, the constitutive parameters. A primary objective is to investigate the effect of thermal aging on these parameters. The laths scale is considered to estimate them. Thus, an upscaling combining a finite element unit cell and a mean-field homogenization method is presented. It provides fields that can be compared with the lath packet scale measurements. To predict the macroscopic response of CDSS, a last upscaling from lath packets to millimetric volumes is introduced. This scale is where the ferritic grain network and their subdivision into lath packets are described. We have chosen to explicitly model their geometry based on the present understanding of the microstructure formation process. This way, the relevance of this complex layout and all underlying parameters are expressly assessed.

The first part briefly introduces basic formulations of crystal plasticity laws to choose the most relevant one to the present case. Parameter identification methods for this type of constitutive law are subsequently presented in the same manner. The selected formulation was implemented in code_aster and written within Mfront, a code generator dedicated to constitutive laws [Hel15]. A methodology to identify parameters of the chosen laws using full-field measurements is presented in light of literature reviews and constraints linked to available data. The different steps of the two-scale homogenization from laths to the millimetric α-grains layout are discussed. The approaches considering essential microstructural and mechanical parameters are then explained. Last, we propose a workflow to generate synthetic CDSS microstructures based on the knowledge acquired for the study. The simplified representation is meant to provide a tool enabling the analysis of microstructural properties in mechanical fields.

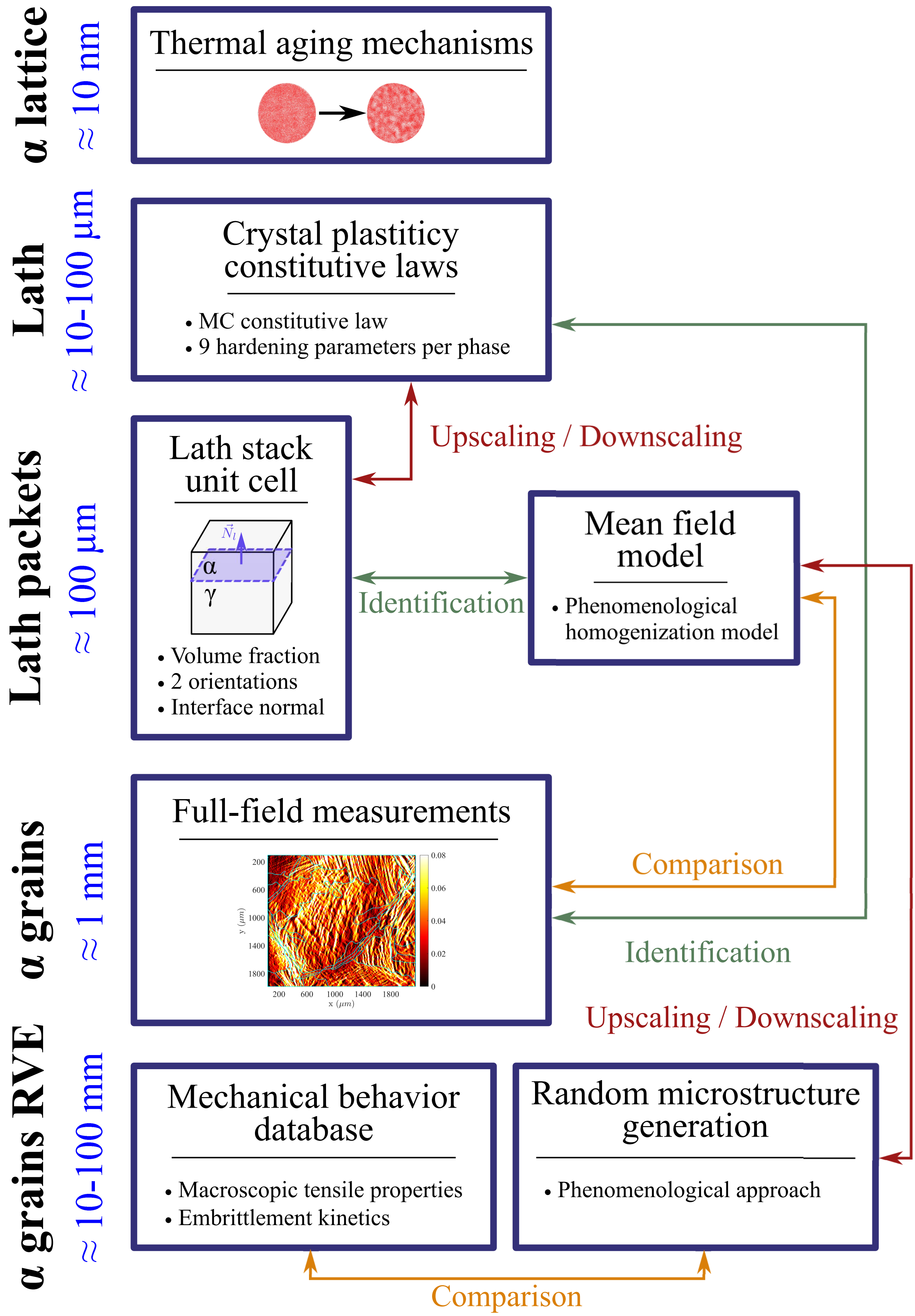

Figure 4.1: Global workflow for comparing experimental and simulated mechanical fields at all microstructural scales.

4.1 Homogenization of polycrystals

4.1.1 Local approaches to crystal plasticity modeling

4.1.1.1 Single crystal

Displacement fields in polycrystals result from the interplay between each crystal mechanical bevior as well as structural effects due to geometrical grain entanglement. These two aspects should be conveniently defined to build a model consistent with experimental observations. Descriptors for the grain layout are most often specific to the material composition and history and were detailed for CDSS in Chapter 2. The description of crystal deformations is more generic. A unified thermomechanical framework to model crystal elasto-viscoplasticity is already available to develop constitutive laws [For02]. We introduce basic principles for describing mechanical fields hereafter and give the corresponding hypotheses accordingly.

Elasticity

Deformation in a single crystal is generally decomposed into elastic and plastic parts. The elastic response of crystalline systems is significantly but the number of parameters describing this behavior is conveniently reduced according to the crystal symmetry group. In the case of cubic systems, to which BCC and FCC structures of austenite and ferrite belong, the Voigt stiffness tensor is expressed with three independent constants C_{11}, C_{12} and C_{44} (in the orthotropy basis)

$$\boldsymbol{C} = \begin{bmatrix} C_{11} & C_{12} & C_{12} & 0 & 0 & 0 \\ C_{12} & C_{11} & C_{12} & 0 & 0 & 0 \\ C_{12} & C_{12} & C_{11} & 0 & 0 & 0 \\ 0 & 0 & 0 & C_{44} & 0 & 0 \\ 0 & 0 & 0 & 0 & C_{44} & 0 \\ 0 & 0 & 0 & 0 & 0 & C_{44} \end{bmatrix} \tag{4.1}$$

Rate independant plasticity

Plasticity in monocrystals results from the motion of dislocations [Tay34, Oro40, Suz91] at the atomic scale. At the grain scale, dislocation motions produce slip or twinning [Gro63, Jao65, Mar99] under sufficient stress. Since slip is observed in many polycrystals as the main plastic deformation mechanism, considerable efforts were invested to model polycrystals from the description of this phenomenon. The occurence and characteristic properties of observed slip plane traces is dependent on atom arrangement, material history and local stresses. Slip plane trace orientations correspond to specific directions in the lattice frame along which dislocations "easily" move, thereby creating the relative motion of atoms on either side of the plane. These crystal slips can elegantly be cast into a continuum mechanics formalisms. Phenomenological models aiming to describe displacement fields resulting from crystal plasticity subsequently emerged. The basic concepts are presented hereafter to derive a convenient framework for CDSSs.

The driving force for dislocation in a given slip system of the family $\boldsymbol{S}$ depends on the resolved shear stress τ_{RSS} *i.e.*, the tangential stress applied on the corresponding crystallographic plane. The shear component on each system is deduced from the local stress tensor $\boldsymbol{\sigma}$ and crystal orientation

$$\tau^i_{RSS} = \boldsymbol{\sigma} : \boldsymbol{\mu}^i \tag{4.2}$$

where $\boldsymbol{\mu}^i$ is the Schmid tensor describing the projection on the i-th slip system of $\boldsymbol{S}$

$$\boldsymbol{\mu}^i = \frac{1}{2}\left(\boldsymbol{m}^i \otimes \boldsymbol{n}^i + \boldsymbol{n}^i \otimes \boldsymbol{m}^i\right) \tag{4.3}$$

$\boldsymbol{m}^i$ and $\boldsymbol{n}^i$ are respectively the slip direction and slip plane normal for the i-th system. The onset of plasticity in a crystal roughly corresponds to a threshold for the resolved shear stress on the corresponding slip system, τ_{CRSS} below which dislocations hardly moves and the behavior is elastic. Using the previous equations, this assertion stipulates the existence of a threshold, the critical resolved shear stress τ_{CRSS} under which slip does not occur and the crystal behavior is elastic. This simple threshold model, however, is somewhat limited by the thermal activation that allows a small plastic "viscous" flow. Additionally, in a slowly varying stress field, all slip planes of the same orientation reach their threshold simultaneously. Thus the plastic flow problem inside a grain is not well defined. From experimental observations, we assume that the continuous approach coupled with the threshold model is sufficient to reproduce the observed behavior essentially explained by basic crystallographic observations and CDSS-specific grain entanglement measured by EBSD.

Work-hardening

Above a certain threshold, subsequent deformation increase contributes to the monocrystal work-hardening. Hardening of slip systems is complex because it originates from processes of dislocation development. Dislocations may interact between themselves, creating new ones and (latent hardening). Additionally, particles (interstitials, precipitates) or sub-grain boundaries may participate in the behavior evolution. A self-hardening can thus develop on unit slip systems from dislocation interaction with the subgrain structure. The latter is inherently a material dependant feature. Dislocation densities are the most relevant internal variables to describe monocrystal work-hardening, considering the two previous mechanisms. One may envision the complexity of locally describing each contribution, and kinetics are not always locally defined (*e.g.*, grain structure change is a global variable at the monocrystal scale).

Two modeling approaches for crystal plasticity behavior can be distinguished: *phenomenological* and *physics-based*. Both cases consist of expressing the slip rate $\dot{\gamma}^i$ for each system i as a function of the resolved shear stress τ^i_{RSS} on the same system. The two approaches differ in the choice of internal variables. Physical laws rely on hardening-based dislocation density growth while phenomenological laws provide a direct mathematical description of the slip rate. The local plastic strain rate tensor $\dot{\boldsymbol{\varepsilon}}_p$ is linked to the slip rate $\dot{\gamma}_S$ by

$$\dot{\boldsymbol{\varepsilon}}_p = \sum_i \dot{\gamma}^i \boldsymbol{\mu}^i \tag{4.4}$$

One of the first proposed laws accounting for hardening mechanisms expresses the resolved shear stress τ^l_{RSS} as a weighted contibution of all interacting slip amplitudes

$$\dot{\tau}^l_{RSS} = \sum_l h^{li} \dot{\gamma}^i \tag{4.5}$$

in which h_{li} are moduli of the matrix $\boldsymbol{h}$ describing slip self-hardening (diagonal terms) and latent-hardening (off diagonal terms). As previously discussed, this contribution is likely to evolve with increasing plastic strain but each interaction between systems and with the grain sub-structure will evolve in their own way. Consequently, laws describing $\boldsymbol{h}$ with various levels of sophistication exist from uniform empirical evolutions to non local dislocation density driven hardening.

4.1.2 Homogenization of crystal plasticity laws

The transition from monocrystal to upper scales involves homogenization techniques. These modeling techniques allow the properties of continuous media (“macroscopic” scale) to be determined, which are equivalent to the average mechanical fields of heterogeneous media (“microscopic” scale). An important hypothesis is to assume that a representative volume element (RVE), statistically representing the local behavior, can be derived. Such methods are naturally suited to predict the macroscopic behavior of composites and polycrystals while allowing homogenized fields to be relocalized. In this way, they provide an estimation of average fields from the smallest scale of the model. A fair solution is sufficient in most cases because numerous aspects have already been left aside. Multiple methods were developed to address the most complex cases. They are classified into two general categories: theoretically-derived and numerical methods. Hereafter, we briefly describe the two approaches to derive convenient scale transitions for CDSS.

4.1.2.1 Theoretically-derived approaches

One basic assumption of homogenization theory is that mechanical fields are homogeneous in each phase of the small scale model. Therefore, theoretically-derived approaches do not reproduce intra-phase inhomogeneities. The original homogeneization problem boils down to a Dyson-Schwinger equation, and the Eshelby problem is instrumental for a proper treatment of the local singularity of the elastic stress and strain Green functions. The Eshelby solution of the elastic inclusion problem in an infinite medium, reveals the remarkable property that stress and strain are homogeneous, and this result holds true for any ellipsoidal shaped inclusion. This solution provides a link between the macroscopic mechanical field $\boldsymbol{\Sigma}$ and $\boldsymbol{E}$ to microscopic ones $\boldsymbol{\sigma}$ and ε in the inclusion (respectively the stress and strain fields) through localization tensors $\tilde{\boldsymbol{A}}$ and $\tilde{\boldsymbol{B}}$

$$\varepsilon = \tilde{\boldsymbol{A}} : \boldsymbol{E} \tag{4.6}$$

$$\boldsymbol{\sigma} = \tilde{\boldsymbol{B}} : \Sigma \tag{4.7}$$

Such models can also implement simple shape description (*e.g.*, ellipsoidal inclusions) and texture. While the solution is relatively straightforward for purely elastic problems, non-linear behaviors require refinements of the localization law linking macroscopic to microscopic fields. Among noteworthy localization laws, Berveiller and Zaoui (BZ) [Ber78] proposed an extension of the self-consistent homogenization scheme to elastoplastic matrices. Compared to classical self-consistent schemes [Kro61, Hil65], the BZ formulation is more flexible and was thus applied by Bugat [Bug00] to determine the macroscopic behavior resulting from cross-shaped patterns used to model the α/γ interlaced behavior. However, the result of BZ homogenization is limited to simple monotonic loads.

4.1.2.2 Full-field homogenization

An alternative approach to predicting the macroscopic behavior is to resort to full-field simulations of the microstructure. Generally speaking, full-field homogenization relies on the explicit definition of the microstructure morphology used by a mechanical solver (*e.g.*, FE, or FFT based methods). There are many benefits in computing the mechanical response of an explicitly defined microstructure. First, complex experimental data can be included in the model. Grains morphology and spatial correlations are often too sophisticated to be described in a mean-field approach but can be implemented in the numerical model. Mechanical field distributions induced by specific RVE configurations are apprehended, and local properties can be characterized (*e.g.*, local incompatibilities between orientations). Microstructure generation techniques (tesselation of surfaces or volumes) were extensively developed to reproduce experimental observations [Mø92, Zha12, Wat98, Zhe22]. Moreover, microstructure characterized by experimental techniques, for instance EBSD, can directly be converted to geometrical models [Gus19, Dep20]. Dedicated experimental methods and tools were developed to capture full volume [Gro06, Guy16, Ech20, DeM21]. They partly solve the mechanical non-representativeness of the microstructure observed on a sample surface. However, these experimental procedures are limited because they require specific tools and a compromise between acquisition time and accuracy. Moreover, they are often destructive techniques preventing testing a characterized sample. Shi *et al.* [Shi17a, Shi17b] proposed a method to counter this disadvantage by acquiring in-depth microstructure data after performing the mechanical test. Nonetheless, it requires more precaution than classical *in situ tests* (*e.g.*, small plastic strains) and dedicated numerical methods.

4.1.3 Parameters identification using full-field measurements

Multiple factors contribute to the challenge of identifying crystal plasticity laws. Their formulation includes many parameters due to the phenomenology of slip mechanisms. In the simplest cases, many are related to coupled phenomena (*e.g.*, hardening interaction matrix). Identifying all parameters individually may require experimental setups that are out of reach for complex industrial alloys. For instance, testing a specimen with a small number of grains (monocrystalline or bicrystalline) is a great way of achieving configurations enabling for single parameter identification (*e.g.*, through a specific loading and specimen orientation to trigger a specific slip system) [Ber16b]. However, such specimens are undoubtedly restricted to materials with large grains size and complex experimental setups. Identification is often based on inverse analyses to overcome the difficulties associated with experimental setups or complex microstructure configurations. A wide range of experimental characterizations can be conveniently modelled using crystal plasticity constitutive laws while providing data relating to parameters value. These experiments often consist in miniaturizing more conventional tests like tensile [Gue14a, Shi18a], compression [Che19], bending [Hé06], torsion [Koi16] or indentation [Ren20] tests.

Using either full-field or mean-field simulations, parameter identification can be translated to an optimization problem aiming to match simulated fields to experimental measurements. Inverse analysis does not cope with an experimental setup relevance to identifying precise parameters nor the errors induced by a wrong choice of constitutive laws. Yet, it allows to exploit the dense data provided by mechanical tests followed with field measurements, potentially leading to approximate solutions. It also has invaluable additional merit in assessing its possible incompatibilities with the observed data. With these measurements, constitutive parameters can be estimated together with their uncertainties.

Considering the above comments, full-field measurements are a formidable and flexible tool to calibrate and validate constitutive law parameters. Displacement field measurements with DIC have been extensively used to successfully calibrate models in various thermomechanical frameworks [Var18, Ber17, Her19]. In the case of crystal plasticity, it was demonstrated that a successful identification methodology could be achieved in combination with *in situ* tensile tests inside an SEM [Hé06, Gue16, Shi18a]. However, some challenges remain regarding the influence of the underlying microstructure. Surface fields obtained from SEM images are influenced by the underlying microstructure [Gue14a], which is *a priori* unknown. Grains "extrusion" in the direction normal to the observation surface is often a very poor approximation with a large impact on the identified result. In some exceptional cases, materials display a columnar grain growth that allows for a trustful 3D morphological and crystallography representation [Zha08, Mon14]. In-depth grain layout can only be guessed or obtained *post mortem*. An indirect way of avoiding this effect is to design specific tests *e.g.*, ultra-thin specimen testing, but such a solution comes at the cost of precise and expensive setups [Ver22]. In the case of reactors pressure vessels, one of the most appropriate method was proposed by Shi *et al.* [Shi17a]. Under moderate plastic strain, the microstructure can be reconstructed using the standard FIB-EBSD technique after loading and backtracked to the undeformed state using FEM simulations and full-field measurements. Again, CDSS microstructures may complicate the process as large microstructural features require considerable amounts of material to be removed while smaller scales call for a high in-depth resolution. Moreover, let us add that in addition to the 3D microstructure, the simulation will require appropriate boundary conditions (either Dirichlet or Neumann) in 3D, which remain unknown, and should be somehow estimated in the identification process. This estimation was possible in the method proposed by Shi *et al.* [Shi17a] because the near perfectly plastic behavior allowed for simplifications to be made.

4.1.4 Proposed approach

Constitutive law

As seen in Section 3.2, plastic deformation in austenite FCC frame was consistently along $\{111\}\langle 110\rangle$ systems while multiple planes along $\langle 111\rangle$ directions for ferrite BCC frame were observed. Yet, a large majority of $\{110\}$ plane traces were experimentally observed. Above the scale describing slip bands in the two phases, strain field distributions were mostly interpreted from laths and ferritic grains morphology and resolved shear stress intensity (*i.e.*, Schmid factor). All these aspects are accurately embedded in the phenomenological description of crystal plasticity. Then, the Méric-Cailletaud [Mer91a, Mer91b] (MC) constitutive law implemented in MFront is expected to offer satisfactory descriptions at the considered scales. The MC formulation includes phenomenological constitutive equations while a Norton inelastic flow rule and a Armstrong-Frederick kinematic hardening law. Each slip system follows a hardening rule weighted by the interaction matrix coefficients. Hence, the slip rate on each system reads

$$\dot{\gamma}^i = \dot{p}^i \operatorname{sign}\left(\tau^i - cx^i\right) \tag{4.8}$$

with the cumulated plastic strain rate expressed with a unidirectional Norton law

$$\dot{p}^i = \left\langle \frac{|\tau^i - c\alpha^i| - r^i(p^i)}{k} \right\rangle_+^n \tag{4.9}$$

where $p^i = \int |\dot{\gamma}^i| dt$ is the equivalent plastic strain, k and n the Norton law parameters. Hardening on each slip system is coupled with the others

$$r^i = r_0 + q \left(\sum_l h^{li} \left(1 - e^{-bp^l}\right) \right) \tag{4.10}$$

where $\boldsymbol{h} = [h^{li}]$ is the interaction matrix, r_0, q and b the isotropic hardening parameters. The kinematic hardening is defined through the growth of the back-stress x^i

$$\begin{cases} x^i = c\alpha^i \\ \dot{\alpha}^i = \dot{\gamma}^i - d\alpha^i \dot{p}^i \end{cases} \tag{4.11}$$

Plastic deformation in the two phases is described by different slip systems (see Section 3.2.2). The austenite FCC lattice has a unique {111}<110> slip system. The interaction matrix between the twelve planes symmetrically equivalent to the $\langle 110 \rangle$, is described with six independent coefficients denoted h_i^γ for $i = 1, \ldots, 6$ [Man65]. Conversely, multiple slip systems are involved in BCC crystals. As a result, the interaction matrix complexity increases rapidly. For instance, the combination of the two principally reported slip systems in BCC crystals, {110}<111> and {112}<111>, having each twelve equivalent slip planes, leads to a 24 x 24 interaction matrix composed of seventeen independent coefficients [Mad04]. Experimental identification of these coefficients is challenging and this topic was mainly investigated with dislocation dynamic (DD) simulations [Que09, Mad17]. For simplification purposes, only the $\{110\}\langle 111 \rangle$ is first considered. The α-phase interaction matrix is then described with six coefficients h_i^α for $i = 1, \ldots, 6$.

Nonetheless, the capability of the phenomenological formalism to model austenite slip activity and the complex slip mechanisms of embrittled ferrite (*e.g.*, discontinuous slip) must be investigated. Little information is available in the literature regarding the interaction coefficients. This is because experimental identification is difficult, and the coefficients identified by DD are not directly comparable to the chosen model [Gue16]. In the limited data available, there is a strong dispersion. For example, the MC model coefficients in $\boldsymbol{h}$ are proportional to those in $\boldsymbol{a}$ (the interaction matrix of the DD-CFC model [Mon09]). Still, this proportionality relationship evolves with the dynamics of dislocations. Nevertheless, there is a remarkable correspondence at the initiation of plasticity and saturation of strain hardening [Gue16]. Still, the DD simulations seem to agree on a particular hierarchy between the interactions. Given the relationship between the interaction matrix for the two model types, this hierarchy applies to both $\boldsymbol{h}$ and $\boldsymbol{a}$ coefficients. In materials with FCC structure, the different data gives the inequality [Han12]

$$h_3^\gamma < h_4^\gamma < h_5^\gamma < h_6^\gamma \tag{4.12}$$

Note that except for h_5^γ, this hierarchy seems to be well respected by the identification proposed by Guery [Gue16]. The data are still less numerous for materials with a BCC structure in the literature. We can nevertheless note that some authors consider, based on DD calculations, that the latent strain hardening is preponderant on the self strain hardening and should be one or more orders of magnitude higher. It is, however, challenging to attest to the accuracy of these quantifications.

The interaction coefficients are nevertheless of significant importance in understanding the deformation mechanisms. From a numerical point of view, they condition the stability of crystal plasticity laws integration [Hil66, For98]. At high levels of plastic deformation, a bifurcation of the slip is sometimes observed. The bifurcation manifests by the localization of the plastic slip. A preferential system among all those initially activated is selected. Since the localization is sudden, the plastic strain level must be "caught up" by the remaining activated planes. We then observe a transition in which the apparent behavior is softening. This phenomenon leads to a localization of the strain and is strongly dependent on the model parameters. Forest [For98] notes that the latent hardening ratio (importance of latent hardening over self-hardening) controls its appearance and kinetics. The Norton parameters K and n also intervene insofar as the softening stage is damped only by viscous effects, without which the integration of such behavior would be impossible. If we refer to the values identified by Guery [Gue16] and those used by Shi [Shi18a] in their identification process, this ratio is globally higher than 1. It means that the phenomenon of plastic bifurcation is likely to appear.

An initial set of parameters is required for the first calculations. Despite the different chemical compositions, the parameters identified by Guery [Gue16] and Shi [Shi18a] for austenite and ferrite respectively using full-field measurements are assumed to provide a good approximation. They are reported in Table 4.1. Note, however, that Shi [Shi18a] used Guilhem [Gui11] parameters for the interaction matrix. These parameters correspond to an austenitic steel, while the material in Shi's study is a ferritic alloy. Shi [Shi18a] identified the strain hardening parameters r_0, q, and b, from this initial data set without including $\boldsymbol{h}$ in the identification process. It raises the question of how representative $\boldsymbol{h}$ is in this case. However, identifying r_0, q, and b only allowed him to obtain a satisfactory result in his case. The fair agreement may also reflect a low sensitivity of measured mechanical fields regarding $\boldsymbol{h}$ components.

Table 4.1: Initial sets of constitutive parameters for the Méric-Cailletaud law.

Elastoplasticity parameters

	E (GPa)	ν	G (GPa)	n	k (MPa.s$^{1/n}$)	c (MPa)	r_0 (MPa)	q	b	d
α (From [Shi18a])	223	0.35	84.6	12	20	10400	170	30	12	494
γ (From [Gue16])	194	0.3	74.6	10	25	10400	38	162	1.57	494

Interaction matrix coefficients

	h_1	h_2	h_3	h_4	h_5	h_6
Interaction nature	Dipolar	Coplanar	Edge	Collinear	Asymmetrical junction	Symmetrical junction
α (Chosen from [Shi18a])	1	1	0.60	2.60	1.60	12.3
γ (Identified in [Gue14a])	1	1.64	0.10	2.60	0.87	12.5

Homogenization approach

In light of the macroscopic strain maps from Chapter 3, distinct microstructures scales unveiled in Chapter 2 seem to make sense from a mechanical point of view. Assuming that these scales can be individually homogenized, a multi-step mean-field model is highly desirable to compute the macroscopic behavior as it would drastically lower computational costs. Two-step procedures involving nested mechanical homogenizations were already conducted in composite materials [Fri06]. The basic idea of the envisioned two-step homogenization is to decompose the RVE into substructures that are individually homogenized (*i.e.*, extracting homogeneous properties) with a self-consistent scheme. Such an approach appears in accordance with the hierarchical description of CDSS microstructures and is appropriately developed in the Ph.D. dissertation of Tsekpuia [Tse22].

Assuming the relevance of the mean-field homogenization approach still necessitates the validation of "microscopic" fields prediction. We demonstrated in Chapter 3 that they are not easily obtained experimentally because of the microstructure. We have chosen to first rely on a full-field approach explicitly including the different scales and their properties to bridge the gap between the RVE behavior and the "mesoscale" that has been characterized with *in situ* tests. We use EBSD maps to provide a model, including a detailed description of microstructural features. This model is expected to provide a sufficiently accurate description for identifying the two sets of parameters at the lath scale. From the schematic description of the laths layout conducted in Chapter 2.4, it is proposed to introduce a simple laminated crystalline composite to perform the scale transition from individual laths to lath packets.

The effective model will be implemented in upper scales employing a standard homogenization procedure. A second scale transition from lath packets to the millimetric ferritic grain network will be carried out. In the most recent study, Bugat [Bug00] introduced an intermediate scale between the macroscopic response and the laths close to the proposed layered cell. The effective behavior at this scale was afterward homogenized inside a self-consistent scheme assuming a random frame orientation. Therefore, the spatial extent of ferritic grains, the geometry of laths packets and the thin austenitic layer at primary grain boundaries were not considered. In light of experimental full-field measurements, we believe that the previous properties should be introduced. A full-field approach using a detailed description of the microstructure is deemed necessary. Accordingly, we derive a representative microstructure generation algorithm from the understanding of its generation process in the last section.

Identification procedure

Performing constitutive law parameter identification requires selecting relevant observable, simulated data and a minimization scheme. The measured and simulated data must be adapted to provide sufficient sensitivity to the constitutive parameters. The minimization scheme offers the best approximation, *i.e.,* the set of parameters with minor uncertainties. The present material microstructure complexifies experimental and simulated data choices. Due to its multi-scale aspect, average and microscopic mechanical fields are required, regardless of the chosen identification method, to compare the model's predictions at all scales. Stable trends for average mechanical properties in CDSSs are only obtained for very large specimens that are simply not available [Lat18]. Large-scale averaging is also detrimental to sensitivities to crystal plasticity parameters. Conversely, small-scale mechanical fields are only obtained in very limited configurations requiring sophisticated mechanical setups. Although "microscopic" scales provide a relevant sensitivity to the sought parameters, correlation with experimental fields may be difficult.

In the present study, detailed mechanical and microstructural data are available. They were successfully correlated in Section 3.2. One must comply with the underlying crystallographic and mechanical data to identify the constitutive laws. Direct "EBSD-based" models are then considered to simulate the response of the dual-phased structure observed during *in situ* tensile tests (Figure 4.2). EBSD spatial maps are used to define "grains", regions with nearly homogeneous crystal orientations for the two phases without adding information about the lath description. Therefore, no bias is introduced in the direct comparison of raw strain maps and mechanical models built from pointwise definitions of phase and orientation maps. In a similar manner to previous studies [Gue14a, Shi18a], boundary conditions on the model are prescribed from experimental measurements. This approach allows impactful microstructural effects to be accounted for at relevant nodes and to describe traction-free surfaces. Resorting to the full tensile specimen width would also be relevant. It has been emphasized that including other measurements is beneficial to the identification [Gue14a, Shi18a, Ber16b]. As additional information, the force is usually measured and should be introduced in the procedure with a weight based on the measurement uncertainties [Rou20]. However, resulting forces corresponding to the measured displacement field are not always accessible. Hypotheses regarding in-depth microstructure or homogenized behavior must be formulated [Gue14a, Shi18a] potentially introducing new biases.

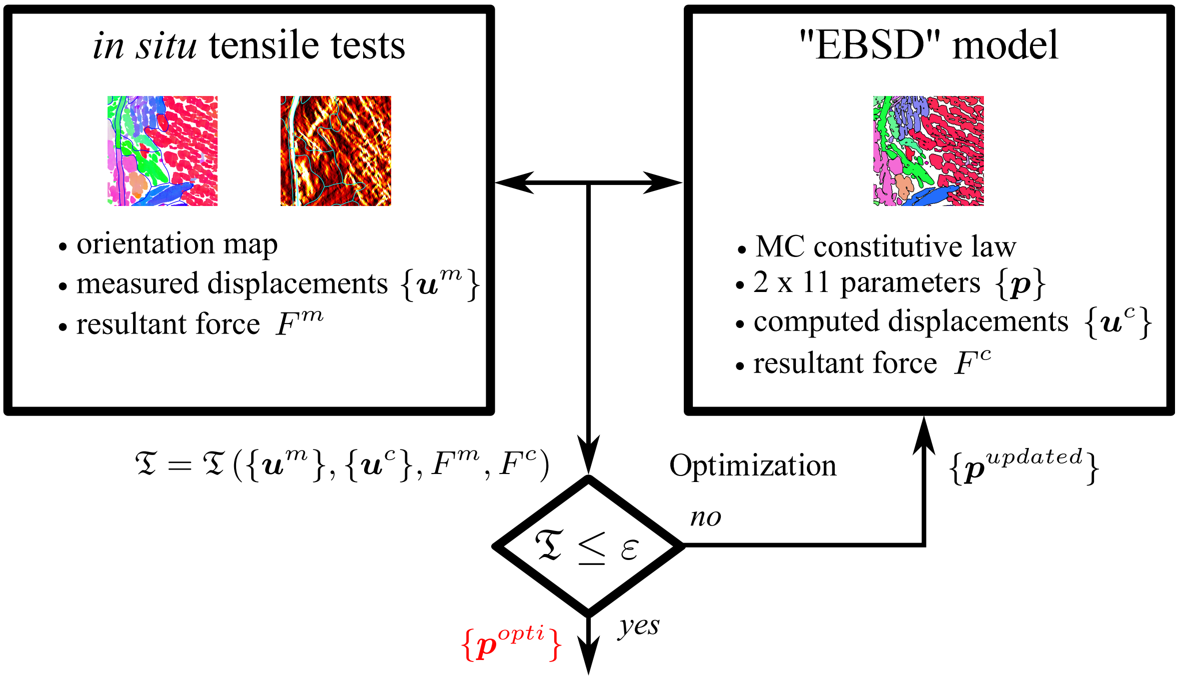

Figure 4.2: Identification scheme for the identification of MC parameters using full-field measurements.

The developed identification algorithm follows the finite element model updating (FEMU) method [Gre13]. The aim is to determine the optimal set of constitutive parameters $\{\boldsymbol{p}\}^{opti}$ minimizing the cost function $\mathfrak{T}$ representing differences between measured and computed data and usually defined by the Euclidean (L2) norm

$$\{\boldsymbol{p}\}^{opti} = \underset{\{\boldsymbol{p}\}}{\operatorname{Argmin}}\, \mathfrak{T}\left(\{\boldsymbol{p}\}\right) \tag{4.13}$$

Following the above considerations, all acquired experimental data are to be considered in the identification process, therefore the cost function $\mathfrak{T}$ reduces to

$$\mathfrak{T} = (1-w)\left\|\{\boldsymbol{u}^m\} - \{\boldsymbol{u}^c\}\right\|^2 + w\left\|\boldsymbol{F}^m - \boldsymbol{F}^c\right\|^2 \tag{4.14}$$

Measured and computed nodal displacement $\{\boldsymbol{u}^m\}$ and $\{\boldsymbol{u}^c\}$ are expressed on the same basis (a finite element mesh) in the chosen global DIC approach. Therefore, it can be shown that the functional displacement component is a cumulative norm over all time steps t including the measurement uncertainties computed in DIC

$$\left\|\{\boldsymbol{u}^m\} - \{\boldsymbol{u}^c\}\right\| = \frac{1}{2\eta_f^2 N_{dof} N_t} \sum_t \{\delta \boldsymbol{u}\}_t^T \left[\boldsymbol{M}\right] \{\delta \boldsymbol{u}\}_t \tag{4.15}$$

with

$$\{\delta \boldsymbol{u}\}_t = \{\boldsymbol{u}^m\}_t - \{\boldsymbol{u}^c(\{\boldsymbol{p}\})\}_t \tag{4.16}$$

In the present case, $[\boldsymbol{M}]$ is the DIC matrix, which is inversely proportional to the measured displacement field covariance matrix $[\boldsymbol{C}]$ [Bes06]. This metric prescribes a weighting of *dof* according to the corresponding uncertainties resulting from DIC. That is to say, components in $\{\delta \boldsymbol{u}\}_t$ having a large uncertainty, are attributed a low weight in the identification procedure. $\{\delta \boldsymbol{u}\}_t$ is made dimensionless by including the noise variance η_f^2 determined for SEM images and the number of *dof* N_{dof} of the finite element mesh and the number of time steps N_t considered.

The same developments are conducted for the load $\|\boldsymbol{F}^m - \boldsymbol{F}^c\|^2$. They are detailed in [Gue14a] and [Shi18a] but the load measured on the specimen cannot be used here because of uncertainties related to the microstructure. More details are given in Section 4.2.1.2.

From an initial guess of the parameter set $\{\boldsymbol{p}\}^{(0)}$, the optimal set of parameters satisfying $\mathfrak{T}\left(\{\boldsymbol{p}\}^{opti}\right) \leq \varepsilon$ is computed iteratively with a Gauss-Newton iterative scheme where the set $\left\{\boldsymbol{p}^{(k)}\right\}$ at the k-th iteration is computed from the sensitivity to each parameter

$$[\boldsymbol{H}^{(k-1)}]\{\delta \boldsymbol{p}^{(k)}\} = [\boldsymbol{N}^{(k-1)}] \tag{4.17}$$

with the Hessian matrix

$$[\boldsymbol{H}^{(k-1)}] = \sum_t [\boldsymbol{S}^{(k-1)}]_t^T [\boldsymbol{M}][\boldsymbol{S}^{(k-1)}]_t \tag{4.18}$$

and the gradient vector

$$[\boldsymbol{N}^{(k-1)}] = \sum_t [\boldsymbol{S}^{(k-1)}]_t^T [\boldsymbol{M}]\{\delta \boldsymbol{u}\}_t \tag{4.19}$$

expressed as a function of the kinematic sensitivity matrix of the displacement field

$$[\boldsymbol{S}^{(k-1)}]_t = \left[\frac{\delta \boldsymbol{u}^{(k-1)}}{\delta \boldsymbol{p}}\right]_t \tag{4.20}$$

The set of parameters is updated from its current estimation by corrections $\{\delta \boldsymbol{p}\}$

$$\{\boldsymbol{p}^{(k)}\} = \{\boldsymbol{p}^{(k-1)}\} + \{\delta \boldsymbol{p}^{(k)}\} \tag{4.21}$$

4.2 Parameterization and calibration at different scales

Full-field measurements from *in situ* tensile tests display striking correlations with microstructural features extracted from EBSD maps. Creating a model as close as possible to the microstructure description revealed by EBSD maps is legitimate. However, the microstructural features giving rise to the morphology of the deformation fields are large. As evidenced by the deformation fields, small micrometer-scale perturbations making the laths "globular" aspect have little influence on the apparent behavior of the lath packets. The difficulty resulting from this observation is that the boundary conditions acting at these scales are unknown at depth. They are still of paramount importance in understanding surface measurements.

A first approach considering straightforward modeling from EBSD maps has been considered and is presented hereafter in Section 4.2.1. This modeling intends to demonstrate the difficulties associated with high precision computations and the non-representativity of the surface microstructure. Following the hierarchical nature of the microstructure, it is then proposed to homogenize the behavior at the laths packets first. The transition from small-scale structures to their macroscopic response is derived. Perspectives toward an improved identification method and the representativity of a simple geometrical model describing the lath packets are given.

4.2.1 Direct identification from EBSD and SEM-DIC measurements

4.2.1.1 Representativity of surface models and feasibility of detailed computations

Creating a geometrical model of microstructures from EBSD maps involves two key procedures: classifying and segmenting crystal orientations and meshing each entity. While the first step has been thoroughly described for the particular case of CDSS in Chapter 2, many general approaches already exist for more general cases [Bac11]. The basic principle is always to detect and label grains *i.e.,* to find sets of connected pixels in orientation maps having a misorientation lower than a prescribed threshold. Afterward, grain boundaries can be computed as geometric entities by retrieving the boundaries of each set. Since FE computations are sensitive to mesh quality, regularization of these boundaries is desirable. It is performed from the determination of triple points *i.e.,* grain boundary intersections (in the observation plane) belonging to more than two grains [Dep20]. All meshes are obtained using the previous workflow for the direct identification scheme from EBSD maps. Grains are reconstructed using the MTEX algorithm [Bac11], allowing convenient handling of geometric entities. Two-dimensional vertices are given as inputs to the meshing algorithm Gmsh [Geu09] that handles splines for smooth boundaries and optimization of the element quality for the crystal-plasticity FE solver. The procedure was first fully implemented in Matlab in which MTEX is written before being substituted to the version of Depriester [Dep20] that generalizes this homemade program with much more flexibility and features.

The present approach only relies on surface data as in-depth microstructures could only be obtained using destructive techniques. It is noteworthy that the previously mentioned method [Shi17b] may provide in-depth "*post mortem*" data but could not be tested within the present time frame. We may indicate, however, that the method does not solve the in-depth boundary conditions problem. Consequently, surface mechanical fields must be assumed to be representative of in-depth microstructures (without significant influence on the underlying microstructure), and a quasi-2D modeling approach considered. Still, this hypothesis depends on the local microstructure, particularly on austenite growth direction. It is therefore required to assess the relevance of these models first. The volume reconstructed by Simonet [Sim19] displayed in Figure 4.3 was used. Serial sectioning by mechanical polishing was carried out to acquire six layers (2400 µm x 1600 µm EBSD maps with a 3 µm pixel size) evenly spaced between 0 and 60 µm (Figure 4.3 (a)). Each polishing step takes several hours to accurately control the kinetics. The acquisition of EBSD maps has been reduced to half an hour for these mappings. All microstructural features are captured, and small properties likely to influence surface mechanical fields are geometrically modeled in the in-depth direction. The volume was reconstructed by spatially correlating crystal orientations in DREAM3D [Gro14] (Figure 4.3 (b) and (c)) and the meshes were generated with Gmsh [Geu09]. One should keep in mind that the weight of the vanishing shear stress on the rear surface is such that little flexibility is given to microstructural effects in the direction orthogonal to the observation plane. Hence, this example may not be fully representative of the in-depth microstructure influence. However, decisive data on calculation times and representativity of simulated fields can be observed. The reconstruction also shows the complexity of reconstructing the microstructure on a specimen with sufficient accuracy.

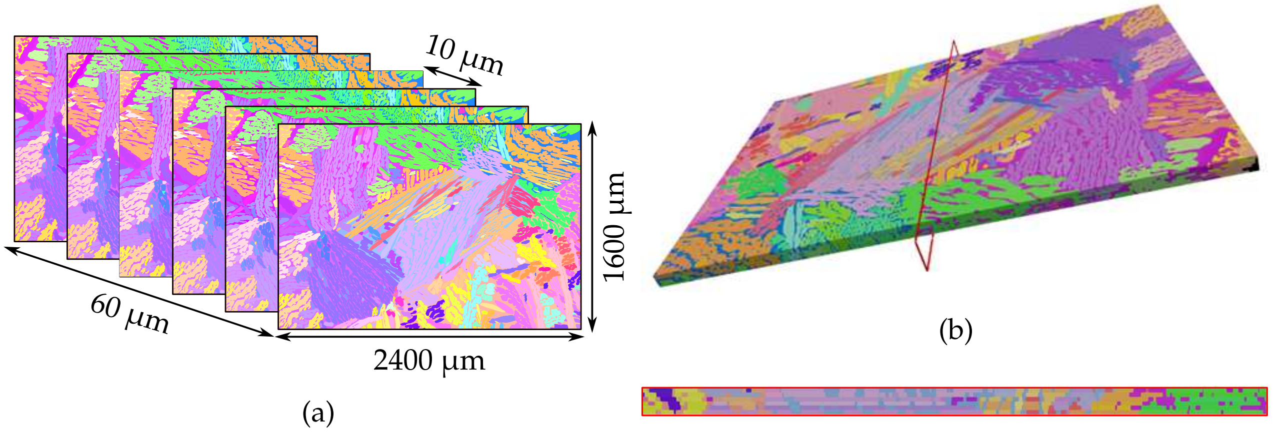

(a)

(b)

(c)

Figure 4.3: Illustration of the EBSD volume reconstructed from the six layers acquired by serial mechanical polishing. (a) Illustration of the layer dimensions and in-depth position. (b) Representation of the 3D reconstructed volume by spatially correlating orientations in DREAM3D [Gro14]. (c) Cross-section view of the six stacked layers.

Two models were considered from these acquisitions. The first one is a mesh of the 3D reconstructed volume. The second one is a quasi-2D approach consisting in an extrusion of the first layer along the normal plane. The quasi-2D model reproduces the same kind of calculations used in the identification procedure. The multiscale aspect of CDSS microstructures calls for small element sizes in almost all places. In particular, the ferritic matrix requires a fine resolution in the lath normal direction, creating meshes with a large number of elements in both cases. However, the mesh is not constrained in the in-depth direction in the quasi-2D case. Extruding elements only multiply the number of elements in the front layer. In the real 3D microstructure, in-depth definition forces mesh adjustments, thereby needing more elements. As a result, the number of degrees of freedom N_{dof} increases from 1.5 M to 4.5 M, and the number of elements increases by an order of magnitude (Table 4.2). In contrast with experimentally correlated models, only basic boundary conditions are assumed here. The observed surface is left unconstrained. Left, bottom and rear surface normal displacements are blocked, and right surface normal displacements are uniformly prescribed to reach a 0.5% macroscopic strain level. The constitutive parameters are those given in Section 4.1.4. Computation statistics for the two configurations are given in Table 4.2.

The increase in the number of elements/*dof* goes along with a substantial increase in the computation time. Both types of computation seem inappropriate to perform any identification in an acceptable time. More interestingly, most of the time is spent integrating the constitutive law (more than 60 % of the total calculation time). The integration limits the convergence of the FE solver. Consequently, small time steps are enforced during the whole simulation, thus increasing computation times to a great extent. This observation emphasises that only limited area models with detailed microstructure can be implemented in the identification procedure.

Table 4.2: Computation statistics for the 3D and quasi-2D models.

	N_{dof}	Tetrahedra	Cores	Time
3D	4.5 M	11 M	128	65 h
Quasi-2D	1.5 M	2.3 M	64	21 h

Longitudinal strain (ε_{xx}) and stress (σ_{xx}) fields computed with 3D and quasi-2D models are shown in Figure 4.4 at 0.5% macroscopic strain. They are introduced alongside the microstructure acquired by EBSD on the first layer (Figure 4.4 (a) and (b)). The strain level is driven by the austenite ability to deform (*i.e.,* by the local Schmid factor). Thus, the two models lead to similar maps (Figure 4.4 (c) and (d)). Yet, the quasi-2D model (Figure 4.4 (c)) overestimates the strain level in ferrite on the surface compared to the complete 3D model (Figure 4.4 (d)). The whole strain distribution is more diluted and some strain bands in austenite do not appear considering the simple extruded model. Regarding the stress fields, high levels concentrate in thin ferritic islets (Figure 4.4 (e) and (f)) owing to greater critical resolved shear stress of ferrite 4.1. The two surface stress maps are comparable but some local stress localizations may develop in the bulk owing to the microstructure complex layout.

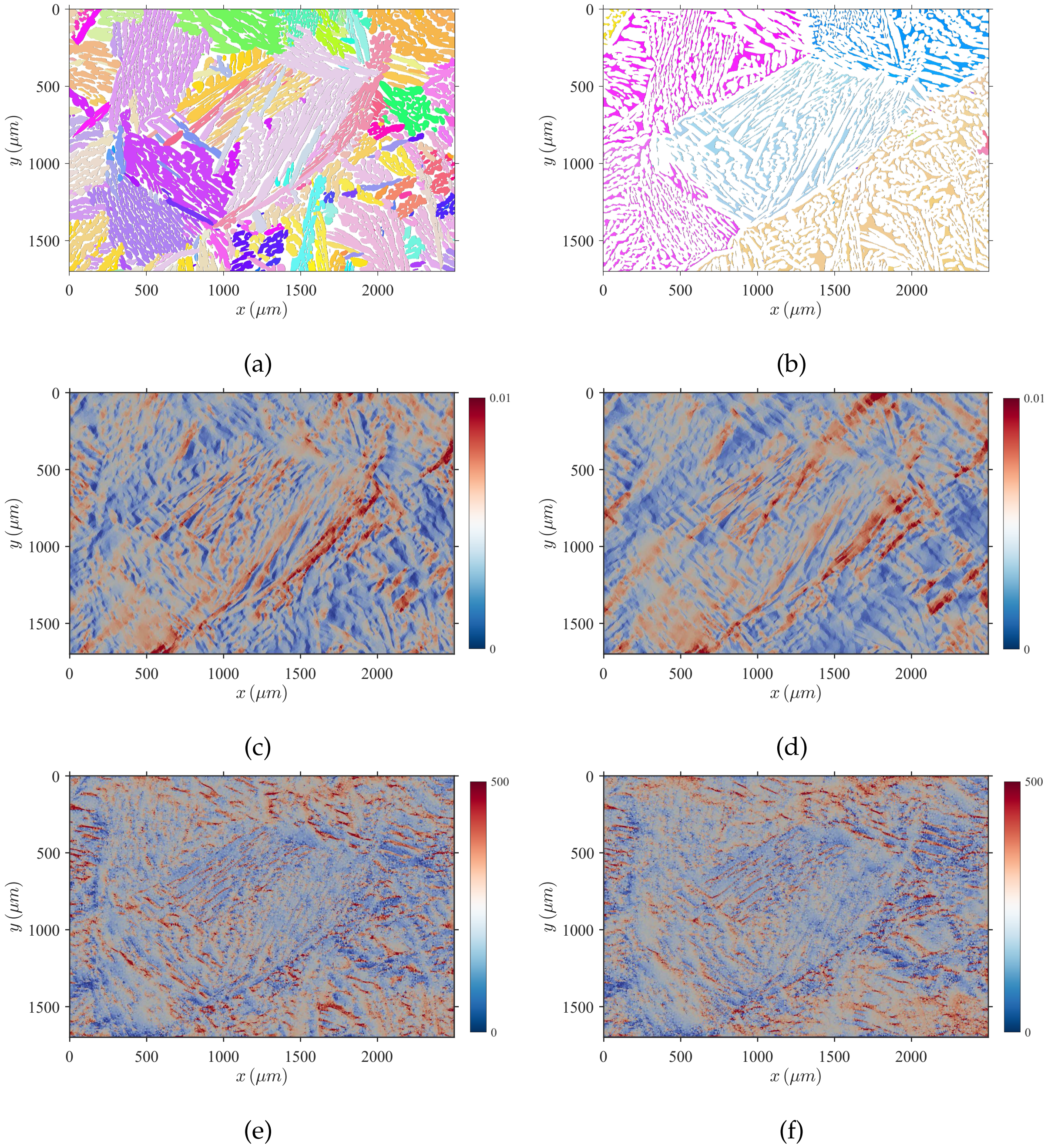

(a) (b) (c) (d) (e) (f)

Figure 4.4: Comparison between computed 3D (c-e) and quasi-2D (d-f) models. The loading direction is x. (a) Surface austenite orientation map. (b) Surface ferrite orientation map. (c-d) Strain maps and (e-f) stress maps computed with the 3D and 2D models.

From a statistical point of view, the mechanical fields from both models are very similar. Figure 4.5 presents stresses and strain level distributions at 0.5% macroscopic strain. Besides extrema values, the quasi-2D model seems to offer a good representativity for a much cheaper experimental and modeling cost than 3D. However, we cannot conclude about these fields representativity. Local microstructural effects in the direction normal to the plane are likely not represented because of the boundary conditions imposed here. The comparison with experimental fields is essential to answer this question.

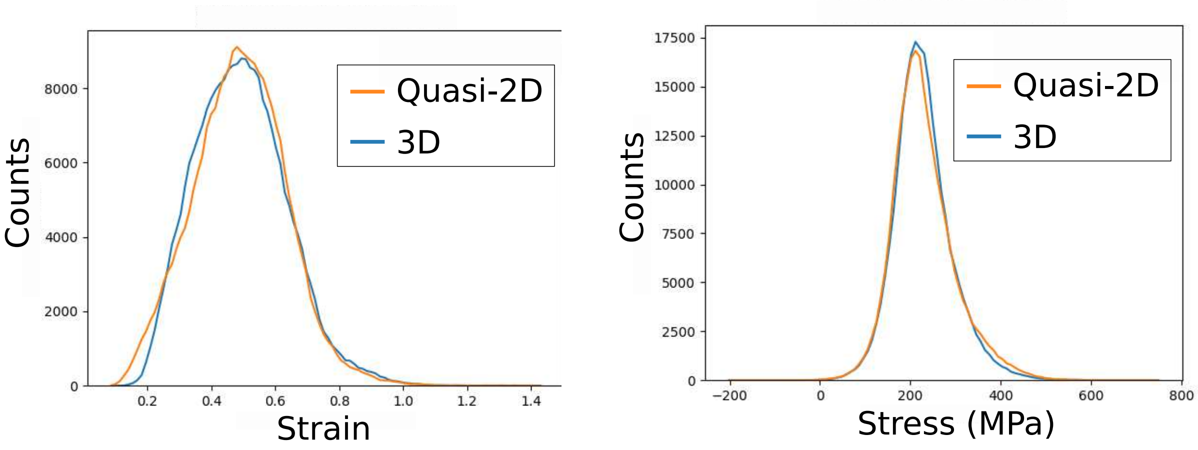

(a) (b)

Figure 4.5: Comparison between computed strain (ε_{xx}) and stress ($\boldsymbol{\sigma}_{xx}$) histograms for 3D and quasi-2D models. (a) Strains distributions. (b) Stresses distributions.

4.2.1.2 Identification from explicit lath layout

Direct EBSD model

Results from the previous computations emphasized the need to create a relevant microstructure layout model. Rational computation time for the identification will not be achieved without simplifications. Considering the quasi-2D extruded approach, small features from the observation plane are to be removed as their mechanical response is insignificant, but their contribution to computation time is considerable. Basic operations, including erosion-dilation loops, are commonly used with the grain formalism in EBSD processing softwares [TSL16]. We conduct such a procedure in the following to demonstrate that taking the surface data into account alone is insufficient. A corresponding coarsening process is illustrated in Figure 4.6 using MTEX. Grains are computed and removed when smaller than an input threshold (grain surface less than 300 µm^2 in the present example). Grains are reconstructed another time, considering empty pixels. The latter are attributed to the orientation of the closest grain to go from an experimentally measured map displayed in Figure 4.6 (a) (with a 3 µm pixel size) to a “cleaned” map (Figure 4.6 (b)).

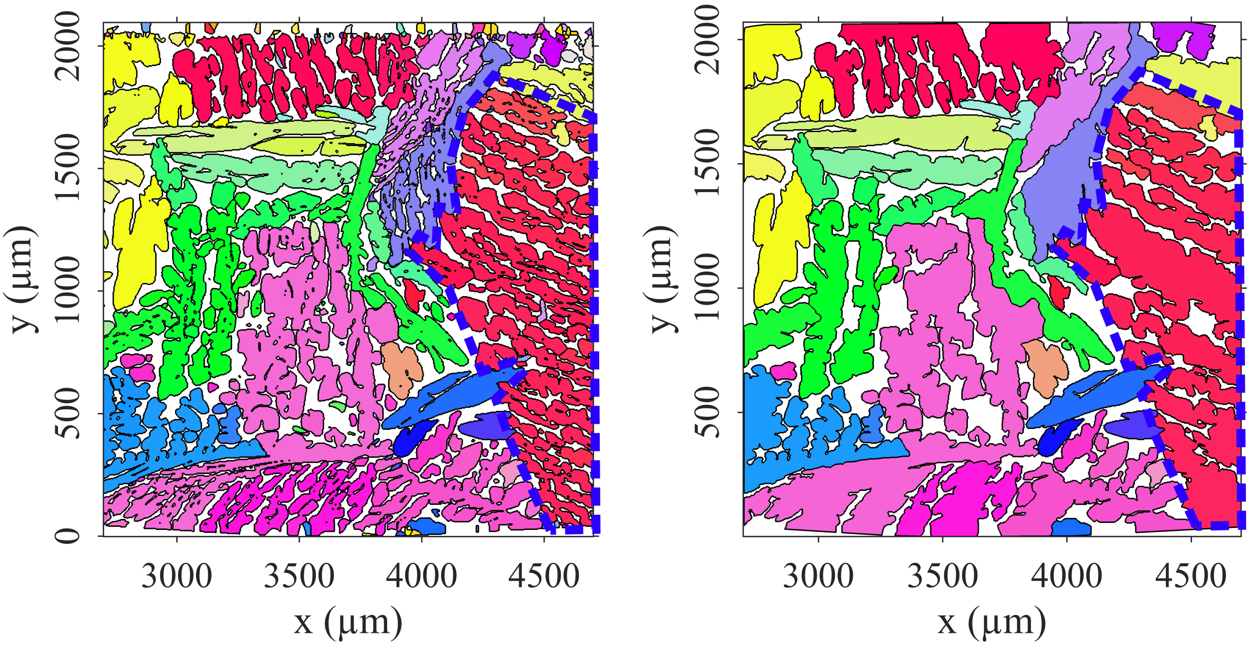

(a)

(b)

Figure 4.6: Illustration of an EBSD cleaning procedure using standard grain size input. The dashed box corresponds to the area simulated in the following. (a) Measured crystal orientation map (IPF) with a 3 µm pixel size. (b) Cleaned map with a 300 µm^2 grain size threshold.

Interestingly, the efficiency of this method that has been proven in the case of more regular microstructures (say a microstructure close to a Voronoi tesselation or even lathy dual-phase steel microstructures [Dep19]) does not produce very satisfactory results for the CDSS microstructure. Because of dual-phase and globular aspects, basic coarsening processes do not preserve the volume fraction of phases and keep seemingly unnecessary complex boundaries. However, it raises interesting questions regarding the representativity of the strain distributions in an “EBSD-based” model. The CDSS microstructure displays fundamental features to understand the mechanical behavior naturally described in 3D but poorly captured in EBSD cross-sections. One of the fundamental features not well preserved in “EBSD-based” models is the continuity of the ferritic phase in the lath growth directions that endows the observed mechanical strength to aged packets. In several regions in EBSD maps, ferrite locally appears scattered and consequently discontinuous in the plane transverse direction. Without introducing continuity in the growth direction, the mechanical behavior of some regions computed from quasi-2D models differs from the observed one. To illustrate this bias, the blue dashed box in Figure 4.6 (a) is considered and meshed using a quasi-2D approach. Figure 4.7 (a) shows the strain map measured experimentally in this region for a 4% macroscopic strain. The mesh is extruded to reach a 100 µm thickness, and experimental displacements are prescribed on the mesh boundary (Figure 4.7 (b)). The identification algorithm from Section 4.1.4 is applied to fit the computed surface field to the experimentally measured one. Only the hardening parameters of the two phases *i.e.*, $\{r_0, q, b\}_\alpha$ and $\{r_0, q, b\}_\gamma$ are included considering the strain amplitudes. Figure 4.7 (c) displays the strain field obtained from the initial set of parameters.

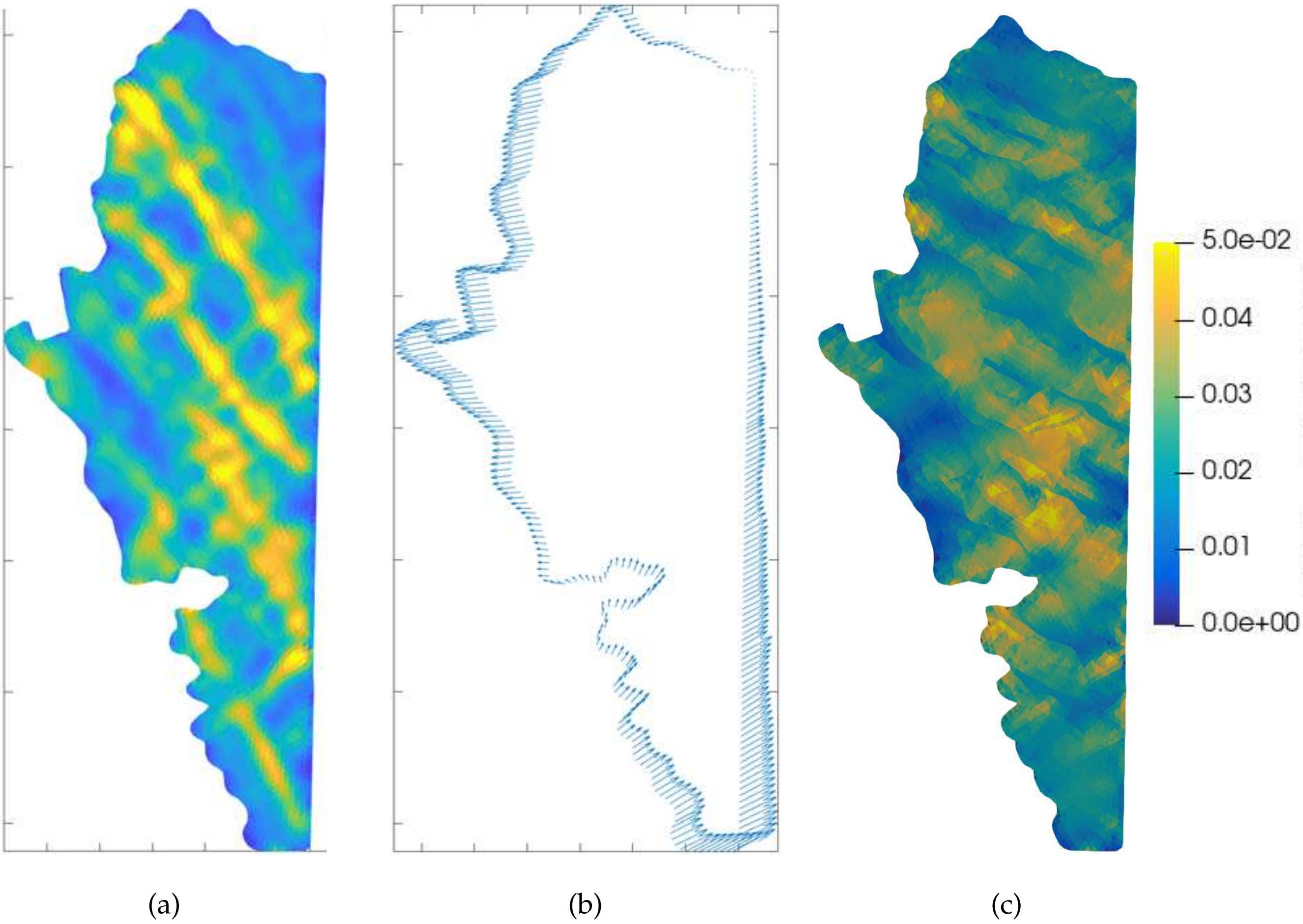

(a) (b) (c)

Figure 4.7: Illustration of the experimental to model comparison and identification procedure. (a) Measured strain map on the selected region. (b) Measured boundary displacements. (c) Strain map resulting from the "EBSD-based" model using the initial set of parameters and prescribed boundary conditions.

As initially thought, this identification approach does not allow determining an optimal set of parameters. The sensitivity on ferrite parameters is so small that meaningless values are reached. The sensitivity fields for the three parameters of the α-phase law are shown in Figure 4.8. The most influential parameter, the critical resolved shear stress r_0, provides a maximum sensitivity of about 1 μm on the computed displacement field for a 5% perturbation (Figure 4.8 (a)), which is about twice the experimental measurement uncertainty. The other two parameter contributions are about ten times lower (Figure 4.8 (b-c)). Additionally, the influence range of these parameters is quite limited. These restrictions are largely attributed to the lack of representativity of the current "EBSD-based" model regarding the ferritic spatial distribution (and by extension of some austenitic regions).

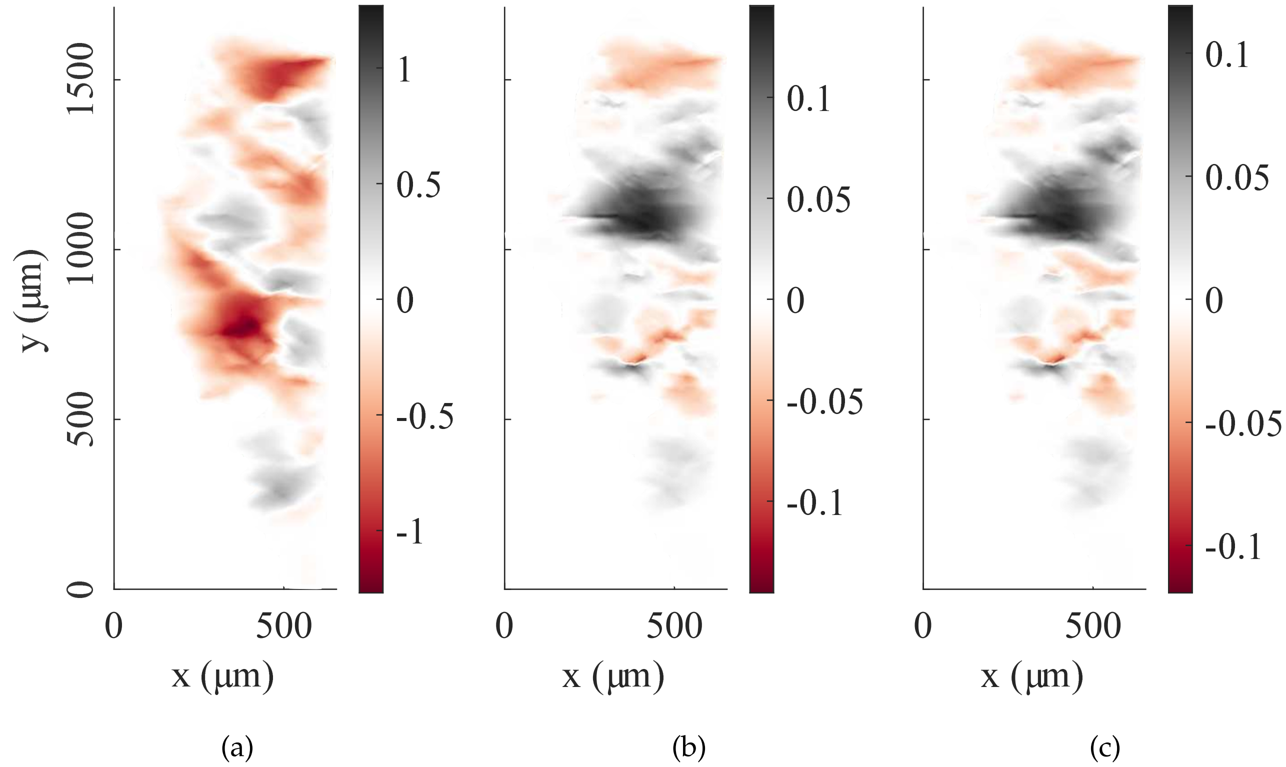

Figure 4.8: Sensitivity fields $[\boldsymbol{N}^{(opti)}]$ (in μm) for ferrite constitutive parameters considering a 5% perturbation. (a) r_0. (b) q. (c) b.

We have thus highlighted that surface data alone does not allow us to come close to a satisfactory solution. These cross-sections do not include the preferential growth direction of austenitic laths giving the same elongated shape to the ferritic matrix, and the boundary conditions are possibly a highly limiting factor. The analyses conducted in Chapter 2 highlighted the anisotropic nature of the two phases spatial distribution at the (large) lath packet scale. Consequently, the cleaning step considering actual cross-section data that does not give more credit to the laths principal directions is insufficient. The extrapolation of both microstructure and boundary conditions only restricts simulated fields sensitivity to low-frequency mechanical components. Conversely, the measured fields manifest the behavior of a more macroscopic structure. The latter is, by all accounts, not represented here. One way to improve the cleaning process would be to consider the elongated morphology and perform an "anisotropic" cleaning giving more weight to the lath growth direction. The latter could be obtained from the Pitsch variant affiliations or directly read from the image for packets lying outside Bain groups using a structure tensor (see Chapter 2.4.4) or more sophisticated morphology characterization. Regarding the boundary conditions, a fair extrapolation of in-depth data is required.

Parameterized EBSD model

It was previously proven that the local geometry of the two phases is not precisely known from a unique plane observation, leading to spurious modeling. Another way to identify crystal plasticity parameters is to resort to the microstructure knowledge acquired in Chapter 2. EBSD image processing showed that in a large majority of lath packets, austenite (and consequently ferrite) is lath shaped. Each lath in the packet can therefore be depicted by its growth and normal directions related to the Pitsch variant it belongs to (Chapter 2.4.4). Likewise, mechanical fields exhibit a quasi-periodicity. From these observations, a parametric description of the lath network can be built for lath packets where a geometrical description is known *i.e.,* lath packets lying on Bain circles. Other packets are likely to move away from this simple lath stack. Resorting to a simplified parametric model raises two points of concern. First, the number of resulting parameters for a relevant description is to be determined. Second, the definition of lath packets for orientations belonging to Bain groups only restricts the number of regions qualified for the identification procedure. One must ensure that this limitation is not detrimental to correct calibration. It can already be stated that cases where the full specimen width is attributed to Bain groups were not met. It is consequently difficult to identify parameters from a full-width model and thus to consider the measured load in the identification.

An example of plausible parameterization is shown in Figure 4.9. This simple description assumes that the lath layout is unimodal and uniform in a given packet. Therefore, it can be described by four independent parameters: the lath normal, austenite and ferrite lath thickness (d_1 and d_2), as well as a spatial shift. Depending on the mode, some parameters may be included in the identification procedures. For instance, the lath normal is a known parameter in the previously proposed model. Besides, the two phases thicknesses and the spatial shift could be either identified or set.

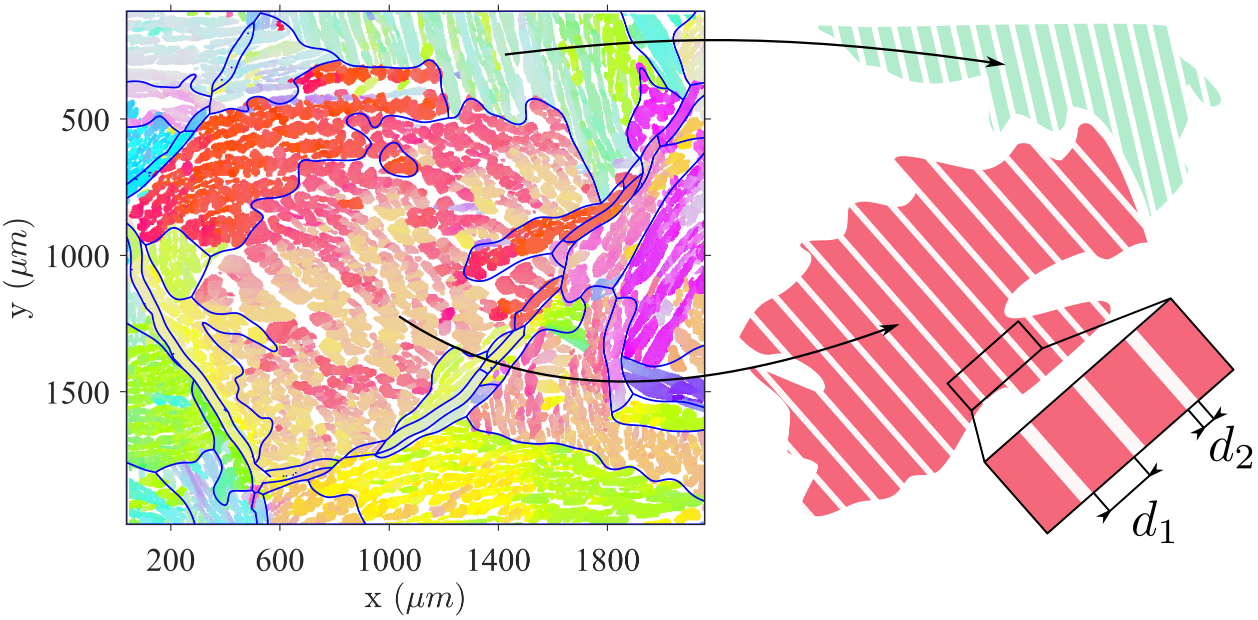

Figure 4.9: Schematic view of a plausible lath parametrization model.

4.2.2 Homogenization at the lath packet scale

Predicting large scale responses while keeping an explicit small scale description *i.e.*, a precise microstructural description, would be practically impossible for an entire PWR component. Therefore, an intermediate homogenized model relying on the hierarchical aspect of the microstructure is to be introduced to allow for upscaling. This mesoscale model aims to describe the lath packet behavior through a unit cell including crystallographic and morphological properties described in Chapter 2. First the basic asumptions leading to this intermediate scale description are introduced before discussing the effect of aging. Last, recommandations for extracting a representative average response are given.

Lath packet unit cell definition

From the gathered experimental observations, most primary ferritic grains are organized into packets in which austenite and ferrite distributions are described by a nearly periodic pattern of elongated shapes. The interlaced packet network is conveniently segmented inside each α-grain by attributing austenitic orientations to the closest Pitsch variant of the parent grain. Experimental field measurements also emphasized that strain fields inherited properties from the elongated shapes of the two phases. Given these observations, a simple unit cell representing a periodic lath stack is introduced (Figure 4.10). It embeds lath extent directions and crystallographic properties of both phases. This unit cell is fully represented by ferrite orientation (3 parameters), austenite orientation (3 parameters), and the normal to the lath *i.e.*, the unit cell interface directions (2 parameters). In total, 8 independent parameters are needed to describe the unit cell configuration locally. However, they may be reduced from the previous observations. We demonstrated that Pitsch OR is regularly followed and gives access to the lath normal. Thus, austenite orientation and lath normal parameters can be reduced to a single parameter, the Pitsch variant, describing a local and apparently random orientation selection. The Pitsch OR corresponds to a child orientation in the parent crystallographic frame. Hence, the twelve possible austenite orientations $\boldsymbol{g}_\gamma^i$ are deducted from the corresponding parent grain orientation $\boldsymbol{g}_\alpha$ following $\boldsymbol{g}_\gamma = \boldsymbol{g}_\alpha \boldsymbol{m}_i$ for $i = 1, ..., 12$ where $\boldsymbol{m}_i$ are the twelve symmetric equivalents to the Pitsch OR. The numerical value to compute child orientations and lath normal from the parent crystallographic frame are given in Table 4.3.

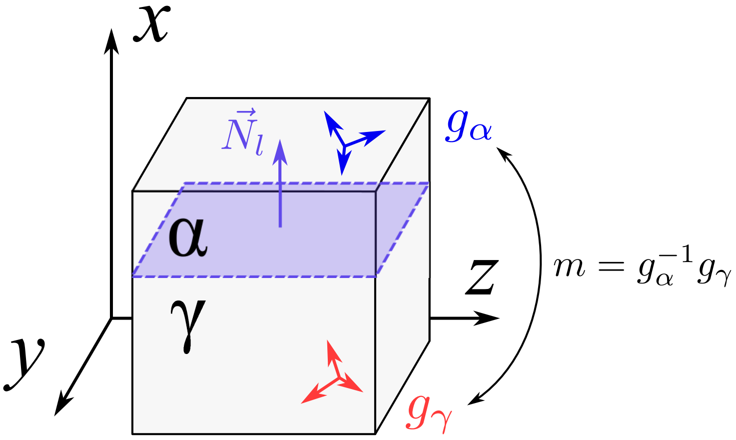

Figure 4.10: Schematic representation of the unit cell chosen to represent lath packet for austenitic orientations belonging to Bain groups.

Table 4.3: Correspondence between variant, austenite orientation and lath normal (in hkl convention). Angles for the orientation $\boldsymbol{g}_\gamma$ are given in rad. following the Bunge convention.

Variant id	g_γ			N_l		
	φ_1	ϕ	φ_2	h	k	l
1	0.17	0.79	0	2	1	-1
2	4.88	1.57	3.93	-1	1	2
3	1.74	1.57	0.79	-1	1	-2
4	3.31	2.36	4.71	1	2	-1
5	3.31	0.79	1.57	-1	2	1
6	0.17	2.36	3.14	-2	1	-1
7	1.74	1.57	2.36	1	1	-2
8	3.31	2.36	0	-2	1	1
9	3.31	0.79	3.14	2	1	1
10	4.88	1.57	5.50	1	1	2
11	0.17	0.79	4.71	1	-2	1
12	0.17	2.36	1.57	1	2	1

To evaluate the average response resulting from this unit cell, a finite element model made up of two elements (one for each phase) is set up. The lath normal is aligned with the cartesian frame because it enables an easy geometric parameterization of the model. Hence, $\boldsymbol{g}_\alpha$ is defined so that $\boldsymbol{g}_\alpha \vec{\boldsymbol{N}}_l = \vec{\boldsymbol{x}}$. The γ-phase orientation is deduced from $\boldsymbol{g}_\gamma = \boldsymbol{g}_\alpha \boldsymbol{m}$. The macroscopically measured volume fraction (25% α | 75% γ) is first considered. Periodic boundary conditions were implemented (in code_aster) and enforced on pairs of faces sharing the same normal using Lagrange multipliers to compute the average behavior. The parameters for the first variant are used. The mechanical behavior follows the symmetries of the geometry (*i.e.,* of the Pitsch OR). The response of other variants is obtained by rotating the unit cell frame using symmetry operators describing the OR. The model response can be driven either by strain or stress. In the present case, we prescribe the average strain tensor $\boldsymbol{\varepsilon}$ by imposing surface nodes displacements $\{\boldsymbol{u}\}$ on boundary nodes located by their position $\boldsymbol{x}$ such that they respect the periodicity

$$\{\boldsymbol{u}(\boldsymbol{x})\} = \boldsymbol{\varepsilon}\boldsymbol{x} + \{\boldsymbol{u}^p(\boldsymbol{x})\} \tag{4.22}$$

where $\{\boldsymbol{u}^p(\boldsymbol{x})\}$ is the periodic part of the displacement field. In the following, unixial tension conditions are assumed locally representative of observed loadings. Therefore, isochoric strains are prescribed. Illustrations are given for a loading located in the XY plane of the unit cell. The input strain tensor $\boldsymbol{\varepsilon}$ is parameterized by an amplitude ε_0 and an angle θ

$$\boldsymbol{\varepsilon} = \varepsilon_0 \begin{pmatrix} \cos(\theta) & 0 & 0 \\ 0 & \sin(\theta) & 0 \\ 0 & 0 & -\cos(\theta) - \sin(\theta) \end{pmatrix} \tag{4.23}$$

We may mention that all the following developments are still valid for any isochoric strain. Only XY results are considered to simplify the illustrations.

Figure 4.11 illustrates the anisotropy resulting from this composite behavior as compared to unit FCC and BCC mechanical response. A load surface section corresponding to an uniaxial strain path oriented in the XY plane by an angle θ is plotted for multiple plastic strain levels and a 0 to 360° θ range. Figure 4.11 (a) and (b) depict the Tresca-like yield surfaces for the unit crystal plasticity behaviors (with prescribed $\boldsymbol{g}_\alpha$ and $\boldsymbol{g}_\gamma$ orientations). Small perturbations at the early stages of plasticity can be noticed due to a temporal discretization error, although they do not jeopardize the global surface definition. These surfaces are slowly dilated with the increasing plastic strain but keep their faceted boundaries that are more pronounced in the BCC system (Figure 4.11 (a)). The plastic bifurcation discussed in Section 4.1.4 manifests at facets junction when sufficiently high plastic strain levels are reached. Both FCC and BCC show this specificity, which reflects a behavior inherent to the formulation of crystal plasticity laws. Load surface corners present a stress overshoot damped by the viscosity effects. However, no conclusions can be made about these effects. The viscosity parameters of the two phases are probably not representative because they were identified on quasi-static tests. Even so, they play a significant role in plastic bifurcation numerically. Similarly, it is not easy to attest to the accuracy with which the interaction matrix coefficients have been identified, although their importance in the phenomenon is explicit [For98]. Experimentally, no plastic bifurcation can be observed because of its transient nature. The image acquisition method is not adapted for observing dynamic phenomena.

Compared to FCC and BCC unit behaviors, it appears clearly that the lath stack model is regularized by the composite effect, particularly at high plastic strain levels (Figure 4.11 (c)). Moreover, similar average strain levels lead to higher strain in austenite compared to the unit FCC law. Thus, plastic bifurcation seems more pronounced in Figure 4.11 (c).

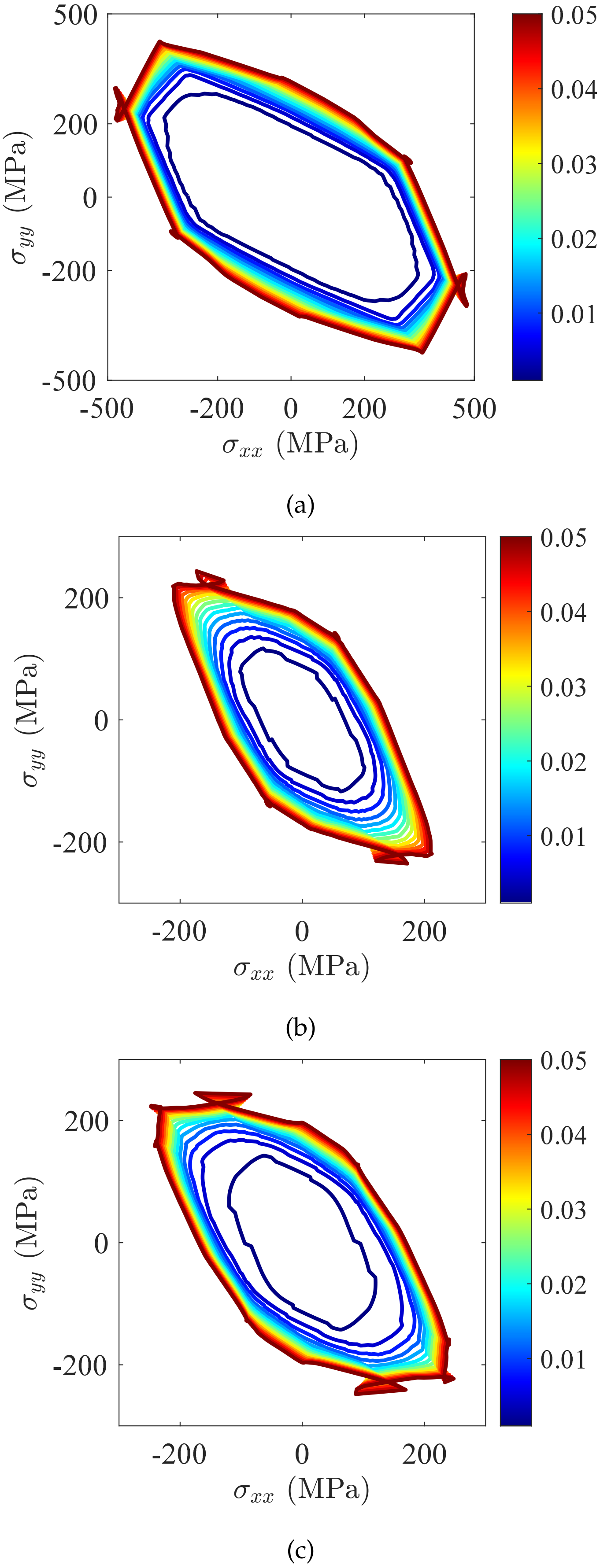

(a)

(b)

(c)

Figure 4.11: Load surfaces evolution for the three unit behaviors. (a) Ferrite. (b) Austenite. (c) Unit cell (ferrite-austenite composite). The colorbar represents the plastic strain level.

While the effect of aging cannot be linked to the change of an identified parameter from the experimental field, it can be inferred from the multiple mechanical characterizations available in the literature and EDF database. The number of mechanical tests directly probing the ferritic mechanical behavior change is limited. Micro and nano hardness measurements are probably the most accessible. The hardness change is linear with the logarithm of the aging time [Li13a, Bad19, Zha19b] and it is known that hardness is intrinsically related to the change of tensile properties [Pav08]. An internal project at EDF also demonstrated employing micropillar compression tests that aging acts with comparable kinetics on the critical resolved shear stress of {110}<111> and {112}<111> slip systems in ferrite with no significant change in the hardening rates. On a similar CF8M alloy, the critical resolved shear stress was measured between 170 MPa (unaged) and 1000 MPa (long-term aging). Consequently, it may be argued that a first-order description of aging in the constitutive law can be implemented by considering this logarithmic evolution of the critical resolved shear stress

$$r_0(t) = r_{t_0} + \beta(\log(t) - 1) \tag{4.24}$$

where r_{t_0} is the initial (unaged material) critical resolved shear stress, β the ageing rate and t the aging time.

The effects of an increase in hardness on the mechanical behavior of the lath stack unit cell are illustrated in Figure 4.12. Von Mises stress and equivalent strain are plotted for four values of r_0 (170, 300, 500, and 1000 MPa) and five different loading directions in the unit cell XY plane. Again, uniaxial tensile conditions are assumed. An increase of r_0 appears essentially as an increase of the effective "yield stress". Some features of the unit cell behavior are preserved and amplified (*e.g.*, the two-step hardening in $\theta = 45°$ and $\theta = 180°$ directions) because the increase of ferrite strength delays the occurrence of slip in this phase. Conversely, changes of regime are likely caused by the embrittlement (*e.g.*, the uneven hardening of the same mechanical response in $\theta = 0°$, $\theta = 90°$ and $\theta = 135°$ directions). This is likely caused by the redistribution of stresses inside the two phases. However, the effect on local mechanical fields is difficult to capture from these observations only. They may also be irrelevant since the parameters were not identified on our material. Nonetheless, the disruption in the equivalent strained discussed above are of insignificant magnitudes at the lath packet scale. Embedding the resulting behavior inside an average formulation is then appropriate.

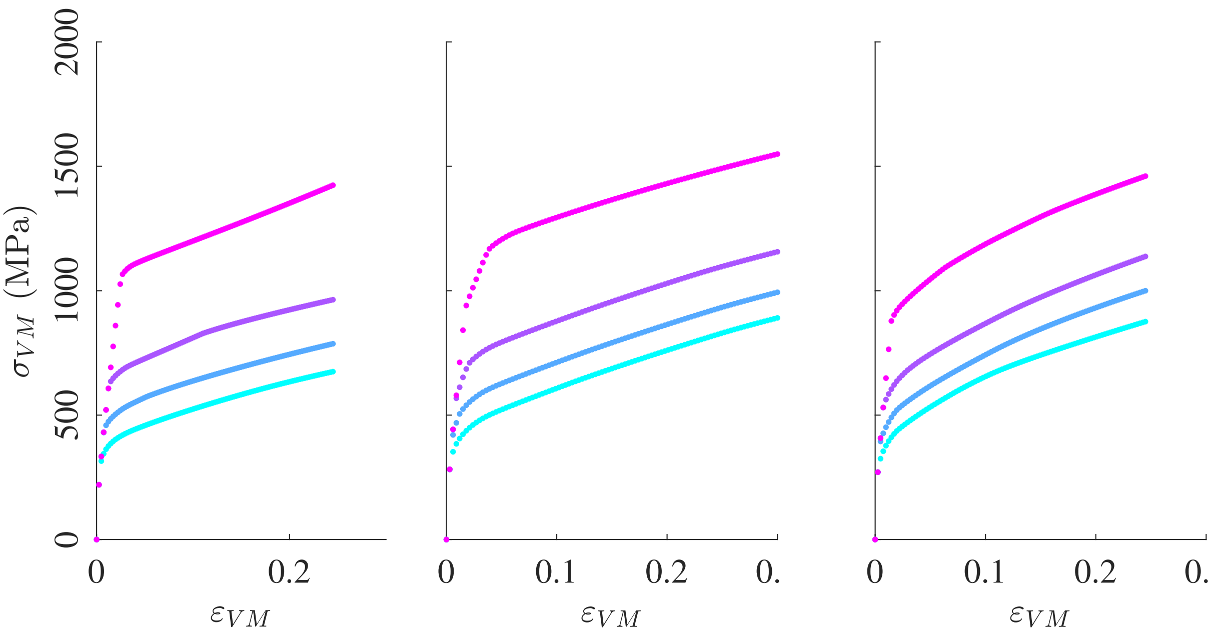

(a) θ = 0°

(b) θ = 45°

(c) θ = 90°

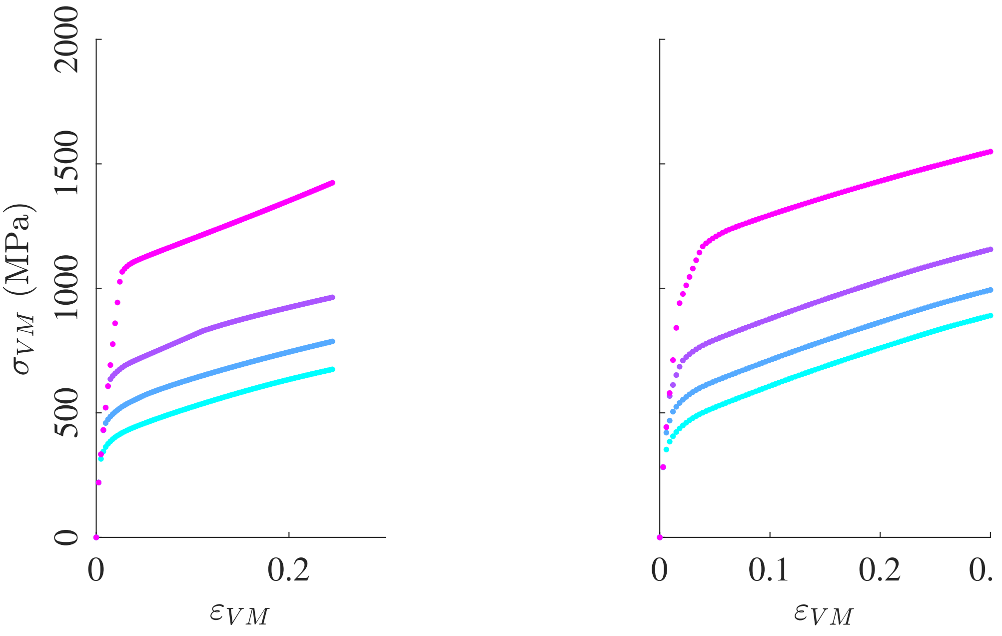

(d) θ = 135°

(e) θ = 180°

Figure 4.12: Effect of an r_0 increase on the layered unit cell behavior for four different critical resolved shear stresses and five loading directions. r_0 ranges from 170 MPa (cyan) to 1000 MPa (magenta).

Lath packet equivalent behavior

To implement the previous unit cell behavior for every Gauss point of larger scale simulations, that is, to perform the scale transition from laths to lath packets, its equivalent behavior must be described. Phenomenological stress and strain concentration equations were proposed in the case of polycrystals [Kro61, Hil65, Ber78, Cai16]. The goal is to accurately reproduce mean fields in each phase, including the microstructure information. In some specific cases, local mean fields are derived explicitly. For instance, Berbenni *et al.* [Ber13] wrote macroscopic fields in the precise instance of a laminated bicrystal, including orientations, phases volume fraction, and interface direction. These homogenization approaches require numerical developments that could not be achieved within the current time frame. Yet, the remote behavior's anisotropy and regularity were assessed by a more generic constitutive law. Up to now, the combined crystallographic and interface effects at the lath cluster scale are unknown. With this in mind, we planned to introduce a mean field solution inside each packet and characterize the effects of this intermediate scale anisotropy on the resulting macroscopic fields.

For this purpose, an orthotropic yield function developed by Cazacu *et al.* [Caz01] denoted *CB2001* was implemented in Mfront. It consists of generalizing the stress deviator invariants to orthotropy and using them in an invariant-based yield function. In the case of the *CB2001* yield criterion, orthotropic invariants are implemented in Drucker's yield function [Dru49]. Many other anisotropic yield function exist (*e.g.*, linear transformation-based yield function developed by Barlat *et al.* [Bar05]). *CB2001* was retained because the weighting of relative shear stresses in the third invariant allows one to introduce asymmetry in the yield locus. Such an asymmetry is to be expected due to a combination of the two crystallographic systems. *CB2001* defines an equivalent stress following Drucker's function

$$\sigma_{\text{eq}} = \sqrt{3}\sqrt[6]{\left(J_2^O\right)^3 - c\,\left(J_3^O\right)^2} \tag{4.25}$$

where J_2^O and J_3^O are the generalized J_2 and J_3 invariants embedding the material orthotropy. They are fully determined from the coefficients $a_k\,(k = 1...6)$, $b_k\,(k = 1...11)$ and c (18 coefficients in total)

$$J_2^O = a_6\,s_{yz}^2 + a_5\,s_{xz}^2 + a_4\,s_{xy}^2 + \frac{a_2}{6}\left(s_{yy} - s_{zz}\right)^2 + \frac{a_3}{6}\left(s_{xx} - s_{zz}\right)^2 + \frac{a_1}{6}\left(s_{xx} - s_{yy}\right)^2 \tag{4.26}$$

$$
\begin{aligned}
J_3^O =& \frac{1}{27}\left(b_1+b_2\right) s_{xx}^3+\frac{1}{27}\left(b_3+b_4\right) s_{yy}^3+\frac{1}{27}\left(2\left(b_1+b_4\right)-b_2-b_3\right) s_{zz}^3 \\
&-\frac{1}{9}\left(b_1\, s_{yy}+b_2 s_{zz}\right) s_{xx}^2 \\
&-\frac{1}{9}\left(b_3\, s_{zz}+b_4\, s_{xx}\right) s_{yy}^2 \\
&-\frac{1}{9}\left(\left(b_1-b_2+b_4\right) s_{xx}+\left(b_1-b_3+b_4\right) s_{yy}\right) s_{zz}^3 \\
&+\frac{2}{9}\left(b_1+b_4\right) s_{xx}\, s_{yy}\, s_{zz} \\
&-\frac{s_{xz}^2}{3}\left(2\, b_9\, s_{yy}-b_8\, s_{zz}-\left(2\, b_9-b_8\right) s_{xx}\right) \\
&-\frac{s_{xy}^2}{3}\left(2\, b_{10}\, s_{zz}-b_5\, s_{yy}-\left(2\, b_{10}-b_5\right) s_{xx}\right) \\
&-\frac{s_{yz}^2}{3}\left(\left(b_6+b_7\right) s_{xx}-b_6\, s_{yy}-b_7\, s_{zz}\right) \\
&+2\, b_{11}\, s_{xy}\, s_{xz}\, s_{yz}
\end{aligned}
\tag{4.27}
$$

The model reduces to an isotropic behavior when the 18 orthotropy parameters are equal to 1.

In this case the hardening is isotropic and follows an exponential law $R(p) = R_{inf} + (R_0 - R_{inf})\exp(-bp)$ where R is the hardening variable, p the plastic strain increment, R_0, R_{inf} and b three parameters. The equivalent stress is defined in Equation (4.25). It is noteworthy that for a uniaxial loading in the XY plane, only 8 parameters (a_1, a_2, a_3, b_1, b_2, b_3, b_4 and c) over the 18 are necessary to describe the yield surface. They are the only one reported in the following for clarity.

Parameters of this phenomenological model were fitted from the average response of the lath packet unit cell (Figure 4.11 and Figure 4.12) by enforcing the unit cell average stress to be equal to the stress $\boldsymbol{\sigma}^m$ computed by the *CB2001* model

$$
\frac{1}{V}\int_V \sigma_{ij}\mathrm{d}V = \sigma_{ij}^m \tag{4.28}
$$

where V is the unit cell volume.

The unit cell average behavior follows both phases hardening rates, but their individual evolution is not monotonic with the macroscopic imposed load. It results in an evolution of the effective load surface shape that cannot be modeled by the isotropic hardening law considered for now. The combination of two behaviors and the coupling phenomena between slip planes in each of the laws contribute to the anisotropy of work hardening. Although these phenomena are complex, it is worth recalling the actual result of the field measurements from the previous chapter. The deformation mechanisms at the lath pack scale do not change (or change slightly) during loading. They initiate by following local morphological and crystallographic properties and amplify with the imposed strain. Conducting a *limit analysis* of this behavior seems appropriate. In this sense, the mechanisms at the beginning of the plasticity have very little influence on the behavior at a high strain level. Therefore, we chose to give more importance to high strain levels in calibrating the *CB2001* model parameters. The hardening parameters are identified considering all strain levels. On the other hand, the orthotropy coefficients are identified for plastic strain levels ranging from 10% to 30%.

The optimal parameters for the lath packet behavior computed with the initial set of parameters given in Section 4.1.4 (unaged case) and for an initial critical resolved shear stress r_0 of 1000 MPa in ferrite (longly aged case) are summarized in Table 4.4. Figure 4.13 compares the load surfaces for the unaged case at four different plastic strain levels for the identified *CB2001* constitutive law and the unit cell response in the XY plane of the unit cell frame. The identified model shows that such a simple model makes it difficult to accurately represent the anisotropy of the elemental cell strain hardening at all strain levels. In contrast, the model also shows that we obtain a fair approximation at high strain levels with these simplifications. *CB2001* formulation adequately reproduces the significant anisotropy resulting from the unit cell configuration. The error cannot be quantified precisely pointwise because of the plastic bifurcation. A quick reading of the graphs gives an approximate maximum error of 20 MPa, where the composite surface is the most disrupted.

Table 4.4: Optimal *CB2001* constitutive parameters for the lath packet unit cell.

	R_0 (MPa)	R_{inf} (MPa)	b	a_1	a_2	a_3	b_1	b_2	b_3	b_4	c
unaged	142	297	48	0.60	1.05	0.83	1.44	0.51	-1.48	-0.50	1.50
aged	122	644	51.8	0.60	1.00	0.83	1.50	0.50	-1.50	-0.50	1.50

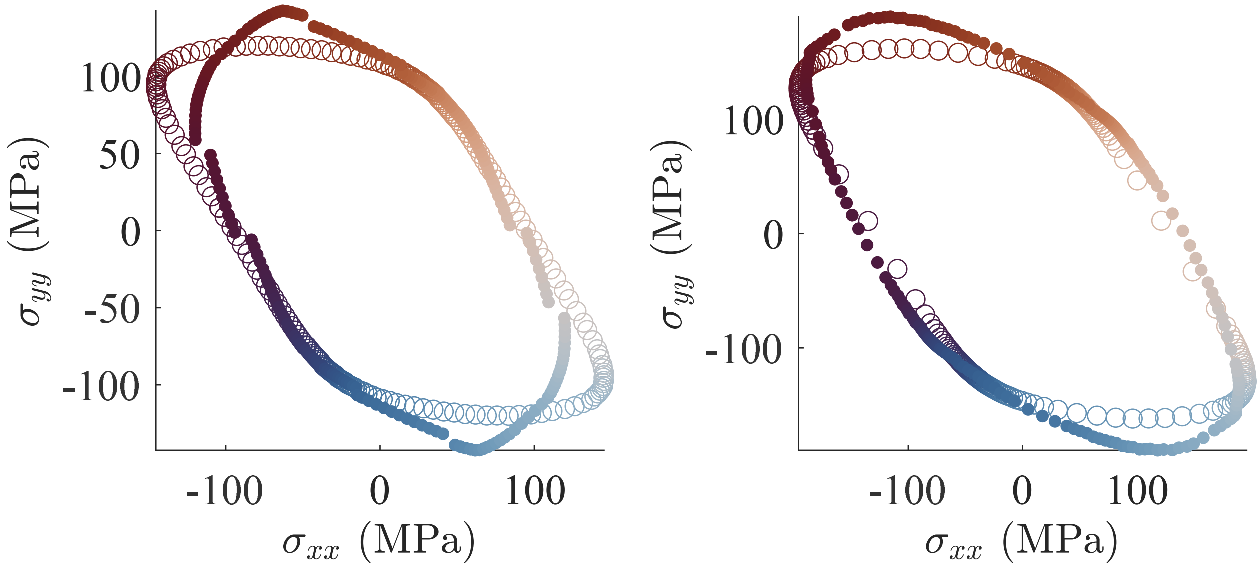

(a) $\varepsilon_p = 0.001$ (b) $\varepsilon_p = 0.01$

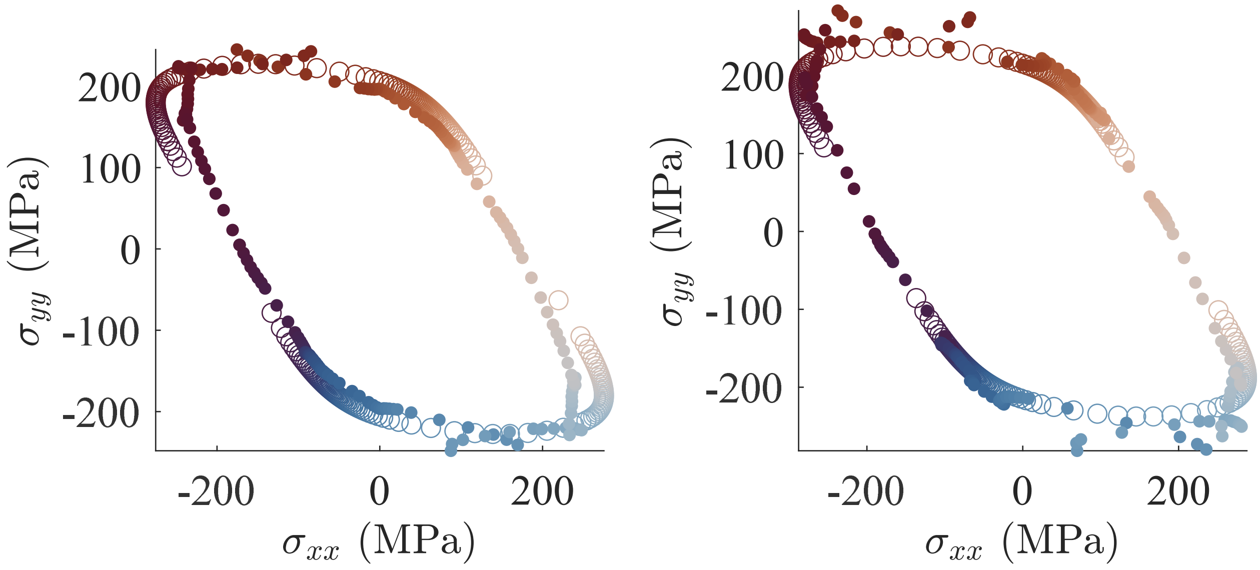

(c) $\varepsilon_p = 0.05$ (d) $\varepsilon_p = 0.1$

Figure 4.13: Comparison between load surfaces in the *XY* plane for average unit cell behavior and *CB2001* identified behavior for the unaged case. Filled circles correspond to the unit cell, empty markers correspond to the identified law response.

Regarding the assumed aged state case depicted in Figure 4.14, conclusions on the representativity of the mean-field model at the different strain levels are the same. We also naturally find a higher tensile strength. Nonetheless, if it turns out that the coarse description of aging chosen is confirmed, we show that an increase of the critical resolved shear stress has minimal impact on the effective anisotropy.

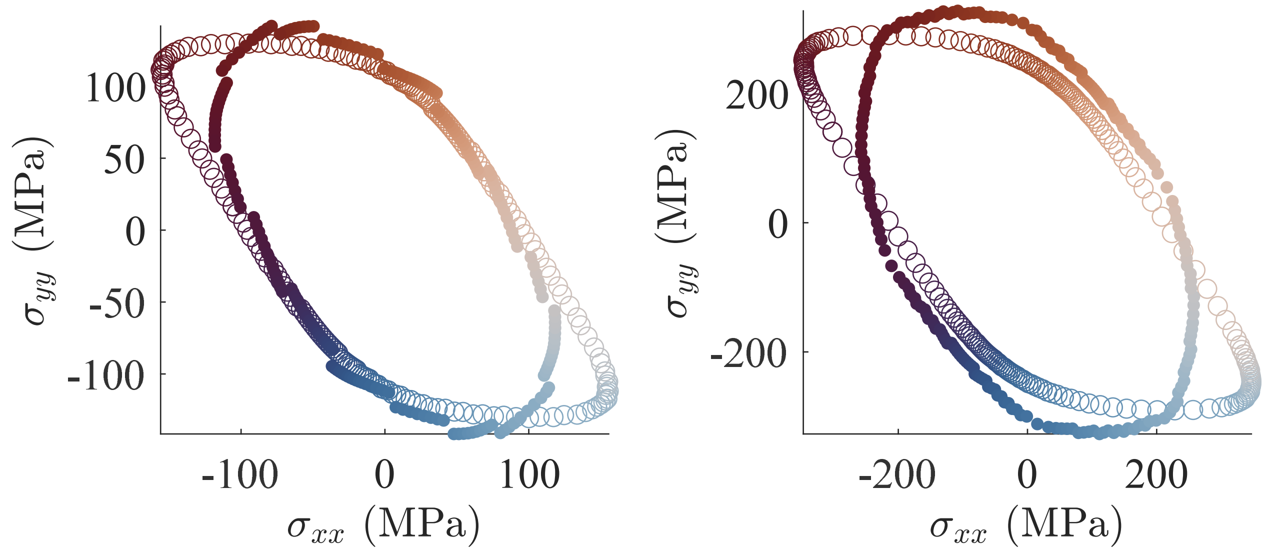

(a) $\varepsilon_p = 0.001$

(b) $\varepsilon_p = 0.01$

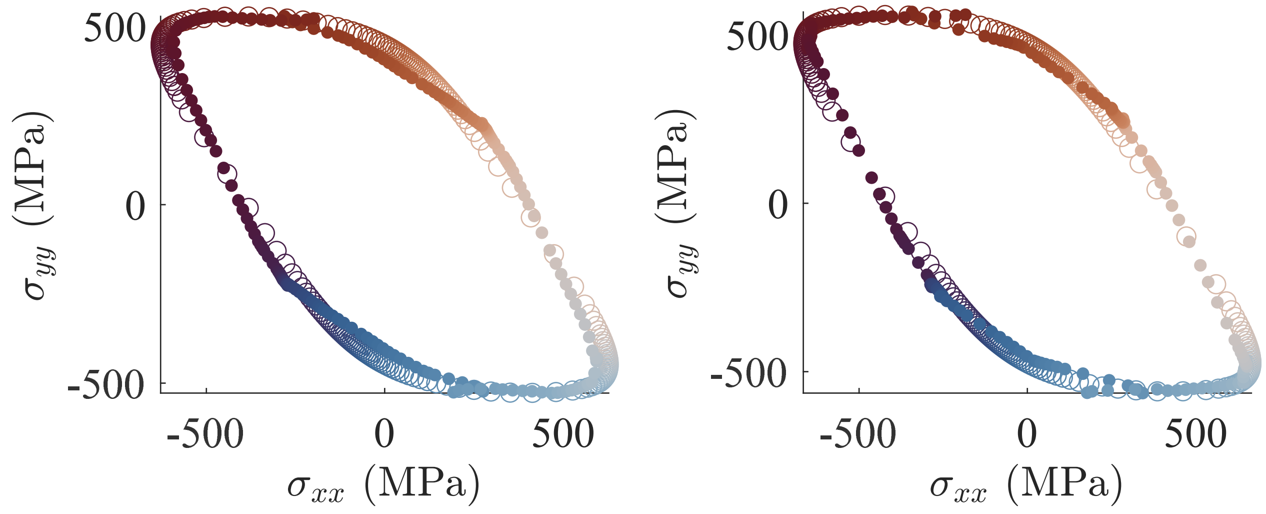

(c) $\varepsilon_p = 0.05$

(d) $\varepsilon_p = 0.1$

Figure 4.14: Comparison between load surfaces in the *XY* plane for average unit cell behavior and *CB2001* identified behavior for the longly aged. Filled circles correspond to the unit cell, empty markers correspond to the identified law response.

The previous results show that it is possible to reproduce the equivalent behavior of lath packets accurately. In particular, the anisotropy at high strain levels is reliably reproduced from a relatively simple formulation. This anisotropy is pronounced and appears insensitive to a variation in the ferrite critical resolved shear stress. If this simplified modeling of the influence of aging on mechanical behavior is relevant, then the latter does not give more weight to the anisotropy of the behavior. In this case, the transition between anisotropy at the onset of plasticity and high plastic strain may require further investigation.

4.3 Toward representative synthetic CDSS microstructures

4.3.1 Benefits of microstructure generation models

This section deals with preliminary steps for a CDSS microstructure generator. Direct acquisition of microstructures is complex because it involves experimental measurements that are time-consuming and difficult to perform. Moreover, the CDSS microstructure is likely to be described by a large number of parameters compared to more conventional ones. All these specificities ensue from sophisticated solidification mechanisms explained in Chapter 2. Studying the effect of all parameters would require a considerable amount of material that is not available. However, explicitly modeling microstructures is beneficial as it allows one to generate realistic 3D microstructures from 2D observations and hence to come up with extrapolation procedures that would allow statistical sampling and further assess the robustness of the 2D identification. In the case of “standard” microstructure layouts, the macroscopic mechanical response is well estimated by generating models with basic tesselation algorithms. Tesselations consist in subdividing a given spatial domain into subsets called cells and representing grains in the microstructure framework. For instance, the most straightforward implementation of the well-known Voronoï tesselation allows one to study grains size, shape, and constitutive law effects on macro and microscopic fields by subdividing space into convex polytopes [Zeg07]. More complex tesselation algorithms include multiple parameters aiming at reproducing grain morphology. In this way, grain size, aspect ratio or grain boundary curvature distributions can be followed to fit those observed experimentally.

Generating a microstructure from statistical descriptors is not always easily achieved. The CDSS microstructure is a nice example with visible recurrent features (such as laths or crystallographic homogeneous regions corresponding to ferritic grains) that are not necessarily easy to describe geometrically. In particular, the lath cluster shape is not easy to apprehend but is required to build a geometrical model, including the intermediate scale described in Section 4.2.2. An entire thesis was devoted to understanding this lath structure to generate representative models based on morphological descriptors [Mes97]. Unfortunately, experimental techniques were not as developed as in the present framework, and physical data were not included in the aforementioned model. Understanding physical data allowed the morphological features to be described from the solidification steps and laths growth directions to be unveiled (see Chapter 2). Consequently, they should be embedded in a microstructure generation procedure.

4.3.2 Approach for CDSSs microstructure

The following approach is devoted to interpreting experimental and "EBSD-based" models meaning rather than comparing quantitatively experimental fields and simulations. The latter would require comparing morphological descriptors that are not yet defined in generated and experimental microstructures. The overall idea is then to reproduce the hierarchical geometry resulting from the two main steps of the microstructure formation with a phenomenological approach choosing the most simple assumptions. These steps include the first transformation from liquid to solid, resulting in a complete α-grain network and the growth of austenitic laths. One can expect that the interlocking of the two phases resulting from the preferential growth of the laths in specific directions will have the properties observed experimentally. The remarkable properties that have a now demonstrated effect on the deformation fields are:

- The morphology of the primary ferritic grain network.
- The austenitic border replacing the primary grain boundaries.
- The network of lath packets in each ferritic grain.

The parameters that would attest to the good representativity of the generated models are discussed in the following. Since they could not be characterized, only qualitative aspects are given for the time being. Thus, a particular effort is made to reproduce the mechanisms of microstructure formation as they have been understood. To a reasonable extent, the relevance of the model can therefore be certified without quantitative comparison.

Primary ferrite grain network

The primary ferrite grain network results from a liquid to solid transformation. In the whole study, it was chosen to focus on the core microstructure of statically cooled components having equiaxed ferritic grains. The geometrical configuration of random equiaxed grain growth is accurately described by spatial processes of simple geometries (*e.g.*, spheres for a Voronoi tesselation) providing an input probability (*e.g.*, spatial distribution of seeds). The CDSS primary α-grain radius is millimetric. Thus, a volume containing several grains in the three cartesian directions (say ≈3 full grains) is defined. Such a configuration roughly corresponds to a set of N_{seed} = 50 uniformly distributed in a unitary volume. The Voronoi unit cells corresponding to each seed are computed and regularized to remove small edges following the method proposed by Nygårds and Gudmundson [Nyg02] and further applied by Quey in Neper software [Que11]. This regularization step is essential for the following steps not to introduce extra junctions between grains that would not be relevant from a physical point of view. We may note that reconstructed primary ferrite grains in Chapter 2 display grain boundary curvature that may be accurately reproduced, adding a surface tension interpretation of this process and a corresponding time-scale for relaxation driven by surface tension. The resulting space partition is given in Figure 4.15.

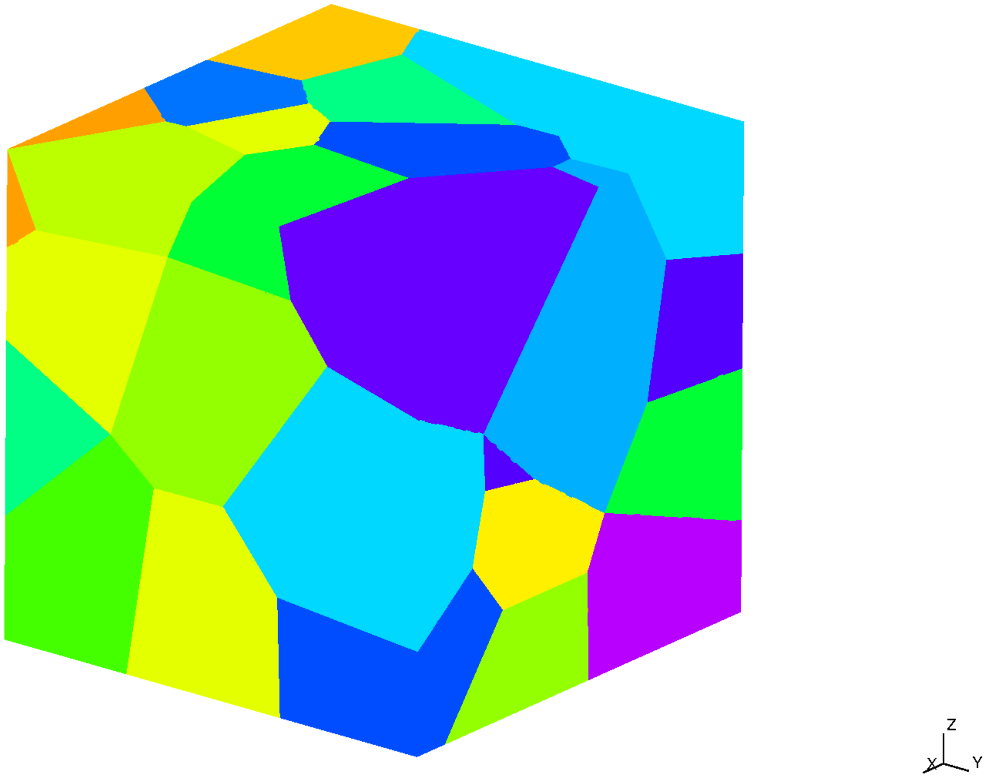

Figure 4.15: Ferrite Voronoi microstructure for N_{seed} = 50.

Primary grain subdivision

The second scale highlighted in the microstructure is the lath packet network. This geometrical description is required to carry out the upscaling (along the lines of the previous section). Lath packets are encapsulated in ferritic grains. However, adjacent packets at ferritic grain boundaries may share properties depending on the local configuration (termed coherent and incoherent in Chapter 2). It was deduced from this observation that, in the observation plane, the former ferritic grain boundaries were first transformed into a thin austenitic layer. Then, laths grew from these austenitic layers. In the 3D geometry, the γ-lath nucleation sites are presumably geometrical points where the grain boundary interface energy is relatively high *i.e.,* points joining three or more grains. Figure 4.16 depicts an orientation map where the observation plane is close to a real junction point in the complete 3D microstructure (denoted V_{j_1}). This hypothesis is deduced from the fact that the orientation corresponding to this junction (colored in orange-red) propagated in the three available grain boundaries (of the observation plane) from this starting point to meet the transformation front from other junctions (V_{j_2} and V_{j_3}). The farther the observation plane from such point, the more likely to present multiple orientations at boundaries instead of one. We can note that the position of the interface between the two transformation fronts indicates an asymmetry in growth rates or relative nucleation times. However, it would be necessary to know the exact position of all these points in 3D to be able to quantify them.

A second feature to introduce is the compatibility of a selected γ-orientation with adjacent ferritic grains. In Figure 4.16, the orange-red orientation selected at junction point V_{j_1} is compatible with the primary grain denoted G_1. In other words, the austenite layer that grows from the ferritic grain boundary and subsequent inner laths growing from this layer satisfy an orientation relationship with G_1 only. That is, red-orange "laths" truly are laths in G_1 (represented by dashed arrows in Figure 4.16) but grew with more constraints (wavy dashed arrows) in G_2 and G_3 because of crystallographic "incompatibility". This aspect may influence the final geometry of the α-γ composite ranging from sharply defined laths to more globular spinodoid microstructures. Similarly, it may also control the packet extent with respect to the point from which they nucleate, but this information is difficult to characterize without a detailed 3D view inside the microstructure.

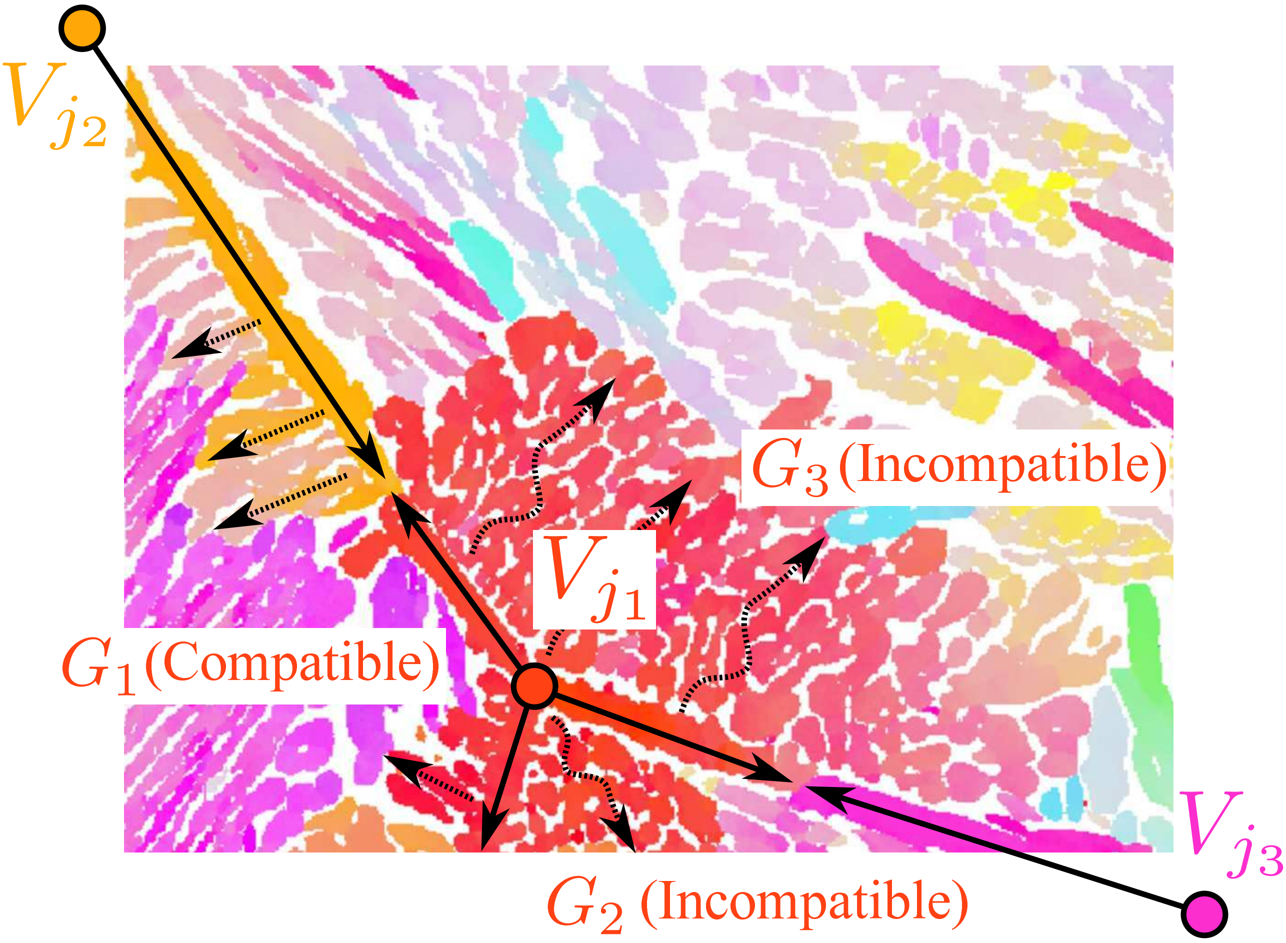

Figure 4.16: Schematic view of γ-laths growing from ferritic grain boundary junctions.

Lath packet extent is thus resulting from that of their constitutive laths. Therefore, lath and lath packet scales are not independent, but simplifications can be tolerated when formulating a very first growth model. The main steps for subdividing α-grains into lath packets considering the phenomenology of lath growth are summarized in Figure 4.17. For the sake of clarity, the focus is put on a single grain shown in Figure 4.17 (a). Junction points are to be retrieved from the α-grain network depicted in Figure 4.15. This simple operation consists in extracting vertices defining the grain edges. However, the number of primary grains connected to each junction point fluctuates, and they are not all associated with an actual nucleation site. Assuming that the interface energy at grain boundary junctions is increasing with the number of grain meeting at these junctions, a first simplification is to keep only the vertices connecting four grains or more to be lath nuclei. This operation defines the seed point set $\{V_{j_i}\}$ for boundary austenitic layers. The colored points depicted in Figure 4.17 (b) correspond to the vertices kept for the top surface. The blue points are the other junctions belonging to this grain and connected to four or more grains. Each vertex is then assigned to a Pitsch variant of one connecting grain. Thus, a junction point also includes the information of the parent grain from which the child orientation was chosen (and stored in an *id* vector $\{G_{id_i}\}$ of the size as $\{V_{j_i}\}$). To model the austenitic layer at grain boundaries, boundary points of all grains are then linked to the closest vertex *i.e.,* an isotropic growth in the boundary planes from these junction points is assumed (Figure 4.17 (c)). A differential growth rate is assumed to have little influence on the final shape of the network. In particular, its influence in front of the morphological anisotropy of the packets is assumed to be negligible. Moreover, we did not observe any case where a junction propagated over a long enough distance to occupy an entire primary grain boundary. Subsequently, if this parameter proves essential in view of new observations, it is easily parameterized to follow an imposed growth rate.

The last step is to attribute inner grain points to a lath packet. The contour of lath packets can sometimes be very irregular. This irregularity is mostly attributed to a few laths whose spatial extent is much greater than the other laths in the bundle. To reproduce this effect, boundary planes are discretized into a finite number of points representing initial lath nuclei at the boundary (Figure 4.17 (d)). The preferential growth direction is determined from the Pitsch variant of their parent junction. While these directions are known in grains whose austenitic orientation belongs to a Bain group, the growth direction is unknown in other cases. Since junction points are shared between four or more grains by definition, more than 75 % of lath packets would be incoherent with the ferritic grain in which they grow. This trend is not observed experimentally because some accomodation steps in the growing process are at play (variation of the θ parameter introduced in Chapter 2.4.3.1 and laths nucleating inside grains instead of boundaries). To better comply with the statistics observed experimentally, a strong simplification is to replace incompatible inner orientations with random compatible ones. This hypothesis is debatable but can be defended for several reasons. More than 70% of the experimentally measured lath packets are on Bain circles. Since only about a quarter of the nuclei do not respect Pitsch, three scenarios can reach this 70%.

- The first is to assume that the non-coherent packets have a much lower growth rate in the grain than the coherent packets. In this scenario, only one or two packets cover the 70% coherent volume unless the number of germination sites is underestimated (this number strongly depends on the regularization conducted in the generation of the ferritic grain network).

- A second scenario is a non-negligible proportion of lath packets whose germination occurs inside the ferrite grains and not at the boundaries as postulated so far. Thus, they have no initial crystallographic constraints and can freely belong to the Bain groups. This scenario is implausible. We do not exclude that the conditions are met to have internal seeds. However, the numerous orientation maps observed during this study almost always show a continuity of orientation at the primary grain boundaries. When this is not the case, the packet is large enough to come from an out-of-plane grain boundary with which the continuity exists. We then find ourselves in the configuration of the first scenario.

- The last option is that inconsistent grain boundaries are quickly accommodated by crystallographic rotation in most cases. Over a short distance, laths grow with difficulty because they are incoherent with the parent grain. A rotation towards the nearest Pitsch variant occurs to grow under more favorable conditions.

The final microstructure is probably the result of scenarios one and three, which could be observed in the EBSD sections. The simplest one to implement is the third one because we can neglect the accommodation zone to retain only the coherent volume. For simplification and illustration, only this scenario is retained for the following. However, it can easily be combined with the first for model refinement purposes, especially to reach the experimental coherent/incoherent ratio.

Thus, we postulate that all laths obey the Pitsch OR. Hence, the growth direction is known for all lath packets. From the known growth direction, each point $\boldsymbol{x}_i$ inside the current grain is attributed to the closest boundary lath nuclei n_{id_i} located by the vector $\boldsymbol{n}_i$ by computing the following distance

$$\boldsymbol{n}_{id_k} = \underset{i}{\operatorname{Argmin}}\, \mathrm{d}_{\boldsymbol{x}_k}(\boldsymbol{n}_i) \tag{4.29}$$

with

$$\mathrm{d}_{\boldsymbol{x}_k}(\boldsymbol{n}_i) = \sqrt{\lambda a_i^2 + b_i^2 + c_i^2} \tag{4.30}$$

where $\boldsymbol{w}_i = (a_i, b_i, c_i)$ and $\boldsymbol{w}_i = \boldsymbol{R}_{\boldsymbol{x}_k}\boldsymbol{n}_i$ with $\boldsymbol{R}_{\boldsymbol{x}_k}$ a rotation centered about $\boldsymbol{x}_k$ aligning the global frame with the lath normal, λ the anisotropy factor characterizing the preferential direction. It is set to 10 in the following. The nuclei selection process is illustrated in Figure 4.17 (e).

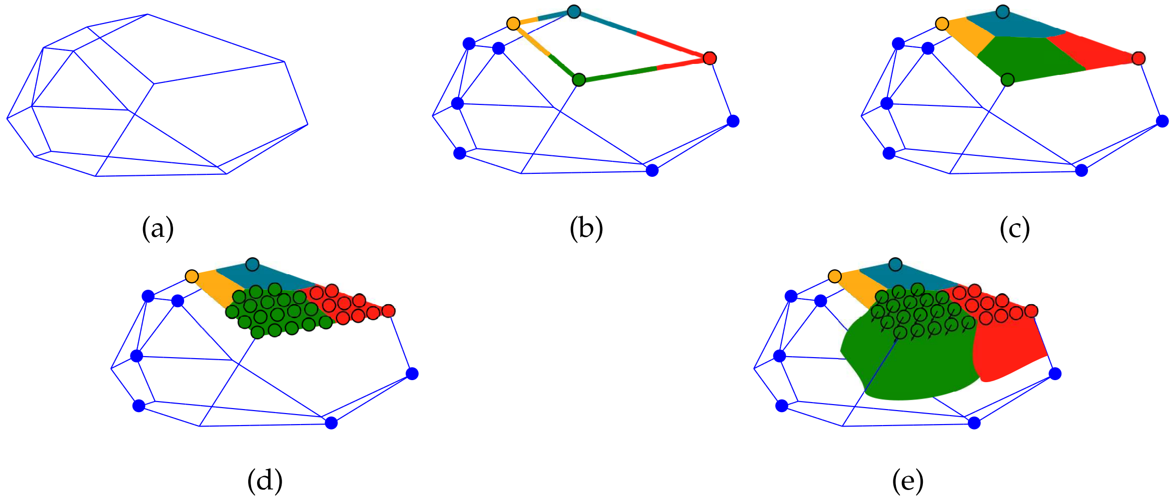
(a) (b) (c)

(d) (e)

Figure 4.17: Illustration of the different steps for subdividing ferritic grains into lath packets. (a) A single ferritic grain is extracted from the regularized Voronoi tesselation. (b) Detection of junction points defining boundaries nucleation sites. (c) Assignment of ferritic grain boundaries to a junction point. (d) Discretization of ferritic grain boundaries into lath nuclei. (e) Anisotropic growth of lath packets from segmented boundaries into preferential directions following $\{\overline{2}, 1, 1\}_\alpha$

The final segmentation on a small volume is displayed in Figure 4.18. A unique ferrite grain network is considered for two orientation draws. Figure 4.18 (a,c) shows the ferrite grain orientations in the two cases. The subdivisions of the same grain networks into lath packets are given in Figure 4.18 (b,d). The specific shape of lath packets seems well reproduced. Despite some irregularities due to the coarse mesh discretization, properties like packets non-convexity are allowed with the current procedure while respecting the phenomenology of lath nucleation. Figure 4.18 (b,d) emphasize the complex layout at the scale of a small volume, including several ferritic grains. A relevant coarse description of packets seems to be reached. Of course, these considerations are purely qualitative. They arise from the fact that we explicitly included our experimental observations. The result is that the entanglement of the packets inside the grains visually matches that observed experimentally. However, we have introduced enough parameters to influence the properties of each entity significantly. It is, therefore, still necessary to introduce the proper parameters measurable on the experimental microstructure to calibrate this model. Suitable morphological descriptors are still to be determined. The model could be improved using a better discretization of the volume, particularly of the ferritic grain boundaries, to reproduce the extension of laths rather than isolated points. However, the developed tool provides the first meaningful representation of CDSSs microstructures. Data at boundaries permit the restoration of the thin austenitic layer embedding ferritic grains, and laths packets can be explicitly discretized in laths to compute costly but meaningful mechanical responses. Last, the present model provides means for studying the last upscaling, including geometric parameters that were so far missing. The construction of RVEs enables the determination of macroscopic response from the constitutive laws introduced in the previous parts. Nevertheless, most of this program remains to be done in the future.

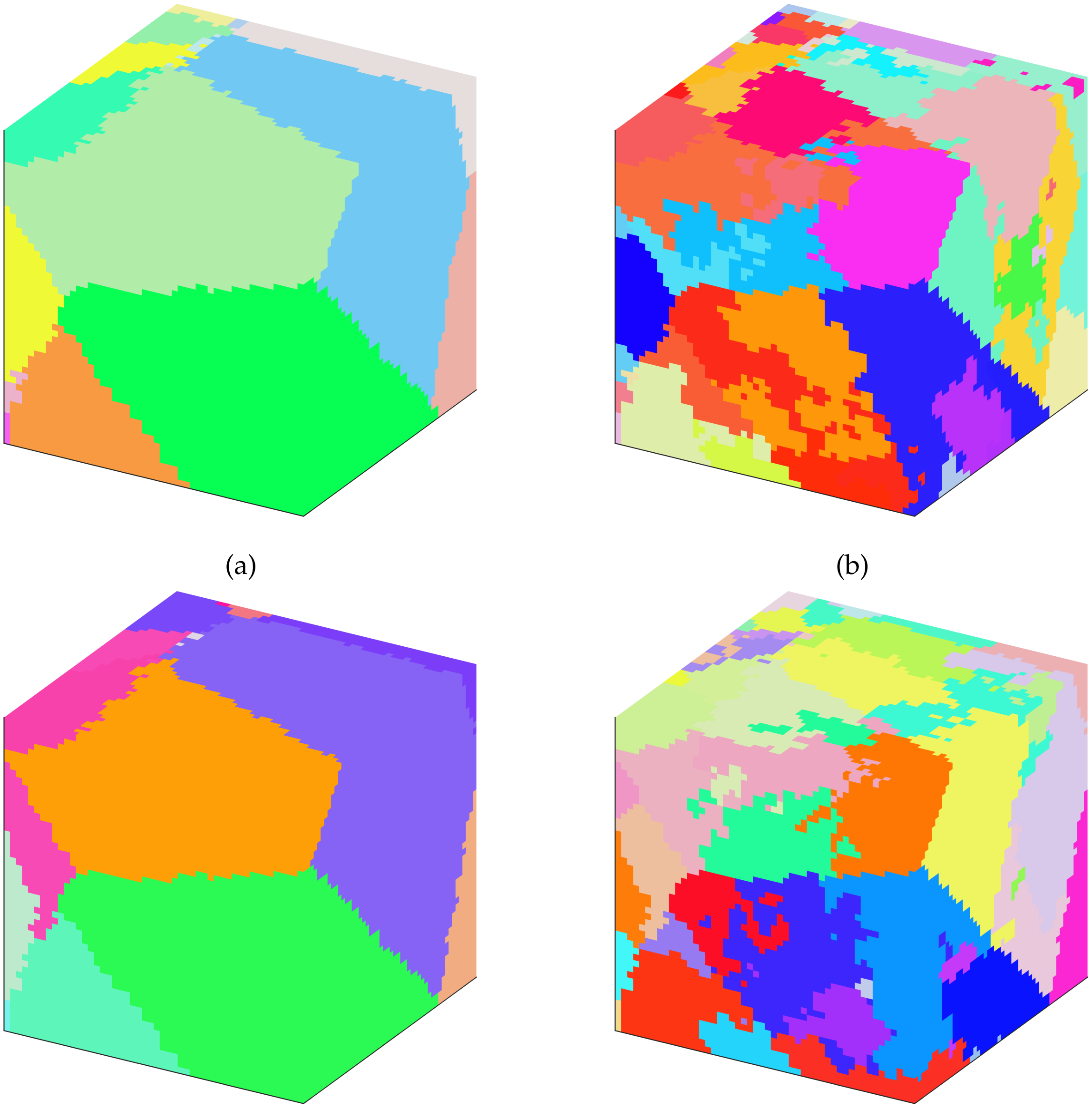

(a) (b)

(c) (d)

Figure 4.18: Illustration of the lath packet segmentation in a small volume containing several ferritic grains for two ferritic orientations draw. Orientations for both phases are colored using an IPF color code. (a) Ferritic grain layout in the volume for the first orientation draw. (b) Lath packet segmentation for the first draw. (c) Ferritic grain layout for the second orientation draw. (d) Lath packet segmentation for the second draw.

4.4 Conclusion

A general workflow to identify and model the behavior of CDSSs was proposed by taking into account microstructural and experimental data from the previous chapters. Phenomenological constitutive laws and associated hypotheses deemed representative for the two phases were presented. A global homogenization approach has also been introduced to predict the macroscopic response from this microscopic scale description. It is decomposed into two steps consistent with the hierarchical microstructure description and follows both mean-field and full-field approaches.

Regarding the workflow application, challenges for identifying parameters from the present full-field measurements were addressed. The difficulty in building a multi-scale model of CDSS matches the complexity of their microstructure. The results of the simplified computations illustrate that the material behavior cannot be faithfully reproduced without data in thickness. The quasi-2D and 3D models on a thin layer significantly constrain the in-plane shear stresses. As a result, the mechanical components emanating from the small geometric features become very prominent compared to experimental results. Given this conclusion, the development of models of knowledge or extrapolation of the microstructure from the surface measurements is necessary. Thus, field measurements could be exploited to identify the constitutive parameters while evaluating the uncertainties related to the missing underlying data.

With the available data, the two intended homogenization steps were studied. The first upscaling providing a schematic definition of lath packets was introduced using a mean-field approach. The apparent geometric simplicity does not conceal the underlying complexity of the combined polycrystal model resulting in non-linearities that are not easily modeled by simple homogenization rules. Therefore, a dedicated method may be necessary in the future to determine phases and effective mechanical fields correctly. The last upscaling covering the geometrical specificities of CDSS microstructure may be a relevant tool to assess the relevance of the previous modeling steps at lower scales. It was proposed to resort to a random microstructure generation. This model for the grain microstructure was based on our understanding of the formation of the different phases and was designed to capture the physical mechanisms of their entanglement. Taking into account the ferritic grain layout and laths preferential growth directions, the subdivision of primary grains has been reproduced. The proximity between generated and experimental microstructures is to be assessed quantitatively by extracting relevant morphological descriptors that are not yet available.

Chapter 5

General conclusion

5.1 Summary of the thesis

Microstructural characterization

The present study has contributed to understand deformation mechanisms in CDSSs, considering the role of their specific microstructure. The latter was strongly approximated in previous modeling approaches until now. The large surfaces characterized by EBSD, thanks to the dedicated tools developed along this work, allowed us to quantify the morphological and crystallographic characteristics of the microstructure. Apart from the nanometric scale, where the main aging mechanisms of the ferritic phase are described, one may distinguish four fundamental scales:

- Lath scale
- Lath packet scale
- Primary ferritic grain scale
- RVE scale

The relevance of these scales is not entirely new since they had already been mentioned by previous contributions as relevant in the study of the mechanics of CDSS alloy. However, new results come from the dedicated EBSD maps acquired in this study.

1. The different scales of the microstructure are interlocked. The latter can be decomposed hierarchically.

2. There is a substantial variability in the morphology of the laths at their scale, already observed on optical macrographs. The local morphology is related to the growth mechanisms of the laths and is correlated to the crystallography of the two phases. One speculates that a diffusional-displacive coupling is explaining their growth, but it has not yet been investigated.

3. All these results allow for a schematic approach to decompose the microstructure from the crystallographic data. It gives access to the 3D orientation of the laths and the OR linking the two phases.

Mechanical characterization

On the mechanical side, we developed an accurate method to correlate large *in situ* full-field measurements with EBSD maps. Several results are derived from their observation.

1. The intertwined character of the microstructure seems to be of second order in the description of the mechanical behavior. Conversely, the elongated shape of laths, which was put aside in previous studies, allows us to explain the different deformation modes of the lath packets. The relative orientation of the laths with respect to the macroscopic loading direction seems to be very influential for the deformation modes. A simple schematization by a laminate offers a good description of the microstructure to account for initiation of deformation mechanisms and the distribution of strains in the two phases.

2. Understanding the microstructure has also shown that former ferritic grain *boundaries* are geometrically prone to concentrating strains.

3. The effect of aging is still challenging to quantify, but stress/strain measurements show clear embrittlement. However, the microstructure does not change at the studied scales. The reduced dislocation mobility in aged alloy tends to increase ferrite yield stress drastically. This factor is responsible for stronger macroscopic strain localization and hence severely increased stresses in ferrite that may either enforce (localized) plastic flow or generate damage nucleation sites. Both may lead upon further loading to fracture.

4. Austenite concentrates most of the strains in the as-received state. Ferrite hampers

the transmission of strains initiated in austenite for this state but does not pin them. Austenite and its local properties control strain distributions.

5. Ferrite crystallographic orientation is of increasing importance with aging. The orientation of very aged ferrite becomes a determining factor in the localization of strain despite its low volume fraction.
6. Combining all crystallographic parameters limits the number of easily strained regions in the highly aged material. As a result, strains are very localized for very aged states.
7. Ferrite embrittlement seems to put more pressure on primary ferritic grain boundaries.

Multiscale modeling of CDSS alloy

A multiscale model in agreement with the previous observations has been proposed to describe the behavior of CDSS alloy. Due to the above-discussed (underlying) hierarchy, it would have been tempting to propose an equivalent behavior to the four introduced scales through a multi-step homogenization scheme. On the one hand, homogeneous orientation and morphology regions describe the lath distributions appropriately over a large volume. The same holds true for lath packets since they are a natural extension of the previous description. On the other hand, the scale of ferritic grains is not uncorrelated from sub-scales. If the continuity of the ferritic phase is preserved, strong inhomogeneities are observed within the domains they delimit. These heterogeneities increase with aging. We concluded that the lath packet network is the last relevant homogenization scale before the RVE. The proposed homogenization scheme is thus composed of two steps:

- A homogenization of laths with a schematic unit-cell and a mean-field model. A phenomenological crystal plasticity law describes the lath behavior.
- A homogenization of the lath packets by a phenomenological full field model.

It has been shown that it is possible to correctly approximate the behavior of the selected unit cell with a simple model. We have chosen to focus on the behavior at high strain levels, with particular emphasis on the anisotropy that seems very pronounced even for macroscopic tests. The chosen approach can be suitably refined if necessary in the application of this method.

To perform the homogenization up to the RVE, it was proposed to describe the geometry of lath packets. The continuity of the ferritic phase and the austenitic band at the boundary of the primary grains are also described as they proved influencial in the mechanical fields. For this purpose, a phenomenological model of microstructure generation was set up. This model describes the different steps of the formation process and has enough flexibility to be adjusted to experimental microstructures. Given its simplicity, extracting the relevant morphological parameters to calibrate this model may prove interesting. It may provide a simple comparison of mechanical fields at the scale of the batten bundles with the experimental one.

Concerning the identification of constitutive parameters, the optimal approach using the same mesh for DIC and simulations could not be achieved until the end. The problem of extrapolation of the microstructure and boundary conditions in depth persists.

5.2 Perspectives

Toward a micromechanical model including thermal aging effects

With the proposed multiscale model, micromechanical modeling of CDSS, including all essential microstructural features, seems feasible. It remains to be verified that the increase of the critical resolved shear stress with thermal aging at the lath scale is a good description of the embrittlement mechanisms. Nevertheless, the evolution of this parameter is not yet well understood quantitatively. To identify it precisely, along with the other parameters of the model, it will be necessary to address the remaining challenges in the identification process based on field measurements.

Intending to conduct the upscaling to the RVE, it is also necessary to identify and measure the suitable morphological parameters to match those of the lath packet network generation model. The experimental data acquired in this study should be sufficient to propose a good statistic.

Subsequently, the generation model can be extended to the columnar microstructure constituting the skin of CDSS pipes by considering the elongated ferritic grain shape and crystallographic texture of the two phases.

Eventually, the model can be refined to understand damage mechanisms where the distribution of lath sizes and particular morphological aspects seem to play a more preponderant role.

Finer characterization of mechanical fields

A very large-scale characterization technique with a good compromise on the measurement resolution has been developed during this study. If it was necessary to refine the model, performing more local measurements with a higher resolution could be beneficial. The current measurements do not allow one to understand precisely the activation of slip planes in both phases and the strain distributions at the lath scale. Such study could help understand damage onset and growth in ferrite.

Additional characterizations may also be considered to identify the two phase behavior. Tests on micro-pillars conducted at GPM Rouen in collaboration with EDF have shown interesting results on the evolution of the behavior with ferrite. Other studies proved successful by coupling nano-indentation tests and topographic measurements by AFM [Zam12, Ren16]. Both could be considered to complete the current measurements and overcome the identification challenges using full-field measurements. However, these techniques have their own limitations and require a certain mastery.

Robust identification on polycrystals from field measurements

A final point concerns the exploitation of measured fields. They include much richer information than the local characterization methods mentioned above (micro-pillar and nano-indentation). In particular, they translate structural effects, which are essential to understanding deformation mechanisms. All studies addressing the identification of crystal plasticity parameters have faced the problem of extrapolation of the information acquired on the surface. To this day, it remains a challenge and is an obstacle to the full exploitation of rich fields made available by modern measurement techniques. To account for the underlying microstructure better than through a mere extrusion, it is necessary to develop a method for the statistical evaluation of surface field sensitivity. The proposed method will have to answer the following question: *how to predict the in-depth microstructure from data acquired at the surface?* Part of the answer is direct: the continuity between the two must be ensured. The second part involves a descriptive model that does not betray the morphological properties of the microstructure.

Two cases are possible. In the first case, the microstructure is easily parameterized. If these parameters are known and not numerous, a representative statistics on 2D sections to measure them may be within reach. In that case, only the problem of matching the observed planar data remains to be addressed. This problem seems rather well-posed in the case of simple microstructures such as those of Voronoi type. In the second case (to which the CDSS microstructure probably belongs), a simple parameterization is not available. Only a statistical description is possible through the acquired images. Recent developments in statistical image characterization techniques have shown that generating images with a striking similarity compared to inputs is possible. Among them, we may note deep learning convolutional neural network methods [Gat15] or simplified methods based on wavelet transforms [Ust17, Bro22] or random fields [Kum16, Sen22] requiring only one or a few images. The first method allows one to reach exceptional results, but the number of parameters and the resulting statistics is not or hardly interpretable. Moreover, its implementation is expensive and complicated. On the other hand, the second type of methods, embodying a simplification of the first one, seems much more accessible and consistent with the subject of microstructure modeling. In particular, they can be used alongside physical data (extracted from a model or experimental measurements) and link statistical parameters and geometrical features present in the images [Che21]. Such image generation is illustrated in Figure 5.1, having the same statistical properties as the one computed by four different models [Bro22] are depicted. From the only information included in the original images, very convincing images are computed by the same models, thereby preserving some of the original observed properties.

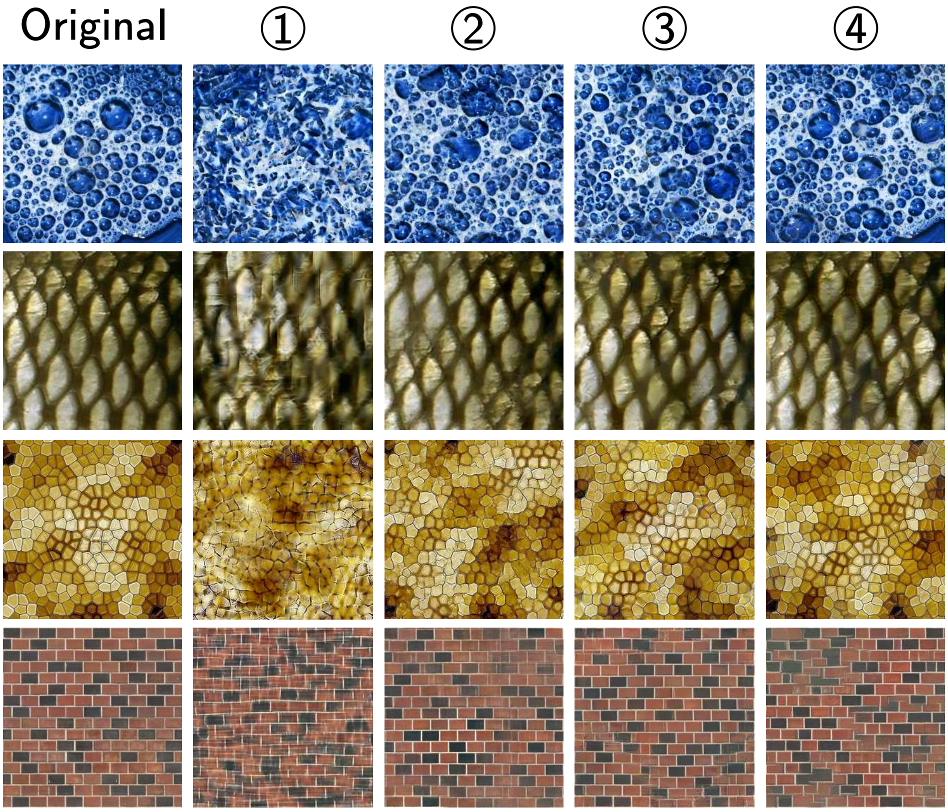

Figure 5.1: Image generation with four different models marked ①,②,③, and ④, from four different textured images (reproduced from [Bro22]).

Additionally, it should be remembered that classical crystallographic data are much richer than simple images commonly used when applying these methods. Combined with the already characterized physical data, image generation techniques constitute an interesting addition to often restrictive (classical) experimental characterization methods. In this sense, we believe micromechanics will benefit considerably from such techniques of generation of artificial microstructures since they convey subtle material microstructure correlations that are essential for understanding full-field measurements precisely.

Bibliography

[AA09] **I. Alvarez-Armas and S. Degallaix-Moreuil**, editors, **2009**. *Duplex stainless steels*. ISTE ; J. Wiley, London. ISBN 978-1-84821-137-7. OCLC: ocn427438273.

[AFC18] **AFCEN, 2018**. Règles de conception et de construction des matériels mécaniques des ilôts nucléaires REP (RCC-M). Rapport technique.

[Aug90] **P. Auger, F. Danoix, A. Menand, S. Bonnet, J. Bourgoin and M. Guttmann**, **1990**. Atom probe and transmission electron microscopy study of aging of cast duplex stainless steels. *Materials Science and Technology*, 6(3):301–313. ISSN 0267-0836, 1743-2847. doi: 10.1179/mst.1990.6.3.301.

[Azi18] **S. M. Azimi, D. Britz, M. Engstler, M. Fritz and F. Mücklich**, **2018**. Advanced Steel Microstructural Classification by Deep Learning Methods. *Scientific Reports*, 8(1):2128. ISSN 2045-2322. doi: 10.1038/s41598-018-20037-5.

[Bac10] **F. Bachmann, R. Hielscher and H. Schaeben**, **2010**. Texture Analysis with MTEX – Free and Open Source Software Toolbox. *Solid State Phenomena*, 160:63–68. ISSN 1662-9779. doi: 10.4028/www.scientific.net/SSP.160.63.

[Bac11] **F. Bachmann, R. Hielscher and H. Schaeben**, **2011**. Grain detection from 2d and 3d EBSD data—Specification of the MTEX algorithm. *Ultramicroscopy*, 111(12):1720–1733. ISSN 0304-3991. doi: 10.1016/j.ultramic.2011.08.002.

[Bac16] **A. Baczmański, Y. Zhao, E. Gadalińska, L. Le Joncour, S. Wroński, C. Braham, B. Panicaud, M. François, T. Buslaps and K. Soloducha**, **2016**. Elastoplastic deformation and damage process in duplex stainless steels studied using synchrotron and neutron diffractions in comparison with a self-consistent model. *International Journal of Plasticity*, 81:102–122. ISSN 07496419. doi: 10.1016/j.ijplas.2016.01.018.

[Bad18] **R. Badyka**, **2018**. *Influence des éléments d'alliage sur la cinétique de vieillissement de la ferrite d'aciers inoxydables austéno-ferritiques moulés*. Ph.D. thesis, Université de Rouen Normandie.

[Bad19] **R. Badyka, G. Monnet, S. Saillet, C. Domain and C. Pareige**, **2019**. Quantification of hardening contribution of G-Phase precipitation and spinodal decomposition in aged duplex stainless steel: APT analysis and micro-hardness measurements. *Journal of Nuclear Materials*, 514:266–275. ISSN 00223115. doi: 10.1016/j.jnucmat.2018.12.002.

[Bai24] **E. C. Bain and N. Y. Dunkirk**, **1924**. The nature of martensite. *trans. AIME*, 70(1):25–47.

[Bar01] **F. Barbe, L. Decker, D. Jeulin and G. Cailletaud**, **2001**. Intergranular and intragranular behavior of polycrystalline aggregates. Part 1: F.E. model. *International Journal of Plasticity*, 17(4):513–536. ISSN 07496419. doi: 10.1016/S0749-6419(00)00061-9.

[Bar05] **F. Barlat, H. Aretz, J. Yoon, M. Karabin, J. Brem and R. Dick**, **2005**. Linear transfomation-based anisotropic yield functions. *International Journal of Plasticity*, 21(5):1009–1039. ISSN 07496419. doi: 10.1016/j.ijplas.2004.06.004.

[Bar15] **B. Barkia, V. Doquet, J. Couzinié, I. Guillot and E. Héripré, 2015**. In situ monitoring of the deformation mechanisms in titanium with different oxygen contents. *Materials Science and Engineering: A*, 636:91–102. ISSN 09215093. doi: 10.1016/j.msea.2015.03.044.

[Bat00] **P. Bate and B. Hutchinson, 2000**. The effect of elastic interactions between displacive transformations on textures in steels. *Acta Materialia*, 48(12):3183–3192. ISSN 13596454. doi: 10.1016/S1359-6454(00)00106-3.

[Bau19] **A. P. Baur, C. Cayron and R. E. Logé, 2019**. On the chevron morphology of surface martensite. *Acta Materialia*, 179:247–254. ISSN 13596454. doi: 10.1016/j.actamat.2019.08.021.

[Ber78] **M. Berveiller and A. Zaoui, 1978**. An extension of the self-consistent scheme to plastically-flowing polycrystals. *Journal of the Mechanics and Physics of Solids*, 26(5-6):325–344. ISSN 00225096. doi: 10.1016/0022-5096(78)90003-0.

[Ber13] **S. Berbenni, B. Paliwal and M. Cherkaoui, 2013**. A micromechanics-based model for shear-coupled grain boundary migration in bicrystals. *International Journal of Plasticity*, 44:68–94. ISSN 07496419. doi: 10.1016/j.ijplas.2012.11.011.

[Ber16a] **R. Bergmann, R. H. Chan, R. Hielscher, J. Persch and G. Steidl, 2016**. Restoration of manifold-valued images by half-quadratic minimization. *Inverse Problems & Imaging*, 10(2):281–304.

[Ber16b] **M. Bertin, C. Du, J. P. Hoefnagels and F. Hild, 2016**. Crystal plasticity parameter identification with 3D measurements and Integrated Digital Image Correlation. *Acta Materialia*, 116:321–331. ISSN 13596454. doi: 10.1016/j.actamat.2016.06.039.

[Ber17] **M. Bertin, F. Hild and S. Roux, 2017**. On the identifiability of the Hill-1948 model with one uniaxial tensile test. *Comptes Rendus Mécanique*, 345(6):363–369. ISSN 16310721. doi: 10.1016/j.crme.2017.04.001.

[Bes06] **G. Besnard, F. Hild and S. Roux, 2006**. "Finite-Element" Displacement Fields Analysis from Digital Images: Application to Portevin–Le Châtelier Bands. *Experimental Mechanics*, 46(6):789–803. ISSN 0014-4851, 1741-2765. doi: 10.1007/s11340-006-9824-8.

[Bet96] **M. Bethmont, Y. Meyzaud and P. Soulat, 1996**. Properties of cast austenitic materials for light water reactors. *Fracture in Austenitic Components*, 65(3):221–229. ISSN 0308-0161. doi: 10.1016/0308-0161(94)00133-4.

[Bha11] **H. Bhadeshia, 2011**. Comments on "The mechanisms of the fcc–bcc martensitic transformation revealed by pole figures". *Scripta Materialia*, 64:101–102. doi: 10.1016/j.scriptamat.2010.07.044.

[Bon90] **S. Bonnet, J. Bourgoin, J. Champredonde, D. Guttmann and M. Guttmann, 1990**. Relationship between evolution of mechanical properties of various cast duplex stainless steels and metallurgical and aging parameters: outline of current EDF programmes. *Materials Science and Technology*, 6(3):221–229. ISSN 0267-0836, 1743-2847. doi: 10.1179/mst.1990.6.3.221.

[Bou06] **J. Bouquerel, K. Verbeken and B. Decooman, 2006**. Microstructure-based model for the static mechanical behaviour of multiphase steels. *Acta Materialia*, 54(6):1443–1456. ISSN 13596454. doi: 10.1016/j.actamat.2005.10.059.

[Bow54] **J. S. Bowles and J. K. Mackenzie, 1954**. The crystallography of martensite transformations I. *Acta Metallurgica*, 2(1):129–137. ISSN 0001-6160. doi: https://doi.org/10.1016/0001-6160(54)90102-9.

[Bri18] **T. B. Britton and J. L. R. Hickey**, **2018**. Understanding deformation with high angular resolution electron backscatter diffraction (HR-EBSD). *IOP Conference Series: Materials Science and Engineering*, 304:012003. ISSN 1757-8981, 1757-899X. doi: 10.1088/1757-899X/304/1/012003.

[Bro91] **J. A. Brooks and A. W. Thompson**, **1991**. Microstructural development and solidification cracking susceptibility of austenitic stainless steel welds. *International Materials Reviews*, 36(1):16–44. ISSN 0950-6608, 1743-2804. doi: 10.1179/imr.1991.36.1.16.

[Bro22] **A. Brochard, S. Zhang and S. Mallat**, **2022**. Generalized Rectifier Wavelet Covariance Models For Texture Synthesis. doi: 10.48550/ARXIV.2203.07902. Publisher: arXiv Version Number: 1.

[Bug99] **S. Bugat, J. Besson and A. Pineau**, **1999**. Micromechanical modeling of the behavior of duplex stainless steels. *Computational Materials Science*, 16(1-4):158–166. ISSN 09270256. doi: 10.1016/S0927-0256(99)00058-0.

[Bug00] **S. Bugat**, **2000**. *Comportement et endommagement des aciers austeno-ferritiques vieillis : une approche micromécanique*. Ph.D. thesis, École Nationale Supérieure des Mines de Paris.

[Bul18] **A. Buljac, C. Jailin, A. Mendoza, J. Neggers, T. Taillandier-Thomas, A. Bouterf, B. Smaniotto, F. Hild and S. Roux**, **2018**. Digital Volume Correlation: Review of Progress and Challenges. *Experimental Mechanics*, 58(5):661–708. ISSN 0014-4851, 1741-2765. doi: 10.1007/s11340-018-0390-7.

[Bun84] **H. J. Bunge, M. Humbert and P. I. Welch**, **1984**. Texture transformation. *Textures and Microstructures*, 6(2):81–95. Publisher: Hindawi.

[Bun03] **H. J. Bunge, W. Weiss, H. Klein, L. Wcislak, U. Garbe and J. R. Schneider**, **2003**. Orientation relationship of Widmannstätten plates in an iron meteorite measured with high-energy synchrotron radiation. *Journal of Applied Crystallography*, 36(1):137–140. doi: 10.1107/S0021889802021386.

[Bur16] **T. Burnett, R. Kelley, B. Winiarski, L. Contreras, M. Daly, A. Gholinia, M. Burke and P. Withers**, **2016**. Large volume serial section tomography by Xe Plasma FIB dual beam microscopy. *Ultramicroscopy*, 161:119–129. ISSN 03043991. doi: 10.1016/j.ultramic.2015.11.001.

[Cai16] **G. Cailletaud and F. Coudon**, **2016**. Scale Transition Rules Applied to Crystal Plasticity. In **P. Trovalusci**, editor, *Materials with Internal Structure*, pages 1–15. Springer International Publishing, Cham. ISBN 978-3-319-21493-1 978-3-319-21494-8. doi: 10.1007/978-3-319-21494-8_1.

[Cai21] **Y. Cai, M. Shan, Y. Cui, S. Manladan, X. Lv, L. Zhu, D. Sun, T. Wang and J. Han**, **2021**. Microstructure and properties of FeCoCrNi high entropy alloy produced by laser melting deposition. *Journal of Alloys and Compounds*, 887. doi: 10.1016/j.jallcom.2021.161323.

[Cay06] **C. Cayron, B. Artaud and L. Briottet**, **2006**. Reconstruction of parent grains from EBSD data. *Materials Characterization*, 57(4-5):386–401. ISSN 10445803. doi: 10.1016/j.matchar.2006.03.008.

[Cay10] **C. Cayron, F. Barcelo and Y. de Carlan**, **2010**. The mechanisms of the fcc–bcc martensitic transformation revealed by pole figures. *Acta Materialia*, 58(4):1395–1402. ISSN 13596454. doi: 10.1016/j.actamat.2009.10.046.

[Cay11] **C. Cayron, F. Barcelo and Y. de Carlan, 2011**. Reply to "Comments on 'The mechanisms of the fcc–bcc martensitic transformation revealed by pole figures'". *Scripta Materialia*, 64(1):103–106. ISSN 1359-6462. doi: https://doi.org/10.1016/j.scriptamat.2010.09.004.

[Cay13] **C. Cayron, 2013**. One-step model of the face-centred-cubic to body-centred-cubic martensitic transformation. *Acta Crystallographica Section A Foundations of Crystallography*, 69(5):498–509. ISSN 0108-7673, 1600-5724. doi: 10.1107/S0108767313019016.

[Cay15] **C. Cayron, 2015**. Continuous atomic displacements and lattice distortion during fcc–bcc martensitic transformation. *Acta Materialia*, 96:189–202. ISSN 1359-6454. doi: https://doi.org/10.1016/j.actamat.2015.06.010.

[Cay20] **C. Cayron, 2020**. What EBSD and TKD Tell Us about the Crystallography of the Martensitic B2-B19 Transformation in NiTi Shape Memory Alloys. *Crystals*, 10(7):562. ISSN 2073-4352. doi: 10.3390/cryst10070562.

[Caz01] **O. Cazacu and F. Barlat, 2001**. Generalization of Drucker's Yield Criterion to Orthotropy. *Mathematics and Mechanics of Solids*, 6(6):613–630. doi: 10.1177/108128650100600603. _eprint: https://doi.org/10.1177/108128650100600603.

[Cha09] **J. Charles, 2009**. Corrosion Resistance Properties. In *Duplex Stainless Steels*, pages 47–114. John Wiley & Sons, Ltd. ISBN 978-1-118-55799-0. doi: https://doi.org/10.1002/9781118557990.ch2.

[Cha10] **K. Chandra, R. Singhal, V. Kain and V. S. Raja, 2010**. Low temperature embrittlement of duplex stainless steel: Correlation between mechanical and electrochemical behavior. *Materials Science and Engineering: A*, 527(16-17):3904–3912. ISSN 09215093. doi: 10.1016/j.msea.2010.02.069.

[Cha12] **J. Charles and P. Chemelle, 2012**. The history of duplex developments, nowadays DSS properties and duplex market future trends. *World Iron & Steel*, 1:46–57.

[Cha21] **M. Charpagne, J. Hestroffer, A. Polonsky, M. Echlin, D. Texier, V. Valle, I. Beyerlein, T. Pollock and J. Stinville, 2021**. Slip localization in Inconel 718: A three-dimensional and statistical perspective. *Acta Materialia*, 215:117037. ISSN 13596454. doi: 10.1016/j.actamat.2021.117037.

[Che00] **J. S. Cheon and I. S. Kim, 2000**. Evaluation of thermal aging embrittlement in CF8 duplex stainless steel by small punch test. *Journal of Nuclear Materials*, 278(1):96–103. ISSN 00223115. doi: 10.1016/S0022-3115(99)00213-5.

[Che10] **C.-L. Chen and R. Thomson, 2010**. The combined use of EBSD and EDX analyses for the identification of complex intermetallic phases in multicomponent Al–Si piston alloys. *Journal of Alloys and Compounds*, 490(1-2):293–300. ISSN 09258388. doi: 10.1016/j.jallcom.2009.09.181.

[Che15] **B. Chen, H. Shu, G. Coatrieux, G. Chen, X. Sun and J.-L. Coatrieux, 2015**. Color Image Analysis by Quaternion-Type Moments. *Journal of Mathematical Imaging and Vision*, 51(1):124–144. ISSN 0924-9907, 1573-7683. doi: 10.1007/s10851-014-0511-6.

[Che19] **L. Chen, T. E. James Edwards, F. Di Gioacchino, W. J. Clegg, F. P. Dunne and M.-S. Pham, 2019**. Crystal plasticity analysis of deformation anisotropy of lamellar TiAl alloy: 3D microstructure-based modelling and in-situ micro-compression. *International Journal of Plasticity*, 119:344–360. ISSN 07496419. doi: 10.1016/j.ijplas.2019.04.012.

[Che21] **S. Cheng and B. Ménard, 2021**. How to quantify fields or textures? A guide to the scattering transform. doi: 10.48550/ARXIV.2112.01288. Publisher: arXiv Version Number: 1.

[Cho90] **O. K. Chopra and A. Sather, 1990**. Initial assessment of the mechanisms and significance of low-temperature embrittlement of cast stainless steels in LWR systems. Rapport technique, Nuclear Regulatory Commission, Washington, DC (USA). Div. of Engineering.

[Cho91] **O. Chopra, 1991**. Thermal aging of cast stainless steels in LWR systems: Estimation of mechanical properties. Rapport technique.

[Chr02] **J. W. Christian, 2002**. Chapter 22 - Crystallography of Martensitic Transformations. In **J. W. Christian**, editor, *The Theory of Transformations in Metals and Alloys*, pages 992–1061. Pergamon, Oxford. ISBN 978-0-08-044019-4. doi: https://doi.org/10.1016/B978-008044019-4/50027-1.

[Chu90] **H. M. Chung and T. R. Leax, 1990**. Embrittlement of laboratory and reactor aged CF3,CF8, and CF8M duplex stainless steels. *Materials Science and Technology*, 6(3):249–262. ISSN 0267-0836, 1743-2847. doi: 10.1179/mst.1990.6.3.249.

[Chu92] **H. Chung, 1992**. Aging and life prediction of cast duplex stainless steel components. *International Journal of Pressure Vessels and Piping*, 50(1-3):179–213. ISSN 03080161. doi: 10.1016/0308-0161(92)90037-G.

[Cla04] **D. Claire, F. Hild and S. Roux, 2004**. A finite element formulation to identify damage fields: the equilibrium gap method. *International Journal for Numerical Methods in Engineering*, 61(2):189–208. ISSN 0029-5981, 1097-0207. doi: 10.1002/nme.1057.

[Col22] **D. A. Collins, E. L. Carter, T. G. Lach and T. S. Byun, 2022**. A comprehensive study of the effects of long-term thermal aging on the fracture resistance of cast austenitic stainless steels. *Nuclear Engineering and Technology*, 54(2):709–731. ISSN 17385733. doi: 10.1016/j.net.2021.08.022.

[Cos97] **J. F. Coste, J. M. Leborgne, J. P. Massoud, O. Grisot, S. Miloudi and R. Borrelly, 1997**. Application of thermoelectricity to NDE of thermally aged cast duplex stainless steels and neutron irradiated ferritic steels. Rapport technique, EDF DER.

[Cra13] **G. Crammond, S. Boyd and J. Dulieu-Barton, 2013**. Speckle pattern quality assessment for digital image correlation. *Optics and Lasers in Engineering*, 51(12):1368–1378. ISSN 01438166. doi: 10.1016/j.optlaseng.2013.03.014.

[Dan04] **F. Danoix, P. Auger and D. Blavette, 2004**. Hardening of Aged Duplex Stainless Steels by Spinodal Decomposition. *Microscopy and Microanalysis*, 10(3):349–354. ISSN 1431-9276, 1435-8115. doi: 10.1017/S1431927604040516.

[Dav81] **S. David, 1981**. Ferrite morphology and variations in ferrite content in austenitic stainless steel welds. *Welding Journal*, 60.

[DeM21] **R. DeMott, N. Haghdadi, C. Kong, Z. Gandomkar, M. Kenney, P. Collins and S. Primig, 2021**. 3D electron backscatter diffraction characterization of fine α titanium microstructures: collection, reconstruction, and analysis methods. *Ultramicroscopy*, 230:113394. ISSN 03043991. doi: 10.1016/j.ultramic.2021.113394.

[Dep19] **D. Depriester and R. Kubler, 2019**. Calculs Éléments Finis à l'échelle des grains depuis des données EBSD. 24ème Congrès Français de Mécanique.

[Dep20] **D. Depriester and R. Kubler, 2020**. MTEX2Gmsh: a tool for generating 2D meshes from EBSD data. *Journal of Open Source Software*, 5(52):2094. ISSN 2475-9066. doi: 10.21105/joss.02094.

[DG98] **L. Devillers-Guerville, 1998**. *Rupture d'aciers inoxydables austéno-ferritiques moules, fragilises par vieillissement à 350-400°C : aspects microstructuraux - simulation numérique de la dispersion et des effets d'échelle*. Ph.D. thesis, Ecole Nationale Supérieure des Mines de Paris.

[Dia05] **O. Diard, S. Leclercq, G. Rousselier and G. Cailletaud, 2005**. Evaluation of finite element based analysis of 3D multicrystalline aggregates plasticity. *International Journal of Plasticity*, 21(4):691–722. ISSN 07496419. doi: 10.1016/j.ijplas.2004.05.017.

[DJ17] **L. De Jeer, V. Ocelík and J. De Hosson, 2017**. Orientation Relationships in Al0.7CoCrFeNi High-Entropy Alloy. *Microscopy and Microanalysis*, 23:1–11. doi: 10.1017/S1431927617012442.

[Don17] **Y. Dong and B. Pan, 2017**. A Review of Speckle Pattern Fabrication and Assessment for Digital Image Correlation. *Experimental Mechanics*, 57(8):1161–1181. ISSN 0014-4851, 1741-2765. doi: 10.1007/s11340-017-0283-1.

[Dru49] **D. C. Drucker, 1949**. Relation of Experiments to Mathematical Theories of Plasticity. *Journal of Applied Mechanics*, 16(4):349–357. ISSN 0021-8936. doi: 10.1115/1.4010009.

[DS99] **L. Di Stefano and A. Bulgarelli, 1999**. A simple and efficient connected components labeling algorithm. In *Proceedings 10th International Conference on Image Analysis and Processing*, pages 322–327. doi: 10.1109/ICIAP.1999.797615.

[Duc13] **A. Ducato, L. Fratini, M. La Cascia and G. Mazzola, 2013**. An Automated Visual Inspection System for the Classification of the Phases of Ti-6Al-4V Titanium Alloy. In *Computer Analysis of Images and Patterns*, volume 8048, pages 362–369. Springer, Berlin, Heidelberg. ISBN 978-3-642-40245-6 978-3-642-40246-3. doi: 10.1007/978-3-642-40246-3_45.

[Ech20] **M. P. Echlin, T. L. Burnett, A. T. Polonsky, T. M. Pollock and P. J. Withers, 2020**. Serial sectioning in the SEM for three dimensional materials science. *Current Opinion in Solid State and Materials Science*, 24(2):100817. ISSN 13590286. doi: 10.1016/j.cossms.2020.100817.

[Eng08] **C. Engin and H. M. Urbassek, 2008**. Molecular-dynamics investigation of the fcc-bcc phase transformation in Fe. *Computational Materials Science*, 41(3):297–304. ISSN 0927-0256. doi: https://doi.org/10.1016/j.commatsci.2007.04.019.

[Fie97] **D. P. Field, 1997**. Recent advances in the application of orientation imaging. *Ultramicroscopy*, 67(1-4):1–9. ISSN 03043991. doi: 10.1016/S0304-3991(96)00104-0.

[Fis53] **R. M. Fisher, E. J. Dulis and K. G. Carroll, 1953**. Identification of the precipitate accompanying 885-Degrees-F embrittlement in chromium steels. *Transactions of the american institute of mining and metallurgical Engineers*, 197(5):690–695.

[Fis81] **H. Fischmeister, 1981**. Digital image analysis in quantitative metallography. In *Computers in Materials Technology*, pages 109–129. Elsevier. ISBN 978-0-08-027570-3. doi: 10.1016/B978-0-08-027570-3.50019-6.

[For98] **S. Forest, 1998**. Modeling slip, kink and shear banding in classical and generalized single crystal plasticity. *Acta Materialia*, 46(9):3265–3281. ISSN 13596454. doi: 10.1016/S1359-6454(98)00012-3.

[For02] **S. Forest, R. Sievert and E. Aifantis, 2002**. Strain Gradient Crystal Plasticity: Thermomechanical Formulations and Applications. *Journal of the Mechanical Behavior of Materials*, 13. doi: 10.1515/JMBM.2002.13.3-4.219.

[Fra88] **F. C. Frank, 1988**. Orientation mapping. *Metallurgical Transactions A*, 19(3):403–408. ISSN 0360-2133, 1543-1940. doi: 10.1007/BF02649253.

[Fra15] **P. Franciosi, L. Le, G. Monnet, C. Kahloun and M.-H. Chavanne, 2015**. Investigation of slip system activity in iron at room temperature by SEM and AFM in-situ tensile and compression tests of iron single crystals. *International Journal of Plasticity*, 65:226–249. ISSN 07496419. doi: 10.1016/j.ijplas.2014.09.008.

[Fri06] **C. Friebel, I. Doghri and V. Legat, 2006**. General mean-field homogenization schemes for viscoelastic composites containing multiple phases of coated inclusions. *International Journal of Solids and Structures*, 43(9):2513–2541. ISSN 0020-7683. doi: https://doi.org/10.1016/j.ijsolstr.2005.06.035.

[Fri12] **F. Fritzen, S. Forest, T. Böhlke, D. Kondo and T. Kanit, 2012**. Computational homogenization of elasto-plastic porous metals. *International Journal of Plasticity*, 29:102–119. ISSN 07496419. doi: 10.1016/j.ijplas.2011.08.005.

[Fuk11] **T. Fukino, S. Tsurekawa and Y. Morizono, 2011**. In-Situ Scanning Electron Microscopy/Electron Backscattered Diffraction Observation of Microstructural Evolution during α - γ Phase Transformation in Deformed Fe-Ni Alloy. *Metallurgical and Materials Transactions A*, 42(3):587–593. ISSN 1543-1940. doi: 10.1007/s11661-010-0285-4.

[Gat15] **L. A. Gatys, A. S. Ecker and M. Bethge, 2015**. Texture Synthesis Using Convolutional Neural Networks. doi: 10.48550/ARXIV.1505.07376. Publisher: arXiv Version Number: 3.

[Ger12] **L. Germain, N. Gey, R. Mercier, P. Blaineau and M. Humbert, 2012**. An advanced approach to reconstructing parent orientation maps in the case of approximate orientation relations: Application to steels. *Acta Materialia*, 60(11):4551–4562. ISSN 13596454. doi: 10.1016/j.actamat.2012.04.034.

[Geu09] **C. Geuzaine and J.-F. Remacle, 2009**. Gmsh: A 3-D finite element mesh generator with built-in pre- and post-processing facilities. *International Journal for Numerical Methods in Engineering*, 79(11):1309–1331. ISSN 00295981. doi: 10.1002/nme.2579.

[God04] **A. Godfrey, 2004**. Edge preservation near triple junctions during orientation averaging of EBSP data. *Scripta Materialia*, 50(8):1097–1101. ISSN 13596462. doi: 10.1016/j.scriptamat.2004.01.035.

[Gre49] **A. B. Greninger and A. R. Troiano, 1949**. The mechanism of Martensite formation. *JOM*, 1(9):590–598. ISSN 1047-4838, 1543-1851. doi: 10.1007/BF03398900.

[Gre13] **M. Grediac and F. Hild, 2013**. *Full-field measurements and identification in solid mechanics*. ISTE Ltd./John Wiley and Sons Inc., Hoboken, N.J. ISBN 978-1-118-57846-9 978-1-299-18660-6 978-1-118-57667-0 978-1-118-57847-6. OCLC: 1317457367.

[Gro63] **G. W. Groves and A. Kelly, 1963**. Independent slip systems in crystals. *Philosophical Magazine*, 8(89):877–887. ISSN 0031-8086. doi: 10.1080/14786436308213843.

[Gro73] **P. J. Grobner, 1973**. The 885° f (475° c) embrittlement of ferritic stainless steels. *Metallurgical Transactions*, 4(1):251–260. ISSN 0360-2133, 1543-1916. doi: 10.1007/BF02649625.

[Gro06] **M. Groeber, B. Haley, M. Uchic, D. Dimiduk and S. Ghosh, 2006**. 3D reconstruction and characterization of polycrystalline microstructures using a FIB–SEM system. *Materials Characterization*, 57(4-5):259–273. ISSN 10445803. doi: 10.1016/j.matchar.2006.01.019.

[Gro14] **M. A. Groeber and M. A. Jackson, 2014**. DREAM.3D: A Digital Representation Environment for the Analysis of Microstructure in 3D. *Integrating Materials and Manufacturing Innovation*, 3(1):56–72. ISSN 2193-9764, 2193-9772. doi: 10.1186/2193-9772-3-5.

[Gue14a] **A. Guery, 2014**. *Développement d'une méthode de corrélation d'images numériques adaptée aux mesures cinématiques dans les polycristaux : application à l'identification de paramètres de lois de plasticité cristalline*. Ph.D. thesis, Ecole normale supérieure de Cachan.

[Gue14b] **A. Guery, F. Latourte, F. Hild and S. Roux, 2014**. Characterization of SEM speckle pattern marking and imaging distortion by digital image correlation. *Measurement Science and Technology*, 25(1):12. ISSN 0957-0233. Place: United Kingdom.

[Gue16] **A. Guery, F. Hild, F. Latourte and S. Roux, 2016**. Identification of crystal plasticity parameters using DIC measurements and weighted FEMU. *Mechanics of Materials*, 100:55–71. ISSN 0167-6636. doi: https://doi.org/10.1016/j.mechmat.2016.06.007.

[Gui11] **Y. Guilhem, 2011**. *Étude numérique des champs mécaniques locaux dans les agrégats polycristallins d'acier 316L sous chargement de fatigue*. Ph.D. thesis, École Nationale Supérieure des Mines de Paris.

[Gus19] **M. Gusenbauer, J. Fischbacher, A. Kovacs, H. Oezelt, S. Bance, P. Zhao, T. G. Woodcock and T. Schrefl, 2019**. Automated meshing of electron backscatter diffraction data and application to finite element micromagnetics. *Journal of Magnetism and Magnetic Materials*, 486:165256. ISSN 03048853. doi: 10.1016/j.jmmm.2019.165256.

[Guy16] **J. Guyon, N. Gey, D. Goran, S. Chalal and F. Pérez-Willard, 2016**. Advancing FIB assisted 3D EBSD using a static sample setup. *Ultramicroscopy*, 161:161–167. ISSN 03043991. doi: 10.1016/j.ultramic.2015.11.011.

[Hag20] **N. Haghdadi, P. Cizek, P. D. Hodgson, Y. He, B. Sun, J. J. Jonas, G. S. Rohrer and H. Beladi, 2020**. New insights into the interface characteristics of a duplex stainless steel subjected to accelerated ferrite-to-austenite transformation. *Journal of Materials Science*, 55(12):5322–5339. ISSN 0022-2461, 1573-4803. doi: 10.1007/s10853-020-04358-3.

[Han04] **N. Hansen, 2004**. Hall–Petch relation and boundary strengthening. *Scripta Materialia*, 51(8):801–806. ISSN 13596462. doi: 10.1016/j.scriptamat.2004.06.002.

[Han10] **K. Han, M. Ciccotti and S. Roux, 2010**. Measuring nanoscale stress intensity factors with an atomic force microscope. *EPL (Europhysics Letters)*, 89(6):66003. ISSN 0295-5075, 1286-4854. doi: 10.1209/0295-5075/89/66003.

[Han12] **X. Han, 2012**. *Modélisation de la fragilisation due au gonflement dans les aciers inoxydables austénitiques irradiés*. Ph.D. thesis, Ecole Nationale Supérieure des Mines de Paris.

[Har79] **J. A. Hartigan and M. A. Wong, 1979**. Algorithm AS 136: A K-Means Clustering Algorithm. *Journal of the Royal Statistical Society. Series C (Applied Statistics)*, 28(1):100–108. ISSN 00359254, 14679876. doi: 10.2307/2346830. Publisher: Wiley.

[Hay20] **T. Hayashi, S. Morito and T. Ohba, 2020**. Local distribution of orientation relationship and microstructure evolution of lath martensite in an ultra-low-carbon steel. *Scripta Materialia*, 180:1–5. ISSN 1359-6462. doi: https://doi.org/10.1016/j.scriptamat.2020.01.011.

[He06] **Y. He, S. Godet, P. J. Jacques and J. J. Jonas, 2006**. Crystallographic relations between face- and body-centred cubic crystals formed under near-equilibrium conditions: Observations from the Gibeon meteorite. *Acta Materialia*, 54(5):1323–1334. ISSN 13596454. doi: 10.1016/j.actamat.2005.11.008.

[Hel15] **T. Helfer, B. Michel, J.-M. Proix, M. Salvo, J. Sercombe and M. Casella, 2015**. Introducing the open-source mfront code generator: Application to mechanical behaviours and material knowledge management within the PLEIADES fuel element modelling platform. *Computers*

& Mathematics with Applications, 70(5):994–1023. ISSN 0898-1221. doi: 10.1016/j.camwa.2015.06.027.

[Her19] **V. Herb, M. Berny, B. Lacombe and F. Hild, 2019**. Developpement d'un algorithme de FEMU-TU pour l'identification de propriétés thermomécaniques d'un CMC à hautes températures à partir de mesures de champs. In *21ème Journées Nationales sur les Composites*. École Nationale Supérieure d'Arts et Métiers (ENSAM), Bordeaux, Talence, France.

[Hie19] **R. Hielscher, C. B. Silbermann, E. Schmidl and J. Ihlemann, 2019**. Denoising of crystal orientation maps. *Journal of Applied Crystallography*, 52(5):984–996. doi: 10.1107/S1600576719009075.

[Hil65] **R. Hill, 1965**. Continuum micro-mechanics of elastoplastic polycrystals. *Journal of the Mechanics and Physics of Solids*, 13(2):89–101. ISSN 00225096. doi: 10.1016/0022-5096(65)90023-2.

[Hil66] **R. Hill, 1966**. Generalized constitutive relations for incremental deformation of metal crystals by multislip. *Journal of the Mechanics and Physics of Solids*, 14(2):95–102. ISSN 00225096. doi: 10.1016/0022-5096(66)90040-8.

[Hil12] **F. Hild and S. Roux, 2012**. Comparison of Local and Global Approaches to Digital Image Correlation. *Experimental Mechanics*, 52(9):1503–1519. ISSN 0014-4851, 1741-2765. doi: 10.1007/s11340-012-9603-7.

[Hoe78] **S. Hoekstra, H. M. M. Van Der Lelie and C. A. Verbraak, 1978**. A general method of habit plane determination in bainitic steels—II. Habit plane determination of the bainite. *Acta Metallurgica*, 26(10):1517–1527. ISSN 0001-6160. doi: https://doi.org/10.1016/0001-6160(78)90062-7.

[Hoe80] **S. Hoekstra, 1980**. A check of the I.P.S. theory with the aid of an accurate determination of habit planes and orientation relationships in bainitic steels. *Acta Metallurgica*, 28(4):507–517. doi: 10.1016/0001-6160(80)90141-8.

[Hum01] **F. J. Humphreys, 2001**. Grain and subgrain characterisation by electronbackscatter diffraction. *Journal of Materials Science*, 36(16):3833–3854. ISSN 00222461. doi: 10.1023/A:1017973432592.

[Huo19] **C. Huotilainen, M. Ivanchenko, U. Ehrnstén and P. Efsing, 2019**. Electrochemical investigation of in-service thermal aging in two CF8M cast stainless steels. *Journal of Nuclear Materials*, 520:34–40. ISSN 00223115. doi: 10.1016/j.jnucmat.2019.04.001.

[Hut64] **J. W. Hutchinson, 1964**. Plastic deformation of b.c.c. polycrystals. *Journal of the Mechanics and Physics of Solids*, 12(1):25–33. ISSN 0022-5096. doi: https://doi.org/10.1016/0022-5096(64)90004-3.

[Hé06] **E. Héripré, 2006**. *Méthode de couplage multi-échelles entre simulations numériques polycristallines et mesures de champs pour l'identification des paramètres de lois de comportementet de fissuration des matériaux métalliques. Application à l'étude des alliages TiAl.* Ph.D. thesis, Ecole Polytechnique.

[Hé17] **S. Hémery, A. Nait-Ali and P. Villechaise, 2017**. Combination of in-situ SEM tensile test and FFT-based crystal elasticity simulations of Ti-6Al-4V for an improved description of the onset of plastic slip. *Mechanics of Materials*, 109:1–10. ISSN 01676636. doi: 10.1016/j.mechmat.2017.03.013.

[Jac91] **A. G. Jackson, 1991**. *Handbook of Crystallography*.

[Jan14] **H. Jang, S. Hong, C. Jang and J. G. Lee, 2014**. The effects of reversion heat treatment on the recovery of thermal aging embrittlement of CF8M cast stainless steels. *Materials & Design (1980-2015)*, 56:517–521. ISSN 02613069. doi: 10.1016/j.matdes.2013.12.010.

[Jao65] **B. Jaoul, 1965**. *Etude de la plasticité et application aux métaux.* Sciences de la matière.

[JG00] **S. Jayet-Gendrot, P. Gilles and C. Migné, 2000**. Behavior of duplex stainless steel casting defects under mechanical loadings. *Nuclear Engineering and Design*, 197:141–153.

[Jia18] **R. Jiang, D. Bull, A. Evangelou, A. Harte, F. Pierron, I. Sinclair, M. Preuss, X. Hu and P. Reed, 2018**. Strain accumulation and fatigue crack initiation at pores and carbides in a SX superalloy at room temperature. *International Journal of Fatigue*, 114:22–33. ISSN 01421123. doi: 10.1016/j.ijfatigue.2018.05.003.

[Joh20] **D. N. Johnstone, B. H. Martineau, P. Crout, P. A. Midgley and A. S. Eggeman, 2020**. Density-based clustering of crystal (mis)orientations and the *orix* Python library. *Journal of Applied Crystallography*, 53(5):1293–1298. ISSN 1600-5767. doi: 10.1107/S1600576720011103.

[Jol92] **P. Joly, 1992**. *Etude de la rupture d'aciers inoxydables austéno-ferritiques moulés, fragilisés par vieillissement à 400°C*. Ph.D. thesis, ENSMP.

[Kam11] **A. D. Kammers and S. Daly, 2011**. Small-scale patterning methods for digital image correlation under scanning electron microscopy. *Measurement Science and Technology*, 22(12):125501. ISSN 0957-0233, 1361-6501. doi: 10.1088/0957-0233/22/12/125501.

[Kaw97] **S. Kawaguchi, N. Sakamoto, G. Takano, F. Matsuda, Y. Kikuchi and L. Mráz, 1997**. Microstructural changes and fracture behavior of CF8M duplex stainless steels after long-term aging. *Nuclear Engineering and Design*, 174(3):273–285. ISSN 00295493. doi: 10.1016/S0029-5493(97)00126-X.

[Kaw02] **Y. Kawaguchi and S. Yamanaka, 2002**. Mechanism of the change in thermoelectric power of cast duplex stainless steel due to thermal aging. *Journal of Alloys and Compounds*, 336(1-2):301–314. ISSN 09258388. doi: 10.1016/S0925-8388(01)01897-7.

[Kim81] **N. J. Kim and G. Thomas, 1981**. Effects of morphology on the mechanical behavior of a dual phase Fe/2Si/0.1C steel. *Metallurgical Transactions A*, 12(3):483–489. ISSN 0360-2133, 1543-1940. doi: 10.1007/BF02648546.

[Kny13] **M. Knyazeva and M. Pohl, 2013**. Duplex Steels: Part I: Genesis, Formation, Structure. *Metallography, Microstructure, and Analysis*, 2(2):113–121. ISSN 2192-9262, 2192-9270. doi: 10.1007/s13632-013-0066-8.

[Koi16] **K. Koiwa, N. Shishido, C. Chen, M. Omiya, S. Kamiya, H. Sato, M. Nishida, T. Suzuki, T. Nakamura, T. Suzuki and T. Nokuo, 2016**. Investigation of continuous deformation behavior around initial yield point of single crystal copper by using micro scale torsion test. *Scripta Materialia*, 111:94–97. ISSN 13596462. doi: 10.1016/j.scriptamat.2015.08.022.

[Kon22] **B. S. Kong, J. H. Shin, C. Jeong, C. Jang and S.-S. Kang, 2022**. Effect of microstructure evolution at the interphase boundary on the thermal ageing embrittlement of CF8M cast austenitic stainless steel. *International Journal of Pressure Vessels and Piping*, 198:104679. ISSN 03080161. doi: 10.1016/j.ijpvp.2022.104679.

[Kra17] **R. Krakow, R. J. Bennett, D. N. Johnstone, Z. Vukmanovic, W. Solano-Alvarez, S. J. Lainé, J. F. Einsle, P. A. Midgley, C. M. F. Rae and R. Hielscher, 2017**. On three-dimensional misorientation spaces. *Proceedings of the Royal Society A: Mathematical, Physical and Engineering Sciences*, 473(2206):20170274. ISSN 1364-5021, 1471-2946. doi: 10.1098/rspa.2017.0274.

[Kro61] **E. Kroner, 1961**. Zur plastischen verformung des vielkristalls. *Acta Metallurgica*, 9(2):155–161. ISSN 00016160. doi: 10.1016/0001-6160(61)90060-8.

[Kum16] **A. Kumar, L. Nguyen, M. DeGraef and V. Sundararaghavan, 2016**. A Markov random field approach for microstructure synthesis. *Modelling and Simulation in Materials Science and Engineering*, 24(3):035015. ISSN 0965-0393, 1361-651X. doi: 10.1088/0965-0393/24/3/035015.

[Kum19a] **A. Kumar, A. Dutta, S. Makineni, M. Herbig, R. Petrov and J. Sietsma, 2019**. In-situ observation of strain partitioning and damage development in continuously cooled carbide-free bainitic steels using micro digital image correlation. *Materials Science and Engineering: A*, 757:107–116. ISSN 09215093. doi: 10.1016/j.msea.2019.04.098.

[Kum19b] **A. Kumar, A. Dutta, S. Makineni, M. Herbig, R. Petrov and J. Sietsma, 2019**. In-situ observation of strain partitioning and damage development in continuously cooled carbide-free bainitic steels using micro digital image correlation. *Materials Science and Engineering: A*, 757:107–116. ISSN 09215093. doi: 10.1016/j.msea.2019.04.098.

[Kun12] **S. Kundu, A. K. Verma and V. Sharma, 2012**. Quantitative Analysis of Variant Selection for Displacive Transformations Under Stress. *Metallurgical and Materials Transactions A*, 43(7):2552–2565. ISSN 1073-5623, 1543-1940. doi: 10.1007/s11661-011-0971-x.

[Kur30] **G. Kurdjumow and G. Sachs, 1930**. Über den Mechanismus der Stahlhärtung. *Zeitschrift für Physik*, 64(5-6):325–343. ISSN 1434-6001, 1434-601X. doi: 10.1007/BF01397346.

[Lag67] **R. Lagneborg, 1967**. Metallography of the 475 °C embrittlement in an iron-30%chromium alloy. *Transactions of the ASM*, 60:67–68.

[Lag93] **K. P. D. Lagerlöf, 1993**. On deformation twinning in b.c.c. metals. *Acta Metallurgica et Materialia*, 41(7):2143–2151. ISSN 0956-7151. doi: https://doi.org/10.1016/0956-7151(93)90384-5.

[Lat18] **F. Latourte, 2018**. Effets de taille sur le comportement en traction d'aciers inoxydables austéno-ferritiques : simulations sur éprouvettes à faible nombre de grains. Note technique EDF 6125-2111-2017-04124-FR.

[LD15] **P. Le Delliou and S. Saillet, 2015**. Integrity and Life Assessment of Cast Duplex Stainless Steel Elbows of EDF PWR Main Coolant Piping. In *Volume 7: Operations, Applications and Components*, page V007T07A014. American Society of Mechanical Engineers, Boston, Massachusetts, USA. ISBN 978-0-7918-5702-1. doi: 10.1115/PVP2015-45231.

[Lea92] **T. R. Leax, S. S. Brenner and J. A. Spitznagel, 1992**. Atom probe examination of thermally ages CF8M cast stainless steel. *Metallurgical Transactions A*, 23(10):2725–2736. ISSN 0360-2133. doi: 10.1007/BF02651752.

[Leo82] **C. Leone and H. W. Kerr, 1982**. The Ferrite to Austenite Transformation in Stainless Steels.

[Leo13] **G. Leopold, P. Le Delliou and C. Landron, 2013**. Main primary piping cast components life assessment: Study of the tensile properties of aged duplex stainless steels. EDF Report.

[Li13a] **S. Li, Y. Wang, S. Li, H. Zhang, F. Xue and X. Wang, 2013**. Microstructures and mechanical properties of cast austenite stainless steels after long-term thermal aging at low temperature. *Materials & Design*, 50:886–892. ISSN 02613069. doi: 10.1016/j.matdes.2013.02.061.

[Li13b] **S. Li, H. Zhang, Y. Wang, S. Li, K. Zheng, F. Xue and X. Wang, 2013**. Annealing induced recovery of long-term thermal aging embrittlement in a duplex stainless steel. *Materials Science and Engineering: A*, 564:85–91. ISSN 09215093. doi: 10.1016/j.msea.2012.11.046.

[Lin14] **E. Lindfeldt, M. Ekh, K. Cvetskovski and M. Schilke, 2014**. Using DIC to Identify Microscale Strain Fields from In-situ SEM Images of a Pearlitic Steel. *Experimental Mechanics*, 54(9):1503–1513. ISSN 0014-4851, 1741-2765. doi: 10.1007/s11340-014-9937-4.

[Lio14] **G. Lionello and L. Cristofolini, 2014**. A practical approach to optimizing the preparation of speckle patterns for digital-image correlation. *Measurement Science and Technology*, 25(10):107001. ISSN 0957-0233, 1361-6501. doi: 10.1088/0957-0233/25/10/107001.

[Lip80] **J. C. Lippold and W. F. Savage, 1980**. Solidification of Austenitic Stainless Steel Weldments: Part 2—The Effect of Alloy Composit ion on Ferrite Morphology.

[Liu18] **T.-h. Liu, W. Wang, W.-j. Qiang and G.-g. Shu, 2018**. Mechanical properties and kinetics of thermally aged Z3CN20.09M cast duplex stainless steel. *International Journal of Minerals, Metallurgy, and Materials*, 25(10):1148–1155. ISSN 1674-4799, 1869-103X. doi: 10.1007/s12613-018-1666-8.

[Lun18] **D. Lunt, A. Orozco-Caballero, R. Thomas, P. Honniball, P. Frankel, M. Preuss and J. Q. d. Fonseca, 2018**. Enabling high resolution strain mapping in zirconium alloys. *Materials Characterization*, 139:355–363. ISSN 1044-5803. doi: https://doi.org/10.1016/j.matchar.2018.03.014.

[Luo06] **C. Luo and J. Liu, 2006**. Crystallography of lath martensite and lower bainite in alloy steels. *Materials Science and Engineering A, Structural Materials: Properties, Microstructure and Processing*, pages 149–152. ISSN 0921-5093. Place: Netherlands.

[Ma10] **X. Ma, H. Shi, J. Gu, G. Chen, O. Luesebrink and H. Hardersd, 2010**. In-situ observations of the effects of orientation and carbide on low cycle fatigue crack propagation in a single crystal superalloy. *Procedia Engineering*, 2(1):2287–2295. ISSN 18777058. doi: 10.1016/j.proeng.2010.03.245.

[Mac54] **J. K. Mackenzie and J. S. Bowles, 1954**. The crystallography of martensite transformations II. *Acta Metallurgica*, 2(1):138–147. ISSN 0001-6160. doi: https://doi.org/10.1016/0001-6160(54)90103-0.

[Mad04] **R. Madec and L. P. Kubin, 2004**. Dislocation Interactions and Symmetries in BCC Crystals. In **G. M. L. Gladwell, H. Kitagawa and Y. Shibutani**, editors, *IUTAM Symposium on Mesoscopic Dynamics of Fracture Process and Materials Strength*, volume 115, pages 69–78. Springer Netherlands, Dordrecht. ISBN 978-90-481-6576-6 978-1-4020-2111-4. doi: 10.1007/978-1-4020-2111-4_7. Series Title: Solid Mechanics and its Applications.

[Mad17] **R. Madec and L. P. Kubin, 2017**. Dislocation strengthening in FCC metals and in BCC metals at high temperatures. *Acta Materialia*, 126:166–173. ISSN 13596454. doi: 10.1016/j.actamat.2016.12.040.

[Mag82] **T. Magnin and F. Moret, 1982**. Mechanical twinning in ferritic stainless steels. *Scripta Metallurgica*, 16(11):1225–1228. ISSN 00369748. doi: 10.1016/0036-9748(82)90471-9.

[Mal12] **A. Malik, H. K. Yeddu, G. Amberg, A. Borgenstam and J. Ågren, 2012**. Three dimensional elasto-plastic phase field simulation of martensitic transformation in polycrystal. *Materials Science and Engineering: A*, 556:221–232. ISSN 09215093. doi: 10.1016/j.msea.2012.06.080.

[Man65] **J. Mandel, 1965**. Generalisation de la theorie de plasticite de W. T. Koiter. *International Journal of Solids and Structures*, 1(3):273–295. ISSN 00207683. doi: 10.1016/0020-7683(65)90034-X.

[Mar64] **M. Marcinkowski, R. Fisher and A. Szirmae, 1964**. Effect of 500°C aging on the deformation behaviour of an iron-chromium alloy. *Trans. Metall. Soc. AIME*, 230:676–689.

[Mar99] **J.-L. Martin and J. Wagner, 1999**. *Dislocations et plasticité des cristaux*. Cahiers de physique.

[Mar19] **S. Maraghechi, J. P. M. Hoefnagels, R. H. J. Peerlings, O. Rokoš and M. G. D. Geers, 2019**. Correction of Scanning Electron Microscope Imaging Artifacts in a Novel Digital Image Correlation Framework. *Experimental Mechanics*, 59(4):489–516. ISSN 0014-4851, 1741-2765. doi: 10.1007/s11340-018-00469-w.

[Mat06] **J.-P. Mathieu, 2006**. *Analyse et modélisation micromécanique du comportement et de la rupture fragile de l'acier 16MND5: prise en compte des hétérogénéités microstructurales*. Ph.D. thesis.

[May12] **A. Maynadier, M. Poncelet, K. Lavernhe-Taillard and S. Roux, 2012**. InfraRed Image Correlation: a new - method for characterizing thermal and displacement fields. In *Proceedings of the 2012 International Conference on Quantitative InfraRed Thermography*. QIRT Council. doi: 10.21611/qirt.2012.166.

[McD92] **P. McDougall and C. Wayman, 1992**. Martensite, eds. by GB Olson and WS Owen. *ASM International*, page 59.

[Mci00] **L. Mcirdi, 2000**. *Comportement et endommagement sous sollicitation mécanique d'un acier austéno-ferritique moulé vieilli*. Ph.D. thesis, ENSAM.

[McM13] **C. McMahon, B. Soe, A. Loeb, A. Vemulkar, M. Ferry and L. Bassman, 2013**. Boundary identification in EBSD data with a generalization of fast multiscale clustering. *Ultramicroscopy*, 133:16–25. ISSN 03043991. doi: 10.1016/j.ultramic.2013.04.009.

[Men19a] **A. Mendoza, J. Neggers, F. Hild and S. Roux, 2019**. Complete mechanical regularization applied to digital image and volume correlation. *Computer Methods in Applied Mechanics and Engineering*, 355:27–43. ISSN 00457825. doi: 10.1016/j.cma.2019.06.005.

[Men19b] **A. Mendoza, J. Schneider, E. Parra, E. Obert and S. Roux, 2019**. Differentiating 3D textile composites: A novel field of application for Digital Volume Correlation. *Composite Structures*, 208:735–743. ISSN 02638223. doi: 10.1016/j.compstruct.2018.10.008.

[Mer91a] **L. Meric and G. Cailletaud, 1991**. Single Crystal Modeling for Structural Calculations: Part 2—Finite Element Implementation. *Journal of Engineering Materials and Technology*, 113(1):171–182. ISSN 0094-4289. doi: 10.1115/1.2903375.

[Mer91b] **L. Meric, P. Poubanne and G. Cailletaud, 1991**. Single Crystal Modeling for Structural Calculations: Part 1—Model Presentation. *Journal of Engineering Materials and Technology*, 113(1):162–170. ISSN 0094-4289. doi: 10.1115/1.2903374.

[Mes97] **L. Messiaen, 1997**. *Recherche de paramètres morphologiques influents pour la prévision des caractéristiques mécaniques d'un acier austénoferritique*. Ph.D. thesis, ENSMP.

[Mic94] **W. F. Michaud, P. T. Toben, W. K. Soppet and O. K. Chopra, 1994**. Tensile-Property Characterization of Thermally Aged Cast Stainless Steels. Rapport technique NUREG/CR-6142, ANL-93/35.

[Mil90] **M. K. Miller and J. Bentley, 1990**. APFIM and AEM investigation of CF8 and CF8M primary coolant pipe steels. *Materials Science and Technology*, 6(3):285–292. ISSN 0267-0836, 1743-2847. doi: 10.1179/mst.1990.6.3.285.

[Min10] **Ministerial Order of 10 November 1999, 2010**. In-service Surveillance of the main primary and secondary systems of PWRs. *Journal Officiel de la République Francaise*, pages 172–176.

[Mit68] **T. E. Mitchell, 1968**. Slip in Body-Centred Cubic Crystals. *Philosophical Magazine*, 17(150):1169–1194. doi: 10.1080/14786436808223194.

[Mol22a] **M. Mollens, A. Guery, D. Loisnard, F. Hild and S. Roux, 2022**. Link between BCC-FCC orientation relationship and austenite morphology in CF8M stainless steel. *Submitted*.

[Mol22b] **M. Mollens, S. Roux, F. Hild and A. Guery, 2022**. Insights into a dual-phase steel microstructure using EBSD and image-processing-based workflow. *Journal of Applied Crystallography*, 55(3):601–610. ISSN 1600-5767. doi: 10.1107/S1600576722004265.

[Mon09] **G. Monnet, 2009**. A crystalline plasticity law for austenitic stainless steels. EDF R&D technical report H-B60-2008-04690-EN.

[Mon14] **M. Montagnat, O. Castelnau, P. D. Bons, S. H. Faria, O. Gagliardini, F. Gillet-Chaulet, F. Grennerat, A. Griera, R. A. Lebensohn, H. Moulinec, J. Roessiger and P. Suquet, 2014**. Multiscale modeling of ice deformation behavior. *Journal of Structural Geology*, 61:78–108. ISSN 0191-8141. doi: https://doi.org/10.1016/j.jsg.2013.05.002.

[Mor04] **A. Morawiec, 2004**. *Orientations and Rotations*. Springer Berlin Heidelberg, Berlin, Heidelberg. ISBN 978-3-642-07386-1 978-3-662-09156-2. doi: 10.1007/978-3-662-09156-2.

[Mor06] **S. Morito, X. Huang, T. Furuhara, T. Maki and N. Hansen, 2006**. The morphology and crystallography of lath martensite in alloy steels. *Acta Materialia*, 54(19):5323–5331. ISSN 13596454. doi: 10.1016/j.actamat.2006.07.009.

[Mor16] **L. Morsdorf, O. Jeannin, D. Barbier, M. Mitsuhara, D. Raabe and C. Tasan, 2016**. Multiple mechanisms of lath martensite plasticity. *Acta Materialia*, 121:202–214. ISSN 13596454. doi: 10.1016/j.actamat.2016.09.006.

[Mor21] **L. Moreau, 2021**. Etude de l'effet de la microstructure sur le comportement en traction d'aciers austéno-ferritiques. Master internship report, Grenoble INP Phelma.

[Mø92] **J. Møller, 1992**. Random Johnson-Mehl tessellations. *Advances in Applied Probability*, 24(4):814–844. ISSN 0001-8678, 1475-6064. doi: 10.2307/1427714.

[Nie22] **F. Niessen, T. Nyyssönen, A. A. Gazder and R. Hielscher, 2022**. Parent grain reconstruction from partially or fully transformed microstructures in *MTEX*. *Journal of Applied Crystallography*, 55(1):180–194. ISSN 1600-5767. doi: 10.1107/S1600576721011560.

[Nis34] **Z. Nishiyama, 1934**. X-ray investigation of the mechanism of the transformation from face centered cubic lattice to body centered cubic. *Sci. Rep. Tohoku Univ.*, 23:637.

[Nol04] **G. Nolze and V. Geist, 2004**. A new method for the investigation of orientation relationships in meteoritic plessite. *Crystal Research and Technology*, 39(4):343–352. doi: https://doi.org/10.1002/crat.200310193.

[Nol07] **G. Nolze, 2007**. Image distortions in SEM and their influences on EBSD measurements. *Ultramicroscopy*, 107(2):172–183. ISSN 0304-3991. doi: https://doi.org/10.1016/j.ultramic.2006.07.003.

[Nol08] **G. Nolze, 2008**. Irrational orientation relationship derived from rational orientation relationships using EBSD data. *Crystal Research and Technology*, 43:61 – 73. doi: 10.1002/crat.200711058.

[Nov09] **S. Novy, 2009**. *Mécanisme de vieillissement à très longue échéance des aciers inoxydables austéno-ferritiques*. Ph.D. thesis, Université de Rouen Normandie.

[Nyg02] **M. Nygårds and P. Gudmundson, 2002**. Three-dimensional periodic Voronoi grain models and micromechanical FE-simulations of a two-phase steel. *Computational Materials Science*, 24(4):513–519. ISSN 09270256. doi: 10.1016/S0927-0256(02)00156-8.

[Oka92] **H. Okamoto and M. Oka, 1992**. A Practical Procedure for Determining Habit Planes of Martensite Plates Containing {112}_\textalpha Twins by One-Surface Trace Analysis. *Journal of the Japan Institute of Metals*, 56(11):1257–1265. doi: 10.2320/jinstmet1952.56.11_1257.

[Oro40] **E. Orowan, 1940**. Problems of plastic gliding. *Proceedings of the Physical Society*, 52(1):8–22. doi: 10.1088/0959-5309/52/1/303. Publisher: IOP Publishing.

[Osm00] **P. Osmont, H. Petitgand and J. Philippe, 2000**. Utilisation de l'analyse d'images dans la sidérurgie. *Revue de Métallurgie*, 97(2):187–196. ISSN 0035-1563, 1156-3141. doi: 10.1051/metal/200097020187.

[Pan10] **B. Pan, H. Xie and Z. Wang, 2010**. Equivalence of digital image correlation criteria for pattern matching. *Applied Optics*, 49(28):5501. ISSN 0003-6935, 1539-4522. doi: 10.1364/AO.49.005501.

[Pan11] **B. Panicaud, K. Saanouni, A. Baczmański, M. François, L. Cauvin and L. Le Joncour, 2011**. Theoretical modelling of ductile damage in duplex stainless steels – Comparison between two micro-mechanical elasto-plastic approaches. *Computational Materials Science*, 50(6):1908–1916. ISSN 09270256. doi: 10.1016/j.commatsci.2011.01.038.

[Par11] **C. Pareige, S. Novy, S. Saillet and P. Pareige, 2011**. Study of phase transformation and mechanical properties evolution of duplex stainless steels after long term thermal ageing (>20years). *Journal of Nuclear Materials*, 411(1-3):90–96. ISSN 00223115. doi: 10.1016/j.jnucmat.2011.01.036.

[Par15] **C. Pareige, J. Emo, S. Saillet, C. Domain and P. Pareige, 2015**. Kinetics of G-phase precipitation and spinodal decomposition in very long aged ferrite of a Mo-free duplex stainless steel. *Journal of Nuclear Materials*, 465:383–389. ISSN 00223115. doi: 10.1016/j.jnucmat.2015.06.017.

[Pav08] **E. Pavlina and C. Van Tyne, 2008**. Correlation of Yield Strength and Tensile Strength with Hardness for Steels. *Journal of Materials Engineering and Performance*, 17(6):888–893. ISSN 1059-9495, 1544-1024. doi: 10.1007/s11665-008-9225-5.

[Pit59] **W. Pitsch, 1959**. The martensite transformation in thin foils of iron-nitrogen alloys. *Philosophical Magazine*, 4(41):577–584. ISSN 0031-8086. doi: 10.1080/14786435908238253.

[Plu97] **K. P. Plucknett, P. F. Becher and K. B. Alexander, 1997**. *In-situ* SEM observation of the fracture behaviour of titanium carbide/nickel aluminide composites. *Journal of Microscopy*, 185(2):206–216. ISSN 0022-2720, 1365-2818. doi: 10.1046/j.1365-2818.1997.1640725.x.

[Pok06] **C. Pokor, P. Thibaut, M. Akamatsu, M. Delnondedieu, S. Saillet, S. Jayet-Gendrot, P. Ould and G. Bezdikian, 2006**. Thermal ageing of cast duplex stainless steels of PWR: material assessment on removed cast elbows. Rapport technique, France. INIS-FR–08-0343.

[Pum90] **P. H. Pumphrey and K. N. Akhurst, 1990**. Aging kinetics of CF3 cast stainless steel in temperature range 300–400°C. *Materials Science and Technology*, 6(3):211–220. doi: 10.1179/mst.1990.6.3.211.

[Pł09] **M. Płuska, A. Czerwinski, J. Ratajczak, J. Kątcki, L. Oskwarek and R. Rak, 2009**. Separation of image-distortion sources and magnetic-field measurement in scanning electron microscope (SEM). *Micron*, 40(1):46–50. ISSN 0968-4328. doi: https://doi.org/10.1016/j.micron.2008.01.009.

[Que09] **S. Queyreau, G. Monnet and B. Devincre, 2009**. Slip systems interactions in α-iron determined by dislocation dynamics simulations. *International Journal of Plasticity*, 25(2):361–377. ISSN 07496419. doi: 10.1016/j.ijplas.2007.12.009.

[Que11] **R. Quey, P. Dawson and F. Barbe**, **2011**. Large-scale 3D random polycrystals for the finite element method: Generation, meshing and remeshing. *Computer Methods in Applied Mechanics and Engineering*, 200(17-20):1729–1745. ISSN 00457825. doi: 10.1016/j.cma.2011.01.002.

[Ram20] **D. C. Ramachandran, S.-D. Kim, J. Moon, C.-H. Lee, J.-H. Chung, E. Biro and Y.-D. Park**, **2020**. Classification of martensite-austenite constituents according to its internal morphology in high-strength low alloy steel. *Materials Letters*, 278:128422. ISSN 0167577X. doi: 10.1016/j.matlet.2020.128422.

[Rao16] **J. C. Rao, V. Ocelík, D. Vainchtein, Z. Tang, P. K. Liaw and J. T. M. D. Hosson**, **2016**. The fcc-bcc crystallographic orientation relationship in AlxCoCrFeNi high-entropy alloys. *Materials Letters*, 176:29–32. ISSN 0167-577X. doi: https://doi.org/10.1016/j.matlet.2016.04.086.

[Ren16] **E. Renner, Y. Gaillard, F. Richard, F. Amiot and P. Delobelle**, **2016**. Sensitivity of the residual topography to single crystal plasticity parameters in Berkovich nanoindentation on FCC nickel. *International Journal of Plasticity*, 77:118–140. ISSN 07496419. doi: 10.1016/j.ijplas.2015.10.002.

[Ren20] **E. Renner, A. Bourceret, Y. Gaillard, F. Amiot, P. Delobelle and F. Richard**, **2020**. Identifiability of single crystal plasticity parameters from residual topographies in Berkovich nanoindentation on FCC nickel. *Journal of the Mechanics and Physics of Solids*, 138:103916. ISSN 00225096. doi: 10.1016/j.jmps.2020.103916.

[Rou06] **S. Roux and F. Hild**, **2006**. Stress intensity factor measurements from digital image correlation: post-processing and integrated approaches. *International Journal of Fracture*, 140(1-4):141–157. ISSN 0376-9429, 1573-2673. doi: 10.1007/s10704-006-6631-2.

[Rou20] **S. Roux and F. Hild**, **2020**. Optimal procedure for the identification of constitutive parameters from experimentally measured displacement fields. *International Journal of Solids and Structures*, 184:14–23. ISSN 00207683. doi: 10.1016/j.ijsolstr.2018.11.008.

[RTE22] **RTE**, **2022**. Futurs énergétiques 2050 : les scénarios de mix de production à l'étude permettant d'atteindre la neutralité carbone à l'horizon 2050. Rapport technique.

[Sah09] **J. Sahu, U. Krupp, R. Ghosh and H.-J. Christ**, **2009**. Effect of 475°C embrittlement on the mechanical properties of duplex stainless steel. *Materials Science and Engineering: A*, 508(1-2):1–14. ISSN 09215093. doi: 10.1016/j.msea.2009.01.039.

[Sch39] **P. Schafmeister and R. Ergang**, **1939**. Das Zustandsschaubild Eisen-Nickel-Chrom unter besonderer Berücksichtigung des nach Dauerglühungen auftretenden spröden Gefügebestandteiles. *Archiv für das Eisenhüttenwesen*, 12(9):459–464. doi: https://doi.org/10.1002/srin.193900829.

[Sch12] **C. A. Schneider, W. S. Rasband and K. W. Eliceiri**, **2012**. NIH Image to ImageJ: 25 years of image analysis. *Nature Methods*, 9(7):671–675. ISSN 1548-7091, 1548-7105. doi: 10.1038/nmeth.2089.

[Sci21] **V. F. Sciuti, R. B. Canto, J. Neggers and F. Hild**, **2021**. On the benefits of correcting brightness and contrast in global digital image correlation: Monitoring cracks during curing and drying of a refractory castable. *Optics and Lasers in Engineering*, 136:106316. ISSN 01438166. doi: 10.1016/j.optlaseng.2020.106316.

[Sen22] **A. Senthilnathan, I. Javaheri, H. Zhao, V. Sundararaghavan, M. DeGraef and P. Acar**, **2022**. Uncertainty quantification of metallic microstructures using principal image moments. *Computational Materials Science*, 215:111775. ISSN 0927-0256. doi: https://doi.org/10.1016/j.commatsci.2022.111775.

[Ser18] **P. Serrano, L. Toualbi, P. Kanoute, M. Thomas and A. Couret, 2018**. Approches multi-échelles appliquées à la modélisation du comportement non linéaire des alliages TiAl: vers la prévision de la durée de vie en fatigue de pièces complexes.

[Sha13] **H. Shao, Y. Zhao, P. Ge and W. Zeng, 2013**. In-situ SEM observations of tensile deformation of the lamellar microstructure in TC21 titanium alloy. *Materials Science and Engineering: A*, 559:515–519. ISSN 09215093. doi: 10.1016/j.msea.2012.08.134.

[Sha18] **M. Shakoor, M. Bernacki and P.-O. Bouchard, 2018**. Ductile fracture of a metal matrix composite studied using 3D numerical modeling of void nucleation and coalescence. *Engineering Fracture Mechanics*, 189:110–132. ISSN 00137944. doi: 10.1016/j.engfracmech.2017.10.027.

[Shi17a] **Q. Shi, F. Latourte, F. Hild and S. Roux, 2017**. Backtracking Depth-Resolved Microstructures for Crystal Plasticity Identification—Part 1: Backtracking Microstructures. *JOM*, 69(12):2810–2818. ISSN 1047-4838, 1543-1851. doi: 10.1007/s11837-017-2585-2.

[Shi17b] **Q. Shi, F. Latourte, F. Hild and S. Roux, 2017**. Backtracking Depth-Resolved Microstructures for Crystal Plasticity Identification—Part 2: Identification. *JOM*, 69(12):2803–2809. ISSN 1047-4838, 1543-1851. doi: 10.1007/s11837-017-2586-1.

[Shi18a] **Q. Shi, 2018**. *Experimental and numerical studies on the micromechanical crystal plasticity behavior of an RPV steel*. PhD Thesis, ENS Paris-Saclay.

[Shi18b] **Q. Shi, S. Roux, F. Latourte, F. Hild, D. Loisnard and N. Brynaert, 2018**. On the use of SEM correlative tools for in situ mechanical tests. *Ultramicroscopy*, 184:71–87. ISSN 03043991. doi: 10.1016/j.ultramic.2017.08.005.

[Shi19] **Q. Shi, S. Roux, F. Latourte and F. Hild, 2019**. Estimation of elastic strain by integrated image correlation on electron diffraction patterns. *Ultramicroscopy*, 199:16–33. ISSN 03043991. doi: 10.1016/j.ultramic.2019.02.001.

[Shi21] **Q. Shi, Y. Zhou, H. Zhong, D. Loisnard, C. Dan, F. Zhang, Z. Chen, H. Wang and S. Roux, 2021**. Indexation of electron diffraction patterns at grain boundaries. *Materials Characterization*, 182:111553. ISSN 10445803. doi: 10.1016/j.matchar.2021.111553.

[Sim19] **T. Simonet, 2019**. Caractérisation et modélisation de la microstructure d'un acier inoxydable austéno-ferritique moulé. Master Internship Report 6125-2111-2019-02230-FR, Polytech Montpellier.

[Sla83] **G. Slama, T. Mager and P. Petrequin, 1983**. *Effect of Aging on Mechanical Properties of Austenitic Stainless Steel Castings and Welds: SMIRT POST Conference Seminar 6 Assuring Structural Integrity of Steel Reactor Pressure Boundary Components (Monterey, 1983.08.29-30)*.

[Sne16] **G. C. Sneddon, P. W. Trimby and J. M. Cairney, 2016**. Transmission Kikuchi diffraction in a scanning electron microscope: A review. *Materials Science and Engineering: R: Reports*, 110:1–12. ISSN 0927796X. doi: 10.1016/j.mser.2016.10.001.

[Sol82] **H. D. Solomon and T. M. Devine, 1982**. *Duplex stainless steels : a tale of two phases*. American Society for Metals.

[Sta05] **N. Stanford and P. Bate, 2005**. Crystallographic variant selection in α–β brass. *Acta Materialia*, 53(3):859–867. ISSN 13596454. doi: 10.1016/j.actamat.2004.10.043.

[Sut83] **M. Sutton, W. Wolters, W. Peters, W. Ranson and S. McNeill, 1983**. Determination of displacements using an improved digital correlation method. *Image and Vision Computing*, 1(3):133–139. ISSN 02628856. doi: 10.1016/0262-8856(83)90064-1.

[Sut06] **M. A. Sutton, N. Li, D. Garcia, N. Cornille, J. J. Orteu, S. R. McNeill, H. W. Schreier and X. Li, 2006**. Metrology in a scanning electron microscope: theoretical developments and experimental validation. *Measurement Science and Technology*, 17(10):2613–2622. doi: 10.1088/0957-0233/17/10/012. Publisher: IOP Publishing.

[Sut07] **M. A. Sutton, N. Li, D. Garcia, N. Cornille, J. J. Orteu, S. R. McNeill, H. W. Schreier, X. Li and A. P. Reynolds, 2007**. Scanning Electron Microscopy for Quantitative Small and Large Deformation Measurements Part II: Experimental Validation for Magnifications from 200 to 10,000. *Experimental Mechanics*, 47(6):789–804. ISSN 0014-4851, 1741-2765. doi: 10.1007/s11340-007-9041-0.

[Sut13] **M. A. Sutton, 2013**. Computer Vision-Based, Noncontacting Deformation Measurements in Mechanics: A Generational Transformation. *Applied Mechanics Reviews*, 65(5):050802. ISSN 0003-6900, 2379-0407. doi: 10.1115/1.4024984.

[Suz91] **T. Suzuki, S. Takeuchi and H. Yoshinaga, 1991**. *Dislocation Dynamics and Plasticity*, volume 12 of *Springer Series in Materials Science*. Springer Berlin Heidelberg, Berlin, Heidelberg. ISBN 978-3-642-75776-1 978-3-642-75774-7. doi: 10.1007/978-3-642-75774-7.

[Tam78] **H. Tamura, S. Mori and T. Yamawaki, 1978**. Textural Features Corresponding to Visual Perception. *IEEE Transactions on Systems, Man, and Cybernetics*, 8(6):460–473. ISSN 0018-9472. doi: 10.1109/TSMC.1978.4309999.

[Tan03] **M. Tane, T. Ichitsubo, H. Ogi and M. Hirao, 2003**. Elastic property of aged duplex stainless steel. *Scripta Materialia*, 48(3):229–234. ISSN 1359-6462. doi: https://doi.org/10.1016/S1359-6462(02)00388-3.

[Tas14a] **C. Tasan, M. Diehl, D. Yan, C. Zambaldi, P. Shanthraj, F. Roters and D. Raabe, 2014**. Integrated experimental–simulation analysis of stress and strain partitioning in multiphase alloys. *Acta Materialia*, 81:386–400. ISSN 13596454. doi: 10.1016/j.actamat.2014.07.071.

[Tas14b] **C. Tasan, J. Hoefnagels, M. Diehl, D. Yan, F. Roters and D. Raabe, 2014**. Strain localization and damage in dual phase steels investigated by coupled in-situ deformation experiments and crystal plasticity simulations. *International Journal of Plasticity*, 63:198–210. ISSN 07496419. doi: 10.1016/j.ijplas.2014.06.004.

[Tat08] **S. Tateyama, Y. Shibuta and T. Suzuki, 2008**. A molecular dynamics study of the fcc–bcc phase transformation kinetics of iron. *Scripta Materialia*, 59(9):971–974. ISSN 1359-6462. doi: https://doi.org/10.1016/j.scriptamat.2008.06.054.

[Tay34] **G. I. Taylor, 1934**. The mechanism of plastic deformation of crystals. Part I.—Theoretical. *Proceedings of the Royal Society of London. Series A, Containing Papers of a Mathematical and Physical Character*, 145(855):362–387. ISSN 0950-1207, 2053-9150. doi: 10.1098/rspa.1934.0106.

[Tik77] **A. N. Tikhonov and V. I. Arsenin, 1977**. *Solutions of ill-posed problems*. Winston. ISBN 0-470-99124-0.

[Tom13] **Z. Tomičevć, F. Hild and S. Roux, 2013**. Mechanics-aided digital image correlation. *The Journal of Strain Analysis for Engineering Design*, 48(5):330–343. ISSN 0309-3247, 2041-3130. doi: 10.1177/0309324713482457.

[Ton21] **V. S. Tong and T. B. Britton, 2021**. TrueEBSD: Correcting spatial distortions in electron backscatter diffraction maps. *Ultramicroscopy*, 221:113130. ISSN 0304-3991. doi: https://doi.org/10.1016/j.ultramic.2020.113130.

[Tra82] **A. Trautwein and W. Gysel, 1982**. Influence of Long-Time Aging of CF8 and CF8M Cast Steel at Temperatures Between 300 and 500°C on Impact Toughness and Structural Properties. In *Stainless Steel Castings*, pages 165–165–25. ASTM International, 100 Barr Harbor Drive, PO Box C700, West Conshohocken, PA 19428-2959. ISBN 978-0-8031-0740-3. doi: 10.1520/STP28441S.

[Tse22] **E. Tsekpuia, 2022**. *Développement et implémentation numérique d'un modèle d'homogénéisation élasto-viscoplastique pour des aciers austéno-ferritiques vieillis*. Ph.D. thesis, Université de Lorraine.

[TSL16] **TSL, 2016**. Orientation Imaging Microscopy (OIM) - Manual.

[Ust17] **I. Ustyuzhaninov, W. Brendel, L. Gatys and M. Bethge, 2017**. What does it take to generate natural textures? In *International Conference on Learning Representations*.

[Var18] **R. Vargas, J. Neggers, R. Canto, J. Rodrigues and F. Hild, 2018**. Comparison of two full-field identification methods for the wedge splitting test on a refractory. *Journal of the European Ceramic Society*, 38(16):5569–5579. ISSN 09552219. doi: 10.1016/j.jeurceramsoc.2018.07.039.

[Veh79] **H. Vehoff and P. Neumann, 1979**. In situ sem experiments concerning the mechanism of ductile crack growth. *Acta Metallurgica*, 27(5):915–920. ISSN 00016160. doi: 10.1016/0001-6160(79)90126-3.

[Ver95] **B. Verhaeghe, 1995**. *Étude microstructurale des modes de déformation et de rupture d'un acier austénoferritique vieilli thermiquement*. PhD Thesis.

[Ver96] **B. Verhaeghe, Y. Brechet, F. Louchet, J.-P. Massoud and D. Touzeau, 1996**. Internal stresses in an austenoferritic duplex stainless steel. *Physica Status Solidi (a)*, 153(1):47–56. ISSN 00318965, 1521396X. doi: 10.1002/pssa.2211530104.

[Ver97] **B. Verhaeghe, F. Louchet, Y. Bréchet and J.-P. Massoud, 1997**. Damage and rupture mechanisms in an austenoferritic duplex steel. *Acta Materialia*, 45(5):1811–1819. ISSN 13596454. doi: 10.1016/S1359-6454(96)00330-8.

[Ver09] **K. Verbeken, L. Barbé and D. Raabe, 2009**. Evaluation of the Crystallographic Orientation Relationships between FCC and BCC Phases in TRIP Steels. *ISIJ International*, 49(10):1601–1609. ISSN 0915-1559, 1347-5460. doi: 10.2355/isijinternational.49.1601.

[Ver17] **J. Verma and R. V. Taiwade, 2017**. Effect of welding processes and conditions on the microstructure, mechanical properties and corrosion resistance of duplex stainless steel weldments—A review. *Journal of Manufacturing Processes*, 25:134–152. ISSN 15266125. doi: 10.1016/j.jmapro.2016.11.003.

[Ver22] **T. Vermeij, J. Verstijnen, T. R. y Cantador, B. Blaysat, J. Neggers and J. Hoefnagels, 2022**. A nanomechanical testing framework yielding front&rear-sided, high-resolution, microstructure-correlated SEM-DIC strain fields. doi: 10.48550/ARXIV.2201.08249. Publisher: arXiv Version Number: 1.

[Wan09] **Y. Q. Wang, M. A. Sutton, H. A. Bruck and H. W. Schreier, 2009**. Quantitative Error Assessment in Pattern Matching: Effects of Intensity Pattern Noise, Interpolation, Strain and Image Contrast on Motion Measurements. *Strain*, 45(2):160–178. ISSN 00392103, 14751305. doi: 10.1111/j.1475-1305.2008.00592.x.

[Wan16] **Y. Wang, Y. Yao, Z. Wang, Y. Jin, X. Zhang and J. Liu, 2016**. Thermal ageing on the deformation and fracture mechanisms of a duplex stainless steel by quasi in-situ tensile test under OM and SEM. *Materials Science and Engineering: A*, 666:184–190. ISSN 09215093. doi: 10.1016/j.msea.2016.04.051.

[Wan19] **D. Wang, J. Jin, Q. Li and X. Wang, 2019**. An Accurate Method for Crystallographic Reconstruction of Parent Austenite from Inherited Martensite in a Low-Alloy Steel. *Crystals*, 9(7):358. ISSN 2073-4352. doi: 10.3390/cryst9070358.

[Wan21] **F. Wang, M. P. Echlin, A. A. Taylor, J. Shin, B. Bammes, B. D. Levin, M. De Graef, T. M. Pollock and D. S. Gianola, 2021**. Electron backscattered diffraction using a new monolithic direct detector: High resolution and fast acquisition. *Ultramicroscopy*, 220:113160. ISSN 03043991. doi: 10.1016/j.ultramic.2020.113160.

[Was35] **G. Wassermann, 1935**. Über den Mechanismus der α-γ-Umwandlung des Eisens. 17:149–155.

[Wat98] **O. Watanabe, H. M. Zbib and E. Takenouchi, 1998**. Crystal plasticity: micro-shear banding in polycrystals using voronoi tessellation. *International Journal of Plasticity*, 14(8):771–788. ISSN 0749-6419. doi: https://doi.org/10.1016/S0749-6419(98)00022-9.

[Wec59] **M. S. Wechsler, 1959**. On the theory of martensitic transformations. The generalized lattice invariant shear and the degeneracy of solutions for the cubic to tetragonal transformation. *Acta Metallurgica*, 7(12):793–802. ISSN 0001-6160. doi: https://doi.org/10.1016/0001-6160(59)90095-1.

[Wil06] **A. J. Wilkinson, G. Meaden and D. J. Dingley, 2006**. High-resolution elastic strain measurement from electron backscatter diffraction patterns: New levels of sensitivity. *Ultramicroscopy*, 106(4-5):307–313. ISSN 03043991. doi: 10.1016/j.ultramic.2005.10.001.

[Wri06] **S. I. Wright, 2006**. Random thoughts on non-random misorientation distributions. *Materials Science and Technology*, 22(11):1287–1296. ISSN 0267-0836, 1743-2847. doi: 10.1179/174328406X130876.

[Wri15] **S. Wright, D. Field and M. Nowell, 2015**. Post processing effects on GND calculations from EBSD-based orientation measurements. *IOP Conference Series: Materials Science and Engineering*, 89:012049. ISSN 1757-8981, 1757-899X. doi: 10.1088/1757-899X/89/1/012049.

[Xu15] **Y. Xu, L. Yu, H. Xu, H. Zhang and T. Nguyen, 2015**. Vector Sparse Representation of Color Image Using Quaternion Matrix Analysis. *IEEE Transactions on Image Processing*, 24(4):1315–1329. ISSN 1057-7149, 1941-0042. doi: 10.1109/TIP.2015.2397314.

[Yan10] **J. Yang, J. Goldstein, J. Michael, P. Kotula and E. Scott, 2010**. Thermal history and origin of the IVB iron meteorites and their parent body. *Geochimica et Cosmochimica Acta*, 74:4493–4506. doi: 10.1016/j.gca.2010.04.011.

[Yar14] **V. A. Yardley and E. J. Payton, 2014**. Austenite–martensite/bainite orientation relationship: characterisation parameters and their application. *Materials Science and Technology*, 30(9):1125–1130. doi: 10.1179/1743284714Y.0000000572. Publisher: Taylor & Francis _eprint: https://doi.org/10.1179/1743284714Y.0000000572.

[Yer10] **A. Yershova, S. Jain, S. M. LaValle and J. C. Mitchell, 2010**. Generating Uniform Incremental Grids on *SO* (3) Using the Hopf Fibration. *The International Journal of Robotics Research*, 29(7):801–812. ISSN 0278-3649, 1741-3176. doi: 10.1177/0278364909352700.

[Yue90] **H. Yuen, J. Princen, J. Illingworth and J. Kittler, 1990**. Comparative study of Hough Transform methods for circle finding. *Image and Vision Computing*, 8(1):71–77. ISSN 02628856. doi: 10.1016/0262-8856(90)90059-E.

[Zam12] **C. Zambaldi, Y. Yang, T. R. Bieler and D. Raabe, 2012**. Orientation informed nanoindentation of α-titanium: Indentation pileup in hexagonal metals deforming by prismatic slip. *Journal of Materials Research*, 27(1):356–367. ISSN 0884-2914, 2044-5326. doi: 10.1557/jmr.2011.334.

[Zeg07] **A. Zeghadi, S. Forest, A.-F. Gourgues and O. Bouaziz, 2007**. Ensemble averaging stress–strain fields in polycrystalline aggregates with a constrained surface microstructure – Part 2: crystal plasticity. *Philosophical Magazine*, 87(8-9):1425–1446. ISSN 1478-6435, 1478-6443. doi: 10.1080/14786430601009517.

[Zha95] **W. Zhang, J. Ge, H. Gong and X. Zhang, 1995**. The variations of martensitic morphology and habit plane in high carbon steel. *Journal de Physique 4*, 5(8,pt1):345–349. ISSN 1155-4339. Place: France.

[Zha08] **Z. Zhao, M. Ramesh, D. Raabe, A. M. Cuitiño and R. Radovitzky, 2008**. Investigation of three-dimensional aspects of grain-scale plastic surface deformation of an aluminum oligocrystal. *International Journal of Plasticity*, 24(12):2278–2297. ISSN 0749-6419. doi: https://doi.org/10.1016/j.ijplas.2008.01.002.

[Zha12] **P. Zhang, M. Karimpour, D. Balint, J. Lin and D. Farrugia, 2012**. A controlled Poisson Voronoi tessellation for grain and cohesive boundary generation applied to crystal plasticity analysis. *Computational Materials Science*, 64:84–89. ISSN 09270256. doi: 10.1016/j.commatsci.2012.02.022.

[Zha19a] **Q. Zhang, S. Ma and T. Jing, 2019**. Mechanical Properties of a Thermally-aged Cast Duplex Stainless Steel by in Situ Tensile Test at the Service Temperature. *Metals*, 9(3). ISSN 2075-4701. doi: 10.3390/met9030317.

[Zha19b] **Q. Zhang, A. S. S. Singaravelu, Y. Zhao, T. Jing and N. Chawla, 2019**. Mechanical properties of a thermally-aged cast duplex stainless steel by nanoindentation and micropillar compression. *Materials Science and Engineering: A*, 743:520–528. ISSN 09215093. doi: 10.1016/j.msea.2018.11.112.

[Zha20] **Y. Zhang, L. You, X. Li, J. Zhou and X. Song, 2020**. In-situ investigation of the fatigue crack initiation and propagation behavior of Zircaloy-4 with different hydrogen contents at RT and 300 °C. *Journal of Nuclear Materials*, 532:152065. ISSN 00223115. doi: 10.1016/j.jnucmat.2020.152065.

[Zha21] **L. H. Zhang, M. J. Cheng, X. H. Shi, J. W. Shuai and Z. Z. Zhu, 2021**. Bain and Nishiyama–Wassermann transition path separation in the martensitic transitions of Fe. *RSC Adv.*, 11(5):3043–3048. doi: 10.1039/D0RA09332G. Publisher: The Royal Society of Chemistry.

[Zhe22] **X. Zheng, T. Sun, J. Zhou, R. Zhang and P. Ming, 2022**. Modeling of Polycrystalline Material Microstructure with 3D Grain Boundary Based on Laguerre–Voronoi Tessellation. *Materials*, 15(6):1996. ISSN 1996-1944. doi: 10.3390/ma15061996.

[Ör17] **C. Örnek, J. Walton, T. Hashimoto, T. L. Ladwein, S. B. Lyon and D. L. Engelberg, 2017**. Characterization of 475°C Embrittlement of Duplex Stainless Steel Microstructure via Scanning Kelvin Probe Force Microscopy and Magnetic Force Microscopy. *Journal of The Electrochemical Society*, 164(6):C207–C217. ISSN 0013-4651, 1945-7111. doi: 10.1149/2.0311706jes.

Appendix A

Cast ingot and specimens

A.1 Cast ingot

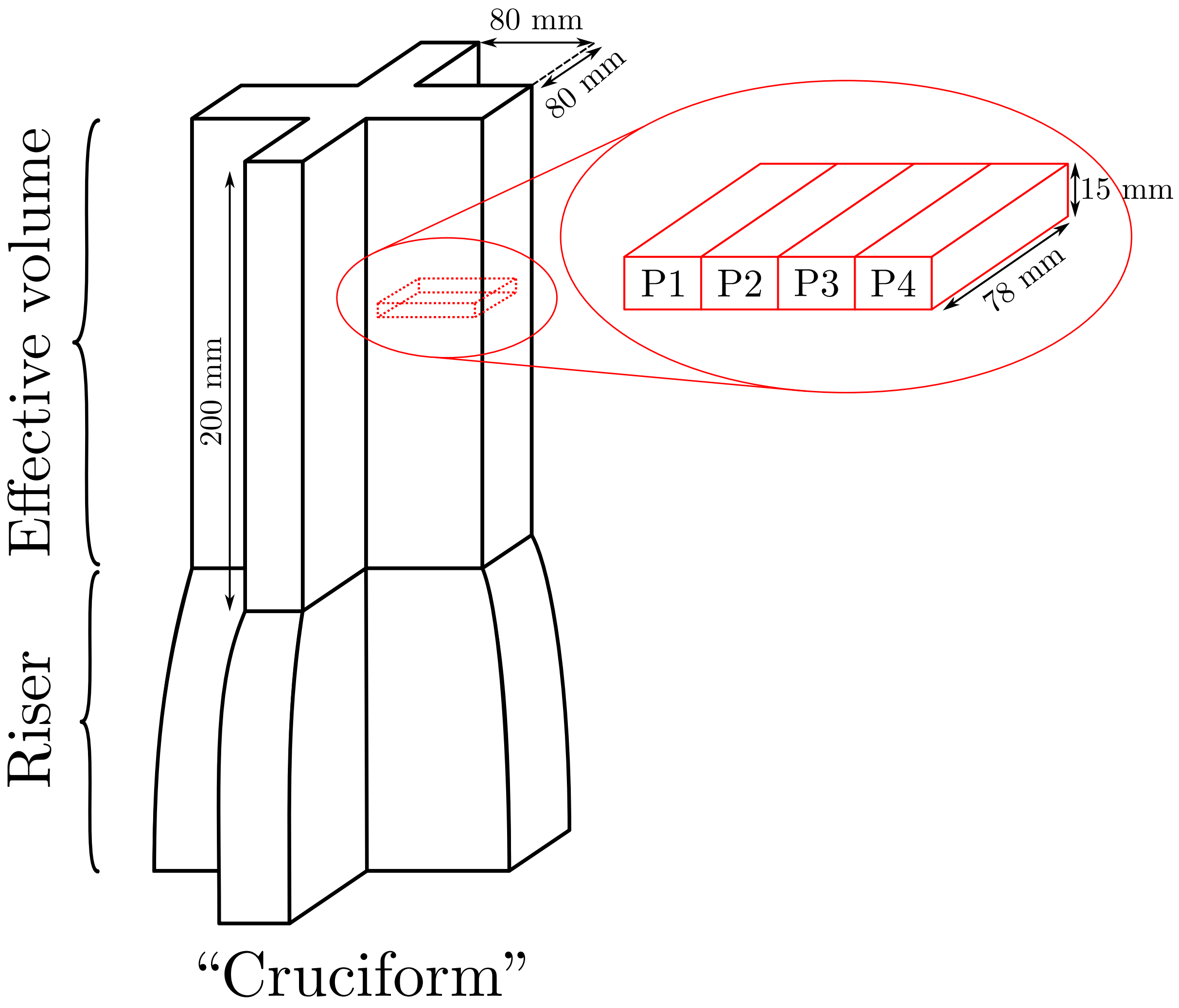

Figure A.1: Schematic view of the cruciform ingot and position of slabs taken from the effective volume.

The specimens used for the mechanical tests are machined from slabs taken from the effective volume of a cruciform cast ingot. Figure A.1 shows the cruciform ingot geometry and the position of the slabs from which specimens are further removed using EDM. Each slab is subjected to an accelerated thermal aging at 350°C. Corresponding designations are given in Table A.1.

Table A.1: Accelerated aging time at 350°C for the four considered slabs P1, P2, P3 and P4, and equivalent operating times of cold and hot legs components.

	P1	P2	P3	P4
Aging time (h)	0	1000	2500	10000
Cold leg equivalent (h)	0	67300	168000	673000
Hot leg equivalent (h)	0	4530	11300	45300

A.2 Specimen machining

The following sampling plan is used to machine specimens from the four slabs (Figure A.2). In each slab, six specimens are machined using EDM:

- 2 macroscopic cylindrical tensile specimens labeled Pi-TC6-1 and Pi-TC6-2 (i = 1...4).
- 4 *in situ* tensile specimens labeled Pi-IS-1, Pi-IS-2, Pi-IS-3 and Pi-IS-4 (i = 1...4).

The two specimen geometries are given in Section A.3 and A.4.

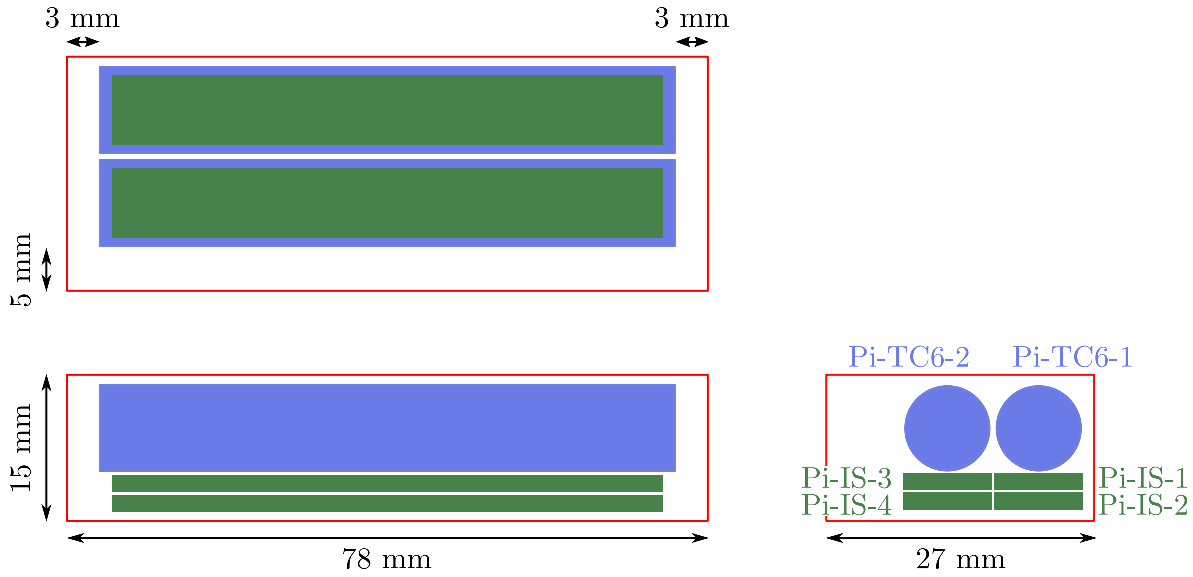

Figure A.2: Schematic view of specimen positions in each slab Pi (i = 1...4).

A.3 "TC6" tensile specimen geometry

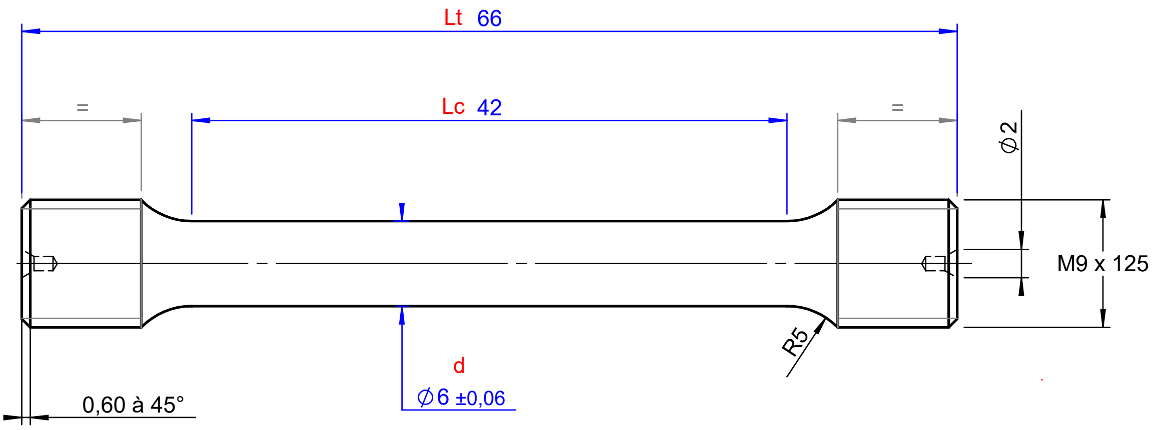

Figure A.3: TC6 specimen geometry. Dimensions are in millimeters.

A.4 *in situ* tensile specimen geometry

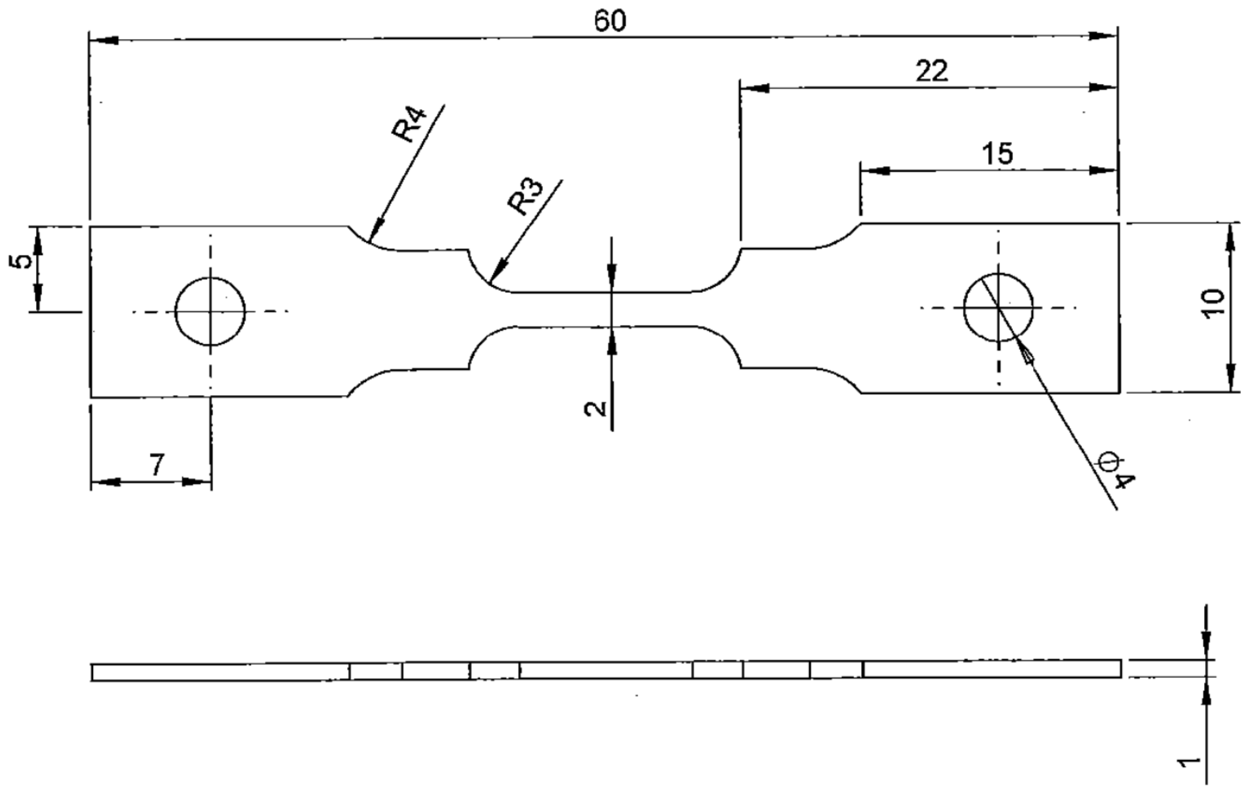

Figure A.4: *in situ* specimen geometry. Dimensions are in millimeters.

A.5 TC6 specimen labels

Additional macroscopic tensile specimens were added to the study in Chapter 3.1. The designations used correspond to EDF references given in Table A.2.

Table A.2: Correspondance between current and EDF labels of tested TC6 specimens presented in Figure 3.2

Current label	EDF label
P1-1	2274-P1-TC6-2
P1-2	2274-P1-TC6-1
P1-3	2269-D1654-1-1-TC6-2
P1-4	2269-D1654-1-13-TC6-2
P2-1	2274-P1-TC6-1
P2-2	2274-P1-TC6-2
P3-1	2274-P1-TC6-1
P4-1	2274-P1-TC6-1
P4-2	2269-1-6-C4-TC-1
P4-3	2269-2-4-C4-TC-1

Appendix B

Digital image correlation framework

B.1 Introduction

The complexity of modern systems requires increased control of their mechanical characteristics. More and more complex experiments are set up to reproduce the working conditions of components of interest for validation or verification purposes. In this context, it is often necessary to measure displacement or strain fields. These measurements are not accessible with classical techniques (extensometer, strain gauge). DIC is one of the popular techniques to measure displacement fields [Sut83]. It is a versatile and non-contact technique based on registering two images [Sut13]. These images can be acquired from different sources. To measure 2D fields, optical camera [Sut83], SEM [Sut07], or AFM [Han10] images can be used. Recent advances in the use of tomographic images allowed to measure volume displacement fields accurately [Bul18].

In a broader sense, full-field measurements enabled by DIC permit direct comparison with complex models [Gue14a, Shi18a]. The comparison is usually made between measured and simulated kinematic fields. However, it can also be done between an experimental image and an image of the model itself when the latter is not perfectly known [Men19b]. Thus, DIC reduces the frontier between experiment and modeling. Yet, the registration of two images is not perfect. It is limited by the precision of the image acquisition systems and the artifacts of each technique [Bul18]. It is, therefore, necessary to properly define the formulation of this DIC problem in a framework of high concern for us: solid. Therefore, the method must provide reliable measurements of mechanical fields and quantify the associated uncertainties.

The following sections describe the global DIC approach used for various tasks throughout this study. In particular, it was employed to measure displacement fields during *in situ* tests and to match EBSD data with BSE images. The principle remains the same: the scalar field of both images assumed to carry the same physical information is correlated. The kinematic field, which allows the passage from one image to another, is deduced from this registration.

B.2 DIC principle

The principle of DIC is to register two images captured at two different times, before and during deformation. In the case of surface measurements, the undeformed image f, is a discrete field embedding the initial gray level (GL) distribution of the observed surface. Assuming that its spatial distribution passively follows the in-plane surface displacements, the "deformed image" g is defined through the optical flow equation

$$g(\boldsymbol{x} + \boldsymbol{u}(\boldsymbol{x})) = f(\boldsymbol{x}) \tag{B.1}$$

where $\boldsymbol{u}(\boldsymbol{x})$ is the sought displacement field expressed at each pixel loaction $\boldsymbol{x}$.

Determining $\boldsymbol{u}$ from f and g only is an ill-posed problem. Therefore, additional assumptions about $\boldsymbol{u}$ must be made. Historically, the registration of $\boldsymbol{u}$ was performed by decomposing f in small regular subsets [Sut13]. In these approaches, the registration is performed locally by matching the information in each reference and deformed image subset. In the end, only the mean displacement over the subsets is kept. Continuity of the displacement field is recovered using interpolations, which practically limit the subset size and, therefore, the resolution of the method for a given experimental setup [Wan09, Hil12]. A second approach that followed the development of DIC consists in considering the complete information on the ROI in the processed image. The displacement field is estimated from the minimization of a criterion that satisfies GLs conservation, including all degrees of freedom chosen for $\boldsymbol{u}$ [Bes06]. These approaches are referred to as global approaches. The same type of interpolation as in the local methods may be used, but it has been shown that a finite element mesh is probably the most appropriate choice [Bes06]. Sub-pixel resolutions are reached with finite element-based global DIC [Hil12]. Additionally, the formulation is more robust than local approaches at the cost of more extensive computation time. Considering the complex cases considered throughout the study, this approach is believed to be the most suited to our needs and is therefore the one described in the following.

As discussed in the previous paragraph, $\boldsymbol{u}$ must satisfy Equation (B.1) *i.e.,* $\boldsymbol{u}$ is the displacement field minimizing the L_2 norm of the pixel-wise correlation residual $\eta(\boldsymbol{x}) = f(\boldsymbol{x}) - g(\boldsymbol{x} + \boldsymbol{u}(\boldsymbol{x}))$ over the entire ROI

$$\Phi_c^2 = \sum_{\boldsymbol{x} \in ROI} \eta^2(\boldsymbol{x}) d\boldsymbol{x} \tag{B.2}$$

A finite element framework is considered to decompose $\boldsymbol{u}$ and cope with the ill-posedness of the problem. $\boldsymbol{u}$ is expressed using a set of shape functions $[\boldsymbol{\varphi}]$

$$\boldsymbol{u}(\boldsymbol{x}) = \sum_i u_i \boldsymbol{\varphi}_i(\boldsymbol{x}) = [\boldsymbol{\varphi}(\boldsymbol{x})] \{\boldsymbol{u}\} \tag{B.3}$$

with $\{\boldsymbol{u}\}$ the vector of nodal displacements. Hence, the problem consists in determining the unknown amplitudes u_i. A Gauss-Newton iterative scheme is used for computing successive corrections $\{\delta \boldsymbol{u}\}$, from which results linear systems of equations to be solved

$$[\boldsymbol{H}] \{\delta \boldsymbol{u}\} = \{\boldsymbol{b}\} \tag{B.4}$$

where $\{\delta \boldsymbol{u}\}$ are the iterative corrections to the degrees of freedom $\{\boldsymbol{u}\}$. $[\boldsymbol{H}]$ is the Hessian matrix formed from the dyadic product of sensitivity fields computed from shape functions $\boldsymbol{\varphi}_i(\boldsymbol{x})$ and image gradients $\boldsymbol{\nabla} f(\boldsymbol{x})$

$$H_{ij} = \sum_{\boldsymbol{x} \in ROI} (\boldsymbol{\varphi}_i(\boldsymbol{x}) \cdot \boldsymbol{\nabla} f(\boldsymbol{x})) (\boldsymbol{\varphi}_j(\boldsymbol{x}) \cdot \boldsymbol{\nabla} f(\boldsymbol{x})) \tag{B.5}$$

and $\{\boldsymbol{b}\}$ the second member accounting for the current image residuals

$$b_i = \sum_{\boldsymbol{x} \in ROI} (\boldsymbol{\varphi}_i(\boldsymbol{x}) \cdot \boldsymbol{\nabla} f(\boldsymbol{x})) \eta(\boldsymbol{x}) \tag{B.6}$$

B.2.1 Mechanical regularization

Without additional information, measurements are limited by the uncertainties on f related to the acquisition technique [Hil12]. Increasing the number of degrees of freedom of the mesh is not acceptable since the pixel intensity alone can lead to local minima, which would make the minimization procedure bound to fail. To obtain a better measurement resolution and to become less prone to uncertainties, a regularization method is introduced [Tik77]. It is important to note that the assumption of a continuous field already constitutes already a form of regularization. Choosing a coarse mesh or specific shape functions limiting the number of degrees of freedom is a further form of regularization. However, when a conformal mesh is needed in complex geometries, for example, to resolve nodal displacements at a grain boundary precisely, it is not always straightforward to control the mesh size. Therefore, one needs a mesh-independent regularization, which can be controlled in accordance with different measurement cases. This is the task given to the mechanical regularization introduced in this section.

Naturally, one would like to construct a regularization based on the behavior or properties of the observed specimen. However, it is necessary to simplify and generalize the method, for example, when one wants to correlate two images distorted by non-mechanical fields expected to have certain regularity. Whether it is a mechanical deformation or a physical imaging distortion, the resulting field is often well described by an elastic solution. This is even truer in a mechanical test when we consider an incremental displacement field between two instants where the strain increment is small. We may then consider a tangent modulus equivalent to the incremental behavior between each image.

The regularization scheme implemented in the present DIC approach relies on the equilibrium gap formulation [Cla04]. The mechanical equilibrium in an FE sense is expressed from the vector of nodal forces $\{\boldsymbol{f}\}$ and the stifness matrix $[\boldsymbol{K}]$

$$[\boldsymbol{K}]\{\boldsymbol{u}\} = \{\boldsymbol{f}\} \tag{B.7}$$

It is necessary in this case to consider bulk nodes and surface nodes separately and to introduce cost functions for each of them. By surface, we mean the boundary nodes of the mesh, which in the case of 2D images, ensure the junction between edges. In the absence of external forces, the nodal forces vanish at all bulk nodes. Thus, the equilibrium gap for these nodes consist of minimizing the L_2 norm of $[\boldsymbol{K}]\{\boldsymbol{u}\}$ or equivalently

$$\Phi_m(\{\boldsymbol{u}\}) = \{\boldsymbol{u}\}^\intercal [\boldsymbol{K}]^\intercal [\boldsymbol{K}]\{\boldsymbol{u}\} \tag{B.8}$$

In the case of surface nodes, the external forces are non-zero but unknown. Therefore, a specific regularization term is introduced. The aim is to reduce irregularities and consequently to tend toward uniform tractions on the surface when the regularization is “large”. In a sense, the surface regularization intends to smooth surface fields but is less “physical” than inner node term [Men19a]. The surface regularization term involves the amplitude and orientation of surface normals. It is defined for each surface $\mathcal{S}_i$ as

$$\Phi_{\mathcal{S}_i}(\{\boldsymbol{u}\}) = \{\boldsymbol{u}\}^\intercal \left[\boldsymbol{K}_{\mathcal{S}_i}\right]^\intercal [\boldsymbol{L}] \left[\boldsymbol{K}_{\mathcal{S}_i}\right] \{\boldsymbol{u}\} \tag{B.9}$$

where $[\boldsymbol{L}]$ is the discrete Laplace-Beltrami operator *i.e.*, the L_2 norm of the traction gradient. This operator is computed from two matrices $A_{ij} = \left\langle \boldsymbol{\varphi}_i^{\mathcal{S}}, \boldsymbol{\varphi}_j^{\mathcal{S}} \right\rangle^{-1}$ and $B_{ij} = \left\langle \boldsymbol{\nabla}\boldsymbol{\varphi}_i^{\mathcal{S}}, \boldsymbol{\nabla}\boldsymbol{\varphi}_j^{\mathcal{S}} \right\rangle$ where $\varphi^{\mathcal{S}}(\boldsymbol{x})$ are the "restriction" of the mesh shape functions $\varphi(\boldsymbol{x})$ on sub-order surface elements and $\langle , \rangle$ the L_2-inner product [Men19a]. The stiffness matrix $\left[\boldsymbol{K}_{\mathcal{S}_i}\right]$ is simply the restriction of $[\boldsymbol{K}]$ to surface nodes

$$\left[\boldsymbol{K}_{\mathcal{S}_i}\right] = \left[\boldsymbol{D}_{\mathcal{S}_i}\right] [\boldsymbol{K}] \tag{B.10}$$

with $\left[\boldsymbol{D}_{\mathcal{S}_i}\right]$ a diagonal binary matrix valued one for any *dof* belonging to $\mathcal{S}_i$ and zero otherwise.

Taking into account the three terms Φ_c, Φ_m and $\Phi_{\mathcal{S}_i}$ introduced above requires an appropriate weighting. To this end, the total functional Φ_t is introduced [Tom13]

$$\Phi_t(\{\boldsymbol{u}\}) = \frac{\omega_c}{\omega_t}\tilde{\Phi}_c(\{\boldsymbol{u}\}) + \frac{\omega_m}{\omega_t}\tilde{\Phi}_m(\{\boldsymbol{u}\}) + \sum_i \frac{\omega_{\mathcal{S}_i}}{\omega_t}\tilde{\Phi}_{\mathcal{S}_i}(\{\boldsymbol{u}\}) \tag{B.11}$$

with

$$\tilde{\Phi}_c(\{\boldsymbol{u}\}) = \frac{\Phi_c(\{\boldsymbol{u}\})}{\Phi_c(\{\boldsymbol{v}\})} \ , \ \tilde{\Phi}_m(\{\boldsymbol{u}\}) = \frac{\Phi_m(\{\boldsymbol{u}\})}{\Phi_m(\{\boldsymbol{v}\})} \ , \ \tilde{\Phi}_{\mathcal{S}_i}(\{\boldsymbol{u}\}) = \frac{\Phi_{\mathcal{S}_i}(\{\boldsymbol{u}\})}{\Phi_{\mathcal{S}_i}(\{\boldsymbol{v}\})} \tag{B.12}$$

The weighting terms $\omega_.$ and the normalized residuals are defined from a trial displacement field $\boldsymbol{v}(\boldsymbol{x})$ of prescribed wave vector $\boldsymbol{k}$

$$\boldsymbol{v}(\boldsymbol{x}) = \sin(2\pi\boldsymbol{k}\cdot\boldsymbol{x}) \tag{B.13}$$

A dimensional analysis [Tom13] shows that $\Phi_c(\{\boldsymbol{v}\})$ does not depend on $\boldsymbol{k}$. Conversely, the $\Phi_m(\{\boldsymbol{v}\})$ and $\Phi_{\mathcal{S}_i}(\{\boldsymbol{v}\})$ dependence on wavelength is of fourth order. Accordingly, the weighting terms are defined as

$$\omega_c = 1 \ , \ \omega_m = (\xi_m|\boldsymbol{k}|)^4 \ , \ \omega_{\mathcal{S}_i} = (\xi_{\mathcal{S}_i}|\boldsymbol{k}|)^4 \ , \text{ and } \omega_t = \omega_c + \omega_m + \sum_i \omega_{\mathcal{S}_i} \tag{B.14}$$

where $\xi_.$ are regularization lengths associated with each term in the total functional, namely, the correlation residual, the equilibrium gap and the surface regularization. Higher $\xi_{\cdot}$ values lead to stronger influence of the regularization associated with the corresponding term in the total cost function and consequently to lower fluctuations.

B.2.2 Brightness and contrast correction

Sometimes, the experimental setting does not allow conservation of gray levels (Equation (B.1)) to be satisfied. Depending on the environment and image acquisition technique, variations inherent to the test are sometimes observed. They may be due to temperature changes [May12], an evolution of the acquisition system [Sut07], or simply variations in brightness [Hil12], for example. Since the conservation of gray levels is a central assumption of DIC, such variations may prevent convergence or introduce artifacts in the measured field.

From the perspective of the global approach, a change in gray levels introduces an additional deviation in the correlation residual η. Provided that a first estimation of the displacement field $\boldsymbol{u}$ is obtained when matching the two images without correction on the gray level, we may define $\eta_{\boldsymbol{u}}$, the correlation residual associated with this first estimation uncluding gray level changes. The first estimation may be corrected using a correction field $q(\boldsymbol{x}, f)$. A first natural correction for gray level images is to consider a pixel-wise affine correction [Sci21]

$$q(\boldsymbol{x}, f) = b(\boldsymbol{x}) + (1 + c(\boldsymbol{x}))f(\boldsymbol{x}) \tag{B.15}$$

where b and c are the brightness and contrast correction fields, respectively. To keep consistency with the displacement field, these two fields can be suitably decomposed on a finite element mesh

$$b(\boldsymbol{x}) = \sum_i b_i \psi_i(\boldsymbol{x}) \ , \ c(\boldsymbol{x}) = \sum_i c_i \psi_i(\boldsymbol{x}) \tag{B.16}$$

where $\psi_i(\boldsymbol{x})$ are the associated shape functions, b_i and c_i the nodal amplitudes to be determined. The amplitudes are obtained similarly to the determination of the nodal displacement amplitudes u_i by minimizing the L_2 norm of the "*b.c.c.* residual"

$$\eta_{bcc}(\boldsymbol{x}) = \eta_{\boldsymbol{u}}(\boldsymbol{x}) + q(\boldsymbol{x}, f) \tag{B.17}$$

The determination of the correction fields enables for the definition of a corrected reference image $\hat{f}$

$$\hat{f}(\boldsymbol{x}) = b(\boldsymbol{x}) + (1 + c(\boldsymbol{x}))\, f(\boldsymbol{x}) \tag{B.18}$$

From this gray level correction scheme, several coupling scenarios with the determination of the displacement field can be considered. They are, of course, dependent on the type of image considered and the nature of the test. The protocol involving both mechanical regularization and *b.c.c.* correction for the measurement of mechanical fields from SEM images is summarized in the next section.

B.3 DIC scheme for SEM images

The mechanical fields of interest are those between the first image f_1 and image f_k. However, the displacement levels between two images taken at two distant loading states may be large. In this case, the registration of the two images is challenging. Yet, enough images are acquired during the test such that the displacements between two consecutive images are small enough to be well measured. Consequently, a first estimate of the displacement field between images f_1 and f_k is given by

$$\boldsymbol{u}_k = \sum_{i=1}^{k-1} \boldsymbol{u}_i^I \tag{B.19}$$

where $\boldsymbol{u}_i^I$ is the incremental displacement field calculated between images f_i and f_{i+1}.

Incremental computations are conducted highly efficiently in the case of the BSE images acquired in this study, without any mechanical regularization (displacement fields converged in less than 5 iterations of the Gauss-Newton algorithm (Equation (B.4)). However, the major drawback of this calculation is that the measurement errors (acquisition noise, topography and channeling contrast effects) are cumulated between the different instants and may become significant in the end. It is, therefore, necessary to make a direct registration of images f_1 and f_k. As previously stated, this calculation is, by nature, complicated when displacements become large. It cannot be conducted without proper initialization. To this end, the global DIC procedure is in two-steps. The "easy" incremental method is conducted as a first estimate. Then, a direct registration is performed using the displacement field computed in a first part as an initialization in the minimization procedure. Then the final displacement field is simply

$$\boldsymbol{u}_k = \boldsymbol{u}_k^D \tag{B.20}$$

In general, no mechanical regularization was necessary for achieving good convergence of the iterative algorithm. In the most complicated cases where regularization was necessary, an incremental approach was adopted. The total displacement field between images f_1 and f_k can be significant. Therefore, the associated penalty term assumes elasticity, thus further distancing the measured field from the actual field. Several approaches are possible to avoid too severe penalty. For example, one can relax the regularization weight by performing a slightly regularized calculation initialized with a more strongly regularized displacement field. Here it has been chosen to write the penalty term not with the total displacement field (of the direct calculation) but on the incremental field. Thus the penalty term is more moderate during the test.

In the present protocol, the speckle signature is sufficiently prevalent that it is almost completely decoupled from gray level changes due to channeling contrast and topography. In this case, *b.c.c.* is not used to obtain a better solution for the displacement field but rather to ensure that the changes in brightness and contrast do not introduce errors in the measured displacement field. We, therefore, proceed with each image to determine the difference between the displacement fields with and without *b.c.c.* The back-deformed image $g_k(\boldsymbol{x} + \boldsymbol{u}_k(\boldsymbol{x}))$ is computed and compared to $f_1(\boldsymbol{x})$ to get the first correlation residual estimate $\eta_{\boldsymbol{u}_k}$. The latter is lowered by introducing the correction fields $b_k(\boldsymbol{x})$ and $c_k(\boldsymbol{x})$. Last, the corrected image $\hat{f}_1 = b_k(\boldsymbol{x}) + (1 + c_k(\boldsymbol{x}))\, f_1(\boldsymbol{x})$ is computed and used in a second registration procedure with g_k from which the displacement field u_k^{bcc} is obtained. The comparison between u_k and u_k^{bcc} has shown that brightness and contrast changes are significant during the test but still have a negligible effect on the displacement field measurement. Therefore, we can quantify the changes in gray levels due to topography changes and prove that the displacement field is well resolved despite their presence. There are interpretable physical data included in these fields, but they were not explored in this study.

Figure B.1 summarizes the whole procedure for measuring displacement fields at the surface of CDSS *in situ* tensile tests from BSE images.

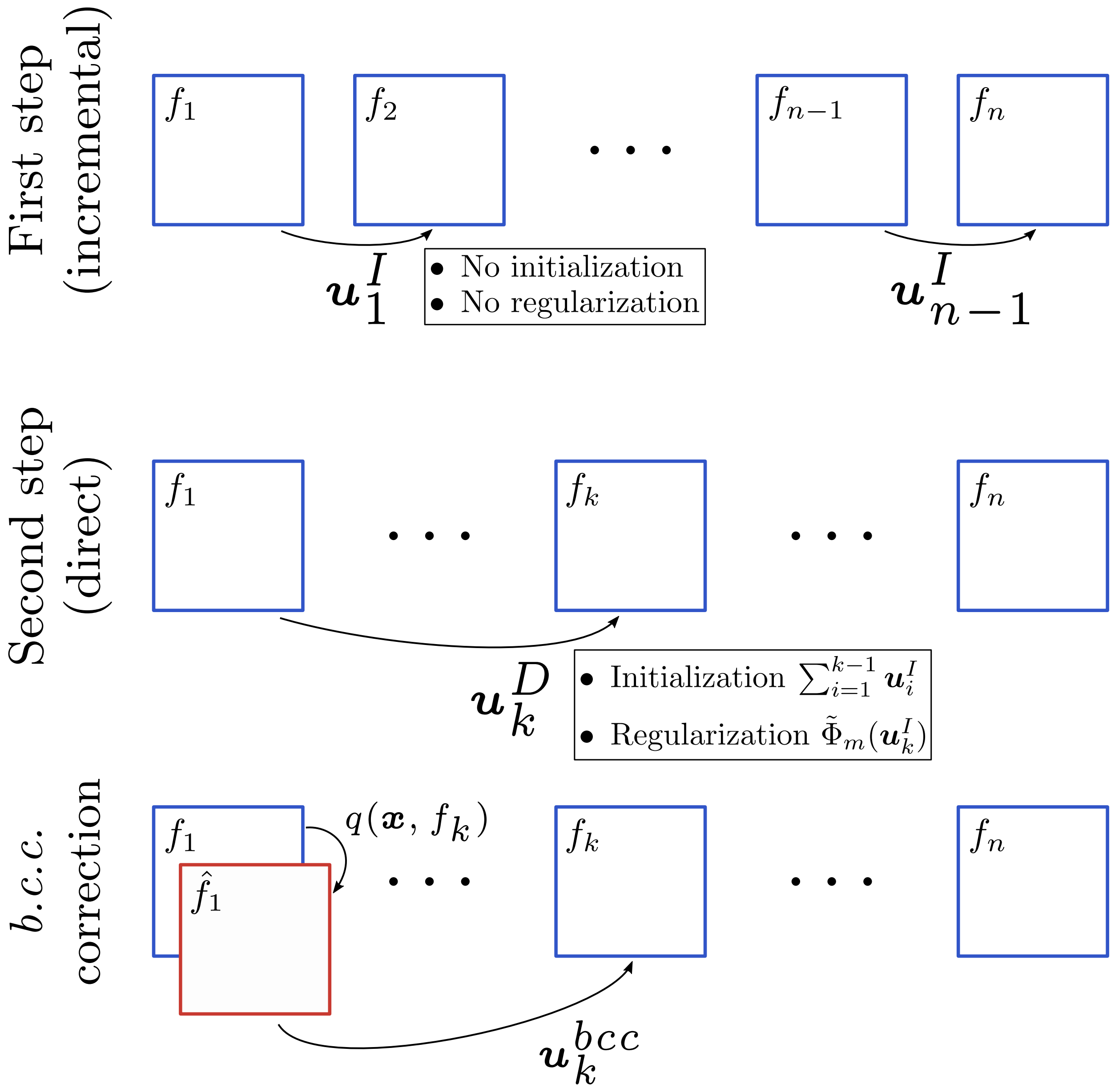

Figure B.1: Schematic view of the DIC procedure for SEM images.

Titre: Modélisation du comportement d'un acier inoxydable austéno-ferritique moulé vieilli par une approche multi-échelle

Mots clés: Aciers duplex, essais *in situ*, EBSD, plasticité cristalline, mesures de champs, MEF

Résumé:

Le suivi de l'intégrité mécanique des composants en acier inoxydable austéno-ferritique moulés des réacteurs à eau préssurisée est d'une importance majeure. La justification de leur tenue mécanique est nécessaire afin d'assurer le bon fonctionnement des centrales nucléaires sur le long terme. Le comportement de ces composants est notamment altéré par un vieillissement thermique à la température de fonctionnement. Ce vieillissement entraîne la fragilisation d'une des deux phases constitutive du matériau par une modification de sa microstructure. La cinétique d'évolution des propriétés de résistance à la rupture avec le vieillissement thermique a été abondamment étudiée et modélisée par des approches empiriques. Cependant, les mécanismes de déformation et d'endommagement à l'origine de la rupture ne sont pas entièrement compris à cause de la complexité de la microstructure. Une caractérisation cristallographique détaillée ainsi que des essais mécaniques *in situ* sont réalisés afin de prendre en compte les particularités de la microstructure et de comprendre leurs effets sur le comportement pour les intégrer dans un modèle micromécanique. Ce modèle a pour objectif de prendre en compte les propriétés multi-échelles de la microstructure ainsi que l'effet du vieillissement.

La complexité de l'agencement des deux phases des aciers étudiés est analysée à partir de données cristallographiques acquises par EBSD (Electron Backscattered Diffraction). Grâce à la compréhension des mécanismes de solidification et au développement de post-traîtements spécifiques, les différentes échelles de la microstrucure ainsi que leurs paramètres cristallographiques et morphologiques déterminants pour modéliser le comportement sont mis en avant.

Dans l'objectif de corréler les champs simulés du modèle aux observations expérimentales, des mesures de champs par corrélation d'images numériques (CIN) sont utilisées pour enrichir les données acquises par les essais *in situ*. Ces mesures doivent permettre de mettre en évidence les mécanismes de déformation et leur redistribution aux différentes échelles de la microstructure et par conséquent de mesurer des déplacements du micromètre à quelques millimètres. Une méthode robuste de mesure et de superposition avec les données acquises par EBSD a été développée à cet effet. Elle permet d'expliciter l'importance de la répartition des phases et de leurs propriétés sur l'hétérogénéité des champs mécaniques et des variations avec le vieillissement thermique.

Enfin, un modèle simplifié s'appuyant sur les observations précédantes est proposé. L'objectif est d'y inclure les paramètres fondamentaux à la compréhension du comportement et de décrire la répartition des champs de contrainte et de déformation dans les phases et aux interfaces menant à l'initiation de l'endommagement.

Title: Development of a multi-scale approach for modeling cast duplex stainless behavior

Keywords: Duplex stainless steels, *in situ* mechanical tests, EBSD, crystal plasticity, field measurements, FEM

Abstract:

Monitoring pressurized water reactors components is of interest in long-term operation of nuclear power plants. Components made out of cast duplex stainless steel are subjected to aging when held at their operating temperature. In the long run, thermal aging results in embrittlement due to a microstructural evolution of one of the two phases constituting duplex steels. Kinetics and impact of aging on fracture mechanics have been studied to a great extent using empirical approaches. However, deformation and damage mechanisms leading to fracture are not yet fully understood owing to the complexity of duplex steels microstructure. In this context, a microstructural characterization is performed jointly to *in situ* mechanical characterization to build a consistent micromechanical model taking the multi scale aspect of the microstructure into account. Eventually, the model must provide a fine description of the material mechanical behavior including the aged state.

The microstructure complexity is apprehended by the means of Electron Backscattered Diffraction (EBSD) acquisitions. The material history and specific post-processings of crystallographic data allow microstructural scale properties that are decisive in describing the mechanical behavior to be unveiled.

In order to relate crystal plasticity finite element computations to experimental observations, digital images correlation (DIC) is used to provide full-field measurements. They must be consistent with the deformation mechanisms of the studied steels and be accurate enough to capture small deformation mechanisms occurring in each phase (at a micrometre scale) and the resulting displacements at the larger scale of the microstructure (several millimetres). Accordingly, a rigorous approach has been developed to accurately capture large displacement fields and precisely superimpose them with crystallographic data obtained by EBSD. Such measurements highlight the heterogeneous mechanical behavior of the two phases according to their crystallographic orientation, morphology and thermal aging.

Finally, a consistent simplified finite element model is proposed to reproduce fundamental features of the mechanical behavior and to further describe stresses and strains distribution in the two phases at the origin of damage nucleation.